City Research Online

City, University of London Institutional Repository

Design and analysis of supercritical carbon-dixoide axial turbines

Salma Salah

Submitted for the degree of Doctor of Philosophy
City, University of London
School of Science and Technology
Department of Engineering

April 2023

To my lovely mother and life companion Mervat Abouelazm, with love. I hope I have made you proud and become the person you wanted me to be. If I had a wish, it would be to have you by my side at this moment. Thanks a lot mum for your support and devotion for our family. Without you, this would not have been possible. You are always in my heart and I always send you my prayers.

. . . .

Declaration

I hereby declare that this thesis has not been and will not be submitted in whole or in part to another University for the award of any other degree. I also grant powers of discretion to the University Librarian to allow the thesis to be copied in whole or in part without further reference to the author. This permission covers only single copies made for study purposes, subject to normal conditions of acknowledgement.

Signature:

Salma Salah.

Acknowledgements

First, I would like to thank my supervisors Prof Abdulnaser Sayma and Dr Martin White for their continuous help and support throughout the PhD journey at City University of London. Their technical support, guidance and feedback allowed me to develop my knowledge and widen my research skills from various perspectives. Their insightful comments and encouragement were crucial for keeping the work momentum and allowing me to reach the set goals within the specified time frame. Thanks for making my overall PhD experience fulfilling and rewarding.

Thanks to Prof Osama Badr and Prof Ahmed Abdelazim who paved my early steps in the academic career path and helped me to pursue this career effectively. Thanks extend to Prof Essam Eldin Khalil and Prof Ahmed Elbaz for their continuous and valuable advice that was always available whenever requested.

I would also like to thank my colleagues, post-doctoral researchers and fellow PhD students, Tala El Samad, Mohsen Ghavami, Hicham Chibli, Abdelrahman Abdeldayem, Omar Selim, Omar Aqel, Ahmad Abuhaiba, Stephen Majebi, Shahrbanoo Amiri and Elli Anemogianni-Sinanidi for the support provided in hard times and the interesting discussions and fun-time that usually helped in reducing the work stress.

Thanks extend to my close friends for providing the necessary support throughout this by offering technical and non-technical advice; Ge Elzamlout, Mahmoud Magdy, Ahmed Emam and Aamir Gulistan.

Last but not least, acknowledgements go to my family; my mother, father and siblings. Their devoted support and prayers along with their psychological support throughout my graduate studies are the main reason behind my successes including the completion of this research.

Special thanks to Radwa Salah and Sherif Elsoudy for their unwavering presence and support throughout my PhD journey, especially during the late stages of completing and submitting my work.

Abstract

Supercritical carbon dioxide (sCO_2) blends have been found to be promising for enhancing the performance of power cycles for concentrated solar power (CSP) applications; allowing for up to 6 percentage points enhancement in cycle efficiency with respect to a simple recuperated CO_2 cycle, depending upon the nature of the used blend and the choice of cycle configuration. Despite this promising potential, there have been limited studies into axial sCO_2 turbine design in comparison to growing interest in the design of radial turbines for small-scale applications. This thesis focuses on the mean-line flow path design of a multi-stage axial turbine operating with sCO_2 blends for installation in a 100 MWe CSP plant.

A multi-stage axial mean-line turbine design tool is first developed. The tool is coupled with multiple loss models which are classically used for axial turbine designs to predict the performance over a range of operating conditions. Following this, the aerodynamic design tool is constrained with both mechanical and rotordynamic design criteria to allow for developing feasible flow path designs from an industrial standpoint. The mean-line design methodology is verified against multiple case studies from the literature in addition to 3D CFD simulation results.

The prediction capability of the loss models is investigated for conventional air, sCO_2 and ORC turbines over a range of scales given that these models were originally developed for conventional working fluids such as air and steam. Following the loss model comparison, multiple flow paths are designed for sCO_2 based blends, namely $CO_2/TiCl_4$, CO_2/C_6F_6 and CO_2/SO_2. Ultimately, similitude theory is used to generate the turbine off-design performance maps and evaluate the turbine performance over a range of operating conditions.

The Aungier loss model was found to be suitable for predicting the performance of large-scale sCO_2 based turbines whilst the Dunham and Came and Craig and Cox models were found to over-predict and under-predict the turbine performance with respect to the Aungier model respectively. Using the Aungier loss model, selected blend and cycle configuration for the 100 MWe CSP plant, a 130 MW 14-stage axial turbine is designed for a precompression cycle operating with CO_2/SO_2 blend. This design is capable of achieving a total-to-total efficiency of 93.8%. A good agreement is achieved between the mean-line design tool and CFD results with a maximum difference of 0.5% in the total-to-total efficiency. Ultimately, the off-design performance of the turbine showed large deviations in the predicted total-to-total efficiencies compared to the CFD results. A maximum deviation of 23% is obtained in the total-to-total efficiency at a mass flow rate of 52% of the design point attributed to the flow separation occurring at the downstream stages.

To conclude, this thesis presents detailed insights into the main mean-line design and performance analysis aspects of large-scale axial turbines for sCO_2 based applications. This has considered aerodynamic, mechanical and rotor-dynamic design aspects in addition to the off-design performance analysis.

Contents

vi

Abbreviations

AMDC	Ainley and Mathieson & Dunham and Came
ASF	Axial scale factor
AN	Aungier
BC	Boost compressor
BP	Balance piston
CSP	Concentrated-solar power
CFD	Computational fluid dynamics
CAPEX	Capital expenditure
CCP	Combined cooling and power
C	Compressor
CC	Craig and Cox
CD	Constrained design
DC	Dunham and Came
3D	Three-dimensional
1D	One-dimensional
DNI	Direct normal irradiance
DGS	Dry gas seals
EoS	Equation of state
GE	General Electric
HTF	Heat transfer fluid
HPT	High-pressure turbine
HP-HE	High pressure heat exchanges
HP-HE	Low pressure heat exchanges
HTR	High-temperature recuperator
HT2C	High temperature heat to power conversion facility
IST	integrated system test
KO	Kacker and Okapuu
KAIST	Korea Advanced Institute of Science and Technology
KAERI	Korea Atomic Energy Research Institute
KIER	Korea Institute or Energy Research
LCOE	Levelised cost of electricity
LPT	low-pressure turbine
LTR	Low-temperature recuperator
MENA	Middle East and North Africa
MISQP	Mixed-Integer Sequential Quadratic Programming
MC	Main compressor
NNL	Naval Nuclear Laboratory

NCD	Non-constrained design
ORC	Organic Rankine cycle
OPEX	Operation expenditure
PR	Peng-Robinson
PSRK	Predictive Soave-Redlich-Kwong
PV	Photovoltaic
RPM	Revolutions per minutes
PHX	Primary heat exchanger
PC	primary cooler
RE	Renewable energy
RSM	Response surface methodology
RSF	Radial scale factor
RMCI	Recompression main compressor intecooling cycle
RC	Re-compressor
Re	Reynolds number
R	Recuperator
(R)	Radial turbomachinery configuration
(A)	Axial turbomachinery configuration
SB	Soderberg
ST	Solar tower
SP	Size parameter
SPT	Solar power tower
SR	Slenderness ratio
SNL	Sandia National Laboratory
SRK	Soave-Redlich-Kwong
sCO_2	Supercritical carbon dioxide.
TIT	The Tokyo Institute of Technology's
TIT	Total inlet temperature
TAC	Turbine alternator compressor
TG	Turbine Generator
TPB	Tilt pad bearing
T	Turbine
VLE	Vapour-liquid equilibrium
TC	Thrust collar
WSF	Weight scale factor

Nomenclature

Roman Symbols

A	Mean blade area [m^2]	
A_k	Total effective area of clearance [m^2]	
b_x	Axial chord [m]	
c	Blade chord length [m]	
c_p	Specific heat [J/kg.K]	
C	Absolute velocity [m/s]	
D	Diameter [m]	
e	Mean radius of curvature ratio	
$f_{(AR)}$	Aspect ratio function [-]	
F_k	Efficiency debit factor [-]	
Δh_{os}	Enthalpy drop across the stage [J/kg]	
Δh_o	Enthalpy drop across the entire turbine [J/kg]	
h	Blade height [m]	
h	Enthalpy [J/kg]	
i	Incidence angle [°]	
K_{mod}	Experience factor [-]	
K_{inc}	Correction for incidence effects [-]	
K_M	Correction for Mach number effects [-]	
K_p	Correction for compressibility effect [-]	
K_{RE}	Correction for Reynolds number effects [-]	
k	Ratio of specific heats [-]	
k_s	Blade surface roughness [-]	
l	Axial flow path length [m]	
m	Mass [kg]	
$\dot{m}$	Mass flow rate [kg/s]	
M	Mach number [-]	
n	The number of turbine stages [-]	
n_s	Specific speed [rad]	
N	Rotational speed [RPM]	
o	Throat opening [m]	
P	Pressure [Pa]	
$\dot{Q}$	Volume flow rate [m^3/s]	
r	Radius [m]	

r_m	Mean blade radius [m]
s	Blade pitch [m]
t_e	Blade trailing edge thickness projection on plane of wheel [-]
t_2	Trailing edge blade thickness [-]
ss	Blade spacing [-]
T	Temperature [°C]
U	Peripheral blade speed [m/s]
s	Blade pitch [m]
V	Total volume [m^3]
w	Relative velocity [m/s]
W_T	The total weight of the machine
ΔW	The difference in weight [Kg]
ΔW	Specific work [J/kg]
X_i	Dopant concentration [%]
Y	Total pressure loss coefficient [-]
$\overline{Y}$	Preliminary loss [-]

Greek Symbols

α	Absolute flow angle [°]
$\alpha_1{}'$	Blade angle [°]
β	Relative flow angle [°]
β_g	Gauging angle [°]
β	Relative flow angle [°]
$\Delta \phi^2$	Kinetic energy loss coefficient [-]
δ	Flow deviation angle [°]
Δ	Diffusion angle [°]
ζ	Enthalpy loss coefficient [-]
ζ^*	Nominal loss coefficient [-]
η_{tt}	Total to total Efficiency [%]
η_{ts}	Total to static Efficiency [%]
η_b	Blading efficiency [%]
η_0	Efficiency at zero tip clearance [%]
θ	Boundary layer thickness [-]
Λ	Degree of reaction [-]
ρ	Gas density [kg/m^3]
σ	Bending strese [Pa]
τ	Torque [-]

ϕ	Flow coefficient [-]	
ψ	Loading coefficient [-]	
ω	Blade row rotational speed [rad/sec]	

Subscripts

a	Axial velocity component
BR	Rotor blading
BS	Stator blading
b	Balancing drum
f	flow path
hub	Blade hub
cr	Critical conditions
inc	Correction for off-design incidence effects
IC	Inner casing
M	Correction for Mach number effects
m	Mean value
OC	Outer casing
R	Rotor
ref	Reference case
S	Stator
S	shaft
S	Secondary flow loss
o	Throat
P	Profile loss
PE	Post-expansion loss
R	Rotor
Re	Reynolds number
$shock$	Shock loss
cl	Clearance loss
tip	Blade tip
TE	Trailing edge loss
w	Tangential velocity component
$0rel$	Total relative
rel	Relative
tt	Total-to-total efficiency
0	Total thermodynamic property
1	Inlet condition
2	Stator exit condition & Rotor inlet condition
3	Rotor exit condition

List of Tables

List of Figures

xix

This page is left intentionally blank

1 Introduction

1.1   Background

The need for sustainable and clean energy supplies, with low carbon emissions, has led to the declaration of multiple sustainable development goals by the united nations among which increasing the share of renewable energy substantially in the global energy mix was acknowledged. This goal was declared to move towards a green energy future and hence avoid environmental damages [1]. According to the Paris historic climate agreement, the global temperature rise should be maintained below 2 °C within this century to tackle the global energy crisis and climate change effectively [2]. Hence, the current annual energy-related CO_2 emissions must be reduced by over 70% by 2050. Nonetheless, global energy consumption is experiencing a rapid increase and most of the world's energy supply comes from fossil fuel sources which are responsible for carbon dioxide (CO_2) emissions [3]. From this standpoint, advancing renewable energy harvesting techniques is crucial for satisfying the increasing energy demand and reducing the level of greenhouse gases; where renewable are anticipated to contribute to an overall reduction in CO_2 level by 30% by 2050, with respect to 2012 [4].

Among the various renewable energy (RE) technologies, concentrated solar power systems (CSP) can potentially influence future energy scenarios by providing low carbon footprints and renewable electric energy. Concentrated solar Power (CSP) converts solar energy into heat, which is then converted to electricity using a heat engine. Though of this potential, the current Levelised Cost of Electricity (LCOE) of CSP, ranging from 150 to 200 €/ kWh_e, is still not competitive among other renewable energy technologies (i.e. Photovoltaic (PV), wind) [5]. Therefore, despite the early development of CSP technology, which was first developed in 1913 [6], only 5.5 GW of CSP power capacities have been available worldwide compared to 100 GW of PV power by 2019 [7]. Therefore, current research studies are interested in further developing the CSP technology through performance enhancement and cost reduction.

CSP systems convert solar energy into heat by using a mirror or lens to focus the sun's rays that fall onto a given area to a much smaller receiver area in order to generate heat, which is subsequently converted into electricity through the power block (Figure 1.1). The key components of the CSP plant are the solar collector, the solar receiver and the power block alongside the thermal energy-storage systems. Among the different solar collector technologies such as parabolic trough, linear Fresnel collector, dish and solar tower (ST), solar power tower systems provides the highest system efficiency due to the high working fluids temperature; point focus power systems that allow for higher working fluids temperatures and hence higher system efficiency [8].
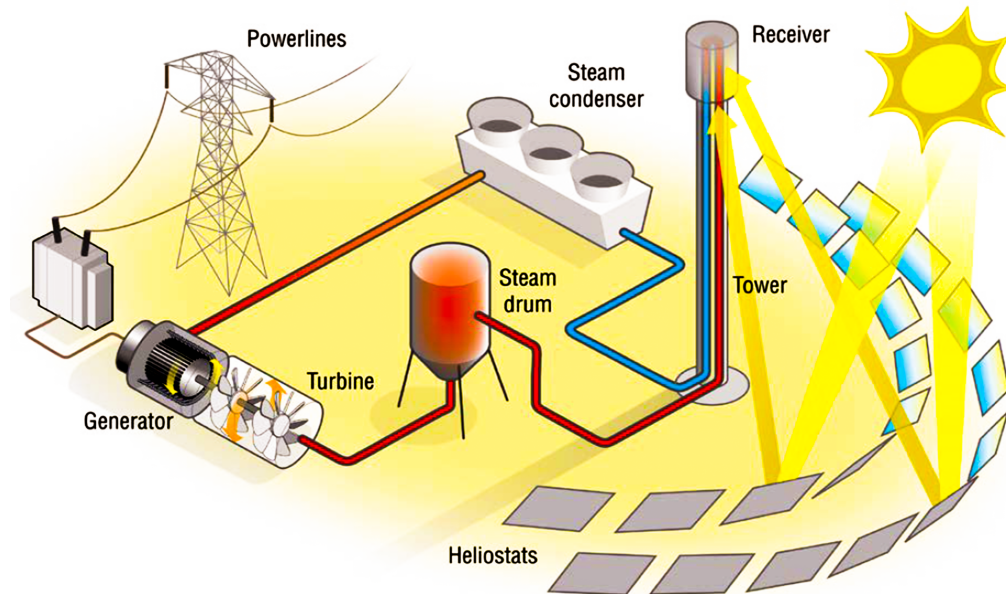
Figure 1.1: Typical heliostat field connected to simple Rankine cycle through thermal energy storage tanks [9]

Commercially available ST plants are based on two main configurations, direct and indirect. In the direct configuration, the steam serves as the working fluid in the power block and the heat transfer fluid (HTF) in the receiver. Whilst, in the indirect configuration the HTF is heated up by solar energy in the receiver and then transfers thermal energy to the power block. Direct steam generation configuration is beneficial for heating up the cycle working fluids up to the maximum temperature attained by the solar collector. Therefore, it avoids exergy losses and the additional costs associated with the intermediate heat exchanger between the ST and the power cycle. Nonetheless, this technology is penalised by the lack of commercially available compatible thermal energy storage systems in compar-

ison to the available storage system for the HTF at low prices [5].

For the indirect configurations, CSP power plants utilise HTF working fluids such as oil, salt, and steam as heat transfer fluids to transfer energy from the solar collector to the power block. However, the thermodynamic properties of those working fluids limit the performance of the power plant. For example, the synthetic oil and nitrate salts have a temperature limit of 400 and 590 °C respectively [10]. Solar tower systems have a higher concentration ratio in comparison to parabolic trough systems and this makes them more suited for employing molten salt heat transfer fluid. Using molten salt allows for achieving higher system performance due to its capability of reaching a maximum temperature of 590 °C compared to a maximum one of 400 °C achieved for parabolic trough systems operating with diathermic oil as HTF (max temperature of 400 °C). The higher operating temperature allows for higher system performance and hence, reduced LCOE [5].

Therefore, to enhance the ST technology performance, developments are needed at the solar energy storage receiver and the power block fronts. With more emphasis on the power block efficiency, achieving high cycle performance may require operating at a temperature above 600 °C to achieve a power block efficiency greater than 50% [8] For the current power systems, steam Rankine cycles have been used in concentrated-solar thermal plants where a maximum efficiency power block efficiency of 42% has been achieved at a maximum steam temperature of 540 °C [11]. In this regard, the sCO_2 is found to be promising as a heat transfer fluid and power cycle working fluid.

1.2 Thermodynamic cycles for CSP applications

The efficiency of thermodynamic cycles depends on the individual processes that make up the whole cycle and hence, the maximum cycle efficiency is achieved for reversible processes in comparison to irreversible ones at the same operating conditions. For given cycle conditions, the maximum cycle efficiency can be achieved by maximising the temperature difference between cycle limits; increasing the maximum cycle temperature and decreasing the minimum cycle temperature. The minimum cycle temperature is a function of the available cooling fluid conditions; which is the ambient air in dry cooling applications

such as CSP plants. Regardless of the implemented configurations, all the ST power plants implement the steam cycles for converting the thermal energy to electric energy; where using water as the working fluid adds a constraint for the maximum operating cycle temperature [5]. Hence, to achieve an efficiency greater than 42% for CSP plants, the steam should operate at a temperature greater than 540 °C [8]. Increasing the steam temperature and pressure (above the critical pressure) results in having supercritical steam cycles which have proven to result in higher efficiency by up to 4.5%. Unfortunately, this would result in an increase in the power block capital cost and in slower plant dynamics (less flexibility) during startup and shutdown [11].

In this regard, Supercritical CO_2 (sCO_2) cycles have been proposed due to their potential to outperform traditional steam cycles for CSP applications if maximum cycle temperatures exceed approximately 550°C [12, 13, 14, 15] due to the enhanced performance and the reduced cost. The efficiency enhancement enabled by supercritical CO_2 cycles is primarily a result of reducing compression work through increasing the working fluid density within the compression process, alongside the subsequent positive impact on the potential for internal heat recovery. This can be enabled by either condensing the working fluid or by performing the compression process close to the critical point of CO_2. Nonetheless, achieving this is not feasible for CSP plants inasmuch as they are typically located in hot, arid regions lacking water/steam-cooling resources. Alternatively, the critical temperature of the working fluid can be increased by doping sCO_2 with other fluids, hence enabling condensation at elevated temperatures of the cooling medium [13, 16, 17, 18].

1.3   SCARABEUS project scope and objectives

This study is a part of the Horizon 2020 SCARABEUS project [19]. The SCARABEUS project, and hence this study, aims to demonstrate the potential of using CO_2 blends for large-scale CSP plants in the order of 100 MW$_e$.

Using CO_2 blends enables condensation at elevated temperatures, as a result of achieving elevated critical temperature for the working fluid, which would increase the conversion efficiencies of supercritical CO_2 power cycles to values of around 50%. Hence, up to

six percentage points increase in cycle efficiency can be achieved compared to a simple re-cuperated CO_2 cycle depending on the implemented cycle configuration and the nature of the selected blend [20]. This results in a significant reduction in the overall capital expen-ditures (CAPEX) of the solar plant due to the reduction of the solar field size for a given power output. Using CO_2 blends has the potential to reduce the CAPEX by 30% and op-erational expenditures (OPEX) by 35% compared to to state-of-the-art steam cycles. This results in a Levelised cost of energy less than 96 €/ MWh [19].

The main components of supercritical CO_2 condensation cycles, similar to conven-tional power plants, are pumps, expanders and heat exchangers; including recuperators and primary and heat rejection heat exchangers. Designing sCO_2 cycle components is a distinctive process with respect to steam and gas turbine cycles owing to the physical properties of the sCO_2 fluid including the high power density, high pressure, low kine-matic viscosity and the abrupt properties changes near the critical point. Meaning that the size of most system components can be considerably reduced, which leads to a smaller plant footprint and possibly lower capital costs. Nevertheless, these properties leads to components with features that challenge the standard components design [21].

Consequently, research interest in sCO_2 cycles increased dramatically during the last decades with more focus on new cycle proposals and components design (such as heat exchangers and turbo-machinery). Considering that the turbine efficiency significantly af-fects the overall plant performance, it is important to explore the design space of CO_2 turbines. This should allow for examining the turbine performance to provide better pre-dictability for the cycle performance and cost of the proposed technology.

1.3.1 Supercritical CO_2 turbines

Turbine design methodologies are well established and have been extensively discussed in many textbooks and publications [22, 23]. However, non-conventional working fluids such as CO_2 impose some challenges and uncertainties on applying those conventional design methodologies. Therefore, turbine design for sCO_2 and sCO_2 based working fluids is still a developing field compared to the well-established designs for air and steam turbines.

Turbines are classified into radial and axial configurations. In radial turbines, the fluid flows radially to the rotating shaft whereas in the axial turbine the fluid is axial along the shaft through the mounted blading. Radial turbines are known to be suitable for small-scale applications with a power ranging from 300 kW to up to 25 MW, allowing for the expansion of working fluid in one single stage [14]. Operating at a higher power rating results in an increased mass flow rate whereas axial turbines proved to be competitive to radial turbines. Hence, the overall aim of this project is to develop design and optimisation tools for 100 MW scale sCO_2 multi-stage axial turbine design for concentrated-solar power applications for power cycles.

1.4 Contribution to knowledge

The SCARABEUS project [19] is composed of seven work packages. Work package three aims to develop turbomachinery components that work efficiently with CO_2 blends across a range of anticipated operating conditions for a 100 MW_e CSP plant. To achieve this goal, work package three is split into four different tasks, which include producing a preliminary turbine design, creating an optimised and detailed design, conducting a cost assessment to ensure economic viability of the produced design, and performing off-design performance analysis to understand how the turbine will operate away from the design point. City, University of London (CITY) and Baker Hughes are collaborating to accomplish the four tasks; where the CITY team are focusing on the producing aerodynamic flow path design including mean-line and CFD based methods. Furthermore, the CITY team have helped in providing the turbine boundary conditions alongside the project partners at the University of Seville.

Two research frameworks are involved in the development of the aerodynamic flow path design. The first research framework is concerned with performing the preliminary sizing and optimisation of the turbine taking into account the trade-off between the aerodynamic performance and the mechanical robustness of the machine. Whilst the second framework is concerned with generating the 3D blade profile and carrying out CFD simulations for the flow path, as well as investigating the different loss mechanisms. This thesis

focuses on addressing the first research framework of work package three, which involves developing the mean-line design of the axial flow turbine operating with CO_2 blends.

To accomplish this, a mean-line design tool is created in MATLAB; where the steady-state mass, energy, and momentum equations are solved at a constant mean diameter and constant hub diameter to obtain the turbine geometry. To evaluate the aerodynamic performance of the turbine, the design tool is integrated with multiple loss models. These models are used to quantify the energy losses that the working fluid experiences during the expansion in the stator and rotor blade rows. The tool is developed to optimise the turbine aerodynamic design along with complying with a set of different design constraints, which include mechanical and rotordynamic constraints. Two different subroutines are developed in MATLAB for designing the turbine using both design techniques: constant mean diameter and constant hub diameter. In addition, multiple subroutines are developed for the loss models implemented in this study. As a part of this work, the mean-line design model is verified against the CFD results, which are interpreted within the second research framework of work package three of the SCARABEUS project.

1.5 Thesis structure and scientific contributions

This thesis consists of seven chapters that cover the progress of this work (Chapters 1 to 7). The introduction and literature review, including the identified research gaps, are presented in Chapters 1 and 2 respectively.

The turbine design methodology is presented in Chapter 3. Within this chapter, preliminary axial turbine design methodology and empirical loss models are all grouped to develop the turbine design that complies with a set of mechanical and rotordynamic design constraints. This chapter includes the verification results of the implemented preliminary turbine design methodology with respect to multiple cases from the literature. The implemented design methodology allows for developing optimised flow path designs considering mechanical and rotordynamic constraints that were set based on industrial recommendations.

Bearing in mind that the empirical loss models were initially developed for turbines operating with conventional working fluids such as air and steam, Chapter 4 focuses on exploring the deviation between the performance predictions of the loss models for non-conventional working fluids; where turbines may differ in design and operation than conventional air or steam turbines. Additionally, this chapter aims to investigate the effect of the turbine scale on the trends in the performance prediction of these models owing to the differences in the fluid flow characteristics.

Chapter 5 presents the results of the effect of sCO_2 blends and their corresponding molar fraction on the achievable turbine efficiency considering aerodynamic, rotor-dynamic and mechanical design constraints. Furthermore, the aim of this chapter extends to examining the differences in the turbine flow path designs generated for pure CO_2 compared to CO_2 blends taking into account aerodynamic, rotordynamic and mechanical design aspects, as assessed during the mean-line design process. Ultimately, the effect of changing turbine design variables, including load coefficient, flow coefficient and degree of reaction on the flow path design and overall aerodynamic performance is also investigated.

In Chapter 6, the off-design performance analysis methodology alongside the application of similitude theory are discussed. This chapter aims to investigate the performance of a selected flow path design operating with CO_2/SO_2 over a range of off-design conditions. Hence, performance maps are presented at the end of the chapter. Finally, the conclusions of this research are summarised in Chapter 7 and recommendations for future work are presented.

1.6   Publications

Journal publications

- **S. I. Salah**, M. A. Khader, M. T. White, and A. I. Sayma, "Mean-line design of a supercritical CO_2 micro axial turbine," *Applied Sciences, vol. 10, no. 15, p. 5069, 2020.*

- **S. I. Salah**, M. T. White, and A. I. Sayma, "A comparison of axial turbine loss mod-

els for air, sCO_2 and ORC turbines across a range of scales," *International Journal of Thermofluids, 2022.*

- **S. I. Salah**, F. Crespi, M. T. White, A. M. noz, A. Paggini, M. Ruggiero, D. Sánchez, and A. I. Sayma, "Axial turbine flow path design for concentrated solar power plants operating with CO_2 blends," *Applied Thermal Engineering, 2023.*

- A. AbdElDayem, **S. I. Salah** , M. T. White, and A. I. Sayma, "A modified loss break-down approach for axial turbines operating with blended supercritical carbon dioxide". *Accepted: the Journal of Engineering for Gas Turbines and Power, 2023.*

Conference publications

- O. Aqel, **S. I. Salah**, A. AbdElDayem, M. T. White, and A. I. Sayma, "Blended supercritical carbon dioxide turbines: opportunities and challenges," *In Proceedings of SEEP2022, 12-16th September 2022, London, United Kingdom.*

- V. Illyés, **S. I. Salah**, A. Abdeldayem, A. Werner, A. I. Sayma, G. Manzolini and M. Haider, "Dry-Cooled Rankine Cycle Operated with Binary Carbon Dioxide Based Working Fluids". *In 28th Solarpaces conference, 27-30 September 2022, Albuquerque, USA.*

- A. AbdElDayem, **S. I. Salah**, O. Aqel, M. T. White, and A. I. Sayma, "Design of a 130 MW axial turbine operating with a supercritical carbon dioxide mixture for the SCARABEUS project," *In 15th European Turbo-machinery conference, 24-28th April 2023, Budapest, Hungry.*

- **S. I. Salah** , M. T. White, and A. I. Sayma, "A Comparison of Flow Path Designs for a 130 MW Axial Turbine Operating with Pure CO_2 and CO_2 Mixtures," *In ASME turbo-expo 2023, 26-30th June 2023, Boston, USA.*

Poster presentations

- **S. I. Salah**, M. A. Khader, M. T. White, and A. I. Sayma, "Supercritical CO_2 axial turbine design for CSP applications". *Department of Engineering, City University of London, Northampton Square, London EC1V0HB, United Kingdom.*

- **S. I. Salah**, M. T. White, and A. I. Sayma, "Axial turbine flow path design for the SCARABEUS CSP power plant operating with CO_2 mixtures". *Department of Engineering, City University of London, Northampton Square, London EC1V 0HB, United Kingdom.*

Technical reports

- M. Khader, **S. I. Salah**, O. Aqel, M. T. White, and A. I. Sayma, "D3.1 – preliminary design of the full-scale axial turbine and pump," tech. rep., *SCARABEUS Consortium, May 2020.*

- **S. I. Salah**, A. Abdeldayem, M. T. White, A. I. Sayma, A. Paggini, M. Ruggiero, M. Fiori, and L. Cosi, "D3.2– aerodynamic design and optimisation," tech. rep., *SCARABEUS Consortium, September 2021.*

This page is left intentionally blank

2 Literature Review

2.1 Introduction

In this chapter, a summary of the advances in cycle analysis and the different aspects of turbine design are discussed for CSP applications with reference to the recent research activities in the field; this discussion includes covering recent research outcomes in regard to the selection of candidate sCO_2 blends for these applications. This chapter includes a review of the thermodynamics of sCO_2 cycles in addition to the different aspects of sCO_2 axial turbine modelling. The scope of this chapter extends to reviewing the aspect of sCO_2 turbine designs; where a detailed review of the existing prototypes, conceptual designs and mechanical design challenges are addressed. At the end of the literature review, a summary is presented to highlight the main research gaps and hence, the research objectives are defined.

2.2 Thermodynamics of supercritical CO_2 cycles

Thermodynamic cycles are categorised into Brayton and Rankine cycles; in the Brayton cycle, the working fluid exists in a single phase (gaseous form). Whilst in the Rankine cycle, the working fluid experiences a phase change throughout the cycle. A simple Brayton cycle consists of four components namely, compressor, turbine and high and low-pressure heat exchanger as illustrated in Figure 2.1a. The gas is firstly compressed in the compressor then heated inside the high-pressure heat exchanger and finally expanded inside the turbine. As a result of that, the turbine produces work where a fraction of this work is used to drive the compressor. The Rankine cycle consists of four components namely, pump, boiler, turbine and condenser (Figure 2.1b). The liquid water is pumped to the boiler where the heat addition process takes place to produce super-heated vapour. The generated steam is used to drive the turbine to produce work and then it condenses into the liquid phase, where the heat rejection takes place, to be pumped again into the cycle [24].

The performance of concentrated-solar power (CSP) systems is significantly affected
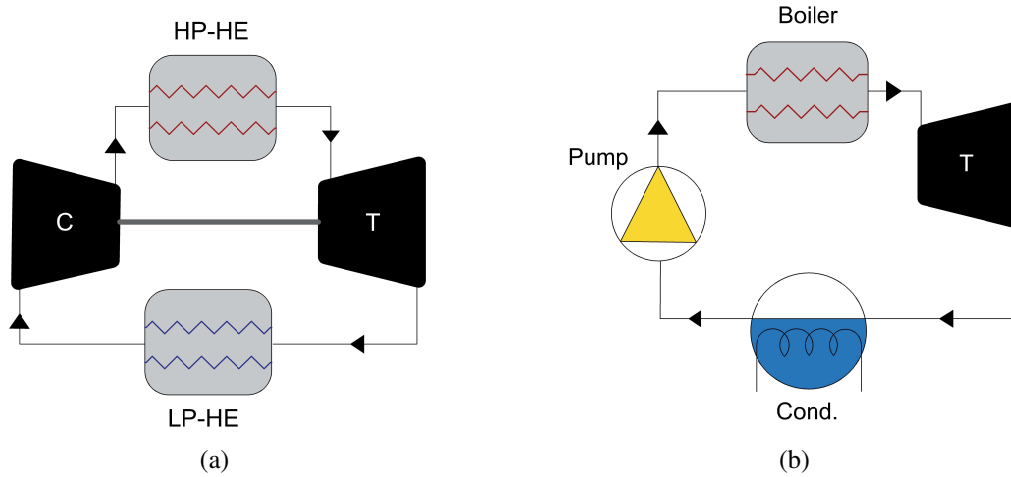
Figure 2.1: (a) Brayton cycle with a compressor (C), high pressure heat exchanges (HP-HE), low pressure heat exchanges (LP-HE), and turbine (T) (b) Rankine cycle with a pump, boiler, condenser (cond.), and turbine (T).

by the efficiency of the power block; where a maximum cycle efficiency of 42% can be obtained by conventional subcritical steam Rankine cycles operating at a maximum steam temperature of 540°C [11]. Further enhancement in conventional steam cycle efficiency, by up to 4.5%, can be achieved by operating at supercritical conditions. Unfortunately, this would result in an increase in the power block capital cost [11].

2.2.1   Supercritical CO$_2$

Supercritical carbon dioxide (sCO$_2$) is a fluid state of CO$_2$ experienced by operating at a temperature and pressure above the critical point; the end point of the pressure-temperature curve where liquid and vapour phases can coexist. Carbon dioxide reaches the critical point at a pressure of 7.38 MPa and temperature of 304.12 K. CO$_2$ is a non-ideal gas, and hence, its density is sensitive to pressure and temperature changes, particularly around the critical point. The density of the CO$_2$ is very high near the critical point as shown in Figure 2.2. Hence, it is beneficial to use a working fluid in power cycles as the compression work of the cycle is significantly reduced by operating close to the critical point resulting in less compression work and hence high thermal efficiency.

Using supercritical carbon dioxide as a working fluid allows for higher turbine inlet temperature > 600 °C and hence, results in higher efficiency compared to steam turbines, alongside retaining the simplicity of Brayton cycles layout [25]. The promising proper-
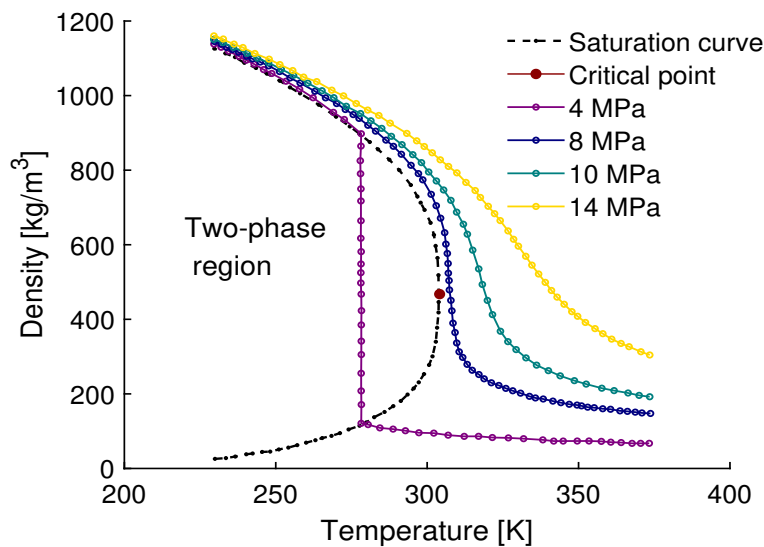
Figure 2.2: Variations of CO$_2$ density over a range of temperatures and pressures [11].

ties of sCO$_2$ working fluid results in sCO$_2$ power cycles with high power density, large power capability and lower cost owing to the small turbo-machinery size and the simple cycle design [10]. Supercritical CO$_2$ is also characterised by superior properties including being non-corrosive, non-flammable, non-explosive, in-expensive, not-toxic and widely available working fluid [26]. Despite the above-mentioned advantages of sCO$_2$ working fluid for power generation, its high solubility and high diffusivity bring a high risk of contamination of CO$_2$ with other fluids and corrosion in cycle components. Considering the promising properties of sCO$_2$, sCO$_2$ plants have the potential to be lower capital and operational costs compared to an equivalent steam cycle [3].

2.2.2   Supercritical CO$_2$ power cycles

Supercritical CO$_2$ power cycles were firstly proposed by Angelino [27] and Feher [28] in 1968. Angelino set several configurations for condensation (transcritical) power cycles starting with a simple fully condensing cycle with a recuperative layout followed by several modifications to reduce cycle irreversibility. Afterwards, in the early 2000s, Dostal's work revived the research interest in sCO$_2$ cycles [29] resulting in a dramatic increase in research studies in sCO$_2$ cycles with more focus on new cycle proposals and components designs.

The fully condensing layout is composed of a recuperator (R) turbine (T), primary heat

exchnager (PHX), primary cooler (PC) and compressor/pump (C) as shown in Figure 2.3. To enhance the performance of the recuperative cycle and reduce the irreversiblities in the recuperator, the recompression cycle layout was proposed. In the recompression cycle (Figure 2.4), the low-pressure carbon dioxide stream is split into parallel compression in the main compressor (MC) and the re-compressor (RC). The bypass flow, compressed in the RC, is used to balance the heat duty across the low-temperature recuperator (LTR) and hence reduce the irreversibilities in the recuperator.
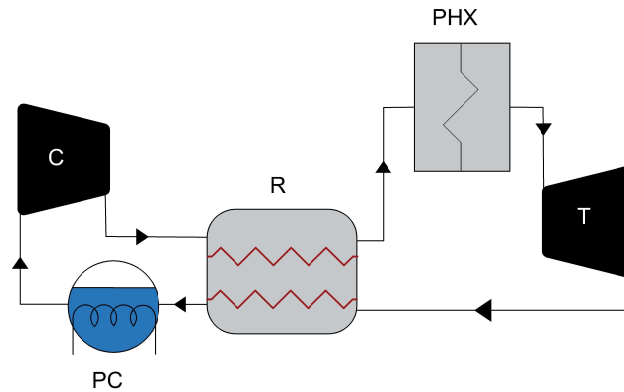
Figure 2.3: Simple recuperated CO_2 cycle with a compressor (C), primary cooler (PC), primary heat exchanger(PHX), recuperator (R) and turbine (T) [30].

Following, the precompression cycle was proposed where a boost compressor (BC) is added between the high-temperature recuperator (HTR) and LTR. This allows for increasing the amount of thermal energy that can be transferred from the hot side of the LTR, and hence, alleviate the temperature pinch point problem in the LTR. Additionally, this cycle allows for achieving higher pressure ratios due to overcoming the constraint imposed by the condensation temperature on the exhaust pressure in the recuperated cycles and hence increases the specific work of the cycle. Similar to the precompression cycle, a partial cooling cycle was considered; where an external cooling medium is added in the cycle so that the low-pressure flow is further cooled after exiting the low-pressure recuperator as represented in Figure 2.5.

Angelino proved that the efficiency of a recompression cycle with an inlet temperature of 650 °C is competitive to a reheat Rankine cycle; in a comparative study between various Angelino layouts and conventional cycles, the recompression cycle showed the highest
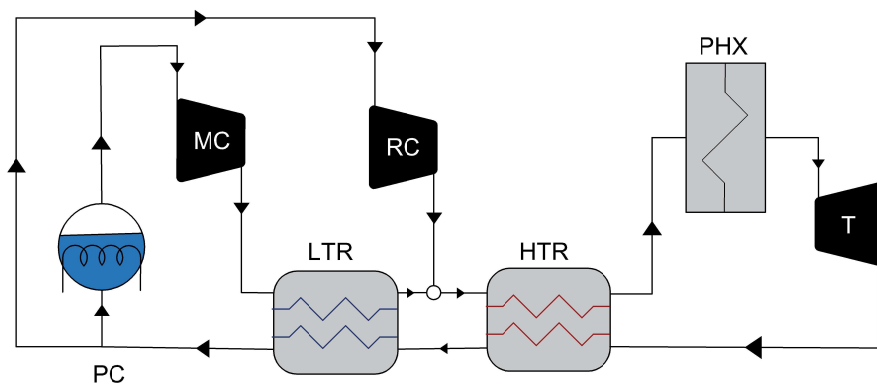
Figure 2.4: Recompression cycle with a high-temperature recuperator (HTR), low-temperature recuperator (LTR), main compressor (MC), primary cooler (PC), primary heat exchanger (PHX), recycle compressor(RC) and turbine (T) [30].

efficiency in comparison to various conventional cycles and architectures as shown in Figure 2.6 [27].
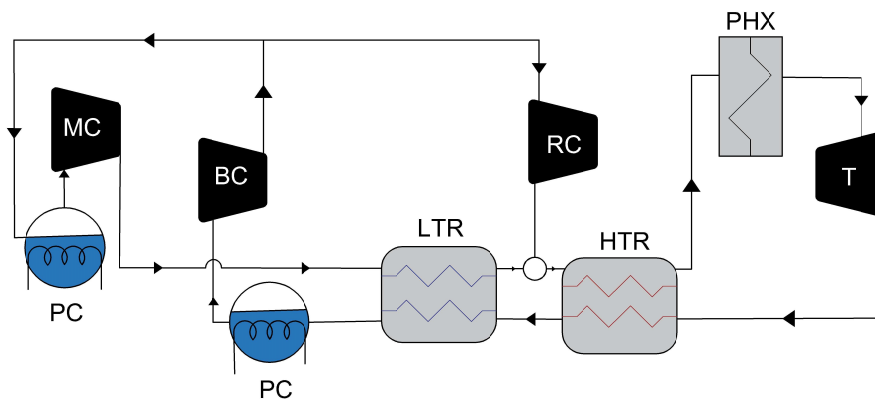
Figure 2.5: Partial cooling cycle with a boost compressor (BC), high-temperature recuperator (HTR) low-temperature recuperator(LTR); main compressor(MC), primary cooler (PC), primary heat exchanger (PHX) and turbine (T) [30].

Similar to Angelino, Feher [28] proposed an alternative power cycle that could potentially improve the performance of both the Brayton and Rankine cycle. The proposed cycle is based on using purely supercritical fluid which can be implemented with both steam and carbon dioxide. The presented cycle has the potential to overcome temperature restrictions, turbine exhaust conditions and a large number of turbine stages in Rankine cycles. Additionally, it overcomes the large compression work needed in Brayton cycles, large heat transfer areas because of the low density of the operating fluids and cycles' sensitivity to pressure drops and compressor efficiency. In the early 2000s, Dostal's work revived the research interest in sCO$_2$ cycles [29] resulting in a dramatic increase in research studies

in sCO_2 cycles with more focus on new cycle proposals and components designs. A thorough review of the different cycle configurations and advances of the sCO_2 power cycles has been covered by Crespi et al. [25]. According to this review study, the average standalone power cycles achieved efficiencies in the order of 40% and combined cycle layouts can reach efficiencies in the range of 50 to 60%.
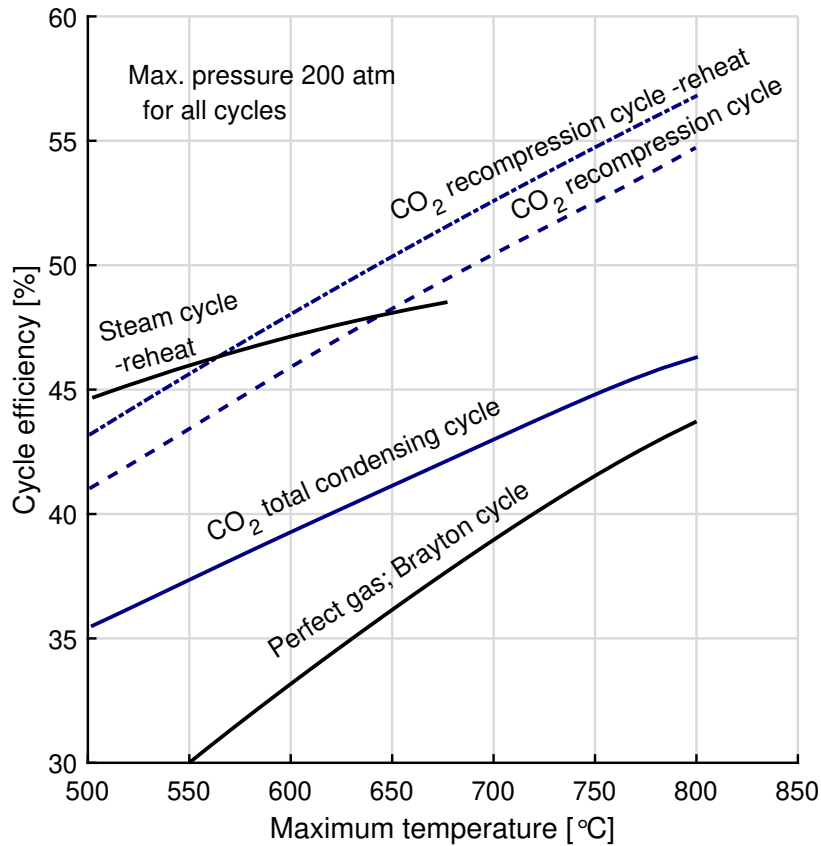
Figure 2.6: The performance of CO_2 condensation cycles compared to steam and perfect-gas cycles [27]

In regards to CSP applications, several cycle configurations have been found to be promising with respect to supercritical or superheated steam cycles for high-temperature CSP applications including recuperated, recompression Brayton and partial-cooling cycle [31, 32]. The recompression cycle was found to achieve the highest thermal efficiency of 52%, among the simple Brayton, simple recuperated, precompression, split expansion cycle for Solar Power Tower (SPT) CSP applications; this conclusion was confirmed assuming the same operating conditions for all cycles [33]. Following the recompression

cycle, the recuperated cycle showed promising results in terms of thermal efficiency and produced power output. Furthermore, a comparative study of the different cycle configurations conducted over a wide range of operating conditions showed that the intercooling cycles offered the highest efficiency followed by the partial-cooling cycle, and the recompression cycles respectively for applications in molten salt SPT systems [34].

Globally, CSP locations are identified using the global distribution of direct normal irradiance (DNI); where high solar radiation is available from the sun. Thus, these regions are defined to be North Africa, the Middle East, the Mediterranean, and vast areas in the United States including California, Arizona, Nevada and New Mexico. The defined locations have massive land areas with extraordinary solar irradiation making it suitable for installing many solar thermal systems. Therefore, the main drawback of using the sCO_2 for CSP applications is that its critical temperature is relatively very low and hence, it does not allow for taking the advantage of the real gas effect and the reduction in compression work; where the minimum cycle temperature may exceed 50°C due to high ambient temperatures in arid regions where CSP plants are typically located, making it unlikely for CO_2 condensation to occur.

To overcome the issue, it has been proposed to develop novel CO_2 based working fluids (a mixture of pure sCO_2 and certain additives) that are operating at a higher critical point in comparison to the pure sCO_2. Substantial enhancement in the performance of sCO_2 cycles can be achieved by operating with a minimum cycle temperature close to or below the critical point, to allow for a significant reduction in the compression work. The means of selecting the different dopants to alter the critical temperature of the new working fluids (sCO_2 blends) will be discussed in the next section.

2.2.3 Supercritical CO_2 blends

The critical point of the CO_2 based working fluids can be increased by doping pure sCO_2 with other additives to allow for condensation at elevated cooling temperatures [13, 16, 17, 18]. Increasing the critical temperature of the CO_2 based working fluid should allow for economically feasible cooling in dry regions and hence, result in a significant reduction in

the compression work.

Figures 2.7a and 2.7b show condensing versus non-condensing sCO_2 cycles. In the non-condensing cycle, the compression occurs above the critical point and hence, a compressor is needed to increase the pressure of the pure CO_2 gas (Figure 2.7a). Alternatively, adding the additives to the pure CO_2 results an increase in the critical point as shown in Figure 2.7b. Therefore, condensation takes place at the ambient air temperature and compression takes place in the liquid phase region where a pump is needed.

(a)   (b)
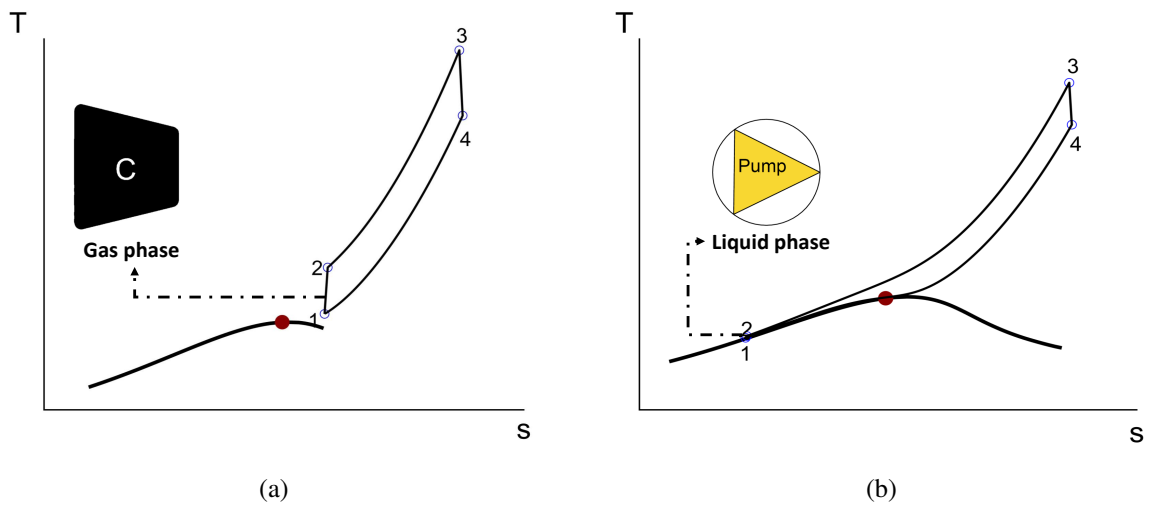
Figure 2.7: Entropy versus temperature ($T - s$ diagram) for (a) non-condensing cycle operating with pure CO_2 (b) condensing cycle operating with CO_2 blends.

The utilisation of sCO_2 blends as working fluids in power cycles is still a developing field. Therefore, there is a need to set a procedure for selecting the candidate dopants and to examine the effects of using the novel working fluids (sCO_2 blends) on the cycle design and performance. To adopt sCO_2 blends in thermodynamic cycles, it is important to set a procedure for selecting of the optimal working fluid. Particularly, if the experimental data of the developed blends is still missing. A procedure for selecting and characterising the novel working fluids for the power plant applications can be summarised as follows [35] :

- Using a reliable equation of state (EoS) that can be easily implemented to the blends and the binary interaction parameters can be calibrated using Vapour-Liquid Equilibrium (VLE) data.
- Assessing the thermal stability of the working fluids and identifying the maximum

operating temperature that the working fluid can sustain before deterioration.

• Assessing the cycle performance achieved with the working fluid when used for the power cycle; the main purpose of this is to evaluate the cycle efficiency as a function of the temperature limits (the maximum and the minimum) [35].

Several dopants have been proposed for CO_2 power cycles and their effects on cycle performance have been investigated; where dopants are classified based on their critical temperature. As shown in Figure 2.8, blending N_2, O_2, He, and Ar dopants with pure sCO_2 resulted in a reduction in the critical temperature of the working fluids compared to the pure sCO_2. Among the three dopants, *He* was found to result in an enhancement in cycle efficiency by 1.73% for a recompression cycle configuration due to the maximum reduction achieved in the critical temperature of the developed blend [36]; where the decrease in the critical point results in an increase in the optimum pressure ratio and hence, enhanced cycle efficiency. Similarly, using Xe and Kr resulted in CO_2 blends with lower critical points and hence, higher thermal efficiency due to the higher cycle pressure ratio.
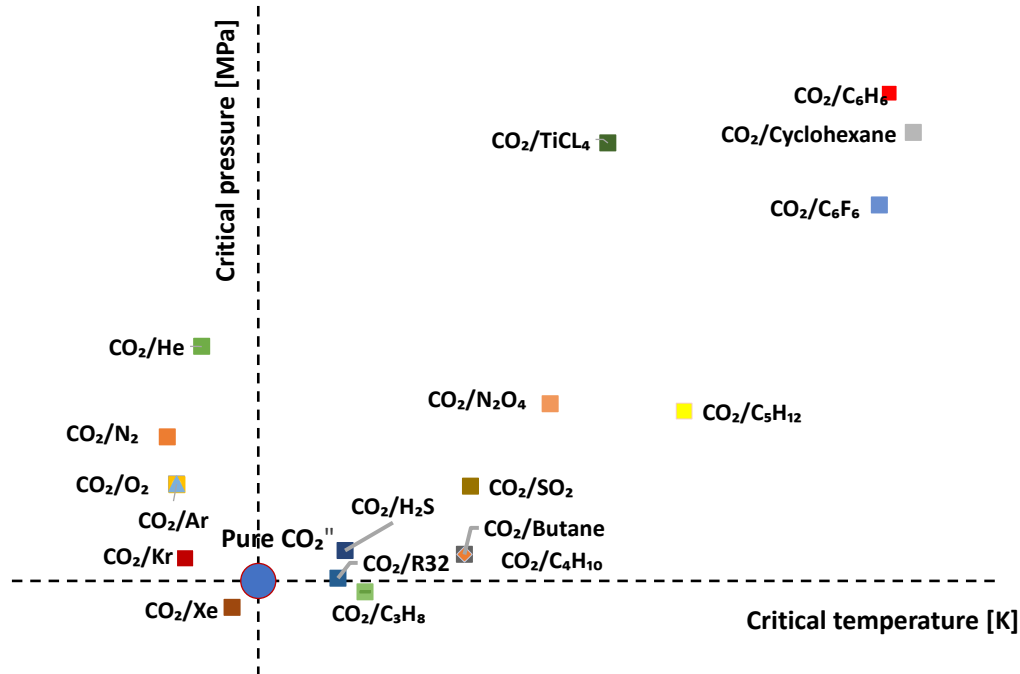
Figure 2.8: CO_2 blends critical pressure and temperature with respect to the pure CO_2 (the blue circle) at a 10% molar fraction.

The implementation of other blends such as CO_2/H_2S and CO_2/cyclohexane resulted

in higher critical points compared to the pure CO$_2$ [37]. Additionally, N$_2$O$_4$ and titanium tetrachloride (TiCL$_4$) dopants have been implemented to elevate the critical temperature of the pure sCO$_2$ and promising results were obtained with respect to the cycle efficiency [18]. Using CO$_2$/N$_2$O$_4$ and CO$_2$/TiCl$_4$ blends resulted in total cycle efficiencies of 49% and 50% respectively for a recuperated cycle configuration. This configuration resulted in power block capital cost of less than 700 $/kW which accounts for 50% and 20% cost reduction compared to steam and pure sCO$_2$ cycles respectively [18]. Using the TiCl$_4$ dopant resulted in an increase in cycle efficiency by 5% and 3% for the recuperative and recompression cycles, respectively, compared to the pure sCO$_2$ case. Further potential dopants such as the C$_4$H$_8$, C$_4$H$_{10}$, C$_5$H$_{10}$, C$_5$H$_{12}$ and C$_6$H$_6$ have been examined for CO$_2$ doping and the application of these blends have proven to enhance the efficiency of a recompression power cycle by 3-4% compared to pure sCO$_2$ [38]. The same conclusion has been confirmed by Crespi et al. [13] where CO$_2$/TiCl$_4$ and CO$_2$/C$_6$F$_6$ blends resulted in an enhancement in cycle efficiency by up to 4-5% compared to the pure CO$_2$ case for recuperated and precompression cycles respectively [13].

According to the aforementioned studies, some of the proposed dopants resulted in a reduction in the critical temperature of the pure sCO$_2$. Nonetheless, given that CSP applications operate in dry regions where the ambient temperature is high, it is required to select a dopant to increase the critical temperature of the developed working fluid. For this purpose, this work focuses on multiple dopants that have been examined by the SCARABEUS consortium to increase the temperature of the CO$_2$ based working fluid. In this regard, Polimeni et al. [5] compared the performance of solar power tower plants operating of CO$_2$/sodium and CO$_2$/KCl−MgCl$_2$ blends; where the analysis included evaluating the performance of simple recuperated, recompression and partial cooling cycle configurations. The used blends resulted in cycle efficiencies ranging from 42% for a simple recuperated cycle to 47.5% for the Recompression Main Compressor Intecooling cycle (RMCI) cycle at a maximum cycle temperature of 750°C; where the cycle efficiencies are obtained at different pressure ratios optimised for each configuration.

Likewise, Binottia et al. [17] evaluated the effect of using dinitrogen tetroxide (N$_2$O$_4$)

dopant for the same application considering a simple recuperated cycle configuration. Using N_2O_4/CO_2 blend resulted in a power cycle efficiency of 46% with a simple cycle operating at a maximum temperature of 700°C. Later, Morosini et al. [39] and Manzolini et al. [40] examined the potential of using CO_2/C_6F_6 blend for a power cycle coupled with a solar power tower system. A simple recuperated cycle efficiency of 42.5% and 46.5% have been obtained by operating at maximum cycle temperature of 550 and 650 °C respectively. The same blend has been further examined by Rodriguezet al. [41] in addition to considering two other blends ($CO_2/TiCl_4$ and CO_2/SO_2). Exergy analysis has been conducted for the three selected blends with respect to a pure CO_2 for simple recuperated cycle configurations. As a result, CO_2 blends achieved thermal and exergy efficiencies as high as 51.6 and 75.3% at 700°C which outperforms the performance obtained by Rankine cycles and pure sCO_2 cycles. Later, Morosini et al. [42] examined the performance of multiple cycles operating with CO_2/SO_2 blend. The results of the analysis showed that the recompression layout results in a power block electric efficiency of 48.67% (2.33% higher than the respective sCO_2 cycle).

Similarly, Crespi et al. [13] examined the cycle performance operating with $CO_2/TiCl_4$, CO_2/C_6F_6 blends for recuperated and precompression cycle configurations respectively. Using these blends resulted in an efficiency gain of 4-5% points with respect to an equivalent cycle operating with pure CO_2. Furthermore, Crespi et al. [20] investigated the potential of introducing CO_2/SO_2 in a transcritical recompression cycle. Introducing the CO_2/SO_2 blend resulted in promising results where cycle thermal efficiencies of $\approx 45\%$ and greater than 51% have been obtained at a maximum cycle temperature of 550 and 700 °C respectively. Thus, CO_2/SO_2 has shown an efficiency equal to or higher than the other promising blends including $CO_2/TiCl_4$ and CO_2/C_6F_6.

Ultimately, for the SCARABEUS project, three candidate dopants have been found to be particularly interesting for CO_2 power cycles including $CO_2/TiCl_4$, CO_2/C_6F_6 and CO_2/SO_2. Given that the previous studies showed that the best cycle configuration is strongly dependent on the used dopant, simple recuperated, precompression and recompression cycles (shown in Figures 2.9a to 2.10) have been selected for $CO_2/TiCl_4$, CO_2/C_6F_6

and CO$_2$/SO$_2$ respectively [43]. It is worth emphasising that these configurations do not include any means of inter-cooling and re-heating processes. Hence, they are considered to be more promising for enhancing the power block efficiency and reducing the capital cost. Considering that the main target of the SCARABEUS project is to reduce the cost of the power block, Morosini et al. [42] carried out an economic analysis for a power block operating with a transcritical CO$_2$/SO$_2$ recompression cycle. A specific CAPEX of 1000 \$/kW$_e$ was obtained for the cycle operating with recompression CO$_2$/SO$_2$ compared to 1160 \$/kW$_e$ for the sCO$_2$ cycle with the same cycle layout. Likewise, the CAPEX of a simple recuperated cycle working with the optimal CO$_2$/SO$_2$ blend was found to be 718 \$/kW$_e$ compared to 795 \$/kW$_e$ for the same cycle layout operating with pure CO$_2$.

(a)   (b)
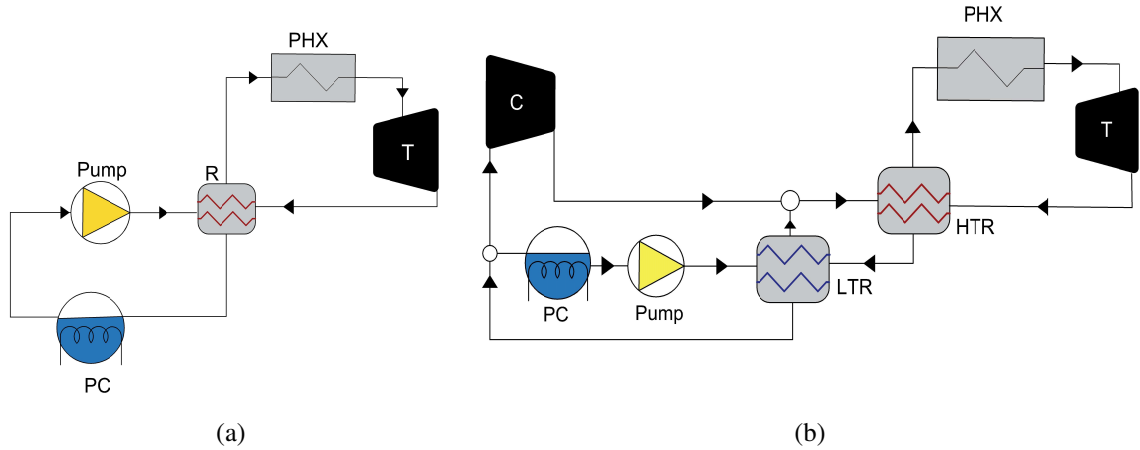
Figure 2.9: (a) Simple recuperated cycle operating with the CO$_2$/TiCl$_4$ blend (b) recompression cycle operating with the CO$_2$/SO$_2$ blend [43].
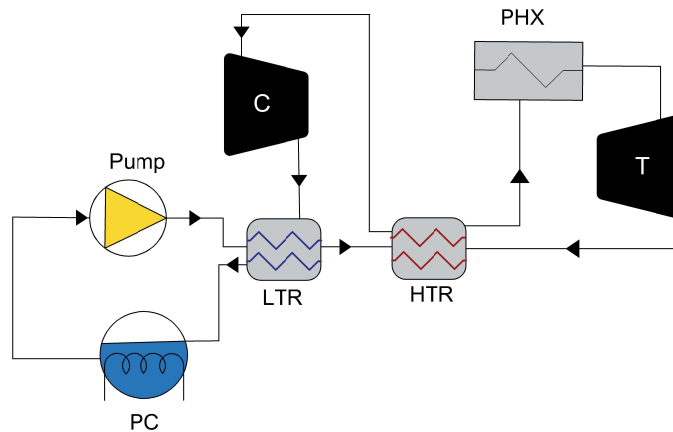
Figure 2.10: Precompression cycle operating with the CO$_2$/C$_6$F$_6$ blend.

Before proceeding further with the implementation of the selected blends within the cycle analysis, it was important to investigate the thermal stability of those blends at the operating conditions. In this regard, several experiments have taken place within the SCARABEUS consortium. It has been found that both $TiCL_4$ and SO_2 are showing promising results where thermal degradation was experienced at temperatures above 700 °C. However, the C_6F_6 has shown some signs of thermal degradation at temperatures above 600°C [44]. Apart from the thermal stability issues, the use of the $TiCL_4$ dopant might face some potential limitations due to the corrosion effects resulting from the high reactivity of $TiCL_4$ with air moisture. Additionally, the formation of H_2SO_4 when the SO_2 combines with water adds some challenges to the use of the SO_2 dopant. It is worth mentioning that the health hazards associated with the SO_2 or $TiCl_4$ are very similar to other fluids that are commonly employed in CSP plants, such as Therminol VP1 [20]. As for the environmental hazards, no global warming potential or ozone depletion is present for the selected mixtures. Therefore, the environmental impact of the selected dopants is considered minimal. A brief overview of safety hazards for the three selected dopants, developed according to standard 704 of the National Fire Protection Association, is presented in Table 2.1. More information regarding these dopants can be found in previous publications [13, 16].

Table 2.1: Dopants thermophysical properties (columns 2 to 6) and hazard according to NFPA 704 [45]

Chemical Compound	MW [kg/kmol]	T_{cr} [C]	P_{cr} [bar]	Molecular Complexity [-]	Thermal Stability	Health Hazard	Flammability	Chemical Reactivity	Special Hazard
CO_2	44.01	31.06	73.83	-9.324	> 700°C	2	0	0	Simple Asphyxiant
SO_2	64.06	157.60	78.84	-8.230	> 700°C	3	0	0	-
C_6F_6	186.06	243.58	32.73	12.740	< 625°C	1	3	0	-
$TiCl_4$	189.69	364.85	46.61	1.922	> 700°C	3	0	2	React with water

2.2.4 Supercritical CO_2 blends thermodynamic properties

The accuracy of the thermodynamic cycle modelling relies on the selection of the Equation of State (EoS) and its capability of predicting the thermodynamic properties for the different fluid phases [46]. Therefore, the calculation of thermodynamic properties is an important step towards conducting accurate thermodynamic cycle analysis and compo-

nents modelling for novel systems operating with CO$_2$ blends.

The cubic equations of state (EoS) are versatile models that can provide accurate calculations for the thermodynamic properties of pure components. Besides, it can be extended to predict the behaviour of mixtures through the introduction of appropriate mixing rules and the calibration of binary interaction parameters (BIP, also named k_{ij} in cubic EoS) using experimental vapour-liquid equilibrium (VLE) data [47]. Hence, cubic EoS, such as Peng-Robinson (PR) [48], Boston-Mathias alpha function (PR-BM), and the Soave-Redlich-Kwong (SRK) [49] have been proposed for predicting the properties of binary CO$_2$ based working fluids [16, 18, 42, 35, 46]. Additionally, other equations of state have been proposed for the same purpose such as PC-saft [50] equation of state [42, 47].

In this regard, Di Marcoberardino et al. [47] examined the influence of equations of state, such as Peng-Robinson, Peng Robinson with Boston-Mathias alpha function, the Predictive Soave-Redlich-Kwong (PSRK), the virial model Lee-Kesler-PLocker and the PC-SAFT, on the estimation of thermo-physical properties of CO$_2$/C$_6$F$_6$ in a transcritical cycle. Additionally, they investigated the sensitivity of the design of multiple-cycle components to the selection of the EoS. It has been found that the cycle efficiency is not significantly sensitive to the choice of the EoS. Nonetheless, the selection of the EoS was found to affect the operating conditions for the cycle components; where variations of about 15% in the pump specific work and of 7% in the turbine specific work were achieved. As a consequence, the cycle specific work (and therefore its mass flow rate) can be affected by up to 5%. Similarly, Morosini et al. [42] investigated the accuracy of using multiple EoS, including the standard Peng Robinson EoS (PR), the PC-SAFT EoS, the REFPROP builtin EoS (extended GERG-2008 EoS [51]), to characterise of the thermodynamic behaviour of CO2/SO$_2$ blend. It has been found that PR EoS has a poor capability for predicting some of the advanced calorimetric properties. Whilst, the PC-SAFT and the REFPROP equations were found to be adequate for predicting the properties of the examined blends.

Further to the growing research interest in identifying the promising blends, EoS, to calculate the thermodynamic properties of the selected blends, and optimum cycle configurations, great attention has been made to developing a detailed component design with

more focus on turbo-machinery and heat ex-changer designs. This step is crucial for developing CSP technologies further considering the different physical properties of the sCO_2 fluid compared to the conventional steam and gas turbine cycles. Developing the state of the art of different cycle components is important for enhancing the overall plant performance and hence, enhancing the competitiveness of the technology. Bearing in mind that CO_2 blends are introduced to allow for condensation, using air condensers, in dry regions for trans-critical power cycles. This will allow for significantly reducing the compression work as a result of compressing the working fluid in the liquid phase rather than the vapour and hence, less work is consumed by the compression making the turbine more crucial for affecting the cycle performance. Nonetheless, precompression and recompression cycles have been identified for some of the selected blends in the literature where the thermal performance of those cycles depends on both the compressor and turbine performance.

By focusing on the turbine design, it is important to review the different aspects of the design process to address the gaps within this research area. With respect to the EoS, Aqel et al. [16] investigated the effect of the equation of state selection on the turbine design accuracy for the different working fluids, namely CO_2/SO_2, $CO_2/TiCL_4$ and CO_2/C_6F_6. It has been found that turbine design for CO_2/SO_2 working fluids is the least sensitive to the fluid model; this indicates that CO_2/SO_2 offer robust property prediction in the absence of experimental data. Among the flow path designs generated for the three blends, a maximum difference in the turbine geometry of 6.3% was obtained due to the use of the different EoS; in particular, using SRK versus PC-SAFT. Hence, the standard Peng-Robinson Equation is used to calculate the thermo-physical properties of all blends using SIMULIS package [52]; where the binary interaction parameters for the selected equation were selected to match those used for the cycle analysis to ensure consistency in the thermodynamic properties obtained by both models.

2.3 Turbine classifications

Turbines are composed of a set of rotating and stationary blades called rotor and stator respectively. Principally turbines are classified based on the direction of the fluid flow

into axial and radial turbines. In radial turbines, the fluid flows radial to the rotating shaft whereas in the axial turbine the fluid is axial through the mounted blading as shown in Figures 2.11a and 2.11b. Radial turbines are capable of handling low mass flow rates more efficiently than axial turbines; due to the change in radius that can achieve a large change in angular momentum allowing for higher pressure ratios over a single stage. Thus, it is the main candidate in most small-size turbine applications. They are known to be effective compact machines for small-scale applications with a power ranging from 300 kW to more than 25 MW, allowing for the expansion of working fluid in one single stage [14]. Increasing the power rating of the equipment ranging from hundreds of kW to a few MW results in an increased mass flow rate where axial turbines proved to be competitive for radial turbines [53]. Furthermore, axial turbines are capable of handling high mass flow rates more efficiently than radial turbines, they can easily accommodate multiple expansion stages on a single shaft [54]. In this regard, axial flow turbines are suited for high-scale applications and hence electrical power generation and propulsion systems usually deploy axial turbine configurations.

(a)   (b)
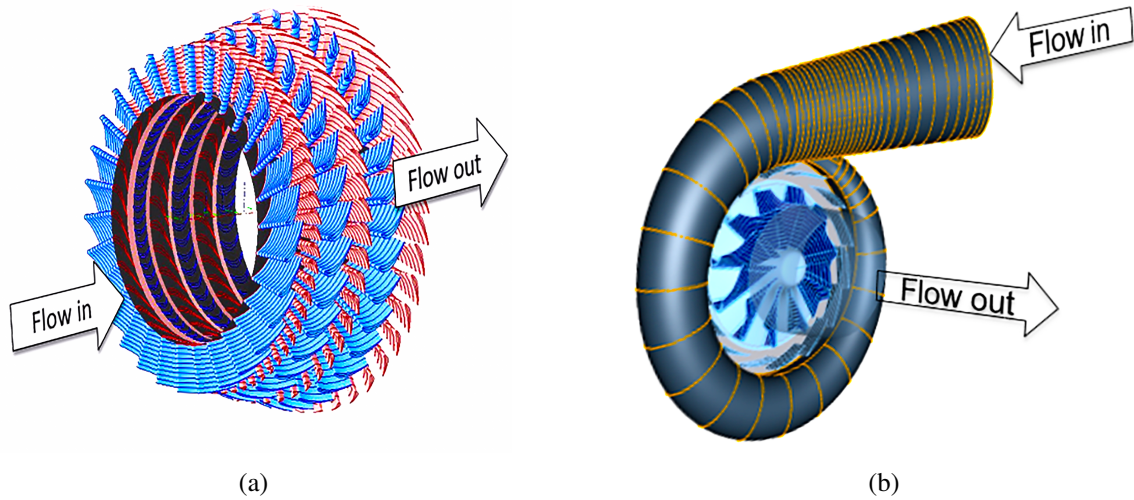
Figure 2.11: (a) Axial turbine [55] (b) radial turbine [56].

Turbines are also categorised into impulse and reaction turbines according to the nature of the pressure drop into stator and rotor blade rows. In impulse turbines, the pressure drop occurs in the stationary stator blades only and for reaction turbines, the pressure drop occurs in both the stationary stator and moving rotor blades. This is expressed by the degree of reaction of the turbine which is a ratio of the enthalpy drop across the rotor

blades with respect to the total enthalpy drop across the turbine stage.

2.3.1   Challenges with supercritical CO_2 turbines

The properties of sCO_2 bring about some advantages as well as challenges for the design of turbo-machinery. sCO_2 power cycles are associated with turbomachinery of a small physical size due to the high density of the working fluid and the low-pressure ratios of the cycle. This could result in more compact turbomachinery, with lower installation costs. Given that sCO_2 turbines operate at high inlet pressures and temperatures, typically between 20 and 25 MPa [57] and 400 and 800°C [58] respectively, they face some design and operational challenges. Furthermore, their performance is highly affected by clearance, windage and frictional losses which are typically associated with the compact turbine design, alongside the high density and low kinematic viscosity of the working fluid. Some of those challenges can be summarised as follows:

1. High clearance and windage losses and aerodynamic loads on the nozzle and rotor blades as a result of the small turbine size.

2. Thrust bearing selection for high thrust loads experienced in sCO_2 turbines due to the high-pressure difference across the rotor.

3. Seal design to keep the oil-lubricated bearing separated from the sCO_2 working fluid.

4. Operation challenges with high pressure, high-temperature environment with high shaft speeds.

5. Operation challenges owing to using a new working fluid such as large frictional losses and corrosion.

6. Erosion in small-scale sCO_2 turbines which provides a threat to safe, reliable and long-duration operation.

7. The placement of the throttle control valve and turbine stop valve upstream of the turbine inlet at the highest temperature point in the cycle.

8. Uncertainties in the existing turbine design methods and loss models for sCO_2 turbines [21].

Developing an accurate and robust design and performance analysis tools is essential for

developing sCO$_2$ turbine designs, and several studies on this topic have been published for different turbine scales and architectures. Preliminary aerodynamic turbine design and optimisation is a necessary step within the turbine design process that precedes advanced 3D blade optimisation and flow analysis studies using computational fluid dynamics (CFD). This step is principally performed using a combination of one-dimensional mean-line design and suitable loss models. Within the next sections, various details of axial turbine modelling will be discussed for sCO$_2$ working fluids; this includes reviewing aspects of mean-line design, performance prediction and off-design performance analysis. Furthermore, several aspects of sCO$_2$ turbine design will be covered; this includes presenting a summary of the existing prototypes, conceptual designs and mechanical design challenges of sCO$_2$ turbomachinery.

2.4 Supercritical CO$_2$ axial turbine modelling

2.4.1 Preliminary design and performance prediction

The preliminary aerodynamic turbine design is initiated by solving the steady-state mass, energy and momentum equations to obtain the geometric parameters of the turbine. Within the preliminary turbine design stages and prior to the three-dimensional (3D) blade generation, the performance of the generated geometry is evaluated using the existing empirical correlations through the quantification of the various types of losses that exists within the flow field. To predict these losses, and hence predict the machine performance, their mechanisms of occurrence should be understood; a geometry of a blade section and a schematic diagram of a turbine stage for axial configuration are shown in Figures 2.12a and 2.12b respectively to enhance the understanding of these mechanisms. A brief description of these mechanisms is presented as::

- Profile losses occur due to the boundary layer effect where the fluid is subjected to viscous forces that slow down the flow and hence, increase the relative entropy in the mainstream. These forces might result in a wake formation, which is the region of disturbed flow downstream caused by the fluid flow around a solid body. Hence,
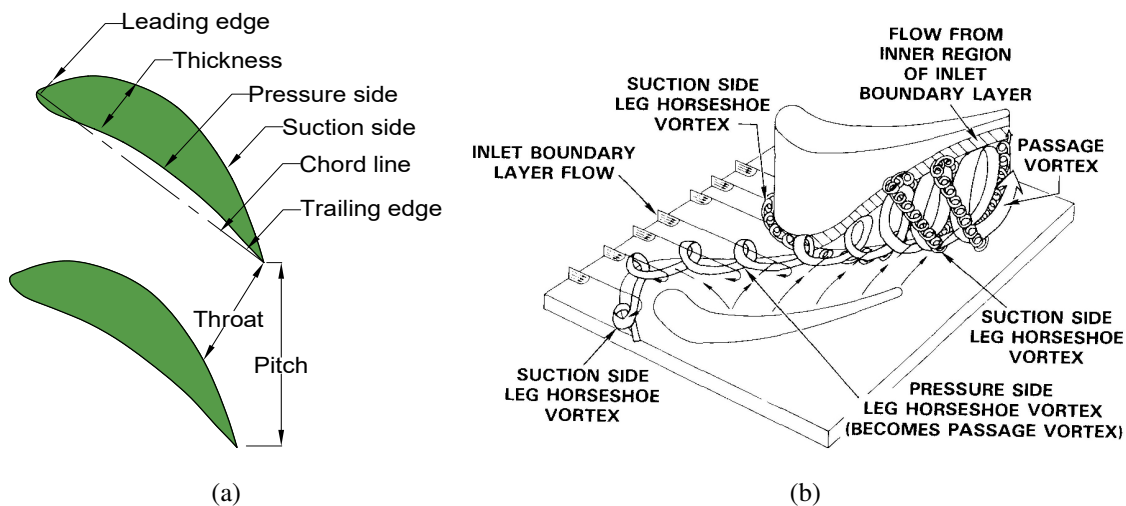
Figure 2.12: (a) Geometry of a blade section (b) endwall flow structure [59].

profile losses can be in the form of friction losses, due to the fluid viscosity, on blade surfaces or losses in blade wakes [60].

- Secondary losses occur due to the wall friction at the tip and root of the blades along with the end-wall effects; the inlet boundary layer separates at the end-wall of the blade, forming a horseshoe vortex as shown in Figure 2.12b. One leg of the vortex migrates to the pressure side (Figure 2.12a) forming a vortex while the other move towards the suction side (Figure 2.12a) forming a counter vortex; the formed end-wall vortex secondary flow is responsible for the secondary flow losses [59].

- Trailing edge losses occurs due to the finite thickness of the trailing edge (Figure 2.12a) at the blade which will result in flow separation at both the pressure and suction surfaces and create re-circulation zone [61].

- Tip clearance loss occurs due to the pressure difference between both blade sides, pressure and suction sides ((Figure 2.12b), along with the leakage over the tips of the blades [61].

- Supersonic expansion losses occur due to the formation of normal shock waves originating at the trailing edge of the blades as a result of reaching the sonic flow which results in higher pressure losses.

- Oblique shock losses occur due to the flow acceleration adjacent to the curved leading edge of the blades.

- Windage loss is experienced by the machine due to the resistance of the fluid to shaft

rotation.

- Leakage losses include losses over the blade tips, around the shrouding, disk balance and diaphragm glands.

Several mathematical correlations have been developed to quantify these losses within axial turbines in addition to including other losses such as partial admission and disk friction losses and others. Soderberg (SB) [62] introduced a set of simplified correlations for predicting profile and secondary flow losses in axial turbines in 1949. Following this Ainley and Mathieson (AM) [63] presented a method where the pressure losses were split into profile, secondary and tip clearance losses. Later, Craig and Cox (CC) [60] split the losses into profile, secondary and loss due to sudden enlargement in the flow path or wall cavity (annulus loss). Dunham and Came (DC) [64] modified the performance correlations developed by AM using updated experimental data. The modifications considered profile, secondary and tip clearance losses. In a similar manner, additional modifications have been applied to the DC model by the Kacker and Okapuu (KO) [65] and the Aungier (AN) models [66]. Alongside the previously discussed losses, some of these models accounted for other types of losses. For example, Craig and Cox considered other losses such as leakage, disk windage, wetness and partial admission losses. Similarly, Aungier also considered lashing wire, leakage bypass, partial admission loss, disk friction and windage loss.

All of the existing turbine models have been derived and validated for air and steam turbines, and have shown a good agreement with experimental data with a maximum efficiency deviation of 3% reported by the AM model [63]. In the meantime, closed-loop super-critical carbon dioxide (sCO$_2$) power cycles are promising candidates for future concentrated-solar power, nuclear and waste-heat recovery applications, having advantages of compact turbomachinery offering a simple layout, high-power density and compact structures and high cycle efficiencies at a heat-source temperature in the range of 400 to 800 °C [14]. Additionally, organic Rankine cycles (ORC) are being widely considered for low to medium-temperature heat source applications (< 400 °C) including waste heat recovery, solar-thermal and geothermal, operating with a range of organic fluids including hydrofluorocarbons, hydrocarbons, hydrofluoroolefins and siloxanes [67]. Within these

new applications, the required turbine designs may differ significantly from air or steam turbines; those novel working fluid experience thermo-physical properties that are different from that of air and steam. As a result, sCO$_2$ turbines experience several operation challenges due to the compact geometries, high density and low viscosity working fluid compared to air turbines which result in high clearance, windage and frictional losses. Whilst ORC turbines are characterised by low enthalpy drop (for a defined pressure ratio compared to air) and low speed of sound which leads to large volumetric ratios and supersonic flows.

To date, there has been limited experimental data to provide sufficient validation that existing turbine models are suitable for non-conventional working fluids like the sCO$_2$ and organic fluid. However, despite this, several researchers have implemented these models for the axial turbine design process for sCO$_2$ and ORC cycles.

2.4.1.1   Studies on supercritical CO$_2$ turbines

With regards to sCO$_2$ applications, Qi et al. [68] presented a mean-line design for a 100-200 kW sCO$_2$ radial turbine; adopting Moustapha et al. [69] design methodology for rotor blade design calculations. Several designs have been developed for a set of load and flow coefficients where the feasible designs have been selected according to the manufacturing and structural constraints. Holaind et al. [70] addressed the design of a small-scale sCO$_2$ radial turbine with an output power ranging from 50-85 kW. The provided design has been done based on similarity considerations using Balje's chart where Cordier's lines were specified at a selected specific speed to obtain the specific diameter for a maximum efficiency criterion. In a similar way, Luo et al. [71] implemented a one-dimensional preliminary design with an optimisation procedure for the design of a 10 MW sCO$_2$ radial turbine. The preliminary design started by assuming a limited rotor radial outlet angle, constant blade height, isentropic expansion in the rotor, stator and vaneless space, flow and loading coefficients. Later, the mixed-integer sequential quadratic programming (MISQP) blade optimisation method has been carried out to achieve an optimised bade geometry [71]. The one-dimensional (1D) design model has been validated against CFD simulations where a

good agreement with the CFD analysis has been achieved.

Furthermore, Zhou et al. [72] proposed a 1.5 MW sCO$_2$ radial inflow turbine design assuming 1D, axisymmetric, steady, adiabatic, and in-viscid expansion in the turbine. The 1D results have been validated against 3D CFD simulations and consistent results have been obtained with a maximum deviation of 5%. LV et al. [73] presented an optimisation study for the performance of radial inflow turbine using sCO$_2$ working fluid. This has been done by combining a one-dimensional design method with an optimisation algorithm for both nominal and off-design performance conditions. The overall total-static efficiency has proven that the 1D design showed a good agreement with the CFD results; where an optimised design with higher total-static efficiency and lower passage and exit velocity losses has been achieved. Saeed et al. [74] implemented the Aungier [66] loss model for the preliminary design calculations of a sCO$_2$ radial turbine within the analysis process of a 10 MWe re-compression supercritical carbon dioxide cycle; where Moustapha et al. [75] loss model has been adopted to analyse the turbine performance. The losses have been evaluated at different geometric parameters as a part of an optimisation process, using response surface methodology (RSM), to minimise the passage losses and maximise the efficiency. The turbine design and optimisation models have been validated against CFD simulations. The validation results for the design and optimisation model showed a maximum difference of six percent of the turbine mass flow rate which was considered to be within the acceptable error range.

In the same way, Lee et al. [76] implemented the mean-line design methodology for a sCO$_2$ axial turbine design; the model has been refined with Balje-Binsley [61] and Kacker-Okaapu [65] loss correlations to analyse the turbine performance considering both profile and secondary flow losses at nominal and off-design conditions. To examine the validity of the design code, including the implemented loss model, the preliminary results have been verified against data obtained from SNL. The design geometry and the off-design analysis results have shown a good agreement with the SNL data [76].

Schmitt et al. [77] employed Soderbergcorrelations [62] to design the aerodynamic features of a first stage for six stages 100 MW sCO$_2$ turbine; adopting Dixon and Horlock[23]

design methodology. Alongside the mean-line design, CFD simulations have been developed to validate the loss model predictability. Hence, it has been proven that the Soderberg model is not sufficient alone to estimate the primary losses for sCO_2 at the studied machine scale owing to the deviation in the predicted losses in comparison to the developed CFD model [77].

Moroz et al. [78] studied some design aspects of a 100 MW sCO_2 turbine; the study included the integration of aerodynamic-structural optimisation with the mean-line design to maximise the turbine efficiency along with satisfying the structural limitations. Hence, the best design configuration has been selected upon various parameters including the number of stages, rotational speed and stage type, impulse versus reaction, and the radial clearance variation [78]. Zhang et al. [79] proposed a design for sCO_2 axial and radial turbine for an output power of 15 and 1.5 MW respectively. The mean-line design model has been integrated with Balje-Binsley [61] loss correlations to analyse the performance of the turbine. The one-dimensional design has been validated against CFD simulations where a good agreement between them has been achieved. Finally, Shi et al. [80] presented an optimal 10 MW three-stages sCO_2 axial turbine design using a 3D CFD model, optimisation methods and off-design analysis.

2.4.1.2 Studies on ORC turbines

Similar to CO_2 turbines, classical loss models have been used to predict the performance of ORC turbines throughout the preliminary design phase. In this regard, Lio et al. [81] and Talluria et al. [82] examined the performance of an axial ORC turbine adopting Aungier [66] loss correlations. New efficiency charts have been produced using the selected model for R245fa and n-hexane respectively operating at different design conditions. In a different study, Lio et al. [83] implemented the same loss model to predict the performance of different ORC working fluids and to examine the effect of fluid characteristics on the ORC turbine performance maps. Agromayor et al. [84] examined the performance of an axial flow ORC turbine using the Kacker and Okapuu [65] model where the model has been validated against experimental data and a maximum efficiency difference of 2.07% has been

achieved. Similarly, Meroni et al. [85] implemented Craig and Cox loss model correlations for the design of an ORC axial turbine, where the model has been validated against experimental data for air turbine and low power output ORC turbine design, reported in the literature, operating with R113 fluid. The model achieved a maximum efficiency difference of 1.3% in comparison to the verification cases. Additionally, Meroni et al. [86] implemented the same model to optimise the performance of an ORC turbine accompanied by cycle optimisation analysis. A summary of the commonly used loss models in the literature for both sCO$_2$ and ORC turbine designs is presented in Table 2.2.

Table 2.2: Summary of the commonly used loss models for axial turbines operating with pure sCO$_2$ and organic fluids.

Study	Loss model	Working fluid	Scale [MW]
Lee et al.[2012] [76]	Balje-Binsley [61] & Kacker-Okaapu [65]	sCO$_2$	-
Schmitt et al. [2014] [77]	Soderberg [62]	sCO$_2$	100
Lio et al. [2014] [81]	Aungier [66]	Organic fluid	0.43
Meroni et al. [2016] [86]	Craig and Cox [60]	Organic fluid	-
Lio et al. [2016] [83]	Aungier [66]	Organic fluid	-
Talluria et al. [2017] [82]	Aungier [66]	Organic fluid	-
Meroni et al. [2018] [85]	Craig and Cox [60]	Organic fluid	-
Agromayor et al. [2019] [84]	Kacker and Okapuu [65]	Organic fluid	0.25,5
Salah et al. [2020] [58]	Soderberg [62]	sCO$_2$	0.1

2.4.2   Off-design performance analysis

The turbine aerodynamic design is principally developed at the point of minimised losses. This means that the airfoil angles are designed to match the direction of the ongoing flow. Nonetheless, turbines essentially operate at conditions away from the design point; this includes operating at starting, idling, variable power and speed conditions. Deviating from the design conditions results in mismatching between the inlet flow velocity triangles and the blade leading edge which results in incidence losses. Incidence losses occur due to the mismatch or the presence of incidence between the design blade angles ($\alpha_1{}'$) and the inlet flow angle (α_1) as indicated in Figure 2.13.

   In multi-stage turbines, the mismatch between flow and blade angles may occur due to
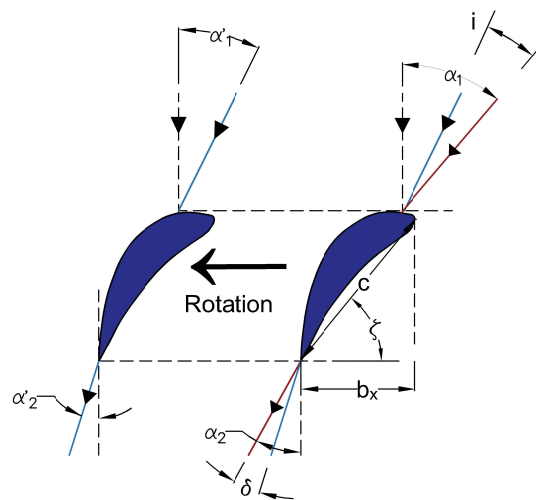
Figure 2.13: Blade profile with labels for incidence, deviation and stagger angles.

the losses in the upstream component that might result in off-design conditions at the flow downstream. Therefore, considering the incidence losses is important for predicting the turbine performance at off-design conditions [75]. An accurate prediction for the turbine off-design performance is important to match the turbine design with other cycle components such as the compressor and pump.

The system performance of both ORC and sCO$_2$ power cycles has been evaluated at constant assumed efficiency in several studies. This assumption is considered to be reasonable for systems under steady-state operation. Nonetheless, power systems are subjected to operate occasionally at off-design conditions due to the variations of the load or the ambient conditions [87]. With respect to CSP applications, the amount of solar energy is variable with the seasons' changes and weather fluctuations. Hence, the electrical energy produced from CSP applications is of an intermittent nature which forms a major challenge in harvesting electricity. Additionally, the mismatch between the amount of produced electricity and the available solar energy affects the continuity of the produced power [88]. In this regard, evaluating the off-design performance of the turbine is an important step for the development of CSP applications. It is worth noting that the degree of accuracy of cycle performance is a function of the accuracy of the performance maps generated for cycle components (including the turbine); it has demonstrated that the turbine efficiency had a great effect on the efficiencies of a trans-critical organic Rankine cycle; where 70%

enhancement in the thermal and exergy efficiencies was achieved with a change in the turbine efficiency from 60 to 90% [89].

The off-design performance of turbines is characterised by performance maps; charts that visualise the turbine performance, expressed as total-to-total or total-to-static efficiency, over a range of mass flow rates, pressure ratios and rotational speeds. Principally, performance maps should be generated through conducted experiments. Alternatively, with the absence of experimental data and test rigs, the maps could be generated using mean-line performance tools and CFD simulations. The dimensional maps are not so useful when investigating the turbine performance within the cycle analysis. Therefore, similitude theory is used to non-dimensionalise the performance map. Similitude theory has been successfully validated and is widely applied for ideal gases such as air [69]. The full mathematical details of similitude theory are discussed in Chapter 6.

Within the mean-line context, the turbine performance can be predicted at off-design conditions through the development of performance models; where these models should be integrated with loss correlations to provide an estimation of the turbine performance over a range of off-design conditions. In this context, two different iterative approaches can be applied. In the first approach, the turbine geometry, the inlet stagnation temperature (T_{01}) and pressure (P_{01}), the total-to-static pressure ratio (PR), and the rotational speed (N) are defined to be the system inputs. Hence, the turbine performance (expressed as total-to-total or total-to-static efficiency) and the mass flow rate ($\dot{m}$) are the system outputs. Alternatively, the mass flow rate can replace the pressure ratio in the system inputs. In this case, the corresponding pressure ratio and system performance are the system outputs. Taking into account the additional losses induced at the off-design operation conditions, incidence losses should be introduced within the mean-line tool to provide accurate performance predictions. To address the incidence losses associated with off-design operation in axial turbines, Ainley and Mathieson [63], Moustapha et al. [75] and Aungier [66] presented corrections for both profile and secondary flow losses due to incidence effects. Once the system outputs are obtained, the mass flow rate and rotational speeds should be non-dimensionalised, using similitude theory, to generate the performance maps.

In reference to air turbines, Kroon and Tobiazs [90] evaluated the performance of a multistage air turbine considering the variations in inlet temperature, inlet pressure, exit pressure and turbine speed. Within this study, non-dimensional parameters were used to evaluate the off-design performance of the turbine and it has been found to be useful for the preliminary design stage [90]. Likewise, Baheta et al. [91] developed a performance model for a gas turbine system. Due to the lack of availability of performance maps for the examined turbine by the manufacturers, the performance maps were generated by scaling methods applied for maps provided in GasTurb map collection [92]. Using those maps, the results of the developed model have been compared to operational data and a good agreement has been obtained with an acceptable error margin.

Later, Touli et al. [93] characterised the aerodynamic performance of a two-stage high-pressure axial air turbine; where CFD simulations have been carried out to evaluate the turbine performance and the maps have been generated by applying similitude theory. As a result, a turbine efficiency ranging from 86.63% to 90.03% has been obtained over variable corrected speeds ranging from 30% to 107.4%. In the same context, Nicoara et al. [94] evaluated the off-design performance of an axial gas turbine using CFD simulations. The effect of changing the clearance gap on the turbine performance has been investigated at multiple off-design mass flow rates ranging from 70-100% of the operating point. It has been concluded that the effect of the clearance gap is highly significant at higher mass flow rates compared to lower ones. A typical performance map can be represented as shown in Figures 2.14a and 2.14b [95]; where the pressure ratio/expansion ratio is plotted against the mass flow rate and the turbine efficiency.

With regards to ORC turbines, Hu et al. [97] expressed the off-design performance of a radial inflow turbine, in sliding pressure operation for installation in an ORC system, using dimensionless quantities defined by similitude theory. It has been concluded from the generated performance maps that there is no significant difference in the performance of an ORC turbine with respect to traditional turbines. Similarly, White & Sayma [98] applied similitude theory to predict the performance of small-scale radial turbines and the results of the similitude theory were compared to the CFD simulation results. According to
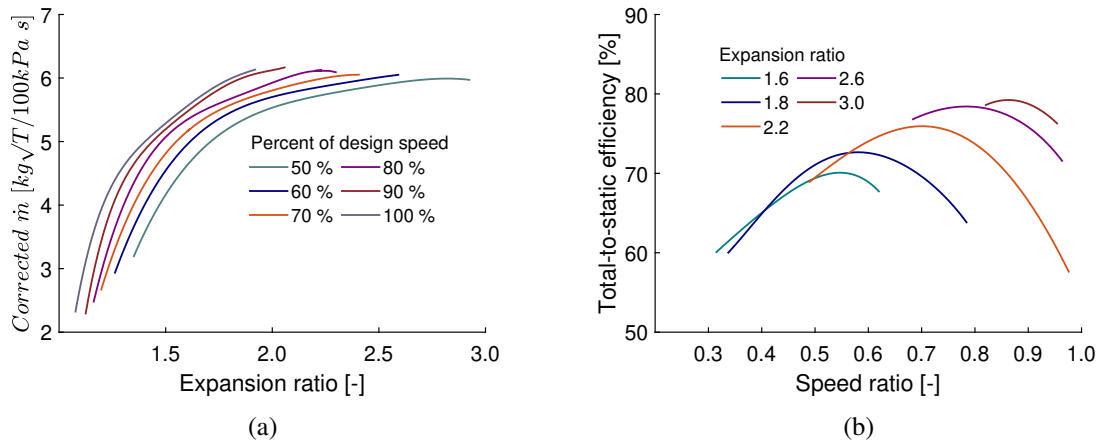
Figure 2.14: Typical turbine performance maps from the literature, expansion ratio versus the (a) corrected mass flow rate (b) total-to-static efficiency [95, 96].

the analysis, it has been concluded the original similitude theory is applicable to a narrow range of operating conditions for the small-scale ORC turbine. Hence, a modified similitude has been suggested considering the chock flow conditions. A good agreement was achieved between the modified theory and the CFD results with a difference of 2%.

Zhang et al. [99] applied similitude theory for a radial turbine operating within an ORC system; where the effect of using R245fa working fluid on the turbine performance has been investigated with respect to air as a conventional working fluid. It has been found that the reduced mass flow rates and reduced rotational speeds of the R245fa are about twice and 0.4 times those of air due to the difference in gas constant; where the gas constant of R245fa is around one-fifth the air constant. The total-to-static efficiency of the ORC turbine, over the velocity ratio range from 0.5 to 0.9, tends to be less than the air turbine case by 3-4 percentage points.

Furthermore, Du [100] examined the off-design performance of a combined cooling and power (CCP) system. This system is integrated with an organic Rankine cycle operating with a radial inflow turbine. The performance of the turbine has been investigated assuming sliding pressure operation, which was considered a feasible and economical operation strategy. The turbine was designed to operate at an efficiency and power output of 84.04% and 107.79 kW respectively. Under the off-design conditions, it has been found that the turbine efficiency drops slightly from 84 to approximately or above 83.5% when

the mass flow rate changes by 70 and up to 130% of the design flow rate. Pili et al. [101] estimated the performance of an axial turbine at off-design conditions operating as a part of a large-scale ORC system. The efficiencies obtained at off-design conditions were plotted versus the output pressure ratio as shown in Figure 2.15b whilst the change of pressure with respect to the corrected mass flow rate is presented in Figure 2.15a; this trend was found to be similar to the trends obtained by experimental analysis for air turbines [102].

(a) [102]   (b) [101]
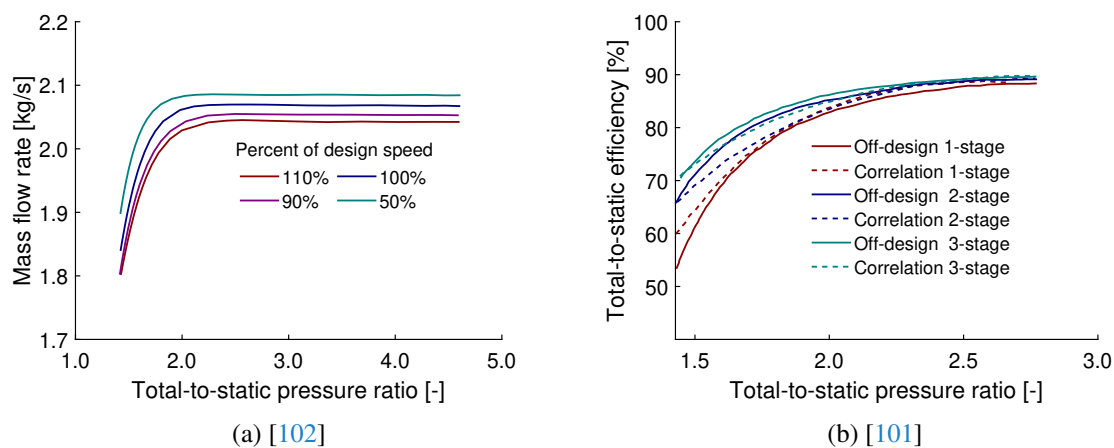
Figure 2.15: Typical turbine performance maps from the literature, total-to-static pressure ratio versus (a) mass flow rate [kg/s] (b) total-to-static efficiency [101, 102].

Ultimately for the sCO_2 systems, Dyreby et al. [103] examined the performance of sCO_2 power cycles under design and off-design operating conditions considering both simple recuperated and re-compression cycle configurations. It has been found that high operating efficiency can be realised for sCO_2 power cycles at design and off-design operating conditions. Similarly, LV et al. [73] evaluated the off-design performance of a radial inflow turbine operating with a pure sCO_2 using a mean-line off-design tool; where the turbine performance is optimised for operation at design and off-design operating conditions. Zhou et al [72] investigated the off-design performance of a radial inflow sCO_2 turbine using both 1D and 3D simulation tools; where the implemented method was based on solving mass, momentum, and energy equations alongside applying some empirical models. It was found that the 1D model predictions were consistent with the numerical solutions in the working range of the sCO_2 radial inflow turbine; where a maximum deviation of 5% was obtained between the 1D model and numerical solutions. Finally, Peng et al. [104] investigated the off-design performance analysis for ORC and CO_2 turbines using a mean-line

performance model at different compositions and inlet temperatures respectively. The off-design performance analysis proved that the CO$_2$ turbine showed higher performance over a range of operating conditions compared to the ORC turbine.

2.5 Supercritical CO$_2$ turbine design

2.5.1 Supercritical CO$_2$ turbomachinery prototypes

Experimental validation for CFD and preliminary design models is crucial for proving the credibility and reliability of the developed numerical models. Hence, the development of test rigs is important for achieving this target. Additionally, the development of test rigs allows for realising the performance of these machines in practice considering the challenging operating conditions and the design space. From this perspective, in 2010, Sandia national laboratory (SNL), in partnership with the Department of Energy and Barber Nichols, developed a sCO$_2$ loop test for an output of 125 kWe [105]. For this test rig, two turbine–alternator–compressor (TAC) units have been developed and tested. According to the test results, the turbo-machinery performed as expected considering the limited heat input reported in this test. Despite the promising turbo-machinery performance, significant challenges have been reported during the initial SNL test. The challenges were initially imposed by the need for using gas-foil thrust bearings, due to the high power density of the turbomachinery, which results in high shaft diameters and high surface diameters. Additionally, thrust bearings failure was observed which is attributed to the used Teflon coat which was not suitable for the high-temperature operation [106].

Later, SNL tested a turbocompressor designed by Peregrine Turbine Technologies which consists of two radial compressor stages and a single radial-inflow turbine on the shaft [107]. Testing issues were reported with both the radial and thrust bearings which experienced rub and failures. The turbine back pressure was adjusted to adapt the thrust and resolve the issue with the thrust bearings. Whilst, for the radial bearings the failure was found to happen due to the non-uniform inlet temperature and/or mass flow rate. Thus, to address this issue, the length-to-diameter ratio of the radial bearings was increased to allow for higher load capacity, resulting in successful operation [108].

Another small scale 100 KW$_e$ integrated system test (IST), was developed by a Bechtel Marine Propulsion Corporation and the Bettis Atomic Power Laboratory; where the system is composed of turbine-compressor, and turbine-generator [109]. It has been indicated that both units exceeded their predicted performance and achieved isentropic efficiencies of 83.6% and 85.2% for a produced power of 56.8 and 52.6 kW respectively [110]. The integrated system test proved that turbomachinery components can be developed for this small scale despite the high windage losses that were experienced due to the high pressure experienced in the cavity that contains the motor generator. Similar challenges to the SNL test were obtained in regards to the heat generated from the gas foil thrust bearings and hence, the rotational speed was limited to 60,000 rpm to maintain a safe bearing temperature.

At a large scale, Echogen [111] developed sCO$_2$ technology for waste-heat recovery applications with a net power output of 8 MW. Similar to the IST unit, it consists of two units; turbine-generator and turbo-compressor. Reported results showed the isentropic efficiency of the turbine-compressor exceeded 80% and it ranged between 20 to 75% for the tested turbine-generator; where the test did not take place at the design point [112].

Other turbomachinery for sCO$_2$ systems has been developed in the US as a part of SunShot, APOLLO and STEP projects. A 1 MW sCO$_2$ test loop was developed by the Sunshot project to develop and test a multi-stage axial turbine. The turbine design consists of a four-stage shrouded axial turbine running at a rotational speed of 27,000 RPM. This design exceeded the isentropic efficiency predicted by the mean-line design and CFD results of 85% [113]. It is worth mentioning that for the large-scale turbine the challenges around high bearing and windage losses are less critical compared to those experienced with the small-scale design considering that other technologies such as shaft-end seals and oil-film bearings should be suitable. Other challenges related to the mechanical design of the shaft and the casing has been experienced in the Sunshot project and will be discussed in detail in Section 3.3.4. On the other hand, initial testing of the Sunshot turbine by monitoring the vibrations, critical speeds and bearings temperature showed a stable operation [114]. Under the APOLLO project, Hanwha Techwin and Southwest Research

Institute developed compressor–expander system in which radial configurations were selected for both the turbine and compressor for 5-25 MW$_e$ modular power block [115]. Additionally, a 10 MW sCO$_2$ plant was constructed within the STEP (Supercritical Transformational Electric Power) project; where the turbine is based on the Sun-shot turbine with reduced stages size from 4 to 3 [116].

Net power is oxy-fuel thermodynamic power cycle with a turbine design provided by Toshiba for 500 MW system [117]. The turbine design was developed to utilise proven technology through testing a scaled turbine used within a commercial plant. Hence, Toshiba developed a preliminary turbine design for a 500 MW$_{th}$ which has been scaled to 200 MW$_{th}$ and subsequently operating at a part load operation to reach 50 MW$_{th}$ thermal input. This design is based on a seven-stage axial turbine that combines both steam and gas turbine proven technologies; this includes the use of an inner and outer pressure casing, coatings and internal cooling of the turbine blades [118].

Moreover, Korea institute of energy research (KIER) developed three experimental loops for sCO$_2$ producing 1, 10 and 60 kWe. For the 1 kW loop, a turbine-generator of a radial turbine type was used with commercial ball bearings [119]. For the 10 kW loop, the TAC unit has been used with a shrouded radial compressor and radial turbine to overcome the thrust balancing issue. Within the 1 KW prototype, gas foil bearing issues were reported [119]. Eventually, a tilting pad bearing was used to overcome high axial and radial thrust for the 60 kW. Nonetheless, the rotational speed was reduced to allow for using these bearings and this resulted in a single-stage axial impulse turbine operating at a rotational speed of 45,000 RPM. The tested turbine reported an isentropic efficiency of 50% [120].

Similarly, a 300 kW Supercritical CO$_2$ Integral Experiment Loop (SCIEL) has been developed by a collaboration between the Korea Advanced Institute of Science and Technology (KAIST) and Korean Atomic Energy Research Institute (KAERI) [121, 122]. The loop is composed of motor-driven compressor and turbine-generator and TAC unit [14]. Another test loop producing 100 kWe was developed by the Naval nuclear laboratory (NNL) in 2012. In the same framework, the Tokyo institute of technology's (TIT) devel-

oped a smaller size loop producing 10 kWe. Further details for the previously mentioned prototypes, including turbo-machinery type, power rating and operating conditions, are summarised in Table 2.3.

On the basis of the developed sCO_2 prototypes, several challenges were addressed by some of the aforementioned facilities. The SNL and NNL prototypes experienced fouling in their sCO_2 loops due to the high density, low viscosity of sCO_2 along with the presence of oil and particles in the loop even in relatively clean environments. This effect resulted in erosion in turbine nozzles at both facilities. Additionally, the windage losses were 16.8 kW and 11.3 kW in the results reported by the NNL, at the peak operating conditions, for the turbine-generator and the compressor-turbine respectively. This accounts for approximately 26% of the total power produced by the two turbines in the test loop. Hence, the rotational speed was limited to 60 kRPM owing to the excessive heat generation due to windage and bearing losses [110]. In a similar manner, the TIT reported that the net power output was much less than the difference between the turbine and compressor work owing to the high windage loss resulting from the high-speed rotor and thrust bearing [123]. Additionally, SNL reported turbine rubbing at high turbine temperature owing to the thermal growth mismatch between the stator and rotor. Furthermore, the small scale of the turbo-machinery resulted in large tip clearance and high leakage losses resulting in low component efficiency [124].

Table 2.3: Summary of the existing sCO$_2$ turbomachinery prototypes [14].

Facility	Power	Cycle[1]	T_{max}	P_{max} (%)	PR (kW)	Type[2]	Seals	Bearings	Architecture[3]	N [kPRM]	D [mm]	$\dot{m}$
SNL [125, 124]	125	RC	537	170	1.8	TAC	Labyrinth	Gas foil	IFR	75	68.1	2.7
									CC (main)	75	37.3	3.5
								Gas foil	IFR	75	68.3	3.08
							Labyrinth		CC (recomp.)	75	57.9	2.4
PTT	–	RC	750	423	-	TC	Leaf	Gas	IFR, CC (x2)	118	–	5.5
IST [125, 124]	100	RE	299		1.8	TC, TG	Labyrinth	Gas foil	IFR (TC, TG)	75	53	-
								CC	(TC)	75	38	–
Echogen	8000	RE	485			TC	–	–	IFR, CC	24–36	–	-
						TG	Dry-gas	Tilting pad	IFR	30	–	–
SWRI/GE	1000	RC	715	251	2.9	T	Dry gas, Tilting pad	4-stage	AT	27	–	8.41
STEP	10,000	RC	715	250	2.7	T	–	–	3-stage AT	–	–	103
NET Power	200,000	AL	1150	300	T	–	–	7-stage AT	–	–	–	—
TIT	10	RE	277	119	1.45	TAC	–	Gas	IFR	100	35	1.1
									CC	100	30	1.1
KAIST [125, 124]	300	RE	500	200	2.67	MC	–	–	CC (twin, shrouded)	70	–	3.2
						TG	–	–	IFR (shrouded)	80	–	5.05
						TAC	–	–	–	68	–	–
KIER [125, 124]	1	RE	200	130	2.27	TG	–	Angular ball	IFR (PA)	200	22.6	–
	10	S	180	130	1.65	TAC	Labyrinth	Gas foil	CC, IFR (shrouded)	70	50	–
	60	RE	392	135	1.75	TG	–	Tilting pad	1-stage AT (PA)	45	73	1.74
sCO2-HeRo	7	S	200	117.5	1.5	TAC	Labyrinth	Angular ball	IFR (shrouded)	50	66	0.65
									CC (shrouded)	50	40	0.65
I-ThERM	50	RE	435	127	1.7	TAC	-	Angular ball	IFR turbine	60	72	2.1
									CC	60	55	2.1

[1]Cycle layout: simple (S), recuperated (RE), recompression (RC), Allam (AL).
[2]Letters refer to components mounted on the same shaft: turbine (T); alternator (A); compressor (C); generator (G); motor (M).
[3]Types of turbine: inward-flow radial turbine (IFR); centrifugal compressor (CC); axial turbine (AT); partial admission (PA)

Further to the STEP [126] and Sun-shot [127] projects, multiple research programs have been initiated to realise the performance of sCO$_2$ machines in practice namely sCO$_2$-Flex [128] and SOLARSCO2OL [129]. The STEP and Sun-shot projects focus on constructing a 10 MWe sCO$_2$-based pilot facility and the design, fabrication, and validation a 10 MWe sCO$_2$ power cycle respectively as discussed earlier in Section 2.5.1. The sCO$_2$-Flex is concerned with developing and validating a 25 MWe CO$_2$ Brayton cycle design. Hacks et al. [120, 130] designed a TAC unit as part of the sCO$_2$-HeRo project. This system comprises a single-stage radial compressor and radial turbine, both with 2D shrouded blades. The shrouded blades were used for both the compressor and the turbine to minimise clearance losses and the rotational speed was limited to 200,000 RPM to reduce windage losses. Whilst SOLARSCO2OL focuses on developing simulation tools for assessing the techno-economic aspects of novel sCO$_2$-CSP layouts. Another project is currently running at Brunel University London, in collaboration with Enogia, where the High Temperature Heat To Power Conversion facility (HT2C) has been developed. This system utilises a TAC unit with un-shrouded single-stage radial compression and expansion stages [14].

2.5.2 Structural and mechanical design of supercritical CO$_2$ turbo-machinery

Structural and mechanical considerations are highly significant in the design phase of turbo-machinery particularly while dealing with dense fluids like sCO$_2$ and operating at high pressures. sCO$_2$ is expected to result in higher aerodynamic loads on the stator and rotor blades compared to air and steam turbines owing to the higher pressure applied by the dense gases. Hence, pressure and centrifugal loads are worth studying. Wright et al. [131] mentioned that the higher operating pressure of the pure sCO$_2$ and its high density can significantly influence the loading on the turbine rotor blades and hence, requires materials with higher strength. This was supported by the outcomes of Wang et al. [132] who found that gas bending is the most significant stress type for CO$_2$ compressors compared to the centrifugal stress in conventional gas compressors.

In the same context, Kalra et al. [113] recommended using a mechanically robust blade

design for sCO_2 turbo-expander to accommodate the high bending stresses. Additionally, shaft design was found to be critical while dealing with the high-density sCO_2 fluid where damping options are required to mitigate vibrations. It has been concluded that it is important to study resonance frequency and make sure that excitation sources within the turbine have a safe margin to prevent resonance. This can be done by selecting the stator number such as the natural frequency is far away from the resonance frequency [113]. Later, Von-misses stresses of $X_{12}Cr_{13}$ alloy have been investigated for a sCO_2 radial turbine by Moroz et al. [78]. For the impulse turbine, the actual stress exceeded the allowable stress by 3 times and 1.6 times for the nozzle and rotor blades respectively. As for the reaction types, it exceeded the allowable stress by 3.65 and 4.7 for stator and rotor blades respectively. Furthermore, optimisation analysis showed that the chord length increased significantly to satisfy the structural requirements and the overall length of the reaction turbine increased by 2.3 times to account for the high-density sCO_2 [78].

Further to the high stresses imposed by the high-density working fluid, sCO_2 turbines experienced several operation challenges due to the compact geometries, high density and low kinematic viscosity of working fluid compared to air turbines. These properties result in challenges in seals and bearings designs, particularly for small-scale demonstrators. Principally, oil-hydrodynamic tilting pad bearings are the primary choice for journal and thrust loads for the power industry. This is owing to their aerodynamic stability, the ability to withstand high axial and radial loads and finally operate at high speeds. For sCO_2 plants, high thrust load capability is important owing to the high pressure difference across the turbo-machinery which leads to thrust load imbalances. Thus, other bearings types were recommended for sCO_2 research and test facilities including gas foil bearings, magnetic bearings, hydrostatic bearings, and hybrid bearings. These bearings have several advantages such as high operating speeds and long shafts by placing the bearing midway along the length of a multi-staged turbo machine. Nevertheless, dealing with these bearings is challenged with the complicated aerodynamics, high windage and heating, with requirements for local cooling, during the turbine operation [21]. As mentioned earlier, the TIT reported that less net power output due to the high windage loss resulted from the high-speed rotor and thrust bearing [123].

Dealing with the sCO_2 causes other operation challenges related to the gearbox or generator equipment. Fuller et al. [133] pointed out that the gearbox or generator equipment is not practical to operate in the dense sCO_2 environment. Also, the high inlet temperature poses challenges to the throttle control and turbine stop valve; where the valves are placed upstream of the turbine inlet at the highest temperature point in the cycle [30].

In brief, structural and mechanical considerations were found to be highly significant while dealing with dense working fluids such as sCO_2. Overall, supercritical CO_2 is expected to result in higher aerodynamic loads compared to air and steam turbines owing to the higher pressure difference applied by the dense gases; hence, structural and mechanical design aspects are worth further investigation throughout the design process.

2.5.3   Conceptual designs of supercritical CO_2 turbomachinery

Though the majority of the developed prototypes are for radial turbomachinery with a few for axial configurations, various conceptual designs were previously proposed to gain a better insight into axial sCO_2 turbomachinery technology. Dostal et al. [29] presented a design for 246 MW recompression cycle with an axial turbine configuration with the best estimate of a total-to-total turbine efficiency of 92.9 %. Similarly, a design of 645 MW recompression cycle was introduced with an axial turbine designed to operate with a total-to-total efficiency of 90 % [124]. Later, MacDowell presented designs of 550 MW and 10 MW recompression cycles with axial turbine configurations. The turbine designs achieved a total-to-total efficiency of 90 and 85.4% respectively. Additionally, a design of a 15 MW axial turbine with a total-to-total efficiency of 83.96% has been proposed by Zhang et al. [79]. Later, Kang et al. [134] presented a design for an axial turbine with a power rating of 102.48 kW with an efficiency of 85%. Further details of the various conceptual designs are presented in Table 2.4. Additionally, some aspects of the conceptual designs reported by Bidkar et al. [135] will be discussed in this section, owing to the relevance of the designs to the scope of this thesis, in terms of the design configuration, scale and application.

Table 2.4: Summary of the conceptual designs of sCO$_2$ turbomachinery.

Author	Turbomachinery-type	Operating conditions				Efficiency (%)	Power rating (MW)
		TIT (°C)	PR (-)	Flow rate (kg/s)	Rotational speed (kRPM)		
Dostal et al. [29]	Main compressor (A)	42	2.20	2604	3.6	95.5	246
	Re-compressor (A)	70	2.20	1145.5		94.8	
	Turbine (A)	550	2.05	3749.5		92.9	
Thimsen [124]	Compressor turbine (A)	704	2.46	1639	5.1	90.0	645
	Power turbine (A)	704	2.46	4515	3.6	90.0	
McDowell et al. [124]	Main compressor (A)	32	3.60	53.6	39.0	79.8	10
	Re-compressor (A)	78	3.60	27.6	39.0	76.8	
	Compressor turbine (A)	704	3.40	26.2	39.0	90.2	
	Power turbine (A)	704	3.40	55.0	25.0	85.4	
Zhang et al. [79]	Turbine (A)	773	1.60	250	10.0	83.96	15
GE and SwRI [124]	Turbine (A)	700	3.77	-	9.5	90.3	50
	Turbine (A) - reheat	700 (HP) / 680 (LP)	3.80	-	3.6	-	450
Kang et al. [134]	Turbine (A)	665	1.80	2	45.0	85.0	0.1
Hanwha and SwRI [124]	Main compressor (A)	22	3.77	2134	3.6	83.0	450
	Re-compressor (A)	55	3.80	1282	3.6	80.1	450

Bidkar et al. [135] developed the designs of 50 MW and 450 MW recompression cycles with axial turbine components for CSP applications. A 1D aerodynamic design tool, developed by general electric (GE), has been used for the turbine design where an iterative approach has been adopted. The output of the design calculation results in flow conditions that have been checked with the target exit total pressure and exit flow angles. From the preliminary design tool, the number of stages and turbine geometry including the number of blades, the stage axial spacing, blade radial height and the mean flow path have been defined. Then, the 1D design output has been used to generate the 3D blade geometry by stacking three radial cross-sections along the centre of gravity. The 50 MW design is a scaling-up design for the sun-shot 10 MW turbine design [113] where the 10 MW design model has been built using GE design model tools [113].

For the 50 MW a turbine balance piston has been used to decrease the net thrust load. A gearbox has been used to connect the axial turbine to a synchronous generator; this has been done to adapt to the high rotational speeds design challenges of the sCO$_2$ turbomachines and the unavailability of the high-speed generator. The authors reported that a feasibility discussion with the gearbox manufacturer confirmed the possibility of 50 MW gearbox design to achieve speed reduction from 12,000 to 3600 rpm. Additionally, the availability of high-speed flexible couplings for the 50 MW power rating and the given rotational speed was confirmed which allows for easy connection between the main compressor and recompressor spinning at the same speed of the turbine. The rotor blades were manufactured out using single forging for a high-strength nickel-based alloy to allow for a high turbine inlet temperature of 700 °C. The solid model of the 50 MW turbine design is represented in Figure 2.16. For the 450 MW turbine design, the primary constraint has been found to be the unavailability of a 450 MW gearbox for the power transmission from high speed to either 3600 or 1800 rpm generators. Hence, the rotational speed is limited to either 3600 or 1800 rpm. Dual flow layout has been selected for the Low pressure (LPT) and high-pressure turbine (HPT) because of the anticipated efficiency loss for the single-flow layout. Hence, contrary to the 50 MW turbine design, a balance piston is not needed for thrust management. Similar to the 50 MW turbine design, a high-strength nickel alloy has been used for a design turbine to accommodate the high inlet temperature. An effi-

ciency of 90.6% has been achieved for the HPT whereas an efficiency of 91.6% has been achieved for the LPT. The solid model of the 450 MW turbine design is represented in Figure 2.17.
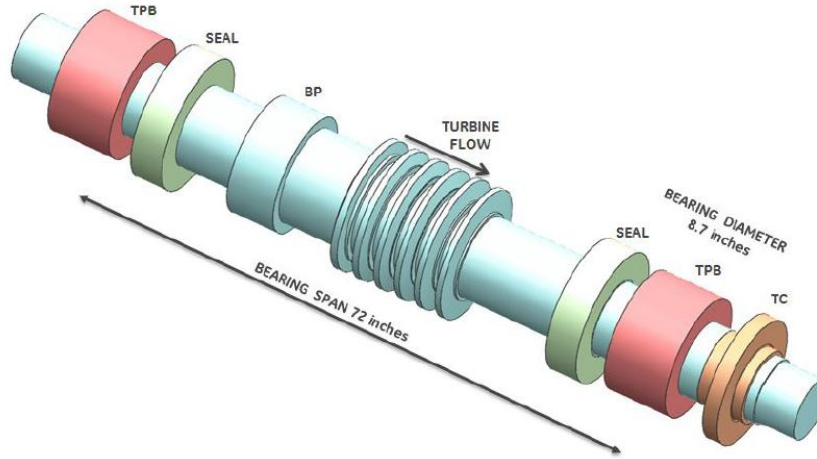
Figure 2.16: Solid model representation of the rotor design of 50 MWe turbine with tilt pad bearing (TPB), turbine end seal (SEAL), balance piston (BP) and thrust collar(TC) [135].
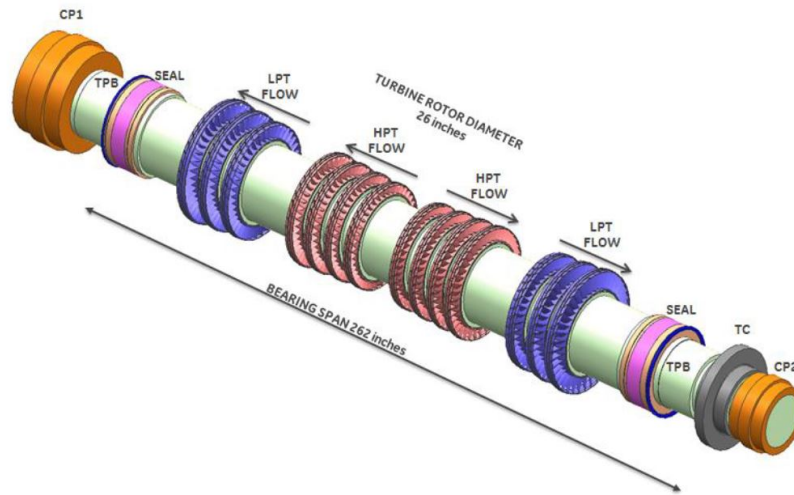
Figure 2.17: Solid model representation of the rotor design of 450 MWe turbine concept with dual flow turbines and reheat. CP1 - generator-side coupling, TPB - tilt-pad bearing, LPT - low-pressure turbine, HPT - high-pressure turbine, TC - thrust collar, CP2 - compressor-side coupling [135].

As for the mechanical integrity analysis, it is worth noting that GE calculated the forces on the rotor blades including bending stress and centrifugal forces and compared them against material limits, including the creep, rupture, ultimate tensile and yield stress, using their own specified criteria. Accordingly, a blade life of around 30 years has been achieved

for the 50 MW turbine design. For the 450 MW turbine, the blades are attached to the rotor using dovetails and hence, the life of the dovetail joins between the rotor and turbine blades was examined and the design criteria were met. In terms of the overall cycle performance, the 50 MW and 450 MW re-compression cycles achieved a thermal efficiency of 49.5% and 51.9% respectively and it has been found that the 1.1% efficiency enhancement between the cycles was achieved as a result of the introduced re-heating.

2.6   Summary

It is evident that CO_2 power cycles are promising candidates for power generation for CSP applications. To reduce the cost associated with power block for CSP applications, CO_2 blends were introduced and have shown promising results in terms of enhancing the cycle efficiency. This is due to increasing the critical temperature of the working fluid to allow for condensation using ambient air in dry regions. With this growing interest in CO_2 cycles and hence components design, three key areas have been identified in light of the previous review with respect to sCO_2 turbo-machinery design and modelling.

Most of the supercritical CO_2 turbomachinery designs presented in the literature review have considered small-scale radial turbines with fewer studies focused on developing the designs for large-scale axial turbines of around 100 MW power rating. However, there is a transition towards axial turbines to produce designs for commercial scale CSP plants rather than developing small-scale radial turbines for pilot projects. Thus there is a need to identify optimal designs for these applications. Given that sCO_2 turbines operate at high inlet pressures and temperatures, they face some design and operational challenges. Additionally, their performance is highly affected by clearance, windage and frictional losses which are typically associated with the compact turbine design, alongside the high density and low kinematic viscosity of the working fluid. The previous studies showed that structural and mechanical considerations were found to be highly significant when dealing with dense working fluids such as sCO_2; supercritical CO_2 is expected to result in higher aerodynamic loads compared to air and steam turbines owing to the higher pressure difference applied by the dense gases. Nonetheless, it is worth noting that the aforementioned projects

and conceptual designs have focused on developing turbomachinery conceptual designs, evaluating off-design performance and testing facilities for CO_2 plants without accounting for the effects of introducing sCO_2 blends. Comparatively, the SCARABEUS project is concerned with the application of sCO_2 blends for large-scale CSP plants (100 MWe). Hence, this thesis focuses on advancing the state of the art of large-scale axial turbine designs operating with novel sCO_2 blends for the 100 MWe SCARABEUS plant.

Preliminary aerodynamic turbine design and optimisation is a necessary step within the turbine design process that precedes advanced 3D blade optimisation and flow analysis studies. On this matter, it is evident that design methodologies are well-established and have been extensively applied in many textbooks and scientific publications. This includes the implementation of several empirical models that have been introduced to predict the performance of axial turbines operating with conventional working fluids like air and steam with the first loss model developed back in 1949 by Soderberg [62] and one of the latest model updates presented in 2006 by Aungier [66].

It is clear from the literature that these models have been implemented in the design process of sCO_2 and ORC axial turbines within which each study has only applied a single loss model and considered a single working fluid, turbine scale or operating condition. Nonetheless, applying those established methodologies for non-conventional working fluids impose some challenges and uncertainties on applying those conventional design methodologies. None of the previous studies attempted to highlight the discrepancies in the different models in predicting the turbine performance for non-conventional working fluids (such as sCO_2 blends). In continuation to the axial turbine design process, evaluating the off-design performance of the turbine is an important step for the development of CSP applications to allow for providing accurate cycle performance analysis. Multiple studies in the literature have investigated the off-design performance analysis of turbines operating with pure CO_2 and organic working fluids for multiple configurations and hence, developing performance maps for those designs.

The following remarks summarise the identified research gaps from the review and hence, highlight the objectives of this study:

- Previous studies have focused on developing turbomachinery conceptual designs and pilot projects for CO_2 based plants; particularly for radial turbine configurations. Hence, it is important to develop turbomachinery design for a large-scale axial turbine operating with sCO_2 blends for installation in CSP plants.

- Loss models have been previously implemented in the design process of sCO_2 and ORC axial turbines. However, none of the previous studies highlighted the discrepancies in the different models in predicting the turbine performance for non-conventional working fluids. Therefore, it is crucial to investigate the applicability of all the common loss models, employed within the literature, for different working fluids and turbine scales.

- Structural and mechanical considerations were found to be highly significant while dealing with dense working fluids such as sCO_2. Bearing this in mind, there are very few published studies for CO_2 where these aspects are considered.

- Evaluating the off-design performance analysis is a necessary step throughout the turbine design process; particularly for CSP applications where the electrical energy produced is of an intermittent nature. Additionally, evaluating the prediction capability of the existing loss models for the off-design performance is important for CO_2 based applications.

2.7   Research objectives

In light of the above discussion, the overall aim of this thesis is to develop design and optimisation tools for 100 MW scale sCO_2 multi-stage axial turbine design for concentrated-solar power applications and to investigate the effect of sCO_2 blends on the turbine performance. The project specific objectives are set as follows:

1. To explore the existing design methodologies for supercritical multistage axial turbine design for sCO_2 blends considering both mechanical design constraints and aerodynamic performance.

2. To adopt a mean-line approach to investigate the behaviour of the commonly used loss models within the literature for different working fluids and turbine scales.

3. To examine the validity and prediction capability of existing loss models for the non-conventional working fluids across a range of scales.

4. To apply the existing design methodologies in the context of the SCARABEUS project and enable the conceptual mean-line flow-path design of a multi-stage axial turbine operating with CO_2 blends, suitable for the 100 MWe plant.

5. To predict the off-design performance of sCO_2 turbines; particularly the SCARABEUS CO_2/SO_2 flow path.

This page is left intentionally blank

3 Axial turbine design methodology

3.1 Introduction

From the literature review, it is clear that the development of sCO_2 axial turbine designs is critical for advancing the state of the art of CSP power cycles. Enhancing the design and performance of the different cycle components should result in better system performance and hence, cost reduction for the overall CSP technology. To realise this development, a multi-stage design process needs to be carried out starting from the preliminary aerodynamic design and optimisation, using a combination of one-dimensional mean-line design and suitable loss models and ending with through-flow analysis and computational fluid dynamic (CFD) analysis.

This chapter presents the preliminary axial turbine design methodology implemented for a large-scale axial turbine to be installed in a 100 MWe CSP plant. This includes presenting the applied one-dimensional mean-line design approach, classical loss models correlations and the verification results of the used approach against multiple case studies from the literature. Ultimately, a parametric study is presented to explore the design space and investigate the effect of the different design parameters on the aerodynamic performance of the turbine.

3.2 Preliminary axial turbine design methodology

3.2.1 Velocity diagram of the axial turbine stage

In axial turbines, the working fluid flows through a set of stationary guide vanes called stator (S) and a row of moving blades called rotor (R) row. The fluid enters the stator row with a static pressure and temperature of P_1, T_1 at an absolute velocity and angle of C_1 & α_1, respectively, and leaves with an increased absolute velocity C_2 at an angle of α_2. Then, the flow enters the rotor blades with static pressure and temperature of P_2, T_2, respectively, and a relative velocity and flow angles of w_2 and β_2 respectively; where the relative velocity, w_2, is found by vectorial subtraction of the blade peripheral speeds (U)

and the axial velocity (C_2) (Figure 3.1a). The gas is deflected and further expanded in the rotor blades to leave at static pressure and temperature of P_3 and T_3, respectively, and relative velocity of w_3 at an angle of β_3. Principally, the turbine is designed at the optimum point where a zero incidence is assumed between the inlet flow angle (α_1) and blade angle (α_1'). The incidence effect is considered in the later stages of the design/simulation process where the off-design performance of the turbine is analysed.

A Mollier h-s diagram (Figure 3.1b) shows the various states through a single-stage axial turbine including the effect of irreversibility; the effect of irreversibility is a result of the aerodynamic losses that the working fluid experiences through the expansion process. Within a single stage, the actual expansion, considering the flow irreversibility, results in a total enthalpy drop from h_{01} to h_{03} compared to an isentropic drop from h_{01} to h_{03ss}. The working fluid expands first in the stator blades from P_1 to P_2. Following this, the pressure decreases in the rotor blades from P_2 to P_3 for reaction turbines whilst, it remains the same for impulse turbines ($P_2 = P_3$); where the amount of pressure drop across the rotor blades with respect to the whole turbine stage is indicated by a dimensionless parameter called the degree of reaction (Section 3.2.2).
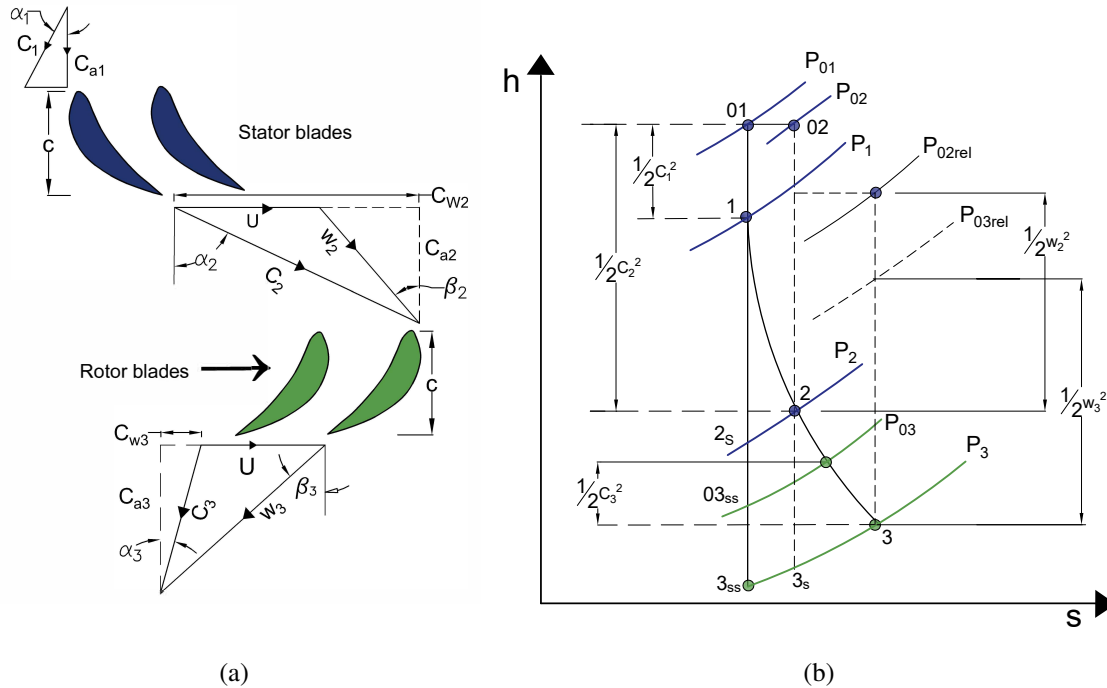
Figure 3.1: Axial turbine (a) velocity triangle (b) Mollier chart (*h-s* diagram) for a single design stage.

57

For a single turbine design stage, the flow enters the blade row with an absolute axial velocity of C_1 at a zero flow angle (α_1) (measured with respect to the axial direction). Whilst, for a multi-stage turbine design, C_1 and α_1 of the next turbine stage should be equal to C_3 and α_3 of the previous turbine stage. The same applies for all other properties where $P_{01(\text{2nd stage})} = P_{03(\text{1st stage})}$, $T_{01(\text{2nd stage})} = T_{03(\text{1st stage})}$.

The mass flow rate passing through the turbine is governed by the continuity equation that can be expressed:

$$\rho_1 A_1 C_{a1} = \rho_2 A_2 C_{a2} = \rho_3 A_3 C_{a3} \tag{3.1}$$

where A is the cross-sectional area, C_a is the axial flow velocity, ρ is the flow density and 1, 2 and 3 subscripts correspond to stator and rotor conditions as specified in Figure 3.1a.

3.2.2   Design parameters

The shape of the turbine velocity triangles (Figure 3.1a) can be related to three commonly defined non-dimensional parameters, that are used throughout the preliminary turbine design phase, namely loading coefficient (ψ) and flow coefficient (ϕ) and degree of reaction (Λ).

The stage degree of reaction (Λ) is the ratio of the static enthalpy drop across the rotor to the static enthalpy drop across the whole turbine stage (Equation 3.2). Therefore, it gives an indication of the amount of pressure drop across the stator blade row compared to that of the stage [23]. Using the degree of reaction, turbines can be classified into impulse and reaction turbines. In impulse turbines, all the pressure energy is transferred to Kinetic energy in the stator blade row and hence, only the kinetic energy of the working fluid is used to spin the rotor shaft and the pressure remains constant across the rotor blade row ($\Lambda = 0$) whilst, in reaction turbines part of the pressure energy of the working fluid is converted to kinetic energy in the stator blade row and hence, both kinetic and pressure

energy rotate the turbine shaft ($\Lambda > 0$). The degree of reaction is expressed as:

$$\Lambda = \frac{h_2 - h_3}{h_1 - h_3} \tag{3.2}$$

The loading coefficient (ψ) is defined as the ratio of the stagnation enthalpy drop across a turbine stage to the square of the peripheral blade speed as presented in Equation 3.3. It provides a non-dimensional measure of the work extraction per stage; where a high stage loading is desirable because it means fewer stages are needed to produce a required work output.

$$\psi = \frac{(\Delta h_0)_{stage}}{U^2} \tag{3.3}$$

The flow coefficient (ϕ) is defined as the ratio of the meridional (axial) velocity (C_a) to the blade peripheral speed U across the turbine stage. A stage with a low flow coefficient value implies highly staggered blades and relative flow angles close to tangential.

$$\phi = \frac{C_a}{U} \tag{3.4}$$

For a multi-stage turbine design, the enthalpy drop across the stage (the specific work done across a turbine stage) can be assumed to be equally divided across the turbine stages and can be expressed as:

$$(\Delta h_0)_{stage} = \frac{\Delta h_0}{n_{stages}} = \frac{h_{01} - h_{03}}{n_{stages}} \tag{3.5}$$

Using the defined loading coefficient and enthalpy drop across the stage, the peripheral blade speed can be obtained as follows:

$$U = \sqrt{\frac{(\Delta h_0)_{stage}}{\psi}} \tag{3.6}$$

It is worth mentioning that the peripheral blade speed varies from the blade hub to tip as a result of the changing radius. However, within the mean-line turbine design approach, the peripheral blade speed is evaluated at the mid-span (mean diameter).

3.2.3 Thermodynamics of the axial turbine stage

As demonstrated in Mollier chart, Figure 3.1b, the specific work done across a turbine stage is defined as the difference between the total enthalpy at the turbine inlet and exit conditions respectively $(\Delta h_0)_{stage}$. From the Euler equation (Equation 3.7), the specific work (W), derived for an adiabatic turbo-machinery, is obtained by applying the principle of angular momentum and expressed as [23]:

$$\tau\,\Omega = \dot{m}\left(U_2 C_{w2} + U_3 C_{w3}\right) \tag{3.7}$$

$$W = h_{01} - h_{03} = U_2 C_{w2} + U_3 C_{w3} \tag{3.8}$$

where Ω is the angular velocity, τ is the torque exerted on the blades, C_w is the tangential velocity components and 2 and 3 subscripts represent rotor inlet and exit conditions respectively. Since there is no work done in the stator blade row, the absolute stagnation enthalpy at the stator inlet h_{01} is equal to the absolute stagnation enthalpy at the stator exit h_{02} and hence:

$$h_1 + \frac{1}{2}C_1^2 = h_2 + \frac{1}{2}C_2^2 \tag{3.9}$$

Hence,

$$h_{01} - h_{03} = h_{02} - h_{03} \tag{3.10}$$

For the rotor blade row, rothalpy (I) (Equation 3.11) is constant along the streamlines assuming an adiabatic irreversible flow process.

$$I = h_{0,rel} - \frac{1}{2}U^2 \tag{3.11}$$

where h_{0rel} is the total relative enthalpy which is equal to $\left(h + \frac{1}{2}W^2\right)$ and hence the rothalpy can be expressed as:

$$h_2 + \frac{1}{2}w_2^2 - \frac{1}{2}U_2^2 = h_3 + \frac{1}{2}w_3^2 - \frac{1}{2}U_3^2 \tag{3.12}$$

At a constant blade speed ($U_2 = U_3$), the equation can be reduced to:

$$h_2 + \frac{1}{2}w_2^2 = h_3 + \frac{1}{2}w_3^2 \tag{3.13}$$

$$h_{02,rel} = h_{03,rel} \tag{3.14}$$

Using the geometry of the stage velocity triangles gives the following the relations:

$$\frac{U}{C_{a2}} = \tan \alpha_2 - \tan \beta_2 \tag{3.15}$$

$$\frac{U}{C_{a3}} = \tan \beta_3 - \tan \alpha_3 \tag{3.16}$$

By integrating Equations 3.15 and 3.16 with the principle of angular momentum (Equation 3.8), the stage specific work can be defined as a function of the flow angles as follows:

$$W = UC_a(\tan \alpha_2 + \tan \alpha_3) \tag{3.17}$$

$$W = UC_a(\tan \beta_2 + \tan \beta_3) \tag{3.18}$$

Using the specific work equation (Equation 3.18) along with Equation 3.3 results in the definition of the loading coefficient as:

$$\psi = \frac{2C_a}{U}(\tan \beta_2 + \tan \beta_3) \tag{3.19}$$

For a constant the axial velocity (C_a) through the turbine and assuming that $C_1 = C_3$, $h_1 - h_3$ can be expressed as:

$$h_1 - h_3 = h_{01} - h_{03} = U\, C_a(\tan \beta_2 + \tan \beta_3) \tag{3.20}$$

Relative to the rotor blades the flow does no work ($h_{02,rel} = h_{03,rel}$) and the steady flow energy equation yields to:

$$h_2 - h_3 = \frac{1}{2}\left(w_3^2 - w_2^2\right) = \frac{1}{2}C_a^2\left(\sec^2 \beta_3 - \sec^2 \beta_2\right) \tag{3.21}$$

$$= \frac{1}{2}C_a^2\left(\tan^2 \beta_3 - \tan^2 \beta_2\right) \tag{3.22}$$

and thus the degree of reaction can be expressed as:

$$\Lambda = \frac{C_a}{2U} \left(\tan \beta_3 - \tan \beta_2 \right) \tag{3.23}$$

By integrating the definition of the loading and flow coefficients Equations 3.3 and 3.4 with Equation 3.23, the loading coefficient and degree of reaction can be expressed as:

$$\psi = 2\phi \left(\tan \beta_3 + \tan \beta_2 \right) \tag{3.24}$$

$$\Lambda = \frac{\phi}{2} \left(\tan\beta_3 - \tan\beta_2 \right) \tag{3.25}$$

Consequently, the gas angles can be defined as a function of the three dimensionless parameters ϕ, ψ and Λ as:

$$\tan \beta_2 = \frac{1}{2\phi} \left(\frac{\psi}{2} - 2\Lambda \right) \tag{3.26}$$

$$\tan \beta_3 = \frac{1}{2\phi} \left(\frac{\psi}{2} + 2\Lambda \right) \tag{3.27}$$

$$\tan \alpha_2 = \tan \beta_2 + \frac{1}{\phi} \tag{3.28}$$

$$\tan \alpha_3 = \tan \beta_3 - \frac{1}{\phi} \tag{3.29}$$

where α_1 and α_2 are the absolute flow angles at the stator inlet and outlet respectively, β_2 and β_3 are the relative flow angles at the rotor inlet and outlet conditions as indicated in Figure 3.1a.

The flow coefficient (ϕ) and loading coefficient (ψ) are selected according to standardised efficiency charts recommended in the literature for optimum design efficiency [136, 22]. Smith [136] provided a generalised chart to predict the efficiency of axial turbines considering various turbine geometries over a range of loading (ψ) and flow coefficients (ϕ) as shown in Figure 3.2, and hence it is widely used during mean-line design. By selecting these dimensionless parameters, flow angles can be obtained and hence, flow velocities as shown in Figure 3.1a. Additionally, the peripheral and axial blade speeds can
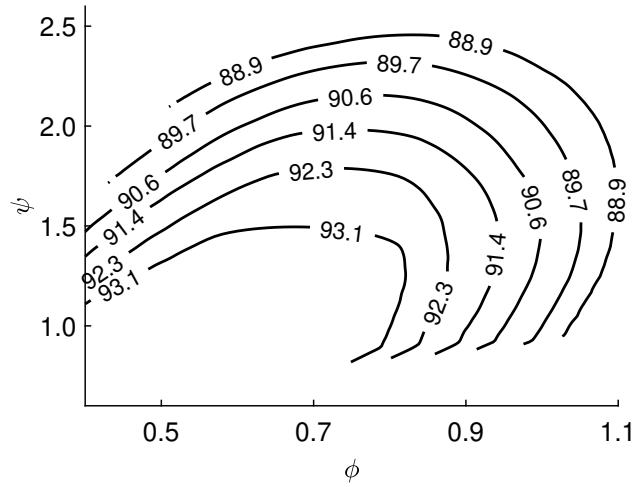
Figure 3.2: Smith chart for axial turbines; representing the total-to-total efficiency [%] (contours) of axial turbines at different flow (ϕ) and loading coefficients(ψ) [136].

be obtained. Hence, the tangential (whirl) velocity components can be obtained as:

$$C_{w2} = C_a \tan \alpha_2 \qquad (3.30)$$

$$C_{w3} = C_a \tan \alpha_3 \qquad (3.31)$$

3.2.4 Design of blade shape

Next to completing the mean-line flow path details, which includes calculating the flow angles and velocity triangles, the blade profiles should be generated. Stator and rotor blade profiles are defined with a curved camber line through which the blade profile thickness distribution is imposed. Hence, several geometrical parameters should be defined to generate the blade profile within the mean-line design context. Those parameters can be summarised as follows:

- Inlet blade angle ($\alpha_1{'}$): the difference between inlet flow angle and incidence angle (i).
- Outlet blade angle ($\alpha_2{'}$): the difference between the inlet flow angle and deviation angle (δ).
- Stagger angle (ζ): the angle between the chord line and the reference direction as indicated in Figure 2.13.

63

- Blade pitch (s): the distance between two consecutive blades as indicated in Figure 3.4a).

- Chord length (c): the length of the cross-section of the blade (Figure 3.4a).

- Blade height: the vertical distance between the blade hub and tip.

- Throat opening (o): the minimum flow area.

- Edge to edge spacing (ss): the distance between the stator and rotor blade row as shown in Figure 3.3.
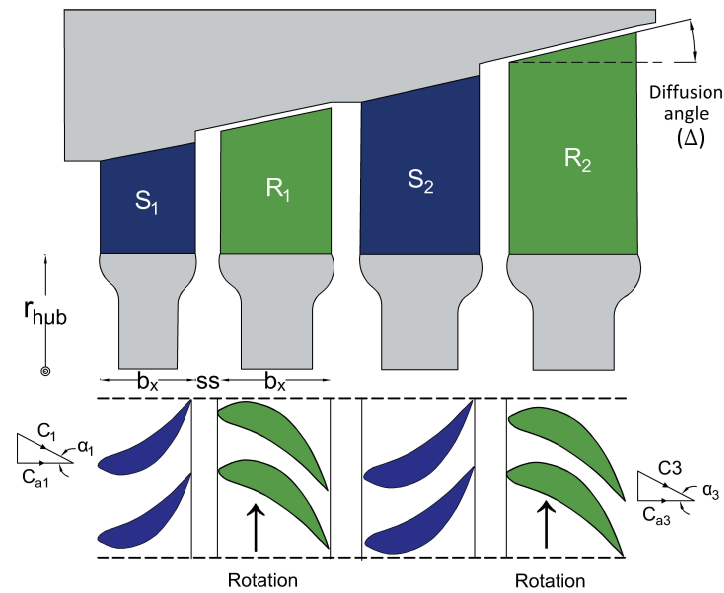
Figure 3.3: Schematic of the axial turbine geometry and meridional cross section

| (a) | (b) |
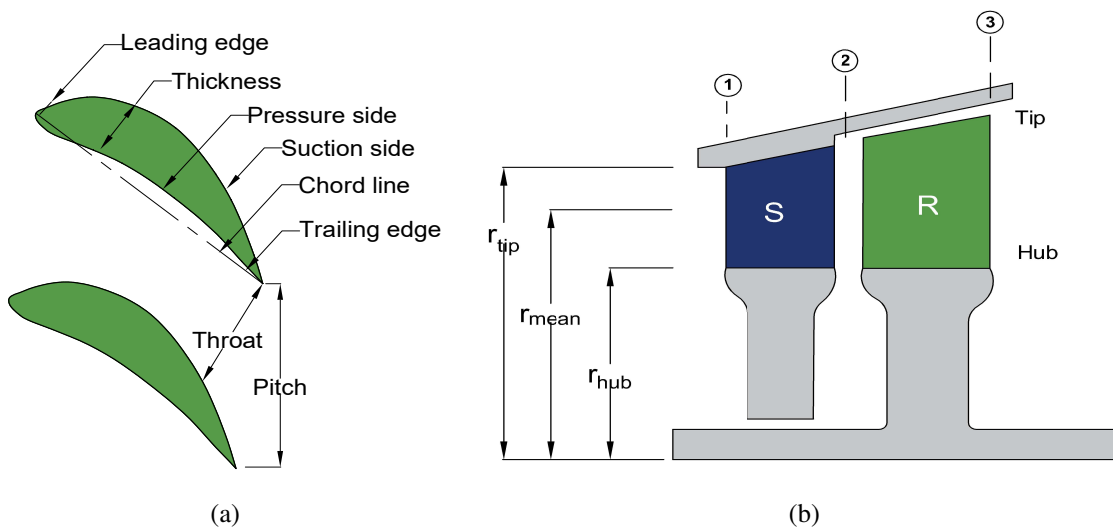
Figure 3.4: (a) Geometry of a blade section (b) schematic of axial flow turbine stage

Principally, the turbine is designed at the optimum point where a zero incidence is assumed between the inlet flow angle (α_1) and blade angle ($\alpha_1{}'$). The incidence effect is considered in the later stages of the design/simulation process where the off-design performance of the turbine is investigated. Ideally, the direction of the working fluid leaving the blade row should be the same as the outlet blade angle. However, in practice, the outlet flow deviates from the intended blade angle due to the fluid's reluctance to pass through the turbine along the required blade angles. The deviation angle (δ) is defined as the difference between blade angle ($\alpha_2{}'$) and the outlet flow angle (α_2). The deviation angle is defined within the mean-line design process using the empirical correlations introduced by Ainley and Mathieson [63] for subsonic outlet conditions as a function of the blade opening-to-pitch ratio (o/s).

$$\alpha_2' = \begin{cases} \alpha_2{}^* - 4(s/e), & \text{if } 0.5 > M > 0 \\ -\cos^{-1}(A_t/A_{2n}), & \text{if } M = 1 \\ \alpha_2{}^* + \alpha_0 & \text{if } 1 > M > 0.5 \end{cases} \qquad (3.32)$$

where s/e is the ratio of the blade pitch to the mean radius of curvature, o/s is the throat-to-pitch ratio, M is Mach number, A_t is the passage throat area, A_{2n} is the annulus area in reference plane downstream of the blade row. $\alpha_2{}^*$ can be expressed as:

$$\alpha_2{}^* = -1.1525 \cos^{-1}(o/s) + 11.47 \qquad (3.33)$$

For the stator blades with $1 > M > 0.5$,

$$\alpha_0 = -3.9873\, M^6 + 27.288\, M^5 - 44.584\, M^4$$
$$+ 26.392\, M^3 - 6.1647\, M^2 + 0.4766\, M - 1.0911 \quad (3.34)$$

for the rotor blades

$$\alpha_0 = -38.416 M^6 + 200.5 M^5 - 311.75 M^4 + 190.23 M^3 - 47.82 M^2 + 4.0673 M - 0.145; \qquad (3.35)$$

Alternatively, Figures 3.5a and 3.5b can be used to get $\alpha_2{}^*$ and α_0. It is worth mentioning that Equations 3.34 and 3.35 are obtained using the least squares polynomial curve fitting of the data presented in Figures 3.5a and 3.5b.

(a)   (b)
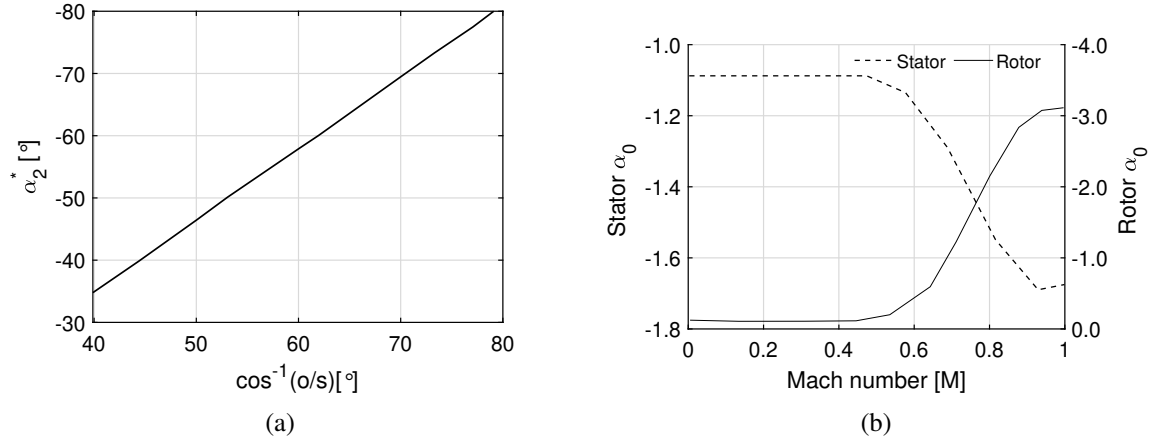
Figure 3.5: (a) Flow outlet angle versus cosin inverse throat to pitch ratio (o/s) for blades operating at low Mach number (b) Flow outlet angle as a function of the outlet Mach number [63].

The stagger angle of the blade can be defined for circular arc camber lines as [23]:

$$\zeta = \frac{1}{2}\left(\alpha_1{}' + \alpha_2{}'\right) \tag{3.36}$$

with the definition of stagger angles, the axial chord length is obtained as follows:

$$b_x = c \cos \zeta \tag{3.37}$$

It is worth noting here that within the current work, the stagger angle ζ is obtained as a function of the blade angle for a specific blade profile provided by the project industrial partners for a selected blade profile.

Following the definitions of blade stagger angle, blade pitch, chord and height should be defined. The annulus area at the different planes can be obtained using the mass flow rate defined by the turbine boundary conditions ($\dot{m}$), axial velocity C_a and operating density ρ.

$$A_1 = \frac{\dot{m}}{\rho_1 \times C_a} \tag{3.38}$$

$$A_2 = \frac{\dot{m}}{\rho_2 \times C_a} \tag{3.39}$$

$$A_3 = \frac{\dot{m}}{\rho_3 \times C_a} \tag{3.40}$$

With the known average blade speed (U), rotational speed (N), and annulus areas (A), blade heights h and mean radius r_m can be obtained at different locations as follows:

$$h = \frac{A \times N}{U} \tag{3.41}$$

$$r_m = \frac{U}{2\pi N} \tag{3.42}$$

To obtain the number of blades in each stator and rotor row, the pitch-to-chord ratio also needs to be defined. As indicated in the Ainley and Mathieson model [63], there is an optimum pitch-to-chord ratio that varies based on the gas deflection to allow for achieving minimum loss coefficients. Hence, the optimum pitch-to-chord ratio is defined as a function of the blade angles as follows (Equations 3.43 to 3.47) [66]. The blade pitch and chord are indicated in Figure 2.12a.

$$X = (90 - \alpha_1{}')/(90 - \alpha_2) \tag{3.43}$$

$$(s/c)_0 = 0.427 + \alpha_2/58 - (\alpha_2/93)^2 \tag{3.44}$$

$$(s/c)_1 = 0.224 + (1.5775 - \alpha_2/90)\,\alpha_2/90 \tag{3.45}$$

$$(s/c)_{opt} = (s/c)_0 + [(s/c)_1 - (s/c)_0]\,|X|X \tag{3.46}$$

where $\alpha{}'$ is the blade angle and α is the flow angle measured from tangential direction, 1 and 2 subscripts stand for the inlet and exit planes of the stator and rotor blade respectively [66]. With the known optimum pitch-to-chord ratio, the pitch (s) can be obtained by assuming an aspect ratio for the blade; where the chord length (c) is the blade height divided by the aspect ratio. Hence, the count of rotor blades is defined as a function of the blade pitch (s) at the mean radius (r_m) as:

$$n = 2\pi r_m/s \tag{3.47}$$

The throat opening can be determined by assuming a trailing edge to throat opening ratio between 0.05 to 0.4 [65]; where it is recommended to keep this ratio close to 0.05 to minimise trailing edge losses. Finally, the edge-to-edge spacing between the stator and rotor blade row is defined. Principally, very small edge-to-edge spacing results in huge losses due to wake development and very large edge-to-edge spacing penalises the turbine performance due to the unguided flow which results in higher losses. Therefore, within the current work, the optimum spacing between the stator and rotor blade row (*ss*) is defined as a function of the pitch value upstream, based on industrial experience. Using the defined spacing and diffusion angle (Δ) labelled in Figure 3.3, the rotor inlet tip radius can be obtained as follows:

$$\Delta = \tan^{-1}\left[\frac{h_2 - h_1}{b_x}\right] \tag{3.48}$$

$$r_{\text{tip(rotor in)}} = r_{\text{tip(stator out)}} + ss\,\tan(\Delta) \tag{3.49}$$

3.2.5 Performance prediction

The next step within the mean-line design is to evaluate the turbine performance. The total-to-total turbine efficiency (η_{tt}) is defined as follows.

$$\eta_{tt} = \frac{\text{Actual work output}}{\text{Ideal work output}} \tag{3.50}$$

$$\eta_{tt} = \frac{h_{01} - h_{03}}{h_{01} - h_{03ss}} \tag{3.51}$$

Considering that the flow conditions are identical at the inlet and exit of the stage (i.e., $C_1 = C_3$ and $\alpha_1 = \alpha_3$) and by assuming that $C_{3ss} = C_3$, the total-to-total efficiency can be expressed as:

$$\eta_{tt} = \frac{(h_1 - h_3)}{[(h_1 - h_3) + (h_3 - h_{3s}) + (h_{3s} - h_{3ss})]} \tag{3.52}$$

Using Clausius inequality defined as: :

$$\oint \frac{dQ}{T} \leq 0 \tag{3.53}$$

where dQ is an element of heat transferred to the system at an absolute temperature T. For a reversible process, $dQ = dQ_R$ and hence:

$$\oint \frac{dQ_R}{T} = 0$$
$$dS = m\,ds$$

(3.54)

The infinitesimal energy change of state is defined as $dE = dQ - dW$. In the absence of motion, gravity, and other effects, the first law of thermodynamics can be represented as:

$$T\,ds = du + p\,dv \tag{3.55}$$

recalling that $h = u + pv$, then $dh = du + pdv + vdp$ and the change in the energy of the system can be expressed as:

$$T\,ds = dh - v\,dp \tag{3.56}$$

Using 3.56, the slope of a constant pressure line on a Mollier diagram (Figure 3.1b) is expressed as $(\delta h/\delta s)_p = T$. Hence, for a finite change of enthalpy in a constant pressure process, $\Delta h \approx T\Delta s$ and the enthalpy drop can be expressed as [23]:

$$h_3 - h_{3ss} \approx T_3\left(s_{3s} - s_{3ss}\right) \tag{3.57}$$

$$h_2 - h_{2s} \approx T_2\left(s_{2s} - s_{2s}\right) \tag{3.58}$$

recalling that $s_{3s} - s_{3ss} = s_{2s} - s_{2s}$, Equations 3.57 and 3.58 can be combined as :

$$h_3 - h_{3ss} = \frac{T_3}{T_2}\left(h_2 - h_{2s}\right) \tag{3.59}$$

The effects of irreversibility through the stator and rotor are expressed by the differences in static enthalpies, $(h_2 - h_{2s})$ and $(h_3 - h_{3ss})$ respectively. Hence, the non-dimensional enthalpy loss coefficients (ζ_S and ζ_R) can be defined in terms of the exit kinetic energy from each blade row. For the stator blade row:

$$h_2 - h_{2s} = \frac{1}{2}C_2^{\,2}\zeta_S \tag{3.60}$$

For the rotor blade row:

$$h_3 - h_{3s} = \frac{1}{2} {w_2}^2 \zeta_R \tag{3.61}$$

combining Equations 3.60 and 3.61 with Equation 3.52 results in:

$$\eta_{tt} = \left[1 + \left(\frac{\zeta_R w_3^3 + \zeta_S C_2^2 \frac{T_3}{T_2}}{2(h_{01} - h_{03})} \right) \right]^{-1} \tag{3.62}$$

where C and w are the absolute and relative velocities respectively as indicated in Figure 3.1a. Within the mean-line design context, losses are introduced in the form of stagnation pressure loss coefficients for the stator and rotor and are defined as:

$$Y_S = \frac{p_{01} - p_{02}}{p_{02} - p_2} \tag{3.63}$$

$$Y_R = \frac{p_{03,rel} - p_{03,rel}}{p_{03,rel} - p_{3,rel}} \tag{3.64}$$

Therefore, to calculate the total-to-total turbine efficiency(η_{tt}), the stator and rotor enthalpy pressure loss coefficients (Y_S & Y_R) should be converted to enthalpy loss coefficients using:

$$\zeta_R = Y_R \times \left(1 + 0.5(k\,M_3{}^2) \right) \tag{3.65}$$

$$\zeta_S = Y_S \times \left(1 + 0.5(k\,M_2{}^2) \right) \tag{3.66}$$

where k is the specific heat ratio, and M_2 and M_3 are the absolute rotor inlet and relative rotor outlet Mach numbers respectively.

Stagnation pressure loss coefficients for the stator and rotor (Y_S & Y_R) are obtained by quantifying the energy losses that the working fluid experiences during the expansion in the stator and rotor blade rows. Several mathematical correlations have been developed to quantify these losses within axial turbines including correlations proposed by Soderberg (SB) [62], Ainley and Mathieson (AM) [63], Craig and Cox (CC) [60], Dunham and Came (DC) [64], Kacker and Okapuu (KO) [65] and eventually Aungier (AN) [66].

3.3 Turbine design approach

In the current work, a multi-stage mean-line design approach has been adopted where the steady-state mass, energy, and momentum equations are solved to allow for obtaining blade geometry, velocity triangles and thermodynamic properties for all design stages. To initiate the turbine design process, a set of turbine boundary conditions, taken from the thermodynamic cycle analysis, are defined. This includes the turbine total inlet pressure (P_{01}), total outlet pressure (P_{03}), total inlet temperature (T_{01}) and mass flow rate ($\dot{m}$). Following the definition of the turbine boundary conditions, a set of decision variables are defined. These decision variables are summarised in Table 3.1.

Table 3.1: Decision variables for the mean-line design approach.

Decision variables	symbol	blade geometry	symbol
Number of stages	n_{stage}	Inlet flow angle	α_1
Rotational speed	N	Pitch-to-chord ratio	s/c
Stage flow coefficient	ϕ	Trailing edge thickness to throat ratio	
Stage loading coefficient	ψ	Thickness to throat ratio	t/o
Degree of reaction	Λ	Pitch to mean radius of curvature ratio	s/e
Surface roughness	k_s	Radial tip-clearance	t_{cl}

To proceed with the turbine design process, the one-dimensional design tool is coupled with two thermodynamic commercial packages, that include NIST REFPROP and SIMULIS [52], to calculate the thermo-physical properties of the examined working fluids. The selection of the equation of state is one of the important aspects that affect the accuracy of thermodynamic cycle performance analysis. Consequently, multiple studies have taken place within the SCARABEUS consortium to investigate the effect of the equation of state selection on the cycle analysis accuracy as discussed in Section 2.2.4. With regards to the turbine design, a maximum difference in the turbine geometry of 6.3% was obtained, among the flow path designs produced for the three candidate blends (namely $CO_2/TiCl_4$, CO_2/C_6F_6 and CO_2/SO_2), due to the use of the different EoS; in particular, using SRK versus PC-SAFT. It has been found that turbine design for CO_2/SO_2 working fluids is the least sensitive to the fluid model; this indicates that CO_2/SO_2 offer robust property prediction in the absence of experimental data. Therefore, Peng-Robinson equation

is used in this thesis to calculate the thermo-physical properties of all blends; where the binary interaction parameters for the selected equation were selected to match those used for the cycle analysis to ensure consistency in the thermodynamic properties obtained by both models.

Ultimately, the developed design tool is integrated with multiple loss models that have been used in the literature to evaluate the aerodynamic performance of the turbine. These loss models are used to quantify and evaluate the aerodynamic losses in the axial turbine stages that include multiple types of losses, that include profile, secondary flow, tip clearance, trailing edge, shock and supersonic expansion losses as introduced earlier in Sections 2.4.1. In addition to evaluating the aerodynamic turbine performance, mechanical design considerations have been considered throughout the mean-line design methodology.

Within this thesis, the developed model is able to design turbines under two assumptions, constant mean diameter and constant hub diameter. Hence, both design procedures will be discussed in Sections 3.3.1 and 3.3.2. Principally, the cord size of the blades can increase due to the reduction in density and through the increased flow area if the hub diameter is changing. On this matter, designing the flow path at constant mean-diameter results in a hub diameter that is decreasing from inlet to exhaust and hence, results in an increased radius ratio along the turbine compared to designing the flow path at a constant hub diameter. Therefore, larger chord sizes are needed to limit the stresses on the blade roots for the increased radius ratio; where larger chord sizes result in larger roots and add additional challenges for the stiffness and rotordyanmics of the rotor. Hence, within the current study, turbine designs for sCO$_2$ based blends are developed at a constant hub diameter to reduce the severity of the potential rotordynamic and mechanical design challenges resulting from designing the flow path at a constant mean-diameter. The design approach discussed in Section 3.3.1 is modified to allow for designing the turbine at a constant hub diameter.

3.3.1   Constant mean diameter

In this section, the details of the iterative process implemented to design the turbine at a constant mean diameter will be discussed.

For given boundary conditions, fluid library, the total isentropic enthalpy drop across the turbine can be obtained $(h_{01} - h_{03})$ as a function of:

$$[h_{01}, s_1] = f(P_{01}, T_{01}) \tag{3.67}$$

$$h_{03ss} = f(P_{03}, s_1) \tag{3.68}$$

With the known total isentropic turbine enthalpy drop to h_{03ss} and assumed total-to-total turbine efficiency η_{tt}, the actual enthalpy drop across each stage $(h_{01} - h_{03})$ can be obtained by assuming equal enthalpy drop across the turbine stages as indicated in Equation 3.5. Following, the flow angles (α_2, α_3, β_2 and β_3) are obtained using Equations 3.26 to 3.29 by assuming some of the commonly known non-dimensional parameters such as flow coefficient (ϕ), loading coefficient (ψ) and degree of reaction (Λ); where the values are specified according to the original Smith chart [136]. It is worth mentioning that the turbine is principally designed at the point of minimised losses where a zero incidence angle is assumed; inlet flow and blade angles are equal ($\alpha_1{'} = \alpha_1$). The deviation (δ) between the outlet flow and blade angles are obtained using Ainley and Mathieson Equations 3.32 to 3.35.

$$\delta = \alpha_2{'} - \alpha_2 \tag{3.69}$$

The average blade speed is obtained using the assumed loading coefficient and known enthalpy drop across the turbine stage using Equation 3.19. Therefore, the axial velocity across the turbine can be obtained as indicated in Equation 3.4. With the known axial velocities and flow angles, the flow velocities can be obtained as follows:

$$C_2 = \frac{C_a}{\cos \alpha_2} \tag{3.70}$$

$$w_2 = \frac{C_a}{\cos \beta_2} \tag{3.71}$$

$$C_3 = \frac{C_a}{\cos \alpha_3} \tag{3.72}$$

$$w_3 = \frac{C_a}{\cos \beta_3} \tag{3.73}$$

Hence, the static pressure (P_1) and temperature (T_1) at the inlet conditions are calculated.

$$P_1 = f(h_1, s_1) \tag{3.74}$$

where the h_1 is computed using h_{01} and the calculated C_1. Given that there is no work done in the stator blades and $h_{02} = h_{01}$, h_2 is computed from the h_{02} and the calculated C_2. To calculate the static conditions at state 2, the stator loss coefficient (ζ_S) is firstly assumed and hence,

$$h_{2s} = f(h_2, \zeta_S) \tag{3.75}$$

$$P_2 = f(h_{2s}, s_1) \tag{3.76}$$

with the known enthalpy drop across the stage ($h_{01} - h_{03}$), h_3 can be obtained using h_{03} the calculated velocity C_3 and hence P_3 is obtained.

$$P_3 = f(h_3, s_3) \tag{3.77}$$

Once, all the thermodynamic properties are obtained at the different stations, annulus areas at the stator inlet, rotor inlet and outlet conditions can be calculated using Equations 3.38 to 3.40 where the densities are obtained as a function of the operating pressure and temperature:

$$\rho_1 = f(P_1, T_1) \tag{3.78}$$

$$\rho_2 = f(P_2, T_2) \tag{3.79}$$

$$\rho_3 = f(P_3, T_3) \tag{3.80}$$

Blade heights and mean diameter are then obtained using the calculated blade speed (U),

rotational speed and annulus area as indicated in Equations 3.41 and 3.42. Ultimately, stator and rotor blade chord length (c) are obtained using the assumed blade aspect ratio and pitch-to-chord ratio s/c, and hence, the number of blades is calculated using Equation 3.47. Using the defined blade geometry and the application of loss models, annulus losses can be estimated. Hence, the total-to-total efficiency (η_{tt}), stator loss coefficient (ζ_S) can be estimated and the design process is reiterated till convergence; where the residual error between the assumed and calculated efficiency satisfies the threshold criterion (< 0.05%).

3.3.1.1   Turbine design process

A multi-stage turbine design model is created in MATLAB with a subroutine for producing the aerodynamic design of a single turbine stage with a constant mean diameter. Additionally, multiple subroutines are created for the different loss models that include Dunham and Came, Kacker and Okapuu and Aungier models. The subroutines contain nested functions that are used to interpret the thermo-physical properties of the working fluids, using before REFPROP and SIMULIS packages, at different operating conditions. By applying the following modelling steps (Figure 3.7), the outputs of the model are obtained including the total-to-total efficiency (η_{tt}), blade geometry and flow thermodynamic properties at the stator and rotor inlet and exit conditions.

1. Define ϕ, ψ, λ, t/o, s/c, t_{cl}, k_s; where t_{cl} is the radial clearance gap and k_s is the blade surface roughness.
2. Assume total-to-total turbine efficiency (η_{tt}, Stator loss coefficients (ζ_S), number of turbine stages (n_{stages})are assumed.
3. Calculate the flow angles and velocity triangles using correlations in Section 3.2.
4. Calculate flow thermodynamic properties including pressure(P), temperature (T), density (ρ), speed of sound, the ratio of specific heats (k) and viscosity (ν) using Peng-Robinson equation of state.
5. Obtain the detailed blade geometry including, blade heights, annulus area, chord and axial chord length, blade pitch and throat-to-pitch ratio (o/c).

6. Estimate annulus losses and hence stage and turbine efficiency (η_{tt} & ζ_S).

7. Calculate the tensile centrifugal and gas bending stresses on the turbine blades.

8. Re-iterate the design with the updated η_{tt} & ζ_S till the residual error between the assumed and calculated efficiency satisfies the threshold criterion ($<0.05\%$).
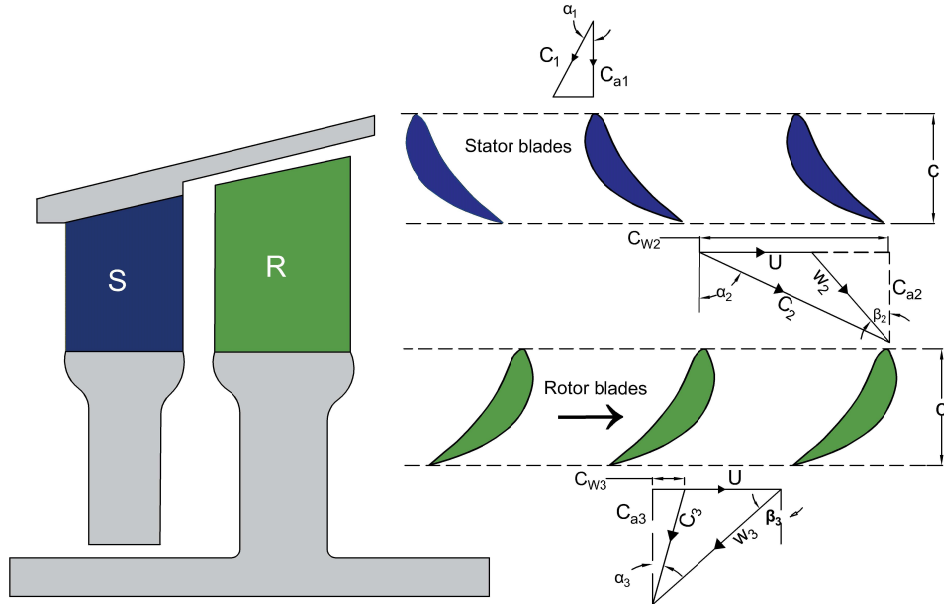
Figure 3.6: Schematic of the axial-flow turbine geometry and meridional cut layout.
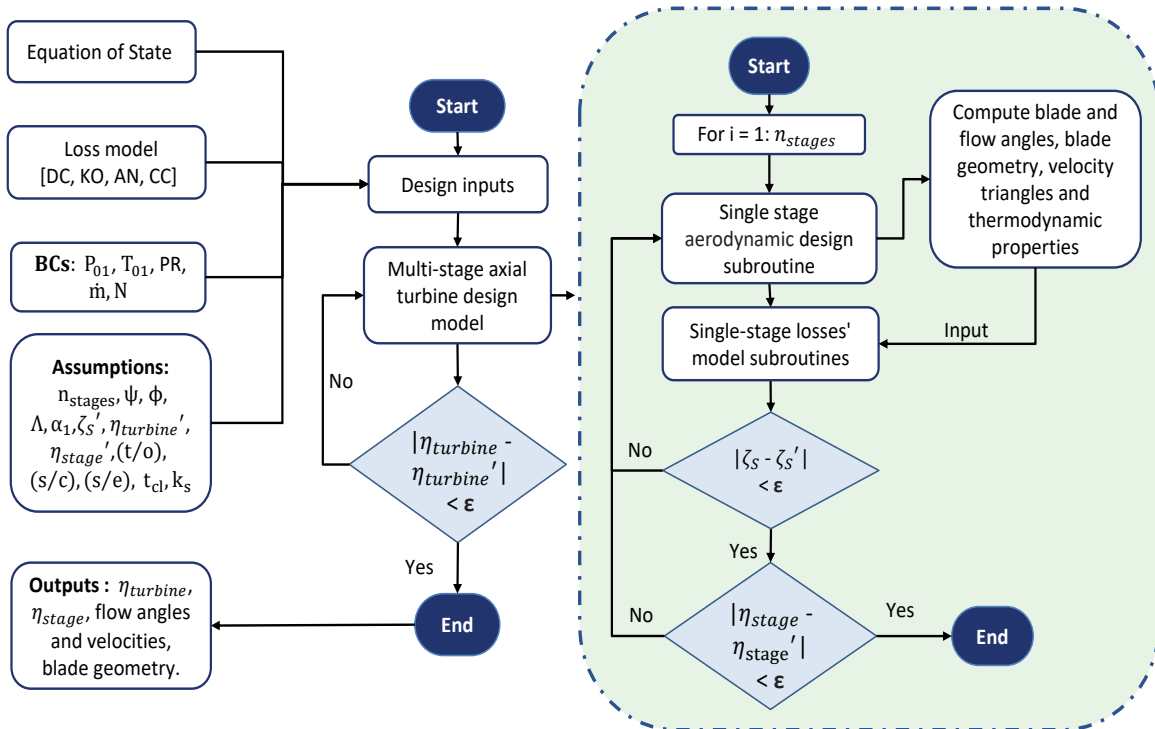
Figure 3.7: Flow chart of a multi-stage axial turbine design methodology at a constant mean diameter.

3.3.2   Constant hub diameter

An iterative design process is implemented to obtain the turbine design at a constant hub diameter. The design process starts with assuming a constant enthalpy drop across the stage ($\Delta h_{0-stage}$), loading coefficient (ψ) of the first design stage, flow coefficient (ϕ) and degree of reaction (Λ). Based on this, the peripheral blade speed at the rotor inlet and the axial flow velocity through the whole machine are obtained:

$$U_2 = \sqrt{\frac{\Delta h_{0(stage)}}{\psi}} \tag{3.81}$$

$$C_a = U_2 \times \Phi \tag{3.82}$$

The relation between total enthalpy and static enthalpy at stations 2 and 3 (Figure 3.4b) and the degree of reaction definition can be expressed as:

$$h_{02} = h_2 + \frac{1}{2}{C_2}^2 \tag{3.83}$$

$$h_{03} = h_3 + \frac{1}{2}{C_3}^2 \tag{3.84}$$

$$\Lambda = \frac{h_2 - h_3}{h_{01} - h_{03}} \tag{3.85}$$

The absolute velocity components C_2 and C_3 are expressed as a function of the axial (C_a) and tangential velocity components (C_w) as:

$$C_2 = \sqrt{{C_a}^2 + {C_{w2}}^2} \tag{3.86}$$

$$C_3 = \sqrt{{C_a}^2 + {C_{w3}}^2} \tag{3.87}$$

The ratio between the inlet blade speed and outlet blade speed (R) is assumed to be equal to U_2/U_3. Using Equations 3.83 and 3.84, the degree of reaction can be expressed as:

$$\Lambda = \frac{\Delta h_0 - \frac{1}{2}C_2^2 + \frac{1}{2}C_3^2}{\Delta h_0} \tag{3.88}$$

hence,

$$\Delta h_0 \left(1 - \Lambda\right) = \frac{1}{2}C_2^2 - \frac{1}{2}C_3^2 \tag{3.89}$$

Using Equations 3.86 and 3.87, this can be expressed as:

$$\Delta h_0 \left(1 - \Lambda\right) = \frac{1}{2}\left(C_a^2 + C_{w2}^2\right) - \frac{1}{2}\left(C_a^2 + C_{w3}^2\right) \tag{3.90}$$

The tangential velocity component at the rotor outlet can then be obtained from:

$$C_{w3} = \sqrt{C_{w2}^2 - 2\Delta h_o \left(1 - \Lambda\right)} \tag{3.91}$$

The enthalpy drop across the stages is defined as:

$$\Delta h_0 = U_2 C_{w2} + U_3 C_{w3} \tag{3.92}$$

Substituting Equation 3.91 in the definition of the angular momentum (Equation 3.92) enables calculating the tangential velocity components at the inlet and outlet of the rotor blades (C_{w2} & C_{w3}). Therefore, the flow angles can be obtained as follows:

$$\alpha_3 = \tan^{-1}\frac{C_{w3}}{Ca} \tag{3.93}$$

$$\alpha_2 = \tan^{-1}\frac{C_{w2}}{Ca} \tag{3.94}$$

$$\beta_2 = \tan^{-1}\left[\,\tan \alpha_2 - U_2/Ca\right] \tag{3.95}$$

$$\beta_3 = \tan^{-1}\left[\,\tan \alpha_3 + U_3/Ca\right] \tag{3.96}$$

Following this, velocities at the inlet and the outlet of the stator and rotor blade rows can be calculated (Equations 3.70 to 3.73) and deviation angles can be obtained using the approach described by Ainley and Mathieson [63]. With the velocities fully defined, the thermophysical properties at the different turbine stations can be obtained through the equation of state:

$$[P,T] = f(h,s) \tag{3.97}$$

$$[\rho, c_p, k] = f(P, T) \tag{3.98}$$

At this stage, the flow areas can be obtained as a function of the density and the axial velocity, which is assumed to be constant across all the design stages. Following this, the hub diameter, mean diameter and diffusion angle can be calculated and U_3 can be updated. The process can then be reiterated until convergence. For the subsequent stages after the first stage, the axial velocity and enthalpy drop across the stage are known from the earlier stage and hence the process is initiated with the assumed degree of reaction, blade velocity U_2 and ratio $R = U_2/U_3$.

3.3.2.1 Design flow chart

To produce the turbine designs at a constant hub diameter, an additional subroutine is created in MATLAB which applies the iterative approach explained in Section 3.3.2. This subroutine contains nested functions that are used to interpret the thermo-physical properties of the working fluids, using before REFPROP and SIMULIS packages, at different operating conditions. The subroutines created for the different loss models are utilised in a similar manner as the design approach for a constant mean diameter, in order to analyse the overall performance of the turbine. Therefore, applying the following modelling steps (Figure 3.11) allows for obtaining, blade geometry at a constant hub diameter, the total-to-total efficiency (η_{tt}) and flow thermodynamic properties at the stator and rotor inlet and exit conditions.

1. Assume ϕ, ψ, λ for the first design stage.
2. Define t/o, s/c, t_{cl}, k_s.
3. Assume the number of rotor blades (n_{blades}), number of stages (n_{stages}).
4. Assume the total-to-total turbine efficiency (η_{tt}), stator loss coefficients (ζ_S), $R = U_2/U_3$).
5. Blade angles and velocity triangles are calculated.
6. Flow thermodynamic properties including pressure (P), temperature (T), density (ρ), speed of sound, the ratio of specific heats (k) and viscosity (ν) are obtained using

Simulis [52].

7. Obtain detailed blade geometry including, blade heights, annulus area, chord and axial chord length, blade pitch and throat-to-pitch ratio (o/c).

8. Estimate annulus losses and hence stage and turbine efficiency.

9. Obtain R and U_2 and re-iterate until the residual error between the assumed and calculated values satisfies the specified criteria.

10. Obtain turbine efficiency (η_{tt}) and re-iterate until the residual error between the assumed and calculated efficiency satisfies the specified criteria.

11. Calculate the tensile centrifugal and gas bending stresses on the turbine blades.

Ultimately, in both design approaches (constant mean and constant hub diameter), the performance of the developed turbine design should be evaluated to predict the total-to-total-to-total turbine efficiency as defined in Equation 3.62.
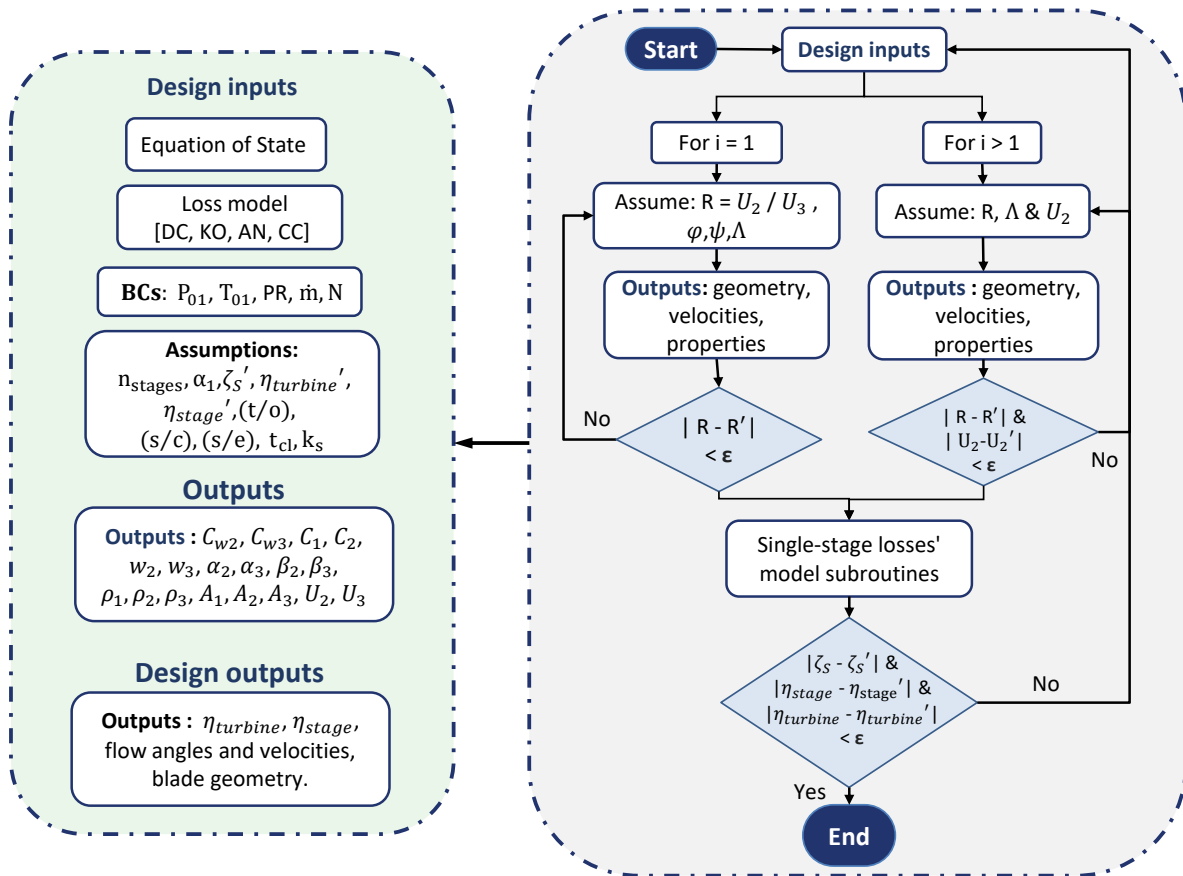
Figure 3.8: Flow chart of a multi-stage axial turbine design methodology at constant hub diameter.

It is worth mentioning that the two design approaches have been developed in Matlab where multiple subroutines are used for the constant hub diameter and constant mean diameter design methodologies. For both cases, the thermophysical properties of the working fluids have been obtained using REFPROP and Simulus fluid packages where the nested functions are added to the code to interpret the properties at different operating conditions.

3.3.3 Performance prediction tools

The performance of the turbine is estimated by quantifying the energy losses that the working fluid experiences through the expansion process in both the stator and rotor blade rows. Fluid energy in turbomachines experiences various types of aerodynamic losses including profile, secondary flow, tip clearance, trailing edge losses, shock and supersonic expansion losses. A brief description of these mechanisms was discussed earlier in Section 2.4.1.

The previously mentioned losses result in actual turbine work less than the work done on the rotor blades due to the reduction in the mass flow rate. To predict the various types of losses in axial turbines, several mathematical correlations have been previously introduced. A brief summary of the loss correlations implemented in the current thesis is presented in the following sections while a full description of the models can be found in Appendix A.

3.3.3.1 Soderberg loss model

Initially, Soderberg [62] introduced one of the simplest correlations for axial turbine losses in 1949; this loss model accounts for the effect of profile and secondary flow losses where tip clearance and trailing edge losses are ignored. The loss coefficients are represented as follows:

$$\zeta^* = 0.04 + 0.06 \left(\frac{\varepsilon}{100} \right)^2 \tag{3.99}$$

$$\zeta_S = \left(\frac{10^5}{Re} \right)^{1/4} \left[(1 + \zeta^*) \left(0.993 + 0.075 \frac{c}{h} \right) - 1 \right] \tag{3.100}$$

$$\zeta_R = \left(\frac{10^5}{Re} \right)^{1/4} \left[(1 + \zeta^*) \left(0.975 + 0.075 \frac{c}{h} \right) - 1 \right] \tag{3.101}$$

$$\varepsilon_S \ = \ \alpha_1 + \alpha_2 \ \& \ \varepsilon_R \ = \ \beta_2 + \beta_3 \tag{3.102}$$

where ζ^* is the nominal loss coefficient, h is the bade height, l is the blade chord length, H/l is the aspect ratio, α is the Stator absolute angles, β is the rotor relative angles and Re is Reynolds number, 1, 2 and 2, 3 subscripts correspond to the inlet and exit conditions for the stator and rotor respectively.

3.3.3.2 Dunham and Came loss model

Following Soderberg's model, Ainley and Mathieson (AM) [63] presented a method for estimating the performance of axial turbines. This model accounts for profile, secondary and tip leakage losses. Later, Ainley and Mathieson correlations have been reviewed by Dunham and Came [64] using more recent data. The review process is performed for all losses including the profile, secondary and tip clearance losses.

Ainley and Mathieson (AM) expressed profile losses as a function of the blade and flow angles α_1' and α_2, respectively, at the inlet and exit condition of the blade row and the maximum blade thickness to chord ratio (t/c) :

$$Y_{p[AM]} = \left\{ Y_{p\ (\alpha_1'=0)} + \left(\frac{\alpha_1'}{\alpha_2} \right)^2 \left[Y_{p\ (\alpha_1'=\alpha_2)} - Y_{p\ (\alpha_1'=0)} \right] \right\} \left(\frac{t/c}{0.2} \right)^{\alpha_1'/\ \alpha_2} \tag{3.103}$$

Dunham and Came (DC) [64] model modified the performance correlations developed by Ainley and Mathieson (AM) [63] using updated experimental data. Hence, profile losses are expressed as:

$$Y_p = Y_p[AM] \times [1 + 60(M_n - 1)^2] \tag{3.104}$$

where $Y_p[AM]$ is the profile loss obtained by the AM model, M_n is the exit Mach number.

The same correlation applies for the rotor profile losses at zero incidence angle where α_1' and α_2 will be replaced with β_2' and β_3 respectively.

For the secondary flow loss, DC modified the AM model to include a constant of 0.0334 and chord-to-blade height ratio (c/h). It is expressed as a function of the lift coefficient

based on vector mean velocity (C_L), pitch-to-chord ratio (s/c) and blade and flow angles as follows:

$$Y_s = 0.0334 \left(\frac{c}{h}\right) \left(\frac{\cos \alpha_2}{\cos \alpha_1{'}}\right) \left[\frac{C_L}{s/c}\right]^2 \left[\frac{\cos^2 \alpha_2}{\cos^3 \alpha_m}\right] \tag{3.105}$$

where

$$\alpha_m = \tan^{-1}[(\tan \alpha_2 - \tan \alpha_1/2)] \tag{3.106}$$

$$C_L = 2 \ (s/c) \ (\tan \alpha_1 + \tan \alpha_2) \cos \alpha_m \tag{3.107}$$

Following, DC [64] applied the *Re* correction to the profile and secondary flow losses collectively as follows:

$$(Y_p + Y_s)_{corrected} = (Y_p + Y_s) \left(\frac{Re}{2 \times 10^5}\right)^{-0.2} \tag{3.108}$$

For the tip clearance loss, the DC model accounted for the power law dependence of the tip clearance (Equation A.43).

$$Y_{cl} = B \left(\frac{c}{h}\right) \left[\frac{t_{cl}}{c}\right]^{0.78} \left[\frac{C_L}{s/c}\right]^2 \left[\frac{\cos^2 \alpha_2}{\cos^3 \alpha_m}\right] \tag{3.109}$$

where $B = 0.47$ for plain tip clearance and 0.37 for shrouded blades.

3.3.3.3   Kacker and Okapuu loss model

In a similar manner, additional modifications have been applied to AMDC model by Kacker and Okapuu (KO) [65] following the advances provided by Dunham and Came (DC) to include the shock losses for the subsonic Mach number as follows:

$$Y_{p,AMDC} = \left\{ Y_{p \ (\alpha_1{'}=0)} + \left|\frac{\alpha_1{'}}{\alpha_2}\right| \left(\frac{\alpha_1{'}}{\alpha_2}\right) \left[Y_{p \ (\alpha_1{'}=\alpha_2)} - Y_{p \ (\alpha_1{'}=0)} \right] \right\} \left(\frac{t/c}{0.2}\right)^{\alpha_1{'} / \alpha_2} \tag{3.110}$$

$$Y_{Shock} = 0.75 \left(f_{hub} \times Ma_{in,rel} - 0.4^{1.75} \right) \left(\frac{r_{hub}}{r_{tip}}\right) \left(\frac{P_{0rel,in} - P_{in}}{P_{0rel,out} - P_{out}}\right) \tag{3.111}$$

where P_{0rel} is the total relative pressure, P is the static pressure, *Ma* is the Mach number, r_{hub} and r_{tip} are the hub and tip radius respectively, in, out and rel subscripts stands for the

inlet, outlet conditions and the relative property respectively.

$$Y_p = 0.914 \left(\frac{2}{3} Y_{p,ADMC} K_P + Y_{Shock} \right) \tag{3.112}$$

where K_P is compressibility effect correction factor.

The DC and AM models were introduced at reference Re of 2×10^5 based on the chord and gas exit conditions. Whilst, the KO model introduced Re correction as:

$$f_{(Re)} = \begin{cases} \left(\frac{Re}{2 \times 10^5} \right)^{-0.4} & Re \leq 2 \times 10^5 \\ 1.0 & 2 \times 10^5 < Re < 10^6 \\ \left(\frac{Re}{10^6} \right)^{-0.2} & Re > 10^6 \end{cases} \tag{3.113}$$

The above correction is applied for the profile losses only and hence,

$$Y_p = f_{(Re)} [Y_p] \tag{3.114}$$

KO [65] introduced a refinement to the DC model including the application of correction factors $f_{(AR)}$ and K_s to account for low aspect ratio and compressibility effects respectively.

$$Y_{s,ADMC} = 0.0334 \, f_{(AR)} \left(\frac{C_L}{s/c} \right)^2 \left(\frac{\cos \alpha_2}{\cos \alpha_1'} \right) \frac{\cos^2 \alpha_2}{\cos^3 \alpha_m} \tag{3.115}$$

$$f_{(AR)} = \begin{cases} \left(\frac{1 - 0.25\sqrt{2 - h/c}}{h/c} \right) & h/c \leq 2 \\ \left(\frac{1}{h/c} \right) & h/c > 2 \end{cases} \tag{3.116}$$

$$Y_s = 1.2 \, Y_{s,ADMC} \, K_s \tag{3.117}$$

Trailing edge losses is expressed using an energy coefficient expression $\Delta\Phi$:

$$\Delta\Phi^2_{TET} = \Delta\Phi^2_{TET_{(\alpha_1'=0)}} + \left| \frac{\beta_1}{\alpha_2} \right| \left(\frac{\alpha_1'}{\alpha_2} \right) \left[\Delta\Phi^2_{TET \, (\alpha_1' = \alpha_2)} - \Delta\Phi^2_{TET \, (\alpha_1'=0)} \right] \tag{3.118}$$

$$Y_{TE} = \frac{1}{1 - \Delta\Phi^2_{TET}} - 1 \qquad (3.119)$$

For the unshrouded blades, KO introduced a new correlation for the blade rows to be:

$$\Delta\eta_{t_{cl}} = \eta_0 \left(0.93 \times \frac{t_{cl}}{h \cos \alpha_2} \times \frac{r_{tip}}{r_{mean}} \right) \qquad (3.120)$$

where h is the blade height, t_{cl} is the clearance gap, r_{tip} is the tip radius and r_{mean} is the mean radius, η_0 is the efficiency at zero tip clearance.

3.3.3.4   Craig and Cox loss model

Craig and Cox [60] split the losses into profile, secondary and annulus losses. They introduced profile losses as a function of the preliminary profile loss $X_{(pb)}$. Followed by corrections for Re, incidence and trailing edge thickness loss effects using N_{pr}, N_{pi} and N_{pt} factors respectively.

$$X_p = x_{pb}\, N_{pr}N_{pi}N_{pt} + (\Delta x_p)_t + (\Delta x_p)_{s/e} + (\Delta x_p)_m \qquad (3.121)$$

where $(\Delta x_p)_t$, $(\Delta x_p)_m$ and $(\Delta x_p)_{s/e}$ are the profile loss increments for the trailing edge thickness losses, supersonic Mach number effects for convergent blade profiles and blade back radius losses respectively.

CC [60] introduced the secondary flow losses as a function of the secondary loss ratio $(N_s)_{h/b}$ and basic secondary flow loss factor $(x_s)_b$.

$$X_s = (N_s)_r (N_s)_{h/b} (x_s)_b \qquad (3.122)$$

Finally, the CC model presented clearance losses correlation for un-shrouded as a function of the efficiency at zero clearance (η_0), total effective area of clearance $(A_{t_{cl}})$, total throat area (A_o) and efficiency debit factor (F_k).

$$\Delta\eta_{t_{cl}} = \Delta\eta_0 \left(1.5 \times F_k \frac{A_{t_{cl}}}{A_o} \right) \qquad (3.123)$$
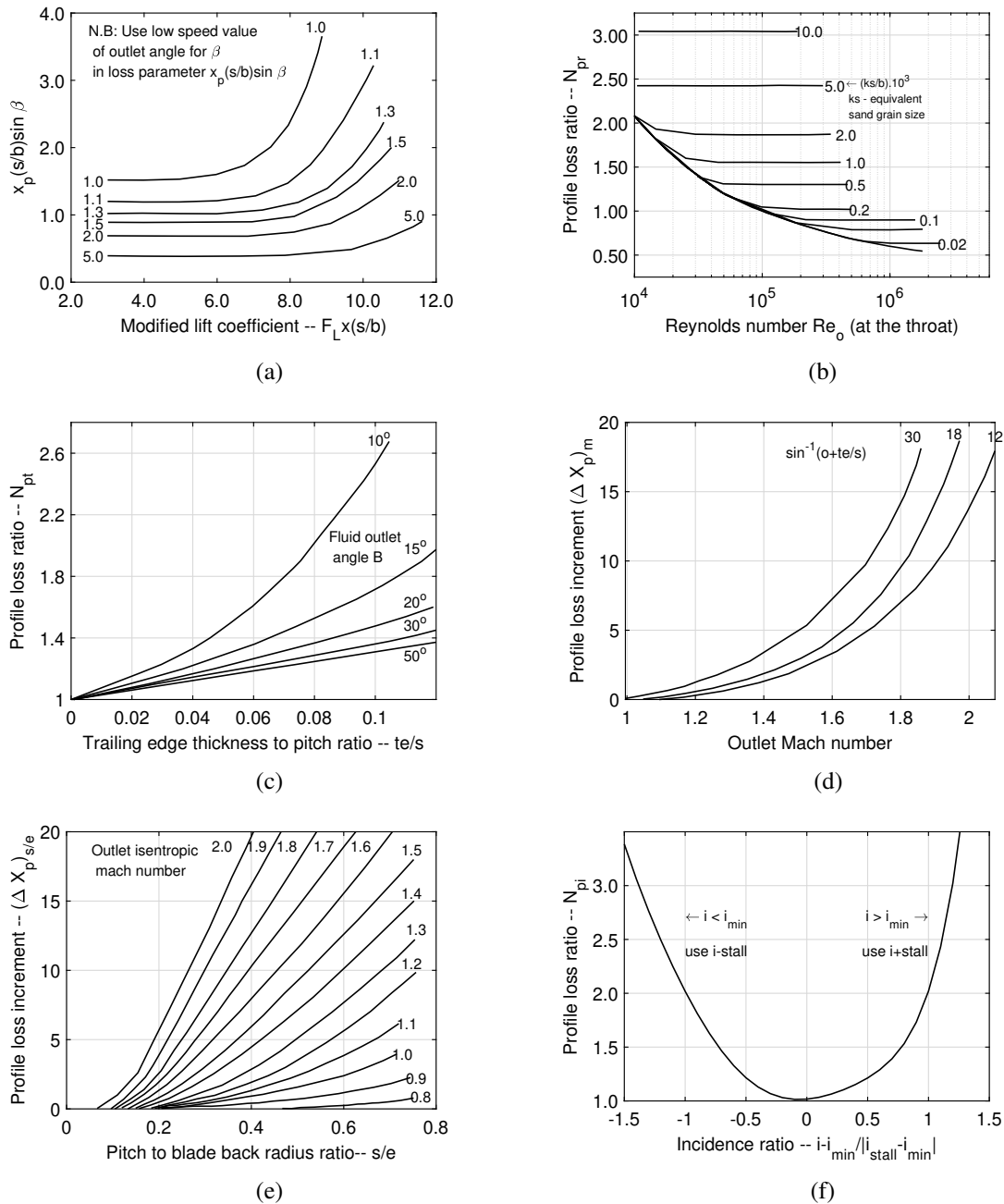
Figure 3.9: (a) Basic profile loss [60] (b) profile loss ratio against Reynolds number effect, (c) trailing edge thickness losses, (d) Mach number loss for convergent blading, (e) blade back radius losses (f) incidence losses.

3.3.3.5 Aungier loss model

Ultimately, Aungier [66] presented a performance model that is mainly based on the model developed by Ainley and Mathieson, modified and refined by Kacker and Okapuu.
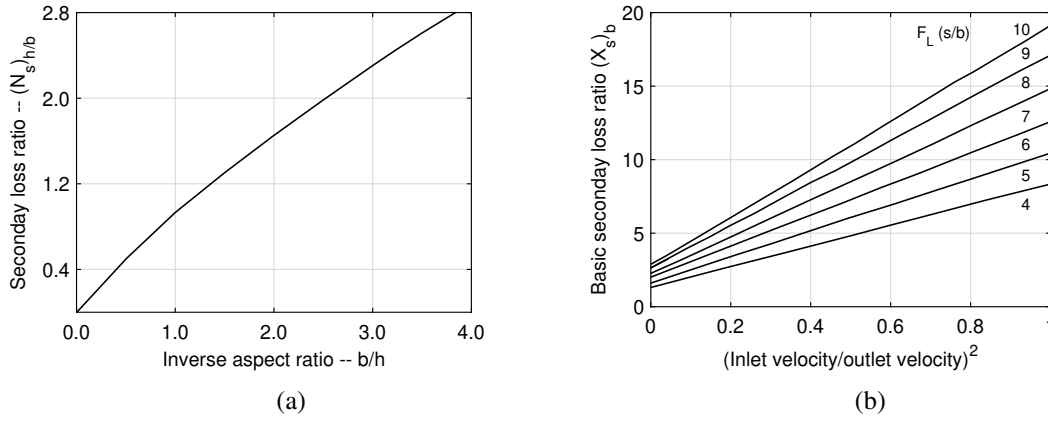
Figure 3.10: Secondary flow loss (a) aspect ratio factor (b) basic loss factor

Aungier [66] imposed some changes on the KO model to include the roughness effect for turbulent flow regimes. Hence, profile losses are expressed as:

$$Y_p = K_{mod}K_{inc}K_M K_p K_{RE} \left\{ \left[Y_{p1} + \left(\frac{\alpha_1'}{\alpha_2} \right)^2 (Y_{p2} - Y_{p1}) \right] (5t/c)^{\alpha_1'/\alpha_2} - \Delta Y_{TE} \right\} \quad (3.124)$$

where K_{mod} is an experience factor suggested by KO, K_{inc} , K_M, K_p and K_{RE} are correction factors for off-design incidence, Mach number, compressibility and Reynolds number effects respectively, Y_{p1} and Y_{p2} are the profile loss coefficients for Stator blades ($\alpha_1' = 0$) and rotor blades ($\alpha_1' = \alpha_2$) respectively.

Aungier [66] modified the KO model correction factors for the low aspect ratio ($F_{(AR)}$) and compressibility effects (K_s) and hence, expressed the secondary flow losses as:

$$\overline{Y}_s = 0.0334 \, F_{AR} \left[\frac{C_L}{s/c} \right]^2 \left(\frac{\cos \alpha_2}{\cos \alpha_1'} \right) \left[\frac{\cos^2 \alpha_2}{\cos^3 \alpha_m} \right] \quad (3.125)$$

$$F_{(AR)} = \begin{cases} (0.5 \, (2c/h)^{0.7} & h/c < 2 \\ (c/h) & h/c \geq 2 \end{cases} \quad (3.126)$$

$$Y_s = K_s \, K_{Re} \sqrt{\overline{Y}_s^2 / (1 + 7.5\overline{Y}_s)} \quad (3.127)$$

The shock loss coefficient is computed by:

$$\overline{Y}_{sh} = 0.8X_1{}^2 + X_2{}^2 \tag{3.128}$$

$$Y_{sh} = \sqrt{\overline{Y}_{sh}{}^2 / (1 + \overline{Y}_{sh}{}^2)} \tag{3.129}$$

where X_1 & X_2 are parameters defined as a function of Ma number.

Supersonic expansion losses are computed as a function of the exit Mach number (M_2):

$$Y_{EX} = [(M_2 - 1)/M_2]^2 \tag{3.130}$$

Aungier computed the trailing edge loss coefficient as:

$$Y_{TE} = \left[t_2/s \, \sin\beta_g - t_2 \right]^2 = \left(\frac{t_2}{o_2 - t_2} \right)^2 \tag{3.131}$$

Where t_2 is the trailing edge blade thickness, β_g is the gauging angle, o is the throat open-ing. Finally, Aungier implements the correlation proposed by DC for predicting the tip clearance losses for un-shrouded blades (Equation A.43).

Using the previously listed correlations, introduced by Ainley and Mathieson, Dunham and Came, Kacker and Okapuu and Aungier models, pressure loss coefficients Y_R and Y_S can be obtained as:

$$Y_S = Y_p + Y_s + Y_{TE} + Y_{cl} + Y_{shock} + Y_{PE} \tag{3.132}$$

$$Y_R = Y_p + Y_s + Y_{TE} + Y_{cl} + Y_{shock} + Y_{PE} \tag{3.133}$$

where Y_p is profile loss, Y_s is the secondary flow loss, Y_{TE} is the trailing edge loss, Y_{tc} is the tip clearance loss, Y_{shock} is the shock loss, Y_{PE} is the post expansion supersonic losses.

Then pressure loss coefficients are converted to enthalpy loss coefficients using Equa-tions 3.65 and 3.66 and hence, the total-to-total efficiency is calculated using Equation 3.62. The estimation of the aerodynamic losses is crucial for obtaining accurate machine design including the blade geometry and velocity triangles (as defined in Section 3.2). The accu-

racy of the antecedent loss models is questionable for recent turbine designs as the flow conditions and geometries are different that those originally used to get these models. This might lead to inaccuracy owing to the difference in working fluids and thermodynamic operating conditions [137]. However, these models have been implemented in the preliminary design process of turbomachines operating with non-conventional cycles including sCO_2 and ORC working fluids, as discussed in the literature (Sections 2.4.1.1 and 2.4.1.2) due to the lack of availability of developed models for these machines. Given that the current work is concerned with designing a multi-stage axial turbine operating with CO_2 blends, the prediction capability of the existing loss models will be investigated as a part of this work for different working fluids (Chapter 4).

3.3.4 Mechanical design

In addition to evaluating the aerodynamic turbine performance, mechanical design considerations are taken into account throughout the mean-line design methodology to allow for a fair comparison of the achievable performance for the different geometrical and process parameters. Stresses on the turbine blades are split into centrifugal and bending stresses. The centrifugal stress applied on the blade can be calculated using the following equation assuming a tapered blade shape; where the taper is assumed to reduce the stress to 2/3 of the value for an untapered blade.

$$\sigma_{Cent.} = \frac{4}{3}\pi N^2 \rho_b A \tag{3.134}$$

where ρ_b is the density of blade material, N is the rotational speed and A is the mean blade area [22].

Additionally, a preliminary correlation provided by the project industrial partners is used to calculate the static bending stress for a specified blade profile. Principally, this correlation is based on accounting for the effect of both the axial and tangential forces to calculate the total static bending stress; where the axial stress is defined as a function of the pressure drop across the turbine blade, turbine diameter and blade height. Whilst, the tangential force is obtained as a function of the variation of the tangential velocity

across the blade row, mass flow rate and the number of blades. With the known axial and tangential forces, the static bending stress can be obtained using the moment of inertia for the selected blade profile. A useful approximation for the bending stress is provided by Saravanamuttoo et al. [22] and is expressed as:

$$\sigma_{bending} = \frac{\dot{m}\,C_a\,[\tan\,\alpha_2 + \tan\,\alpha_3]}{n_R} \times \frac{h}{2} \times \frac{1}{zc^3} \qquad (3.135)$$

where n_R is the number of rotor blades, h is the mean blade height, and z is the smallest value of the root section modulus of a blade of unit chord [22]

In addition to considering the static bending stress in the turbine design, the axial flow path length is constrained. The maximum axial length of the flow path is limited by rotor-dynamic considerations, mainly the stability (positive logarithmic decrement, with adequate margin) of the first natural mode of the rotor plus bearing system. Throughout the preliminary design phase, an empirical correlation is used to evaluate the flow path axial length based on a defined slenderness ratio; the ratio of the total axial flow path length with respect to the hub diameter. The slenderness ratio definition and its limit are both obtained based on previous experiences by SCARABEUS project industrial partners. Accordingly, the implemented design procedure can be summarised into the following points:

- Synchronous designs with a rotational speed of 3,000 RPM (i.e., 50 Hz grid frequency) are selected for a plant power with a net power output of 100 MW sCO_2, due to the difficulty of incorporating a gearbox for such turbine scales.
- Considering that the expanding fluid is characterised by a large power density, it is assumed that the bending stresses generated by the expansion are more critical than the centrifugal stresses generated by blade rotation. Thus, the target in the mean-line design is to keep the static bending stresses under a suitable limit. For the preliminary design phase a limit of < 130 MPa has been set based on industrial experience considering alternating and centrifugal stresses that are consistent with sCO_2 applications.
- The bending stress limit is fixed at a constant value for all stages, regardless of the

different operating temperatures encountered by each stage. This assumption is reasonable since the blade materials identified for this application are all nickel-based alloys, which do not exhibit significant degradation in the mechanical properties of interest within the operating range of the whole turbine (inlet to exhaust).

- The chords of the airfoils of each blade row are scaled targeting bending stresses within the limit established. Static stresses are calculated assuming a constant dimensionless second moment of area of the airfoil and without considering any stress intensification factor, where this factor was considered in the establishment of the bending stresses threshold.

- To allow the preliminary sizing of the blade root, and to subsequently estimate the rotor stiffness parameter, a preliminary value for the airfoil chord length is selected (< 100 *mm*). The rotor stiffness is an essential parameter driving the rotordynamic behaviour of the turbine.

- The number of stages and the estimation of the chord length allow for estimating the overall length of the flow path.

- The estimation of the overall length of the flow path enables a preliminary assessment of rotordynamic stability within the mean-line design with the introduction of the slenderness ratio (*SR*); this is defined as the ratio of the bearing span to the hub diameter. The limiting value for the slenderness ratio has been established based on the results of detailed rotordynamic assessments carried out for other similar turbines for supercritical CO_2 applications (< 9).

Following the design procedure discussed in Sections 3.3.1 and 3.3.2, the designs are evaluated from both the rotor-dynamic and mechanical design aspects to ensure that $\sigma_{bending}$, c and *SR* are within the threshold limits. If the design does not meet the specified criteria, then, the number of blades ($35 < n_{blades} < 100$) and the number of stages should be modified iteratively until the mechanical and rotor-dynamic design constraints are met; for example, the chord should be increased (and the number of blades decreased accordingly to maintain the solidity) to reduce the bending stresses and the number of stages should be reduced to allow for a slenderness ratio within the specified limit.
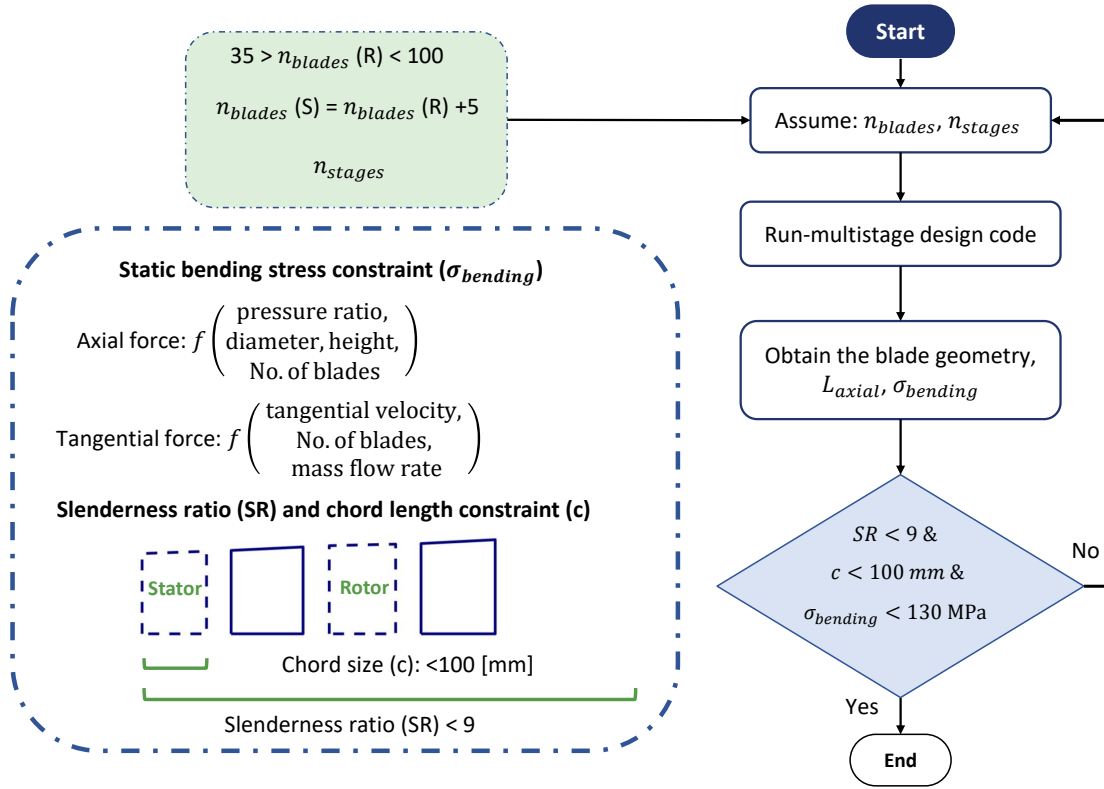
Figure 3.11: Flow path optimisation methodology considering mechanical and rotordynamic design criteria.

3.4 Verification of the turbine design methodology

One of the challenges that face sCO_2 turbine design is the lack of experience and published validation data available within the literature. Most of the experimental test rigs available for sCO_2 turbo-machines have considered small-scale radial turbines, as discussed in detail in Chapter 2. Furthermore, few studies focused on presenting mean-line designs for large-scale axial sCO_2 turbines with more focus on small-scale turbines. To support this work, both the design methodology and performance analysis have been verified against cases from the literature operating with conventional working fluids, such as air, and non-conventional working fluids including sCO_2. The first verification case relates to experimental data for a small-scale 140 kW axial turbine, while the second relates to the design of 440 kW & 1520 kW axial ORC turbine where the results from the mean-line design have been verified against another mean-line design tool. Finally, a 10 MW sCO_2 turbine is selected where the results from the mean-line design have been verified against CFD simulation results. Furthermore, to verify the validity of the implemented loss models over

92

a wide range of loading (ψ) and flow coefficients (ϕ), the loss models are used to construct the Smith chart and the new chart is compared with respect to the original Smith chart [136]. The verification details of the selected cases are reported in Sections 3.4.1-3.4.4.

3.4.1 Verification for 140 kW air turbine

This section is concerned with presenting the verification results of the design methodology and loss models against a small-scale axial turbine investigated at the Technical University of Hannover by Groschup [138, 139, 140]. The turbine is operating with air as a working fluid and is designed to produce 140 KW power output at a degree of reaction of 50%. Ultimately, the flow velocities, angles and blade speeds are all obtained and compared against the experimental results alongside the CFD results presented by Meroni et al. [86].

Table 3.2: Operating conditions of the 140 kW air turbine [138, 139, 140].

Parameter	Symbol	Stator	Rotor
Inlet flow angle [°C]	α_1	10	
Stage loading coefficient [-]	ψ	2.1	
Stator and rotor throat opening [mm]	$o_{n,min}, o_r$	15	14
Stator and rotor axial chord [mm]	c_n, c_r	48.2	37.1
Stator and rotor opening to pitch ratio [-]	$(o/s)_n, (o/s)_r$	0.378	0.358
Rotational speed [rpm]	N	7200	
Inlet axial velocity [m/s]	C_{a1}	55.9	
Rotor flow coefficient [-]	ϕ_r	0.39	
Rotor inlet to stator outlet blade height [mm]	h	1	
Degree of admission [-]	ε	1	
Mass flow rate [kg/s]	$\dot{m}$	6.786	
Total inlet temperature [K]	T_{01}	358.69	
Total inlet pressure [Pa]	p_{01}	1.2486×10^5	
Total outlet pressure [Pa]	p_{03}	0.998×10^5	
Rotor to stator mean radius ratio [mm]	R^*	1.019	
Stator-rotor axial spacing [mm]	ss	34.36	
Radius of blade rear suction side curvature [mm]	e_n, e_r	109.00	166.57
Trailing edge thickness to blade opening ratio [-]	$(t/o)_n, (t/o)_r$	0.0253	0.0357
Blade surface roughness [mm]	k_s	2×10^{-3}	
Rotor tip clearance [mm]	$t_c l$	0.24	
Inlet width arc [mm]	$--$	29.60	34.95
Backbone length [mm]	b_n, b_r	62.10	57.63
Trailing edge thickness [mm]	e_n, e_r	0.38	0.50

Initially, the boundary conditions of the air case study (Table 3.2) are used to design the turbine at a constant mean diameter, using the methodology specified in Section 3.3.1. The turbine design details are shown in Table 3.3. By comparing the generated design with the experimental results in terms of the blade geometries, flow velocities and exit pressures, a good agreement is obtained as shown in Table 3.3. The turbine performance predicted by the Craig and Cox model (CC) is also evaluated against the experimental and the CFD results presented by Meroni et al. [86] and a good agreement is obtained with an efficiency difference of 0.98 pp with respect to the experimental data.

Table 3.3: Verification results of the mean-line design model versus the experimental data and CFD simulations for the 140 kW air turbine [138, 139, 140].

Parameter	Symbol	EXP. Data [138, 139, 140]	CC model	CFD [86]	Error
Stator outlet absolute flow angle [ºC]	α_2	69.84	69.53	68.45	0.31º
Stator outlet relative flow angle [ºC]	β_2	7.13	6.58	4.82	0.55º
Stator outlet absolute velocity [m/s]	C_2	170.8	156.60	153.84	8.3%
Absolute Mach at Stator outlet [-]	M_2	0.457	0.42	0.412	8.1%
Static pressure at Stator outlet [bar]	P_2	1.111	1.10	1.108	0.9%
Static temperature at Stator inlet [K]	T_2	357.4	357.15	357.4	0.07%
Static temperature at Stator outlet [K]	T_2	347.17	346.48	347.06	0.2%
Rotor outlet relative flow angle [ºC]	β_3	68.75	68.79	67.07	0.04º
Rotor outlet absolute flow angle [ºC]	α_3	2.45	0.73	7.58	1.72º
Rotor outlet relative velocity [m/s]	W_3	166.3	151.35	157.51	8.9%
Static pressure at rotor outlet [bar]	P_3	0.994	0.98	0.983	1.4%
Static temperature at rotor outlet [K]	T_3	337.86	336.576	336.60	0.38%
Stator mean radius [mm]	r_{2m}	181.5	186.21	181.5	2.6%
Rotor mean radius [mm]	r_{3m}	185	186.21	185	0.65%
Stator inlet blade height [mm]	h_1	89.2	88.30	89.2	1.0%
Stator outlet (rotor inlet) blade height [mm]	h_2	97	96.03	97	1.0%
Rotor outlet blade height [mm]	h_3	103	104.16	103	1.13%
Number of Stator blades [-]	n_N	29	28	29	3.4%
Number of rotor blades [-]	n_R	30	30	30	0%
Stator loss coefficient [%]	ζ_S	3.79	6.5	5.82	2.71 pp
Rotor loss coefficient [%]	ζ_R	9.08	6.2	6.66	2.88 pp
Total-to-total stage efficiency [%]	η_{tt}	91.62	92.6	93.32	0.98 pp

Further to the verification of the design methodology and the CC loss model, turbine designs and the performance predicted by the other three loss models namely KO, DC, and AN are compared against the experimental and CFD data (Table 3.4). A good agreement is

obtained between the mean-line design, CFD and experimental results in the total-to-total turbine efficiency (η_{tt}). Despite the good agreement with the predicted η_{tt} between the mean-line design and experimental results, a large discrepancy is obtained in the predicted enthalpy loss coefficients (ζ) as shown in Table 3.3. Stator and rotor loss coefficients are found to be over-estimated by the mean-line design compared to the experimental results. It is worth mentioning the same difference is obtained for the results presented by Meroni et al. [86] mean-line design tool which indicates the right implementation of the model. Overall, a good agreement is obtained in the η_{tt} predicted by the four loss models compared to the experimental data with a maximum deviation of 1.21 pp obtained by the AN model.

Table 3.4: Verification results of the Loss models versus the experimental data and CFD simulations for the 140 kW air turbine [138, 139, 140].

Parameter	Symbol	DC	KO	AN	EXP. Data	CFD [86]
Stator outlet absolute flow angle [°C]	α_2	69.53	69.53	69.53	69.84	68.45
Stator outlet relative flow angle [°C]	β_2	6.58	6.58	6.58	7.13	4.82
Stator outlet absolute velocity [m/s]	C_2	156.55	156.38	156.78	170.8	153.84
Absolute Mach at Stator outlet [-]	M_2	0.42	0.42	0.42	0.457	0.412
Static pressure at Stator outlet [bar]	P_2	1.1	0 1.10	1.10	1.111	1.108
Static temperature at Stator inlet [K]	T_2	357.15	357.16	357.15	357.4	357.4
Static temperature at Stator outlet [K]	T_3	346.49	346.51	346.45	347.17	347.06
Rotor outlet relative flow angle [°C]	β_3	68.79	68.79	68.79	68.75	67.07
Rotor outlet absolute flow angle [°C]	α_3	0.73	0.73	0.73	2.45	7.58
Rotor outlet relative velocity [m/s]	W_3	151.30	151.14	151.53	166.3	157.51
Static pressure at rotor outlet [bar]	P_3	0.98	0.98	0.98	0.994	0.983
Static temperature at rotor outlet [K]	T_3	336.59	336.64	336.52	337.86	336.60
Stator mean radius [mm]	r_{2m}	186.15	185.95	186.42	181.5	181.5
Rotor mean radius [mm]	r_{3m}	186.15	185.95	186.42	185	185
Stator inlet blade height [mm]	h_1	88.36	88.55	88.1	89.2	89.2
Stator outlet (rotor inlet) blade height [mm]	h_2	96.08	96.31	95.79	97	97
Rotor outlet blade height [mm]	h_3	104.23	104.47	103.91	103	103
Number of Stator blades [-]	n_N	28	28	28	29	29
Number of rotor blades [-]	n_R	30	30	30	30	30
Stator loss coefficient [%]	ζ_S	6.4	6.8	6.2	3.79	5.82
Rotor loss coefficient [%]	ζ_R	7.8	6.4	7.5	9.08	6.66
Total-to-total stage efficiency [%]	η_{tt}	92.56	92.33	92.83	91.62	93.32

3.4.2 Verification for the Smith chart

Smith [136] provided a generalised chart to predict the efficiency of axial turbines considering various turbine geometries over a range of loading (ψ) and flow coefficients (ϕ) as shown in Figure 3.2, and hence it is widely used during mean-line design. The chart was developed for a four-stage gas turbine test facility operating with a constant axial velocity across all stages, with a degree of reaction ranging from 0.2 to 0.6 and a blade aspect ratio between 3 and 4. Tip clearance losses are also neglected [23]. To verify the implementation of the loss models within the current work, the Dunham and Came, Kacker and Okapuu, Craig and Cox and Aungier loss models are used to map out a new Smith chart as shown in Figures 3.12a to 3.12d. The Smith chart has been mapped for the four-stage 100 MW air turbine design at a degree of reaction of 0.5, an aspect ratio of 4 and a pitch-to-chord ratio of 0.8, whilst zero tip clearance is assumed to match the original Smith chart. A good qualitative agreement is obtained as shown in Figures 3.12a to 3.12d. Additionally, the new charts agree with the Smith charts presented in [66, 60, 65].

The mapped Smith charts for the 100-MW turbine design provide credibility for the developed design tool over a wide range of operating conditions. However, the models provide diverse predictions for turbine efficiency owing to the assumptions made in these models along with the data used to obtain the empirical constants. The four investigated loss models resulted in similar trends to the original smith chart with some deviations from the original data. These differences are due to the fact that the conditions at which the original chart do not perfectly match the design conditions used in the current model; for example, the Smith chart was developed for a four-stage gas turbine test with a degree of reaction ranging from 0.2 to 0.6 and a blade aspect ratio between 3 and 4. Additionally, the original Smith chart was developed based on manufacturers' data for steam and gas turbines and hence, there should be differences between the measured efficiencies and the numerical values obtained by the loss models considering the assumptions made to develop those models. Large deviations are obtained by the Craig and Cox model, compared to the other loss models, as it is correlations are evaluated at the backbone length (camber-line) compared to the chord length in the rest of the models.

(a)

(b)

(c)

(d)
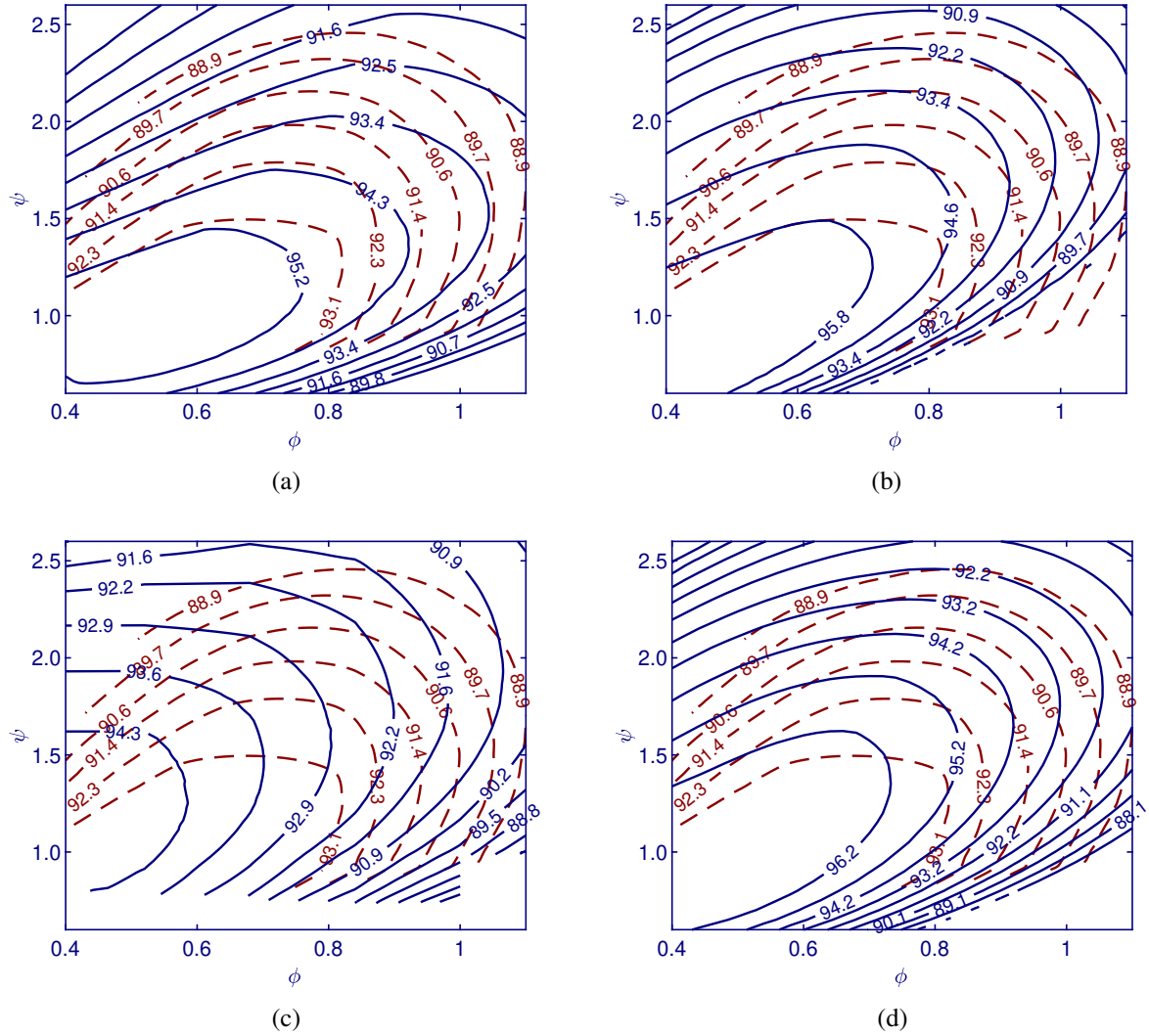
Figure 3.12: Loss models verification against the original Smith chart (total-to-total turbine efficiency (contours) at different loading and flow coefficient ($\psi\&\phi$)) for the 100 MW air turbine design; the original Smith chart is represented by the dashed red lines and the blue solid lines represent the**(a)** Dunham and Came **(b)** Kacker and Okapuu **(c)** Craig and Cox **(d)** Aungier model.

The discrepancy in the efficiency trends obtained by the three other models, the DC, KO and AN, is due to the differences in the definitions and representation for several effects including Reynolds number and compressibility effects. Though of the differences obtained between the Original smith chart and the loss models, the obtained graphs coincide with the presented charts in the original papers by DC, KO, CC and AN [60, 64, 65, 66] and this proves the right implementation of the loss models in the current analysis. Further details about these differences will be discussed in Chapter 4.

3.4.3   Verification for ORC turbines

To further verify the developed models and ensure their versatility for different working fluids, the models are also cross-checked with published numerical studies for non-conventional working fluids including two cases operating with R245fa with power ratings of 440 & 1520 kW respectively. The boundary conditions of these verification cases are reported in Table 3.5 alongside the verification results in Table 3.6. The designs are first generated at the boundary conditions specified in Table 3.5. The turbine designs showed a good agreement with the designs presented in the original paper (Lio et al. [81]) as indicated in Table 3.6.

Table 3.5: Operating conditions of the 0.44 and 1.52 MW ORC turbines [81].

Decision variables	Unit	V1 [81]	V2 [81]
Working fluid	[-]	R245fa	R245fa
Stator total inlet temperature T_{01}]	[K]	323	373
Stator total inlet Pressure [P_{01}]	[MPa]	0.34	1.26
Pressure ratio [PR]	[-]	1.70	6.40
Number of stages [n]	[-]	1.00	1.00
Mass flow rate [$\dot{m}$]	[-]	50	50
Clearance gap [t_{cl}	[mm]	1.10	1.10
Rotational speed [N]	[kRPM]	4.48	9.99
Power output [$\dot{W}$]	[MW]	0.44	1.52

Further to the verification of the design methodology, the loss breakdown obtained by the four loss models has been verified against the case study from the literature (Table 3.7). A good agreement is obtained between the loss breakdown estimated by the developed tool and the published work [81]; this includes the prediction of profile loss (Y_p), secondary flow loss (Y_s), shock loss (Y_{shock}), tip clearance loss (Y_k), supersonic expansion loss (Y_{PE}). Consequently, 0.56% and 1.16% differences in the total-to-static efficiency are obtained by the AN model for $V1$ and $V2$ cases respectively. A maximum efficiency difference is obtained by the KO model compared to the published results accounting for 1.35 and 3.75% for $V1$ and $V2$ cases respectively. Furthermore, the Smith chart has been mapped for R245fa case and compared against Lio et al. [81] and the same charts are obtained (Figures 3.13a and 3.13b).

Table 3.6: Verification results of the mean-line design model versus Lio et al. [81] for the ORC turbines.

Parameter	Symbol	V1			V2		
		Aungier	Ref. [81]	Error	Aungier	Ref. [81]	Error
Stator outlet absolute flow angle [ºC]	α_2	69.59	70.00	0.41 º	71.20	71 .00	0.2º
Stator outlet relative flow angle [ºC]	β_2	10.62	11.00	0.38 º	23.63	24.00	0.37 º
Stator outlet absolute velocity [m/s]	C_2	106.00	106.00	0.0%	203.19	202.00	0.59%
Absolute Mach at Stator outlet [-]	M_2	0.78	0.79	1.27%	1.47	1.4	5%
Rotor outlet relative flow angle [ºC]	β_3	67.69	68.00	0.31º	67.69	68.00	0.31º
Rotor outlet absolute flow angle [ºC]	α_3	-3.58	4.00	0.42º	-3.58	4.00	0.42º
Rotor outlet relative velocity [m/s]	V_3	97.45	99.00	1.6%	172.52	172.00	0.3%
Absolute Mach at rotor outlet [-]	M_3	0.71	0.73	2.7%	1.23	1.23	0%
Mean blade speed [-]	U_m	92.41	94.00	1.7%	163.70	163.00	0.43%
Stator axial chord length [mm]	b_x	41.44	38.00	7.8%	44.39	41.00	8.3%
Rotor axial chord length [mm]	b_x	31.60	31.00	1.9%	53.26	54.00	1.37%

(a)   (b)
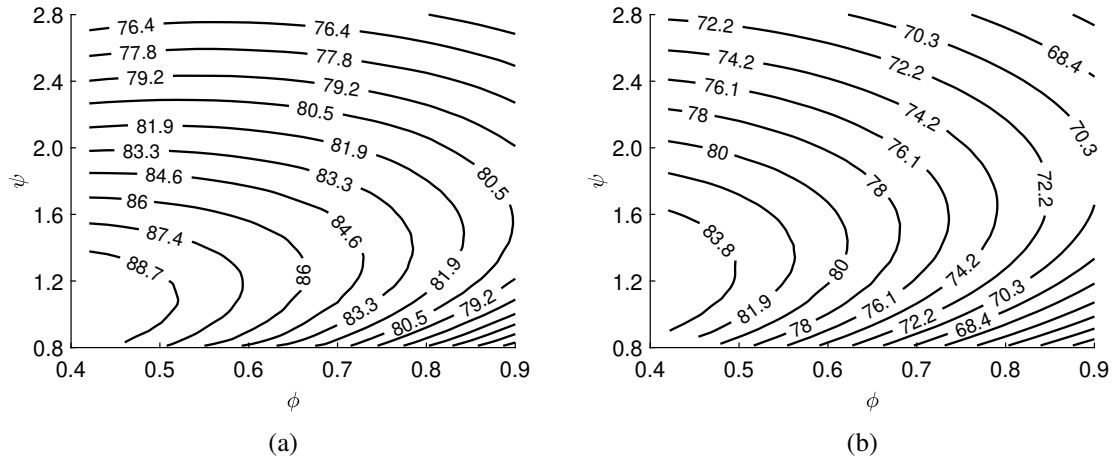
Figure 3.13: Smith chart; representing the total-to-total efficiency (contours) of axial turbines at different flow (ϕ) and loading coefficients (ψ) for verification case (a) V1 (b) V2 operating with R245fa.

3.4.4   Verification for supercritical CO_2 turbine

Finally, the mean-line design tool has been verified against CFD results of a three-stage 10 MW sCO_2 turbine. The boundary conditions and the verification results of the CO_2 verification case are reported in Tables 3.8 and 3.9 respectively. The efficiencies estimated by the four loss models (DC, KO, CC and AN) are compared against CFD simulation results as shown in Table 3.9. A good agreement is obtained between the overall turbine performance (η_{tt}) and the CFD simulation results with a maximum deviation in the turbine

Table 3.7: Verification results of the mean-line loss models versus Lio et al. [81] for the ORC turbines

	Decision variables	Description	Loss models				
			DC	KO	CC	AN	Ref. [81]
Case-study – V1	Y_P	Profile loss	0.037	0.029	0.061	0.034	0.031
	Y_s	Secondary flow loss	0.091	0.092	0.054	0.061	0.061
	Y_{TE}	Trailing edge losses	0.013	0.017	0.010	0.017	0.017
	Y_{shock}	Shock loss	0.000	0.000	0.000	0.000	0.000
	Y_k	Clearance loss	0.072	0.092	0.076	0.072	0.071
	Y_T	Total loss	0.169	0.229	0.199	0.183	0.180
	$\eta_{ts}(\%)$	Total-to-static stage efficiency	0.901	0.879	0.889	0.896	0.891
	$\dot{W}$ [MW]	Power output	0.443	0.432	0.438	0.441	-
	Difference (%)	$\eta_{ts}(\%)$ with respect to Exp.Data	1.12	1.347	0.224	0.561	-
Case-study – V2	Y_P	Profile loss	0.038	0.027	0.089	0.036	0.029
	Y_s	Secondary flow loss	0.263	0.163	0.193	0.099	0.105
	Y_{TE}	Trailing edge losses	0.046	0.019	0.011	0.011	0.012
	Y_{shock}	Shock loss	-	0.012	0.000	0.023	0.024
	Y_k	Clearance loss	0.139	0.229	0.101	0.139	0.139
	Y_{PE}	Post-expansion loss	0.235	0.200	0.081	0.138	0.135
	Y_T	Total loss	0.560	0.645	0.475	0.446	0.444
	$\eta_{ts}(\%)$	Total-to-static stage efficiency	0.839	0.823	0.857	0.865	0.855
	$\dot{W}$ [MW]	Power output	1.48	1.45	1.51	1.52	-
	Difference (%)	$\eta_{ts}(\%)$ with respect to Exp.Data	1.871	3.743	0.234	1.169	-

efficiency by 1.53%.

Table 3.8: Operating conditions and decision variables of the 10 MW sCO$_2$ turbine design [81].

Decision variables	Value	Decision variables	Value
Working fluid [-]	sCO$_2$	Mass flow rate [$\dot{m}$]	184 [kg/s]
Stator total inlet temperature [T_{01}]	773 [K]	Clearance gap [t_{cl}]	0 [mm]
Total inlet Pressure [P_{01}]	15 [MPa]	Rotational speed [N]	10.00 [kRPM]
Pressure ratio [PR]	1.55	Power output [$\dot{W}$]	10 [MW]
Number of stages [n_{stage}]	3		

Table 3.9: Verification results of the mean-line loss models versus CFD simulation results for the 10 MW sCO_2 turbine [80].

	Variables	Description	Loss models				
			DC	KO	CC	AN	Ref. [80]
[1st]	$\zeta_S(\%)$	Stator enthalpy loss coefficient	0.058	0.047	-	0.037	
	$\zeta_R(\%)$	Rotor enthalpy loss coefficient	0.086	0.089	-	0.072	
[2nd]	$\zeta_S(\%)$	Stator enthalpy loss coefficient	0.037	0.034	-	0.027	
	$\zeta_R(\%)$	Rotor enthalpy loss coefficient	0.071	0.082	-	0.066	
[3rd]	$\zeta_S(\%)$	Stator enthalpy loss coefficient	0.034	0.04	-	0.031	-
	$\zeta_R(\%)$	Rotor enthalpy loss coefficient	0.062	0.076	-	0.062	
[Turbine]	η_{t_t} (%)	Total-to-total stage efficiency	90.4	90.2	-	92.1	91.6
	$\dot{W}$ [MW]	Power output	10.360	10.34		10.26	10.00
	Difference (%)	$\eta_{tt}(\%)$ with respect to Exp.Data	1.31	1.53		0.44	-

3.4.5 CFD Analysis

To further verify the mean-line design model, a detailed 3D-CFD analysis is carried out for a 14-stage CO_2/SO_2 flow path as a part of another research framework within the SCARABEUS project. To initiate the CFD simulations, the 3D blades are generated using the 1-D flow path details generated by the mean-line design using the methodology explained in Section 3.3. The boundary conditions of this case are reported in Table 3.10.

Table 3.10: Operatng conditions of the 130 MW turbine operating with CO_2/SO_2 blend.

Parameter	value	Parameter	value
Inlet Temperature $[T_{01}]$	700 K	Mass flow rate $[\dot{m}]$	827.06 kg/s
Inlet Pressure $[P_{01}]$	23.9 MPa	Optimum molar fraction X_i	20 %
Outlet pressure $[P_{03}]$	8.15 MPa		

Further to the geometry provided by the mean-line design tool, other geometric parameters have been assumed within the CFD process to fully define the 3D blade shape such as leading-edge thickness, inlet/outlet wedge angles $\Delta\beta_1$ and $\Delta\beta_2$ (Figure 3.11b), aerofoil curvature control points, and blade base fillet. The 2D aerofoil is then linearly extruded without twist to form the 3D blade since the mean-line design indicates relatively short blades compared to the blade's mean diameter. Afterwards, CFD simulations are

then completed with the generated 3D blade geometry and the results are compared to the mean-line design model. As a part of the CFD simulations, the predicted mass flow rate is compared to the mass flow dictated by the cycle analysis and consequently the 3D blade design assumptions are adjusted to provide a better match with the cycle parameters.

The CFD analysis has been carried out using ANSYS workbench where ANYSY-CFX solver, bladeGen and TurboGrid are used to simulate the flow and generate the blade profile and the mesh respectively. The mesh generated using TurboGrid is structured with the mesh topology designed for turbomachinery applications. This decreases the total number of grid points required to achieve a mesh independent solution compared to the unstructured mesh. To generate a high quality mesh, the mesh size in proximity to the walls was set to satisfy a specified average $Y+$ value, as recommended for the turbulence model. The global mesh size, the number of spanwise layers, and the growth rate were varied, and different grids were examined to ensure a mesh independent solution. It has been found that a total number of grid points per stage of 0.65 million points is sufficient to achieve a total-to-total efficiency tolerance of 0.05% compared to the finest mesh. Within the conducted CFD analysis, a steady-state multi-stage CFD model is set up for flow passage; where the shear stress transport ($k_\omega SST$) turbulence model is used alongside with a mixing plane approach to model the interface between the stator and rotor blades and the pitch ratios defined as the ratio between the number of blades of the downstream blade row to the upstream blade row.

In the developed design, total pressure and the total temperature are used to model the stator inlet conditions whereas the static pressure of the last rotor is used to define the outlet conditions. A summary of the CFD and MLD results is presented in this section. Whilst, the full details of the conducted CFD analysis results can be found in Abdeldayem et al. [141, 142].

To ensure consistency with the cycle analysis and the mean-line design models, the thermo-physical properties of the sCO$_2$ blends were evaluated with the same equation of state, Peng Robinson; where the parameters for the selected EoS were selected to match those used for the cycle analysis. Additionally, a sensitivity analysis for the look-up tables

Table 3.11: Additional design variables for the CFD simulations and a basic geometry for the airfoil.

(a) CFD additional decision variables

Mean-line design	Symbol
Number of blades	N
Inlet/Outlet blade angles	β_1 & β_2
Stagger angle	γ
Hub/tip Radii	R_h & R_t
Axial chord length	c
TE thickness	R_2
Axial spacing	R_2
Assumed parameters	Symbols
LE thickness	R_1
Inlet/Outlet wedge angles	$\Delta\beta_1$ & $\Delta\beta_2$
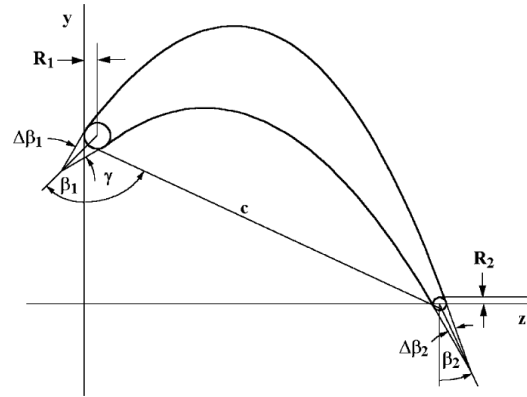
(b) Basic airfoil geometry [66]

and grid independence has been carried out with the framework of the CFD simulations to ensure accurate properties prediction [141, 142].

Table 3.12 summarises the comparison between the mean-line and CFD results including a comparison between the power output, mass flow rate and total-to-total efficiency. Additionally, the pressure, temperature, velocities and Mach number are compared across the stages for both models (Table 3.13). A good agreement is achieved between both models with deviations of 0.51%, 1.0% and 1.4% in the mass flow rate, total-to-total efficiency and power output respectively. Furthermore, the mass flow averaged relative Mach number at the exit from each blade row is compared between the CFD and the mean-line design results. Both models show the the same trend, as shown in Figure 3.14, where the Mach number increases as the flow moves through the turbine.

Table 3.12: Verification results of the mean-line design model versus the CFD results for the 14-stage CO_2/SO_2 turbine.

Parameter	**Mean-line**	**CFD**	**Difference [%]**
Mass flow rate [kg/s]	827.06	822.9	0.51%
Power output [MW]	131.9	130.1	1.38%
Total-to-total efficiency [%]	93.84	92.90	1.01%
Total-to-static efficiency [%]	93.06	91.95	1.21%

The results from the mean-line agree with those from the CFD models. However,

the velocities predicted using the CFD model tend to be slightly higher within the final
stages which is due to the cumulative difference between the two models. The difference
between the flow distribution of the first, seventh and last turbine stages at the design point
is compared at the mid-span plane in Figure 3.14. The average stage Mach number is
higher in the last stage compared to the first stage. However, both stages exhibit a smooth
flow from left to right without any obvious separation vortices.
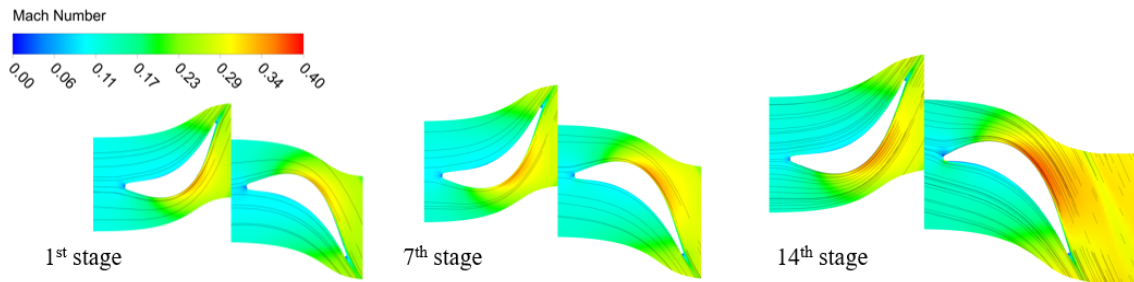
Figure 3.14: Comparison of the flow-field obtained for the 1st, 7th and 14th turbine stage at the
design point [142].
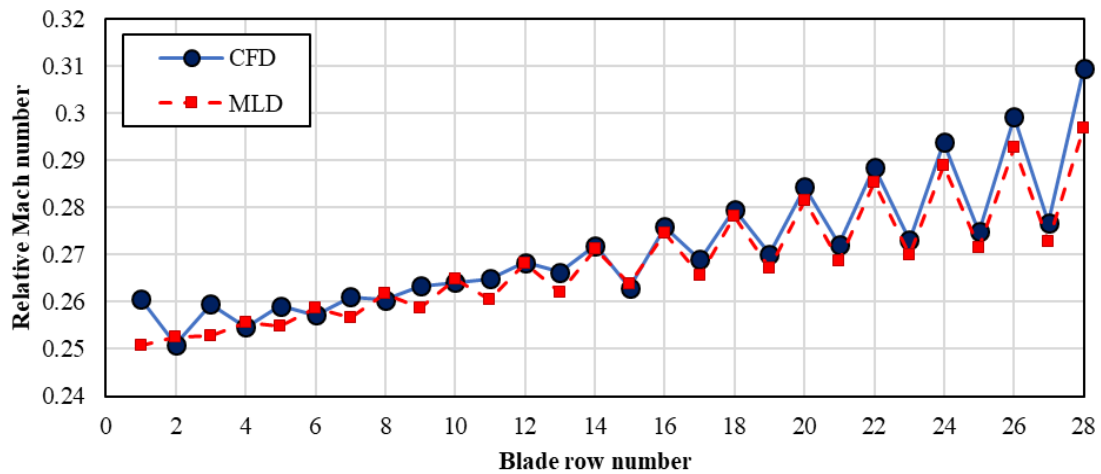
Figure 3.15: Comparison between Mach number obtained using the mean-line design and CFD at
the exit of each blade row [142].

Table 3.13: Comparison between CFD and mean-line design results for CO_2/SO_2 flow path design.

	Parameters	Units	Mean-line design		CFD	
			1st stage	last stage	1st stage	last stage
Stator inlet	Total temperature	[k]	973.0	836.4	973.0	839.0
	Total pressure	[MPa]	239.0	88.6	239.0	89.5
	Static temperature	[k]	971.7	835.0	971.8	837.7
	Static pressure	[Mpa]	237.0	87.7	237.1	88.6
	Absolute velocity	[m/s]	53.5	53.7	53.1	55.1
	Absolute flow angle	[°]	0.0	-4.5	0.0	0.1
Rotor inlet	Total temperature	[k]	973.0	836.4	972.9	839.0
	Total pressure	[MPa]	239.0	88.5	238.7	89.3
	Static temperature	K	966.7	830.0	966.4	832.6
	Static pressure	[MPa]	229.0	84.5	228.8	85.3
	Relative velocity	[m/s]	53.5	53.7	54.6	56.1
	Relative flow angle	[°]	0	-16	2	-14
	Mach number	[-]	0.25	0.27	0.26	0.28
Rotor outlet	Total temperature	[k]	963.0	825.5	963.1	828.2
	Total pressure	[MPa]	223.0	81.5	223.3	82.2
	Static temperature	[k]	961.2	824.0	961.6	826.6
	Static pressure	[MPa]	221.0	80.6	221.2	81.3
	Relative velocity	[m/s]	120.0	115.6	122.2	117.0
	Relative flow angle	[°]	64.9	65.9	63.0	65.5
	Mach number	[-]	0.25	0.30	0.25	0.30

3.4.6 Mean-line model verification summary

To conclude, multiple cases have been selected from the literature to verify the design methodology and implemented loss models. This includes verification against 140 kW air turbine, 440 kW & 1520 kW axial ORC turbines and 10 MW sCO$_2$ turbine. The developed model has shown a good agreement with the selected verification cases with a maximum percentage difference of 1.5 and 3.7% in the total-to-total and total-to-static efficiency respectively. Additionally, the verification against the smith chart and the implemented loss models showed a good agreement. It is worth noting that the loss model that achieves the closest match to the published data varies for each examined case-studies. For example, the KO model obtains the smallest efficiency difference for the air case but results in the largest difference for the sO$_2$ and ORC cases. This is due to differences in the definition and representation of several effects which includes Reynolds number, compressibility, shock and supersonic expansion losses which can be expected to vary with the working fluid and boundary conditions. For example, supersonic expansion and clearance losses

are significant for the ORC turbine, and it is found that the KO model overpredicts these losses compared to the other loss models. Further to the mean-line model verification with respect to cases from the literature, CFD simulations have been carried out within another research framework within the SCARABEUS project. A good agreement has been obtained between the mean-line model and CFD results, for a 14-stage turbine design operating with CO_2/SO_2 working fluid, with a deviation in the mass flow rate and total-to-total efficiency of 0.51% and 1.0% respectively.

3.5 Preliminary parametric study

The turbine design process can be initiated with the selection of some dimensionless design parameters, as discussed in Section 3.2.2, which affects the turbine aerodynamic performance. Therefore, a parametric study is presented in this section to investigate the effect of these parameters, including the flow coefficient (ϕ), and loading coefficient (ψ), on the turbine aerodynamic performance (η_{tt}) within the mean-line design process.

Multiple turbine designs are produced, using the mean-line modelling approach, explained in Section 3.3.1, assuming different values of the design parameters ϕ and ψ for the boundary conditions reported in Table 3.14. The performance of the designs has been estimated using Soderberg model which allows for evaluating the turbine performance for the preliminary design phase as a function of the blade turning ($\alpha_1 + \alpha_2$ and $\beta_2 + \beta_3$) irrespective to the turbine size and hence, these conclusions are valid for different design scales.

Table 3.14: Operating conditions of the single-stage sCO$_2$ turbine.

Design parameter	Value	Design parameter	Value
Turbine inlet temperature [ºC]	650 [143]	Turbine inlet pressure [MPa]	17 [144]
Expansion ratio [-]	3.0	Rotational Speed [kRPM]	150 -250

In the following set of results, Figures 3.16a to 3.16c, ϕ and Λ have been set to 0.2 and 0.5 respectively, whilst ψ is varied from 0.8 to 3.0. Increasing the loading coefficient from 0.8 to 3.0 results in an increase in both rotor absolute and relative inlet flow angles,

α_2 & β_2, from 74 to 81° and -60 to 60 ° respectively as shown in Figure 3.16a. In principle, low loading coefficients result in higher efficiency, though it results in higher blade speed and thus high mechanical stresses; at values of 1.0 and 3.0, the mean blade speed (U_m) reaches approximately 522 and 306 m/s and results in total blade stress of 160 MPa and 76 MPa respectively. Meanwhile, a smaller number of rotor blades is needed at high loading coefficients. Therefore, the design decision should be made based on the selected material, the maximum allowable stress, along with the required number of blades.

Furthermore, increasing the loading coefficient causes a slight decrease in both Ma_2 and Ma_3, at the inlet and outlet of the rotor blades respectively, as shown in Figure 3.16b; where Ma_2 and Ma_3 are the Mach numbers calculated with respect to the absolute and the relative velocity respectively. To achieve a subsonic flow at a flow coefficient of 0.2, the loading coefficient should be greater than 0.8.

Additionally, it was found that increasing the loading coefficient results in an efficiency increase until a maximum is reached at values of ψ ranging between 1.6 to 1.7. It is worth mentioning that ψ has a limited effect on the efficiency for a flow coefficient of 0.2. The highest efficiency is achieved for the turbine designs that keep the swirl angle α_3 close to the recommended value, which is recommended not to exceed 20° [22], along with achieving the optimum difference in the whirl velocity components at the inlet and exit of the rotor. Increasing the exit circumferential velocity, owing to the increased swirl angle, results in an increase in centrifugal force which leads to an increased amount of flow reversal at the rotor outlet. Hence, higher losses and lower efficiencies are observed.

To investigate the effect of the flow coefficient on the turbine performance, the analysis has been repeated at $\Lambda = 0.5$ and $\psi = 1.60$ respectively. Reducing ϕ over the range from 0.2 to 1 results in an increase in rotor outlet flow angle α_2 from 43 to 77° as shown in Figure 3.17a. However, increasing the flow coefficient also resulted in an increase in both Mach numbers, as shown in Figure 3.17b, where Ma_2 increased from 0.88 to 1.30 and Ma_3 increased from 0.93 to 1.34; thus, supersonic conditions occur in both the rotor and stator. To ensure subsonic flow at the rotor inlet, the flow coefficient should be kept below 0.45 for a loading coefficient of 1.6 and a degree of reaction of 0.5.
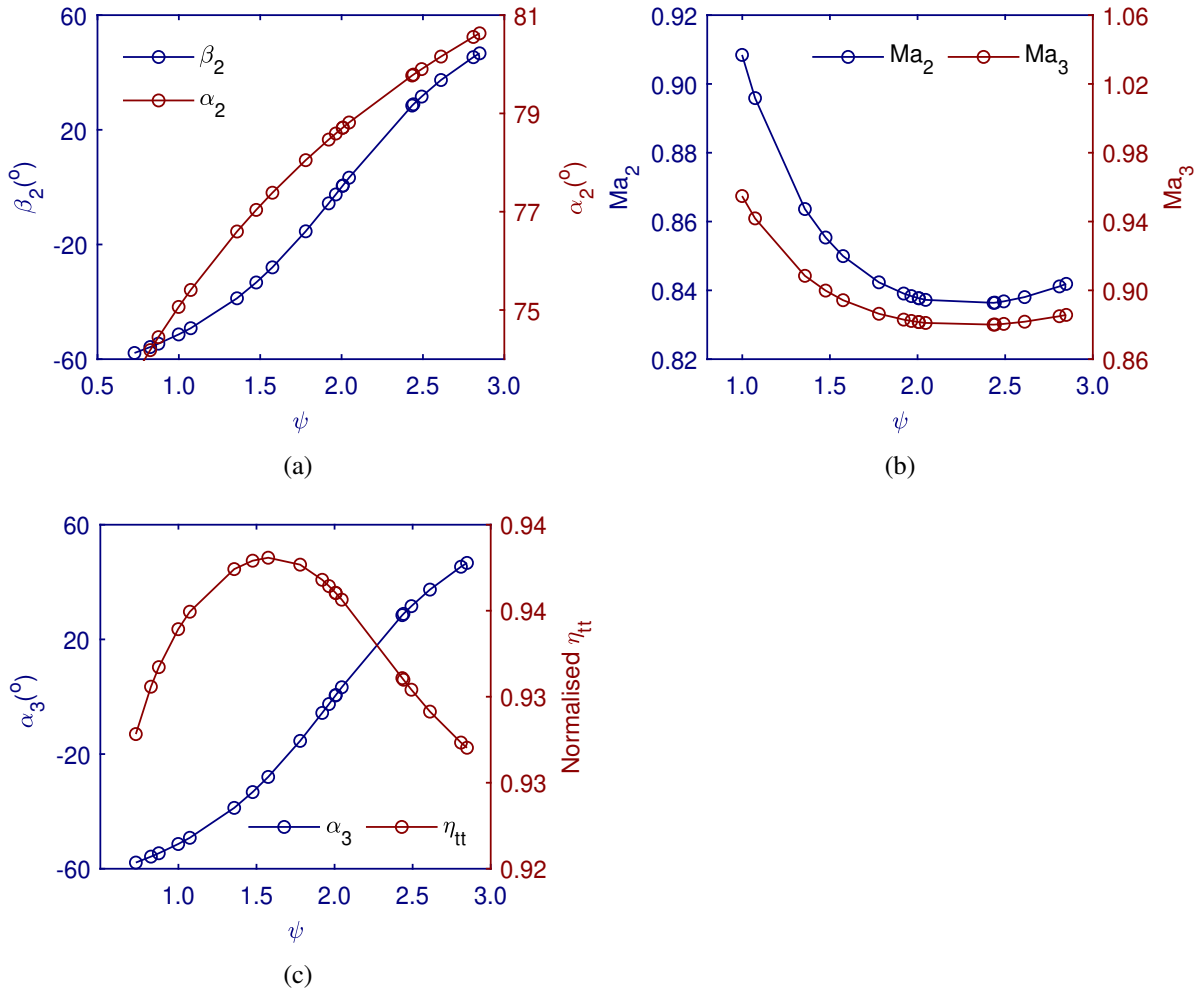
Figure 3.16: Loading coefficient (ψ) versus (a) flow angles [β_2 and α_2] (b) Mach number at the rotor inlet [Ma_2] and exit [Ma_3] (c) normalised efficiency [η_{tt}] and swirl angle [α_3]

Furthermore, increasing the flow coefficient results in an efficiency decrease, as observed in Figure 3.17c. Additionally, it results in a decrease in swirl angle from 26 to 5°. However, at high flow coefficients, low swirl angles and low rotor inlet blade angles (α_2) are achieved. Increasing the flow coefficient results in a higher Mach number at the rotor exit and hence higher losses incurred by the formation of shock waves in the rotor blade passages. Additionally, profile losses will be higher owing to the boundary layer growth, whilst friction losses at the exit are expected to be high. Consequently, a drop-in efficiency is observed at higher flow coefficients.
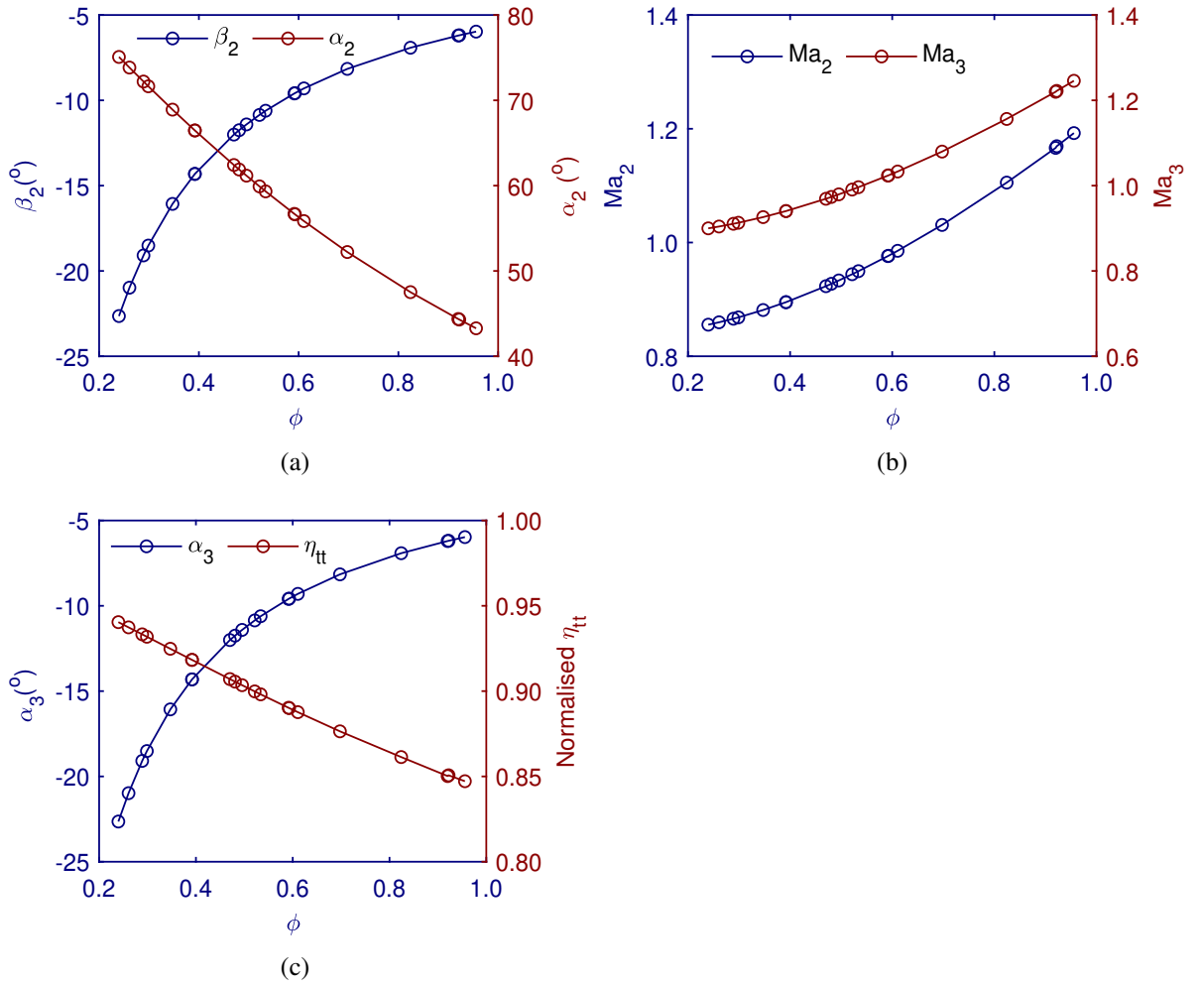
Figure 3.17: Flow coefficient (ϕ) versus (a) flow angles [β_2 and α_2] (b) Mach number at the rotor inlet [Ma_2] and exit [Ma_3] (c) normalised efficiency [η_{tt}] and swirl angle [α_3].

3.6 Summary

The different aspects of the mean-line design methodology used in the current work were discussed in this chapter. This includes a description of the implemented mean-line design approach alongside a discussion about the implemented loss models. Furthermore, the details of the mean-line design tool verification were presented; where the tool was verified against the Smith chart, three case-studies from the literature and CFD simulation results. The verification cases were selected to operate with different working fluids to ensure the versatility of the design tool for non-conventional working fluids. A maximum percentage difference of 1.5% and 3.7% in the total-to-total and total-to-static efficiency, respectively, was obtained between the developed model and the verification cases along with a good

qualitative agreement with the efficiency trends of the original Smith chart. Additionally, a good agreement was obtained with the mean-line and CFD results where a maximum difference in the mass flow rate and total-to-total efficiency of 0.5% and 1.0%, respectively, was achieved. Further to evaluating the turbine aerodynamic design, mechanical design constraints were considered throughout the design methodology discussed in this chapter.

Furthermore, a parametric study was conducted to investigate the effects of flow coefficient and loading coefficient on the performance of axial turbines. The performance of a sCO$_2$ turbine was evaluated over a loading and flow coefficient (ψ & ϕ) range of 0.8 to 3.0 and 0.2 to 1 respectively. Increasing the loading coefficient was found to result in an efficiency increase until a maximum value is achieved at values of ψ ranging between 1.6 to 1.7. Whilst, increasing the flow coefficient resulted in a reduction in the total-to-total turbine efficiency due to achieving a higher Mach number at the rotor exit and hence higher losses incurred by the formation of shock waves in the rotor blade passages.

In summary, the mean-line design tool showed good credibility for operating over a range of operating conditions and working fluids. Nonetheless, some discrepancies in the efficiency trends and values were obtained by the four investigated loss models (i.e., Dunham and Came, Kacker and Okapuu, Craig and Cox and Aungier loss models). This is due to the differences in the definition of loss mechanisms and treatment of several effects such as Reynolds number and compressibility. Consequently, these differences will be discussed in detail in Chapter 4.

This page is left intentionally blank

4 A comparison of axial turbine loss models for air, sCO$_2$ and ORC turbines

4.1 Introduction

Having applied the axial mean-line design methodology and explored the effect of the important design parameters on the turbine performance, the next step is to explore the fidelity of the existing performance analysis tools with regards to operating with non-conventional working fluids such as pure sCO$_2$ and organic working fluids. There exist multiple loss models that have been previously introduced and immensely used in the preliminary 1D designs of air and steam turbines. The literature review highlighted that several researchers have applied these models in the design process of axial turbines ORC and sCO$_2$ systems (Chapter 3). Nonetheless, each study has only applied a single loss model and considered a single working fluid, turbine scale or operating condition. Therefore, none of the previous studies has attempted to highlight the discrepancies in the different models in predicting the turbine performance for non-conventional working fluids. As a result, there are no clear recommendations for selecting the most suitable loss model based on the working fluid, turbine scale or operating conditions.

Therefore, this chapter provides a road map for preliminary axial turbine performance prediction by exploring the deviation between the prediction capability of the different loss models. To achieve this aim, the design tool developed at a constant mean-diameter (explained in Section 3.3.1) is integrated with several loss models to provide an accurate estimation of the turbine performance for the selected case-studies; including Dunham and Came [64], Kacker and Okapuu [65] and Aungier [66] models. Three different case-studies are defined for air, organic Rankine cycle (ORC) and sCO$_2$ turbines and each one is evaluated at two different scales; where the cycle boundary conditions are set based on the operation and application constraints of each cycle as specified in the literature.

The novelty in this current work lies in exploring the deviation between the prediction

capability of the four loss models, derived for air, for non-conventional working fluids where turbines may differ in design and operation from conventional air or steam turbines. This information is considered an important contribution to the field as it aims to provide clarity on the selection of axial turbine loss models for application areas that are becoming increasingly important for future sustainable power production.

4.2   Key features for loss models and loss mechanisms

In this work, losses are classified into profile, secondary, tip clearance, trailing edge, shock and supersonic expansion losses. Further details about the definition of the different loss mechanisms alongside elaborative diagrams can be found in Section 2.4.1. A brief overview of the various loss models is presented here to highlight the key components contributing to the estimated losses. Additionally, significant findings from the literature are presented to clarify the influence of key parameters such as Reynolds number and Mach number. This discussion is intended to provide a background for the prediction differences between loss models for both air and non-conventional working fluids across different scales.

The former loss models, including Ainley and Mathieson [63] (AM), Dunham and Came [64](DC), Kacker and Okapuu (KO) [65] and Aungier [66] (AN), evaluated the flow losses at the blade chord length. However, Craig and Cox [60] introduced a separate loss model to predict the losses based on a new characteristic length defined as backbone (camber-line) length. In the Craig and Cox (CC) [60] model, the backbone length is used to replace the chord length in the pitch-to-chord ratio and the blade aspect ratio.

Throughout the models' development process, several fluid flow phenomena have been considered including the characteristics of flow regime, fluid compressibility and off-design incidence effects. Given that profile losses occur due to the formation of boundary layers on the blade surface, they are highly affected by Reynolds number, surface roughness, Mach number and trailing edge thickness. The effect of the Reynolds number has been previously investigated experimentally for air turbines owing to its significance in controlling both the profile and secondary flow losses; where the critical Reynolds number

provides an indication of the location of the transition from laminar to the turbulent boundary layer. A turbulent boundary layer in known to result in higher pressure losses because of the velocity profile that results in large shear forces at the blade surface [145]. However, a turbulent boundary layer is sometimes desirable to delay the separation in the laminar boundary layer. Thus, the effect of a low Reynolds number on the profile and secondary flow losses has been previously investigated in several studies [146, 147, 148, 149, 150] and it has been concluded that low Reynolds number results in an increase in both the size of the separation bubble and in the amount of flow separation. Therefore, the flow separation dominates the loss in low Reynolds number turbines. Satta et al. [148] concluded that profile losses are expected to decrease with increasing Reynolds number where no boundary layer separation affects the turbine operation at Reynolds number ranging from 1×10^5 to 3×10^5 [148]. Moreover, the effect of a low Reynolds number is pronounced in the secondary flow losses, low Reynolds number results in the development of the secondary flow in the end wall Region. Increasing the Reynolds number results in suppressing the unsteady wakes on the end wall secondary flow. Nonetheless, the effect of a low Reynolds number has been found to be significant on the profile losses more than on the secondary flow losses [146]. On this matter, the Reynolds number is evaluated based on the chord length for all models except for the CC model where it is evaluated based on the throat opening. Additionally, Reynolds number effects have been considered for both profile and secondary flow losses for the DC, CC and AN models. Whilst, the KO model considered it for the profile losses only.

In view of the above effects of laminar and turbulent flow regimes, it is important to determine the critical Reynolds number where the laminar to turbulent boundary layer transition takes place. Boundary layer transition is mainly affected by the pressure gradient, free-stream Mach number, free-stream turbulence, and surface roughness. Increasing the Mach number results in a reduction in the transition Reynolds number. Additionally, it has been found that there is a critical roughness height below which roughness has no influence on the nature of the transition. However, above the critical roughness height flow transition is found to occur at lower Reynolds resulting in a reduction in the Reynolds number required for turbulence initiations. For supersonic flows, the critical roughness height

is found to be greater because of the Mach number effect on boundary layer thickness for supersonic flows [151]. Accordingly, different critical Reynolds numbers have been set within loss models. The DC model evaluates the turbine performance at a Reynolds number of 2×10^5 and hence, a correction factor is applied when the Reynolds number deviates from the specified value without defining the transition region. AN model defines the transition region as $1 \times 10^5 < Re < 5 \times 10^5$ in comparison to $2 \times 10^5 < Re < 1 \times 10^6$ for the KO model, while the CC model defines a correction for Reynolds number effects for a wide range of Reynolds number with a correction factor of 1 at a Reynolds number equivalent to 1×10^5. On another note, the effect of surface roughness on the boundary layer thickness for turbulent flow has been taken into consideration in the CC and AN models only.

Besides the previous effects, fluid compressibility affects profile losses by causing shocks at the blade leading edge and affecting the flow acceleration within blade channels. As the flow accelerates adjacent to the curved leading edge, it experiences large oblique shock losses and thus the inlet Mach number is recommended to be less than 0.6 [65]. It should be emphasised that the leading edge shock loss effect is only considered in the KO and AN models. Further to shock losses occurring at the leading edge, reaching sonic flow conditions results in higher pressure losses occurring as a result of the normal shock wave originating at the trailing edge. To account for supersonic expansion losses, the DC model introduced a correction factor to the profile loss introduced by the AM model. Meanwhile, KO found this correlation overestimates the losses. Similarly, the CC model includes a correction factor for the profile loss to account for the supersonic flow effects. Ultimately, Aungier introduced a separate form for estimating the supersonic expansion loss.

4.3   Selected case-studies

Three case-studies are defined for the assessment of the available loss models which relate to the modern gas turbine, ORC and sCO$_2$ cycles. Steam and gas turbine systems have both been extensively studied and thus only a gas turbine case-study is considered as a comparison between turbines operating with conventional and non-conventional fluids.

Modern gas turbines with a high power rating and thermal efficiency of around 40% are characterised by high turbine inlet temperatures, in the range of 1400 – 1500 °C, compression ratios of more than 20, and multiple stage turbine designs to accommodate the high-pressure ratio [152]. The operating conditions of General Electric's-Frame 9H four-stage turbine have been selected to represent the behaviour of large-scale gas turbines [152]. The ORC cycle operating conditions are taken from one of the authors' previous works [143], which identified R1233zdE, a modern hydrofluoroolefin with a low global-warming potential, as an optimal fluid for waste-heat recovery applications with heat-source temperatures in the region of 200 °C. As for the sCO_2 cycle, previous studies have shown that sCO_2 cycle efficiency is sensitive to both the temperature and pressure ratios. The maximum pressure is limited due to the capital cost related to the piping and measurement systems and is typically around 20-25 MPa [57], whilst inlet temperatures are in the range of 400 to 800 °C [58]. Therefore, the operating conditions of both the ORC and sCO_2 turbine have been set by the authors considering the above operational constraints [143, 57] as detailed in Table 4.1.

Considering the above-mentioned aspects, the case-studies listed in Table 4.1 have been selected to examine the performance of the various loss models for a range of operating conditions for three different working fluids (air, sCO_2 and R1233zd). Additionally, two different turbine scales are selected for each case-study to capture the main differences between the performance of small- and large-scale turbine designs. Hence, 100 kW & 100 MW and 300 kW & 100 MW are set for air and sCO_2 turbines respectively, while 10 kW and 1 MW selected for the ORC turbine. For axial turbines, the optimum efficiency can be expected for specific speed values in the range of 0.1 to 1.0 [23]. Thus, the specific speed is selected in the recommended range for all the design cases, and hence the rotational speeds are obtained as a function of the enthalpy drop and turbine outlet volumetric flow rate for each working fluid. Operating the turbine at high specific speed imposes high level of stresses on the rotor blades and could result in rotordynamic instabilities. Consequently, in the present work, small-scale air, sCO_2 and ORC turbines are evaluated at shaft speeds of 89, 107 and 141 kRPM, corresponding to specific speeds of 0.25, 0.25 and 0.6 rad respectively. However, synchronous designs with a rotational speed of 3,000 RPM

Table 4.1: Operating conditions and decision variables for the selected case-studies (air, sCO$_2$ and ORC turbines).

Inputs	Description	Unit	Case-studies serial					
			C1 [152]	C2	C3 [57]	C4	C5 [143]	C6
Boundary conditions								
-	Working fluid	[-]	Air		sCO$_2$		R1233zd	
T_{01}	Total inlet temperature	[K]	1713.00		923.00		434.21	
P_{01}	Total inlet Pressure	[MPa]	0.60		25.00		3.04	
PR	Pressure ratio	[-]	23.00		2.50		11.57	
n	Number of stages	[-]	4.00	4.00	8.00	6.00	2.00	
$\dot{m}$	Mass flow rate	[kg/s]	0.09	92.50	1.97	655.18	0.22	21.60
s/c	Pitch-to-chord ratio (1ststage)	[-]	1.10		0.80	0.60	1.10	
n_s	Specific speed	[rad]	0.25	0.27	0.25	0.13	0.60	0.60
N	Rotational speed	[kRPM]	89.40	3.00	106.90	3.00	141.10	14.10
$\dot{W}$	Power output	[MW]	0.10	100.00	0.30	100.00	0.01	1.00
Fixed parameters								
k_s	Surface roughness	[mm]	0.002					
t_{cl}	Tip clearance gap	[mm]	0.400 (for large scale design)					

Variable and fixed parameters			Fixed	Variable	
				LL*	UL*
ϕ	Stage flow coefficient	[-]	0.50	0.40	1.10
ψ	Stage loading coefficient	[-]	1.00	0.80	2.50
Λ	Degree of reaction	[-]	0.50	0.00	0.50
t/o	Trailing edge to throat ratio	[-]	0.05	0.05	4.00
h/c	Aspect ratio (height to chord)	[-]	-	0.50	3.50
s/c	Pitch-to-chord ratio	[-]	-	0.50	1.10
* LL and UL stands for the lower and upper variables limit.					

have been selected for the 100 MW sCO$_2$ and air designs to facilitate direct grid connection. The number of stages for air turbines is set to four, as specified in the literature [152]. Meanwhile, the number of stages for sCO$_2$ and ORC turbines are set to allow for a gas bending stress within 10% of the permissible bending stress; where the limit is specified based on previous experience. Similarly, the pitch-to-chord ratio is varied among the various designs over the range from 0.5 and 1.1 [63] to allow for a feasible number of blades for each design case; considering that the number of the blades cannot increase beyond a point set by the blade fixing considerations [22].

In the following sub-sections (Sections 4.3.1 to 4.3.5), a generalised assessment for Dunham and Came, Kacker and Okapuu, Craig and Cox and Aungier loss models is presented for air and non-conventional working fluids operating over a wide design space based on the operating conditions specified in Table (4.1). The predictions of loss models is assessed over a wide range of loading and flow coefficients as recommended by Smith [136]. Furthermore, the degree of sensitivity of the loss models to the aspect ratio

and the pitch-to-chord ratio is highlighted in Section 4.3.6.

4.3.1   Large scale designs across a range of flow coefficients

In the following set of results, Figures 4.1a to 4.1e, the total-to-total efficiency (η_{tt}) is predicted for the large-scale axial turbines designs where ψ, Λ, t/o have been set to 1.00, 0.50 and 0.05 respectively, while ϕ is varied from 0.4 to 1.1. Each case is further examined by considering the loss breakdown ($Y_{breakdown}$) predicted by the DC, KO, CC and AN models, at $\phi_1 = 0.5$ and $\phi_2 = 0.7$; ϕ_1 is the expected optimum design point while ϕ_2 is selected to depict the changes in the predicted loss breakdown at a high flow coefficient. The loss breakdown ($Y_{breakdown}$) value is obtained based on the pressure loss coefficient (Y) obtained by each loss model for the different types of losses (see Table 4.2).

For the air turbine, Figure 4.1a, the dashed blue lines represent the efficiency estimated by the CC model when the Reynolds number (Re) is obtained based on the throat opening while the solid blue lines show the efficiency when the Reynolds number is obtained from the backbone length. The backbone length is calculated by assuming the blade mean-line can be constructed by a circular arc from the inlet to the throat, and then by a straight line to the outlet [153]. It is evident that the dashed blue lines deviate from the predictions of the other loss models. Given that the other loss models determine the Reynolds number based on the chord length, determining the Reynolds number based on the throat opening results in reducing the Reynolds number by approximately half or less. Therefore, using the throat opening leads to significantly larger Reynolds number correction factors and secondary and profile flow loss predictions that are almost double those obtained by the AN and KO models. To alleviate the throat opening effect on Reynolds number (Re) for the 100 MW air turbine, the Re was obtained based on the backbone length. This leads to efficiency predictions that are closer to the other loss models, as denoted by the solid blue line in Figure 4.1a.

Though calculating the Reynolds number based on the backbone length results in close predictions for the air turbine compared to the other loss models, the CC model over-predicts both profile and secondary flow losses as shown in Figure 4.1b. The preliminary

profile and secondary flow losses, excluding both *Re* correction factor and compressibil-
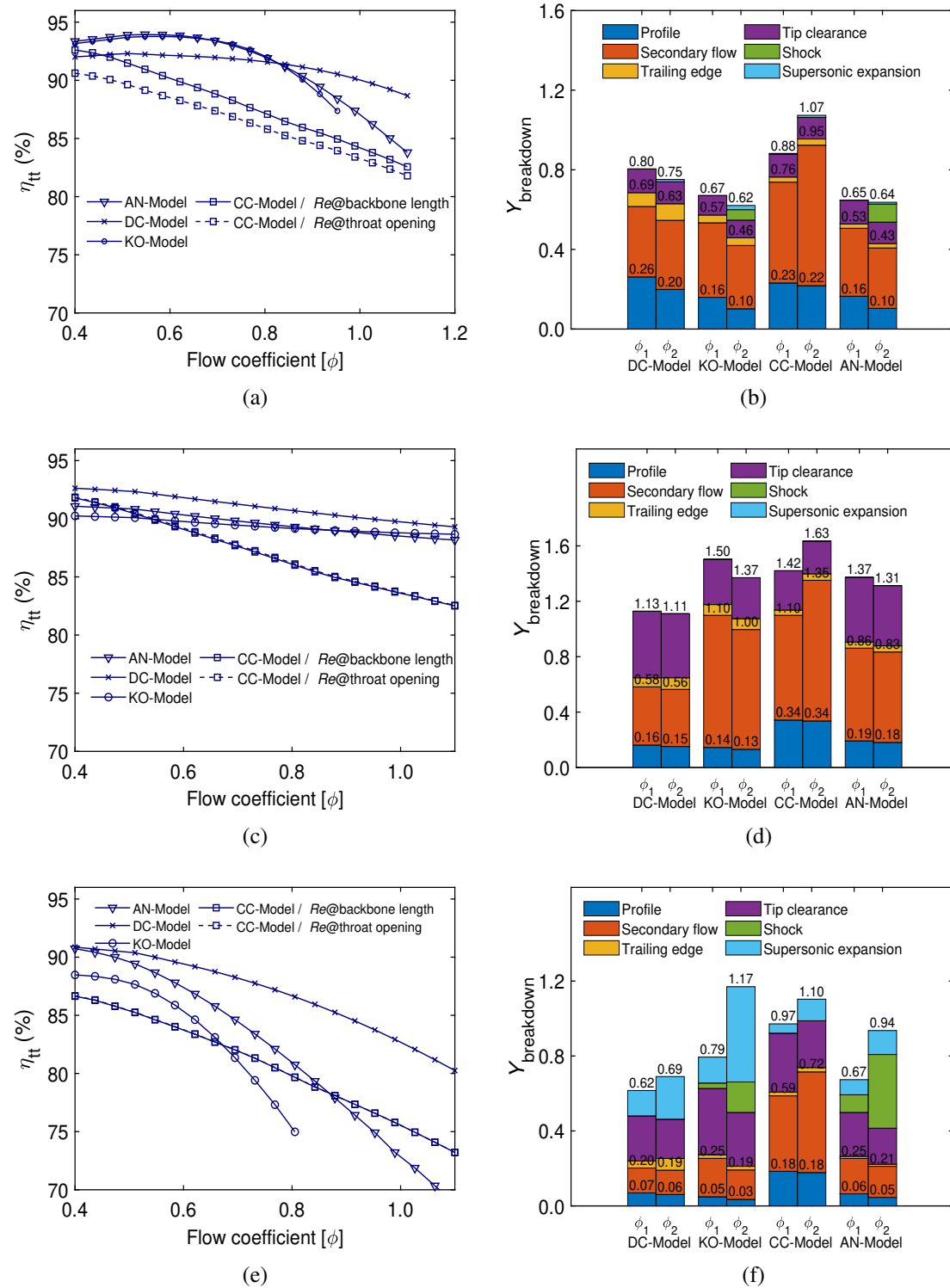
Figure 4.1: Flow coefficient [ϕ] versus the total-to-total efficiency [η_{tt}] and pressure loss coefficient [Y] breakdown at flow coefficients ϕ_1 and ϕ_2 of 0.5 and 0.7 respectively for **(a,b)** 100 MW air turbine, **(c,d)** 100 MW sCO$_2$ turbine, **(e,f)** 1 MW ORC turbine.

ity effects, denoted $\overline{Y_p}$ & $\overline{Y_s}$ respectively, are presented for the various models in Figures 4.2a and 4.2b. The CC model over-predicts $\overline{Y_s}$ compared to AN, KO and DC models at the optimum design point for the 100 MW air turbine as shown in Figure 4.2a. Furthermore, different trends are obtained for $\overline{Y_s}$ with increasing the flow coefficient over the specified range. To explain this, it is useful to recall the methodology used by the loss models to estimate the secondary flow losses. The AM model [63], and hence the DC, KO and AN models obtain $\overline{Y_s}$ as a function of lift coefficient and flow angles. In principle, turbine blades with small flow coefficients generally have large deflection angles [154], and hence increasing the flow coefficient should result in less secondary flow losses based on the methodology used in the AN, KO and DC models. However, the CC model predicts the secondary flow losses based on the velocity ratio between the inlet and exit conditions (inlet/exit velocity) and lift coefficient; where the velocity ratio increases with increasing the flow coefficient. AM pointed out that the secondary flow definition is not appropriate for moderate or highly cambered blades [63]. Additionally, AM correlation was formulated for low blade turning and hence it might be questionable in this regard [155]. Nevertheless, based on the discussions presented in [60], both secondary and profile losses were found to be overly predicted by the CC model when tested by one of the researchers using cascade experimental data. Moreover, it has been stated that the DC model provides a better estimation for the secondary flow losses taking into account the upstream boundary layer thickness [60].

Profile loss predictions ($\overline{Y_p}$) for the 100-MW air turbine, excluding Reynolds number and compressibility correction factors, are presented in Figure 4.2b. Though all the models predict the same decreasing trend with increasing the flow coefficient, it is observed that the CC model over-estimates $\overline{Y_p}$ with respect to DC, KO and AN models at a flow coefficient greater than 0.51. From the literature, the DC model has been found to over-estimate the overall $\overline{Y_p}$ and thus the $2/3$ factor added by AN and KO was found to result in more realistic efficiencies [155]. This explains the differences between loss distributions by AN, KO and DC models as presented in Figure 4.1b.

Given that profile and secondary flow losses, as presented in Figure 4.1b, are obtained
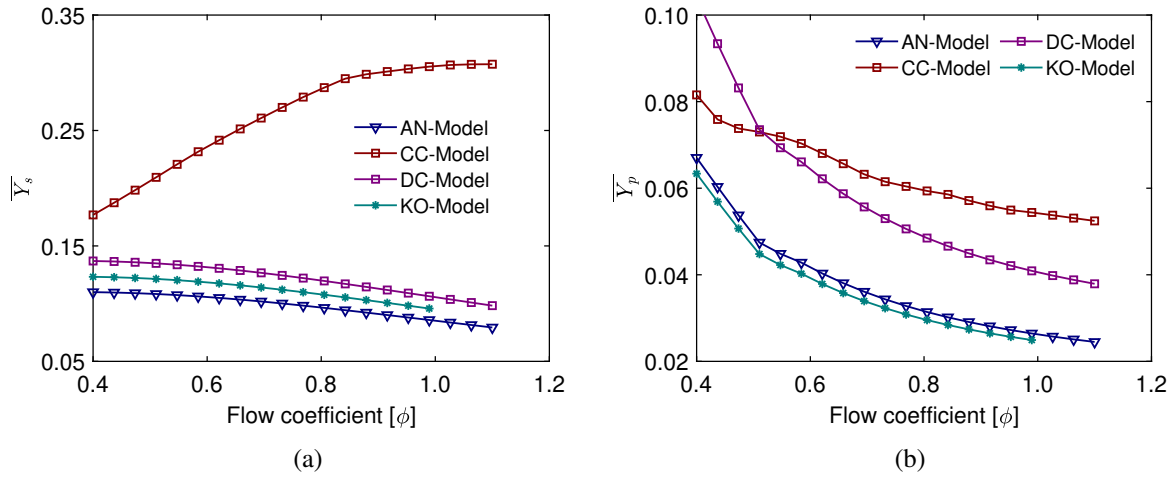
Figure 4.2: Flow coefficient versus (**a**) the preliminary secondary flow pressure loss coefficient $[Y]$ for the 1st stage of 100 MW air turbine (**b**) the preliminary profile loss pressure loss coefficient $[Y]$ for the 1st stage of 100 MW air turbine. **preliminary secondary flow and profile losses stands for the losses excluding both Reynolds number and compressibility effects

Table 4.2: Loss breakdown for air and sCO_2 and ORC turbines at flow coefficients $[\phi_1]$ and $[\phi_2]$ of 0.5 and 0.7 respectively.

	Parameter	Flow coefficient $[\phi_1] = 0.5$				Flow coefficient $[\phi_2] = 0.7$			
		DC	KO	CC	AN	DC	KO	CC	AN
100 MW air	Y_p	0.26	0.16	0.23	0.17	0.20	0.10	0.22	0.10
	Y_s	0.35	0.37	0.51	0.34	0.35	0.32	0.70	0.30
	Y_{TE}	0.07	0.04	0.03	0.02	0.08	0.04	0.03	0.02
	Y_{cl}	0.12	0.10	0.12	0.12	0.11	0.09	0.11	0.11
	Y_{shock}	0.00	0.00	0 .00	0.00	0.00	0.05	0.00	0.09
	Y_{PE}	0.00	0.00	0.00	0.00	0.01	0.02	0.01	0.01
100 MW CO_2	Y_p	0.16	0.14	0.34	0.19	0.15	0.13	0.34	0.18
	Y_s	0.42	0.95	0.76	0.67	0.41	0.87	1.02	0.65
	Y_{TE}	0.07	0.08	0.04	0.04	0.08	0.08	0.05	0.04
	Y_{cl}	0.48	0.33	0.28	0.47	0.46	0.30	0.24	0.44
1 MW ORC	Y_p	0.07	0.05	0.18	0.06	0.06	0.03	0.18	0.05
	Y_s	0.13	0.21	0.40	0.19	0.13	0.16	0.54	0.17
	Y_{TE}	0.04	0.02	0.02	0.01	0.06	0.02	0.02	0.01
	Y_{cl}	0.24	0.35	0.32	0.23	0.21	0.29	0.25	0.19
	Y_{shock}	0.00	0.03	0.00	0.09	0.00	0.16	0.00	0.39
	Y_{PE}	0.14	0.14	0.05	0.08	0.23	0.51	0.12	0.13

by considering Reynolds number effects, the Reynolds number correction factor (K_{Re}) obtained by the loss models are investigated separately. Reynolds number correction factors are obtained by both AN, hence KO and DC, and CC models based on the chord length

and backbone length respectively as shown in Figure 4.3. Using the backbone length instead of the chord length results in a varying range of Re compared to the AN model for the 100 MW air turbine; specifically, the Re varies between 2.7 and 6.0×10^5 for the CC model compared to a range of 2.1 and 3.9×10^5 for the AN model. Furthermore, the AN and KO models define the critical Re in the region of $1 \times 10^5 < Re < 5 \times 10^5$ and $2 \times 10^5 < Re < 1 \times 10^6$ respectively where the K_{Re} is equivalent to 1.00, while in the CC model the Reynolds number range results in a reduction in the correction factor from 0.85 to 0.68, as shown in Figure 4.3a. This results in a reduction in the overall profile and secondary flow losses by the same factor. As for the DC model, close K_{Re} are obtained with respect to both KO and AN models. The change in the preliminary profile and secondary
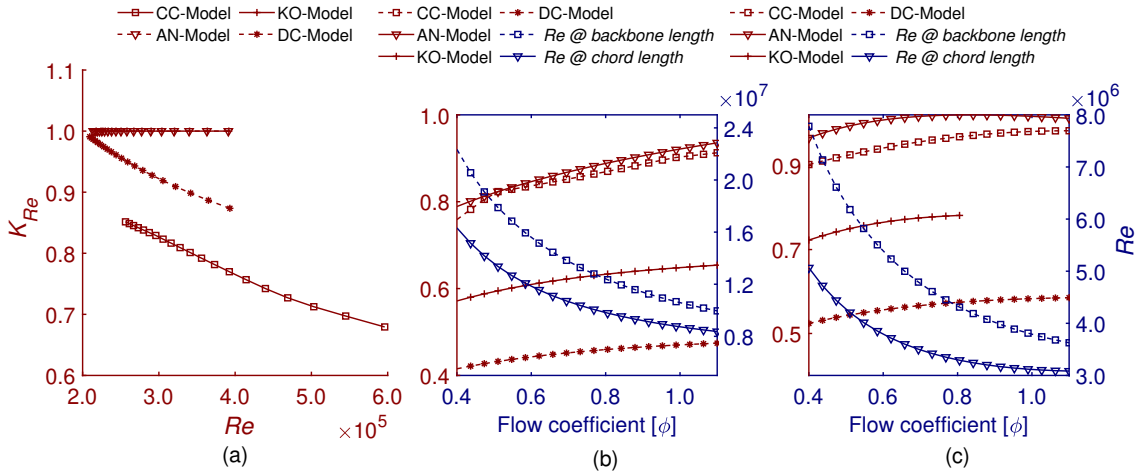
Figure 4.3: **(a)** Reynolds number $[Re]$ versus Reynolds number correction factor $[K_{Re}]$ for the 1st stage of the 100 MW air turbine, flow coefficient versus $[Re]$ and $[K_{Re}]$ for the 1st stage of **(b)** 100 MW sCO$_2$ turbine **(c)** 1 MW ORC turbine.

flow losses over the flow coefficient range is independent of the working fluid properties and hence, profile and secondary flow losses of the non-conventional working fluids experience the same increasing trends reported for the air turbine case (Figures 4.2a and 4.2b). Considering that the 1st stage of the sCO$_2$ turbine is developed at a pitch-to-chord (s/c) ratio of 0.8, compared to 1.1 for both air and ORC turbines, the CC model results in secondary flow losses' predictions closer to the other loss models for the sCO$_2$ turbine compared to the reported air case (Figure 4.2a); while holding the same increasing trends over the flow coefficient range as in the air and ORC turbines' cases. This shows the high sensitivity of the CC model to increasing the s/c ratio and this effect will be discussed in

detail later in Section 4.3.6.

On the contrary, the correction factors introduced for Reynolds number and compressibility effects vary significantly with the working fluid thermodynamic properties. Calculating Re based on the throat opening, for both working fluids, does not result in diverse results from those obtained by estimating the Reynolds number based on the backbone length. At the turbine inlet conditions, the density of R1233zd and sCO$_2$ fluids is 138 and 116 times the density of air and hence Re is in excess of 10^6, where a constant correction factor is obtained in the turbulent flow region for the same surface roughness to characteristic length ratio (chord/backbone length). However, the surface roughness (k_s) to characteristic length ratio is a significant parameter in controlling the boundary layer thickness for turbulent flow regimes and hence it should be considered while estimating the losses for high Re cases. This effect is considered in both AN and CC models where K_{Re} are estimated as a function of the roughness to chord and backbone length ratios respectively.

The Reynolds numbers estimated based on the backbone length (b) and the chord length (c), and corresponding correction factors are plotted against the flow coefficient for the 100.0 MW sCO$_2$ turbine as shown in Figure 4.3b. The AN model results in higher K_{Re} due to the higher (k_s/c) ratio obtained with the smaller characteristic length (chord). Over a flow coefficient range from 0.4 to 1.1, the Reynolds number varies between 2.2×10^7 and 9.9×10^6 for the CC model compared to a range of 1.6×10^7 to 8.4×10^6 for the AN model. Thus, a maximum K_{Re} of 0.94 is obtained for the AN model compared to 0.91 for the CC model. It is worth emphasising that using the throat opening in the CC model results in the same correction factors with smaller Reynolds number values; it ranges between 4.8 to 5.1×10^6 for the sCO$_2$ turbine.

Similar behaviour has been observed for the ORC turbine with higher K_{Re} due to the larger roughness to characteristic length ratio; the ORC turbine reaches a maximum backbone and chord length of 20 and 13 mm respectively in comparison to 51 and 37 mm respectively for the sCO$_2$ turbine. The Reynolds number varies between 7.8 and 3.6×10^6 for the CC model compared to varying from 5.1 to 3.1×10^6 for the AN model. The

smaller backbone length for the ORC turbine, compared to the sCO_2, results in a higher roughness to backbone length ratio and hence higher K_{Re} in the AN model with minimum and maximum values of 0.97 and 1.01 over the flow coefficient range. Using the throat opening in the CC model results in the same correction factors with Re number varying between 2.1 to 2.4×10^6 for the ORC turbine.

In the same context, the DC model results in large efficiencies in comparison to the rest of the models for both the ORC and sCO_2 turbines (Figures 4.1c to 4.1e). The high density of both fluids results in Reynolds numbers in the range of 10^6 compared to 10^5 for air turbines. The DC model implements the same Reynolds number correction factor introduced by AM for machines operating at an average Re of 2×10^5, and also ignores surface roughness effects. Hence, small correction factors are obtained for both sCO_2 and ORC turbines as indicated in Figures 4.3b and 4.3c.

The effect of fluid compressibility on profile and secondary flow losses, discussed in Section 4.2, is considered in both the AN and KO models. However, the CC and DC models were originally derived for low Mach number machines and hence this effect was ignored. The fluid compressibility correction factor ($K_{compressibility}$) is obtained using the AN and KO models for the three working fluids as shown in Figure 4.4a. The ORC turbine experiences the highest compressibility effect, which results in the largest reduction in both profile and secondary flow losses with respect to the air and sCO_2 turbines owing to the high inlet Mach number. Following the ORC turbine, the air turbine experiences the second highest compressibility effect owing to the higher Mach number at the blade inlet condition compared to sCO_2 turbine. For all working fluids, increasing the flow coefficient increases the compressibility effect which results in a smaller correction factor. At the turbine inlet conditions, the compressibility factor of the sCO_2 and ORC turbines is equivalent to 1.05 and 0.59 respectively compared to 1.00 in the air turbine.

In addition to the former effects, fluid compressibility may also result in shock losses at the leading edge of both stator and rotor blades, while supersonic expansion at the discharge of blade row could introduce supersonic expansion losses [156]. In light of the fact that sCO_2 cycles operate at low pressure ratios, and hence low expansion ratios, compared
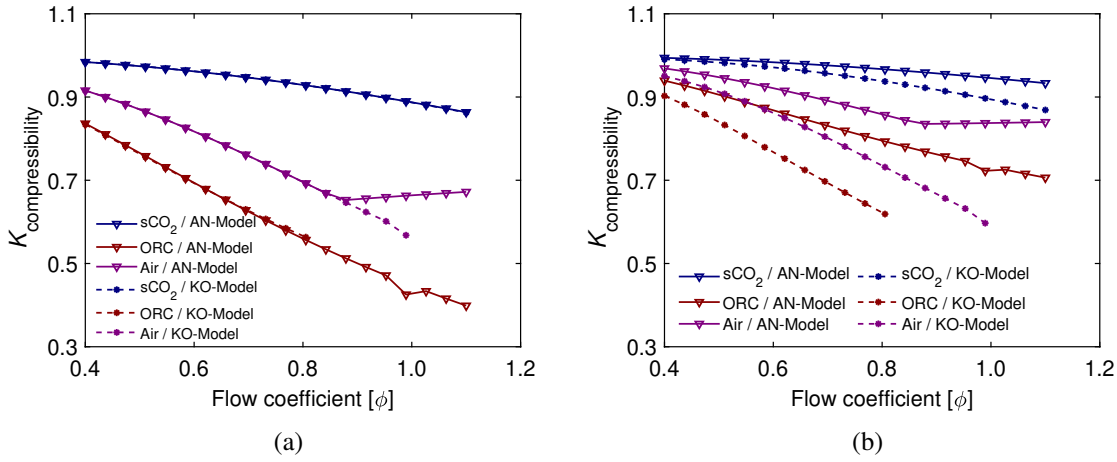
Figure 4.4: Flow coefficient $[\phi]$ versus compressibility correction factor $[K]$ for the 1st stage of large scale air, sCO$_2$ and ORC turbines by AN and KO models for (a) profile loss (b) secondary flow loss.

to the ORC and air turbines, it is not unexpected that they have the lowest Mach numbers at both the inlet and outlet of the blade row. Thus, they are less susceptible to the presence of shock and supersonic expansion losses at the leading edge and discharge of the blade row respectively. On the contrary, the discrepancy between the CC, DC and KO and AN loss models increases with increasing ϕ for the air and ORC cases owing to the possible presence of shock losses. It should be noted that the AN model predicts larger shock losses occurring at the leading edge compared to KO model as shown in (Figures 4.1b and 4.1f). Since the DC and CC models do not account for shock losses, these models result in a different rate of efficiency decrease with increasing flow coefficient compared to both the KO and AN models for both the air and ORC turbines (Figures 4.1a and 4.1e). In addition to the shock losses occurring at the blade leading edge, reaching sonic flow conditions within the blade row also results in the generation of a normal shock wave at the trailing edge which leads to higher aerodynamic losses. The ORC turbine is found to experience large supersonic expansion losses and it is observed that extremely large losses are predicted by the KO model (Figure 4.1f) if the supersonic expansion factor recommended by DC is applied to the KO model. Consequently, the KO model fails for the ORC turbine after exceeding a flow coefficient of 0.8 owing to the over-prediction of the supersonic expansion loss.

As for the clearance loss predictions, KO found that the DC loss model over-predicted

the clearance losses for unshrouded blades and hence KO correlation resulted in less tip clearance loss in the air turbine compared to the other loss models. Ultimately, similar tip clearance loss predictions are obtained for the air turbine; specifically a tip clearance pressure loss coefficient of 0.11, 0.10, 0.12 and 0.12 is predicted for the air turbine by the DC, KO, CC and AN models respectively. Slight differences are obtained for the sCO_2 turbine where pressure loss coefficients of 0.48, 0.33, 0.28 and 0.48 are predicted by the DC, KO, CC and AN model respectively. Similarly, pressure loss coefficients of 0.24, 0.35, 0.32 and 0.24 are predicted by the DC, KO, CC and AN model respectively for the ORC turbine.

Owing to the significant differences in geometries obtained for the sCO_2 and ORC turbines compared to the air turbines, different loss contributions are obtained for the non-conventional working fluids. In the 100 MW air turbine, secondary flow loss is the key loss mechanism at ϕ_1, contributing to the largest loss percentage of the total aerodynamic losses, followed by profile loss and tip clearance loss; contributing with 53%, 25% and 18% respectively as predicted by AN model (Figure 4.1b). The other loss models including DC, KO and CC resulted in the same key loss mechanisms. However, different loss distributions are obtained based the discussions provided earlier.

Based on AN model predictions, for the same turbine scale operating with sCO_2, the secondary flow loss contributes to the highest loss percentage (49%) followed by the tip clearance (34%) and profile loss (14%). Comparatively, for the ORC turbine (Fig 4.1f), tip clearance loss was found to contribute to the highest percentage (35%) followed by secondary flow, shock loss and supersonic expansion and profile loss accounting for 28%, 14%, 12% and 10% respectively. For both the sCO_2 and ORC turbines, the DC and KO models resulted in the same key loss mechanisms predicted by the AN model at the design point of ϕ_1. However, the CC model predicts a larger contribution from secondary and profile losses and a lower contribution from tip clearance losses.

Consequently, the key loss mechanism changes with the working fluid and the implemented loss model. At the optimum aerodynamic design condition (ϕ_1), a total-to-total turbine efficiency of 93.8%, 90.9% and 89.6% is achieved for the air, sCO_2 and ORC tur-

bines respectively, as predicted by AN model. The 100.0 MW air turbine achieves higher total-to-total efficiency compared to sCO_2 turbine of the same scale. This is due to the smaller enthalpy drop across the sCO_2 turbine that results in a smaller specific speed for the same rotational speed (0.27 for air compared to 0.13 for sCO_2). The smaller enthalpy drop is due to a pressure ratio of 2.5 compared to 23.0 for the air turbine. Furthermore, the specified 0.4 mm clearance gap in the sCO_2 turbine results in clearance losses that are at least 3.0 times greater than the air turbine. Air turbines have the largest chord length of the three fluids considered. Smaller chord lengths and blade geometries, as obtained for both the ORC and sCO_2 turbines, result in high clearance loss across the turbine blades, since, for a fixed tip clearance gap of 0.4 mm, the relative clearance gap increases. For all loss models, tip clearance losses contribute by a larger percentage in both sCO_2 and ORC turbines in comparison to the air turbine.

Operating at a high flow coefficient (ϕ_2) results in slight reductions in profile losses for all models. However, it results in contradicting effects for the secondary flow losses; an increasing trend is predicted by the CC model, while a decreasing trend is predicted by the other loss models. Increasing the flow coefficient in the ORC turbine increases both shock and supersonic expansion losses (Figure 4.1f). This is due to the high Mach number experienced for ORC machines due to the large expansion ratio experienced across the turbine expansion stage alongside the low speed of sound. For the air turbine, increasing the flow coefficient from 0.5 to 0.7 results in a total aerodynamic loss change of 6%, 8%, 22% and 2% for the DC, KO, CC and AN models respectively. Likewise, the same increase in the flow coefficient results in a total aerodynamic loss change of 2%, 9%, 15% and 4% for the DC, KO, CC and AN models respectively for the sCO_2 turbine. The ORC turbine experiences the highest sensitivity to changing the flow coefficient compared to both air and sCO_2 turbines due to the increasing shock and supersonic expansion losses; the total aerodynamic losses change by 11%, 48%, 13% and 40% for the DC, KO, CC and AN models respectively.

4.3.2   Large scale designs across a range of loading coefficients

To examine the prediction capability of the various loss models over a range of loading coefficients, ψ has been varied from 0.80 to 2.50, whilst ϕ, Λ and t/o are held constant at 0.50, 0.50, and 0.05 respectively. The total-to-total efficiency is predicted for large-scale axial turbines over the loading coefficient range for air, sCO$_2$ and ORC applications as shown in Figures 4.5a to 4.5e. The plots are further supported with the loss breakdown predicted by the DC, KO, CC and AN loss models at ψ_1 and ψ_2 of 1 and 2 respectively (see Table 4.3); ψ_1 is the optimum design point while ψ_2 is selected to depict the changes in loss breakdown predicted by the various loss models at a higher loading coefficient.

Increasing ψ over the specified range results in an increase in both profile and secondary flow losses with respect to the basic case-study (ψ_1) as shown in Figures 4.5a to 4.5e. Secondary flow losses are estimated as a function of the lift coefficient in all loss models where turbine designs with a higher stage loading coefficient experience higher lift coefficients, and hence higher secondary flow losses. Increasing ψ results in a higher change in the whirl velocity components across the blade row and hence result in higher profile losses [155]. The change in the preliminary secondary flow losses ($\overline{Y_s}$), excluding both Reynolds number correction factor and compressibility effects, with respect to the loading coefficient over the specified range is shown in Figure 4.6 for air, sCO$_2$ and ORC turbines. For the sCO$_2$ turbine case, the CC model over-predicts $\overline{Y_s}$ with respect to the AN model until a loading coefficient of 1.24 and then the AN model predicts higher the losses than the CC model until a maximum loading coefficient of 2.50 as shown in Figure 4.6b. According to Coul et al. [155] the CC model under-predicts the rise in secondary flow losses with lift. Nonetheless, the predictions for $\overline{Y_s}$ is different for both air and ORC turbines as indicated in Figures 4.6a and 4.6c. This is due to the CC model sensitivity to increasing the pitch-to-chord ratio where the 1$^{\text{st}}$ stage of both air and ORC turbines is designed at a s/c ratio of 1.1 compared to 0.8 in the sCO$_2$ turbine; further details about the CC model sensitivity increasing the s/c ratio will be discussed later in Section 4.3.6.

The change in profile loss ($\overline{Y_p}$), excluding both Reynolds number correction factor and

(a)

(b)

(c)

(d)

(e)

(f)

Figure 4.5: Loading coefficient $[\psi]$ versus total-total efficiency $[\eta_{tt}]$ and the pressure loss coefficient $[Y]$ breakdown at loading coefficients ψ_1 and ψ_2 of 1 and 2 respectively for **(a, b)** 100 MW air turbine, **(c, d)** 100 MW sCO$_2$ turbine, **(e, f)** 1 MW ORC turbine.

compressibility effects, with respect to increasing the loading coefficients is reported in Figure 4.7 for the DC, CC and AN loss models over a varying loading coefficient from 0.80 to 2.50. The KO and AN model results in the lowest $\overline{Y_p}$ with increasing loading coefficient for the ORC turbine (Figure 4.7c); as mentioned earlier (Section 4.3.1), the AN model and KO applies a correction factor $(2/3)$ to the DC model which results in less overall profile loss. Meanwhile, at a high loading coefficient, the CC model predicts lower $\overline{Y_p}$ than the AN and KO models for both air and sCO_2 turbines. However, at ψ less than 1.70, different predictions are obtained with the CC model predicting high profile losses and similar to the $\overline{Y_s}$ predictions, the results are slightly different for both air and ORC turbines as shown in Figure 4.7.

Table 4.3: Loss breakdown for air and sCO_2 and ORC turbines at loading coefficients $[\psi_1]$ and $[\psi_2]$ of 1.0 and 2.0 respectively.

| | Parameter | Loading coefficient $[\psi_1]$ of 1.0 | | | | Loading coefficient $[\psi_2]$ of 2.0 | | | |
		DC	KO	CC	Aungier	DC	KO	CC	Aungier
100 MW Air	Y_p	0.26	0.16	0.23	0.16	0.64	0.42	0.31	0.43
	Y_s	0.35	0.37	0.51	0.34	0.57	0.69	0.55	0.60
	Y_{TE}	0.07	0.04	0.03	0.02	0.1	0.04	0.03	0.02
	Y_{cl}	0.12	0.10	0.12	0.12	0.13	0.07	0.06	0.13
	Y_{shock}	0.00	0.00	0 .00	0.00	0.00	0.02	0.00	0.03
	Y_{PE}	0.00	0.00	0.00	0.00	0.00	0.00	0.03	0.00
100 MW CO_2	Y_p	0.16	0.15	0.34	0.19	0.43	0.38	0.43	0.52
	Y_s	0.42	0.95	0.76	0.67	0.72	1.85	0.87	1.11
	Y_{TE}	0.07	0.08	0.04	0.04	0.09	0.07	0.03	0.04
	Y_k	0.48	0.33	0.28	0.47				
1 MW ORC	Y_p	0.07	0.05	0.18	0.065	0.15	0.10	0.24	0.14
	Y_s	0.13	0.21	0.40	0.19	0.20	0.36	0.42	0.28
	Y_{TE}	0.04	0.02	0.02	0.01	0.04	0.02	0.02	0.01
	Y_{cl}	0.24	0.35	0.32	0.23	0.26	0.29	0.08	0.27
	Y_{shock}	0.00	0.03	0.00	0.09	0.00	0.08	0.00	0.16
	Y_{PE}	0.14	0.14	0.05	0.08	0.20	0.17	0.03	0.06

The Reynolds number correction factors (K_{Re}) estimated by the four loss models are presented in Figure 4.8; where results similar to Figure 4.3 are obtained, but an increasing trend is obtained for the Reynolds number over the loading coefficient range. In the 100 MW air turbine, different Reynolds number correction factors and flow regimes are obtained by the DC, KO, AN and CC models over the loading coefficient range (Fig-
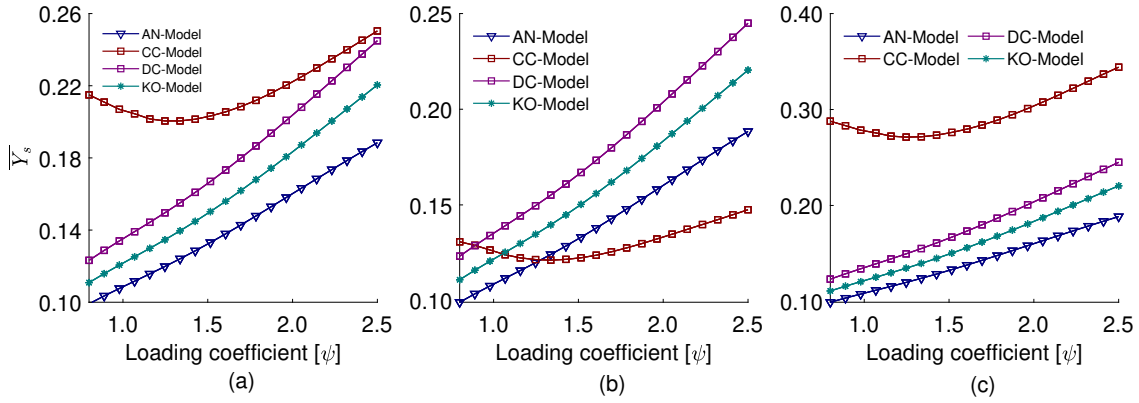
Figure 4.6: Loading coefficient $[\psi]$ versus the preliminary secondary flow pressure loss coefficient $[Y]$ for the the 1st stage of **(a)** 100 MW air turbine **(b)** 100 MW sCO$_2$ turbine **(c)** 1 MW ORC turbine.
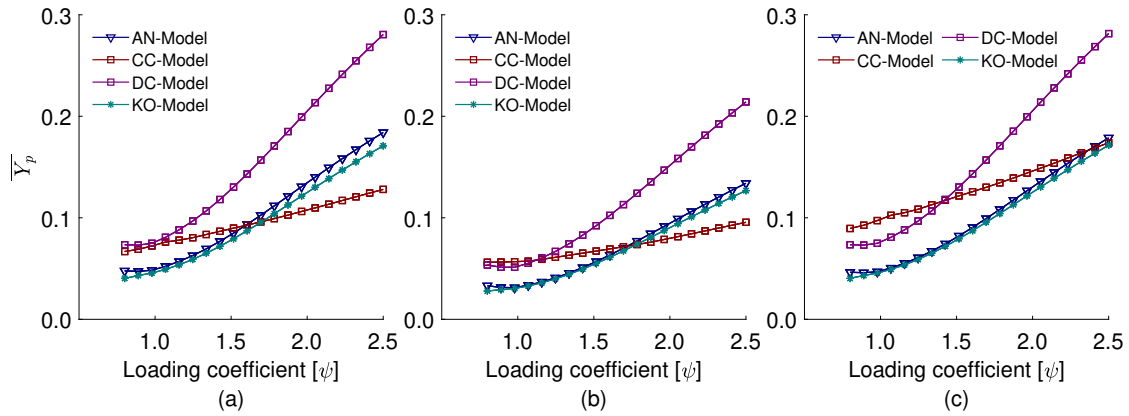
Figure 4.7: Loading coefficient $[\psi]$ versus the preliminary profile pressure loss coefficient for the 1st stage of **(a)** 100 MW air turbine **(b)** 100 MW sCO$_2$ turbine **(c)** 1 MW ORC turbine.

ure 4.8a); K_{Re} ranging from 0.89 to 1.00 is estimated by AN model compared to a factor ranging between 0.59 and 0.79 for the CC model which is due to the difference in the defined transition region. Increasing ψ for the sCO$_2$ turbine results in larger blade heights and hence larger chord and backbone lengths where the roughness effect becomes less pronounced; this is due to achieving low surface roughness to characteristic length ratio, as shown in Figure 4.8b, compared to operating at high flow coefficients (Figure 4.3b). In both the CC and AN, and hence DC and KO, models K_{Re} decreases as the loading co-efficient increases. The Reynolds number varies between 1.5 and 4.9×10^7 for the CC model compared to varying between 1.1 and 3.6×10^7 for the AN model. This results in maximum and minimum correction factors of 0.84 and 0.63 for the CC model and 0.85

and 0.69 for the AN model. Similar behaviour is obtained for ORC turbines where the CC model results in a Reynolds number ranging from 5.2×10^6 to 1.8×10^7 in comparison to varying from 3.6×10^6 to 1.1×10^7 for the AN model. Similar conclusions can be drawn for the DC model predictions at high Reynolds number cases (Figures 4.5c and 4.5e) as discussed earlier in the flow coefficient case (Section 4.3.1).

Figure 4.8: (**a**) Reynolds number $[Re]$ versus Reynolds number correction factor $[K_{Re}]$ for the 1st stage of 100 MW air turbine over a range of loading coefficients, loading coefficient versus $[Re]$ and $[K_{Re}]$ for the 1st stage of (**b**) 100 MW sCO$_2$ turbine (**c**) 1 MW ORC turbine.

The loss breakdown for each working fluid is presented in Figures 4.5b to 4.5f, for large scale turbines operating at ψ_1 and ψ_2 of 1 and 2 respectively. For the air turbine, increasing the loading coefficient from 1 to 2 results in a relative change in total aerodynamic losses of 79%, 85%, 11% and 86% as predicted by the DC, KO, CC and AN models respectively. For the sCO$_2$ turbine, the same increase in loading coefficient results in a total aerodynamic loss change of 56%, 70%, 1% and 60%, for the DC, KO, CC and AN models respectively. Similarly, a total aerodynamic loss change of 37%, 29 %, 19% and 36% for the ORC turbine is predicted by the DC, KO, CC and AN models respectively. Thus, all loss models suggest that the air turbine is more sensitive to the loading coefficient in comparison to the sCO$_2$ and ORC turbines. Additionally, for all three fluids, the CC model appears to be the least sensitive to changes in the loading coefficient.

4.3.3   Tip clearance loss for small-scale designs

Given that clearance losses are likely to contribute more significantly in small-scale tur-
bines than in large-scale designs, this section pays particular attention to the clearance loss
predictions before examining the other loss mechanisms (profile and secondary flow, etc.).
In the current study, un-shrouded blades' design is considered for the developed turbines.
Hence, in this set of results, only three models are examined, namely, Kacker and Okapuu,
Craig and Cox and Aungier model. This is done since the Aungier implements the correla-
tion proposed by Dunham and Came for predicting the tip clearance losses for un-shrouded
blades.

The clearance loss model predictions are reported in Figure 4.9, where the tip clearance
pressure loss coefficient is plotted against the radial tip clearance gap (t_{cl}) to the rotor blade
average height (h) ratio. In view of the fact that all of the loss correlations were developed
for large-scale air turbines, where the standard clearance gap is around 1 to 2% of the
average blade height [157], these plots show the loss model correlations for a wider range
of clearance gap to blade height ratios that are relevant for a small-scale turbine design
assuming a clearance gap up to 0.4 mm [23].

For the small-scale air turbine design, Figure 4.9, the three models achieve very close
predictions up to a clearance gap to rotor blade height ratio of 4.0%. At higher relative
clearances, the models deviate significantly with large tip clearance loss coefficients being
predicted by both the KO and CC models with respect to the AN model. Similar con-
clusions can be drawn for the sCO$_2$ and ORC cases. Owing to the compactness of the
small-scale turbine design, the tip clearance losses are highly significant due to the large
clearance gap to blade height ratios. It can be concluded, from the presented results in Sec-
tion 4.3.1, that the KO and CC underestimate the tip clearance losses with respect to the
AN model for the 100-MW air turbine design. Nevertheless, applying the same models for
the 100 kW air turbine results in contradicting results to those obtained for the large-scale
turbine as shown in Figure 4.9a, with the KO model and CC models over-predicting the tip
clearance losses with respect to the AN model. Furthermore, the small-scale turbine de-

sign experiences a different range of the t_{cl}/h ratio owing to the compactness of the turbine design. ORC turbines experience the highest t_{cl}/h ratio (up to 33%) followed by air turbines (up to 22%) and sCO$_2$ (up to 14%) and hence, they experience high clearance losses compared the large-scale turbines. Due to the compactness of sCO$_2$ turbines in comparison to air turbines, it experienced smaller t_{cl}/h ratio due to the larger sCO$_2$ machine scale (300 kW compared to 100 kW air turbine). It is worth noting that these models estimate the tip clearance losses based on the turbine design geometry along with empirical constants that were obtained and verified for conventional and large-scale air turbines.
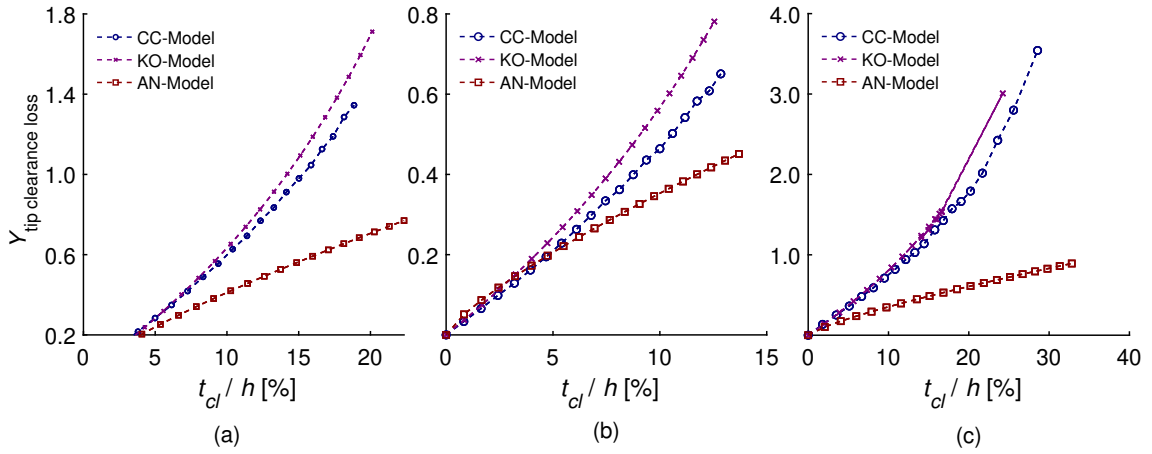
Figure 4.9: Tip clearance gap [t_{cl}] to rotor blade height [h] ratio versus tip clearance pressure loss coefficient [Y] for (**a**) 100 kW air turbine, (**b**) 300 kW sCO$_2$ turbine and (**c**) 10 kW ORC turbine.

4.3.4 Small scale designs across a range of flow coefficients

In this section, the loss models are compared for the small-scale turbines operating at the conditions specified in Table 4.1. Considering the results discussed in Section 4.3.3, it is worth noting that some of the models failed to converge due to very large relative clearance gaps. Thus, for this analysis clearance losses were neglected and hence significantly high efficiencies were obtained for all turbines. This allows a full investigation into the loss model predictions for small-scale air, sCO$_2$ and ORC turbines with power ratings of 100 kW, 300 kW and 10 kW respectively.

To investigate the loss model predictions across a range of flow coefficients, ϕ has

been varied between $0.4 - 1.1$ while ψ, Λ, t/o and has been set to 1.00, 0.50 and 0.05 respectively. The total-to-total efficiency is predicted for small-scale axial turbines over the flow coefficient range designed for air, sCO$_2$ and ORC applications as shown in Figure 4.10a to 4.10e. Furthermore, the loss breakdown is presented for the turbine design operating at ϕ_1 and ϕ_2 of 0.5 and 0.7 respectively.

Contrary to the large-scale air turbine, large discrepancies are obtained for the small-scale air turbine at both the optimum and off-optimum design points ($\psi = 1$ & $\phi = 2$) as shown in Figure 4.10a. The KO model results in the highest efficiency for the small air turbine among all the models due to predicting lower secondary flow losses (Figure 4.10b). This is due to ignoring the Reynolds number effect on the secondary flow losses. For the small-scale air turbine, the Reynolds number correction (K_{Re}) is more significant than for the large-scale air turbine since the Re in the order of 10^4 and thus the flow is more subjected to laminar boundary layer separations and more developed secondary flow at the end wall regions. Within the laminar flow regime, the AN model over-predicts K_{Re} with respect to the CC model in the Reynolds number region $Re < 10^5$. Therefore, over the flow coefficient range, the CC model results in a minimum and maximum Reynolds number correction factor of 1.4 and 1.8 respectively, compared to 2.2 and 3.0 for the AN model. Although the CC model results in lower K_{Re}, it results in the lowest overall efficiency since it predicts higher preliminary profile and secondary flow losses, excluding Reynolds number and compressibility effects, as discussed in Section 4.3.1.

Additionally, it is worth emphasising that the DC model implements the Reynolds number correction provided by AM model where the efficiency is corrected for Reynolds number by $(Re/2 \times 10^5)^{-0.2}$ and this correction holds until 5×10^4. So, operating at a Re lower than the specified limit will result in a rapid reduction in the efficiency compared to the actual values predicted by the model [63]. Consequently, the Reynolds number correction provided by the DC model is valid until the specified threshold limit is reached. For the sCO$_2$ turbine, the DC model predicts the highest efficiency due to the high Re experienced with sCO$_2$ machines. However, the situation is different for the ORC turbine where the DC model provides close predictions to the KO and AN models as a result of

operating closer to the average *Re* for which the correction factor was developed for.
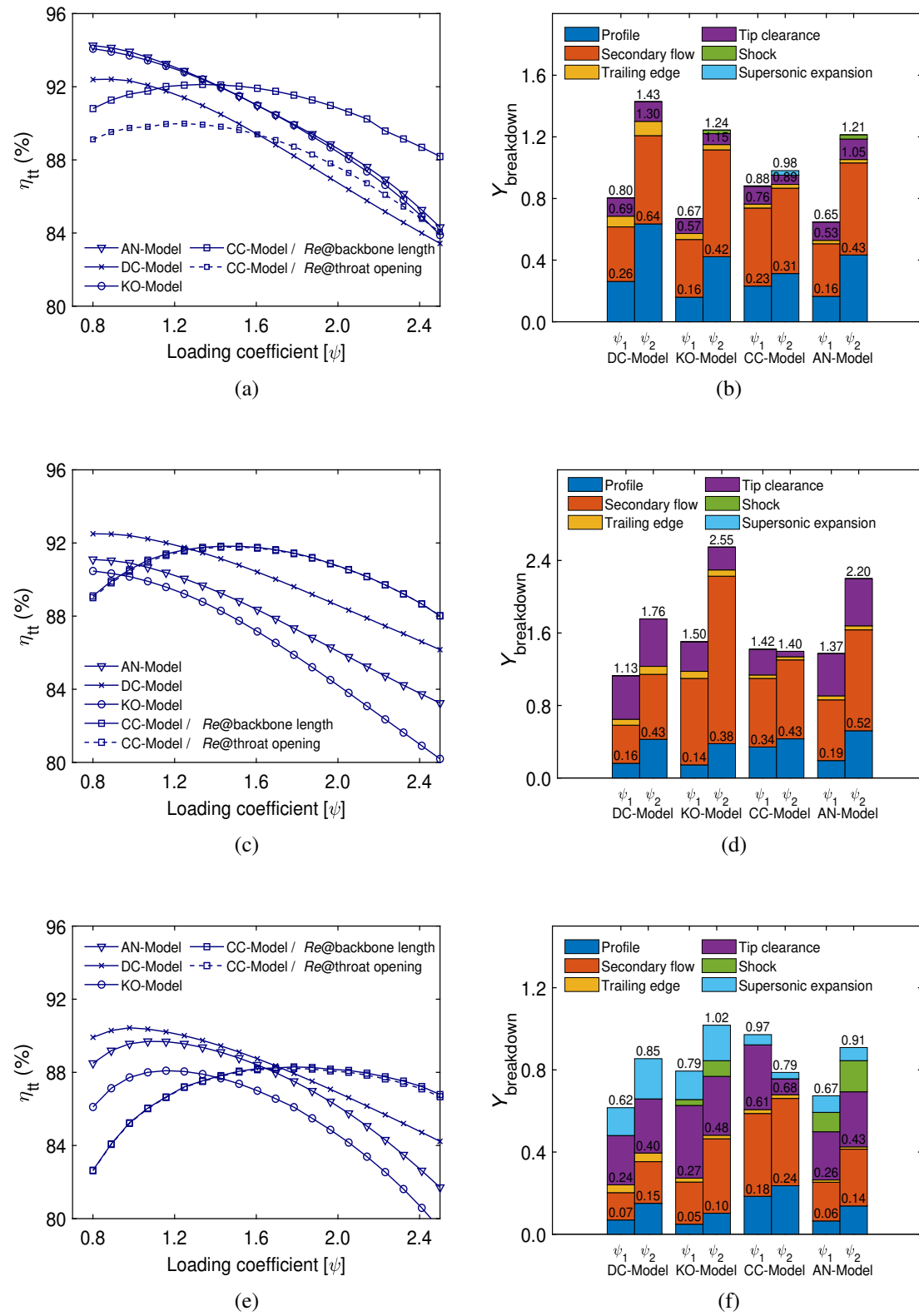

(a)

(b)

(c)

(d)

(e)

(f)
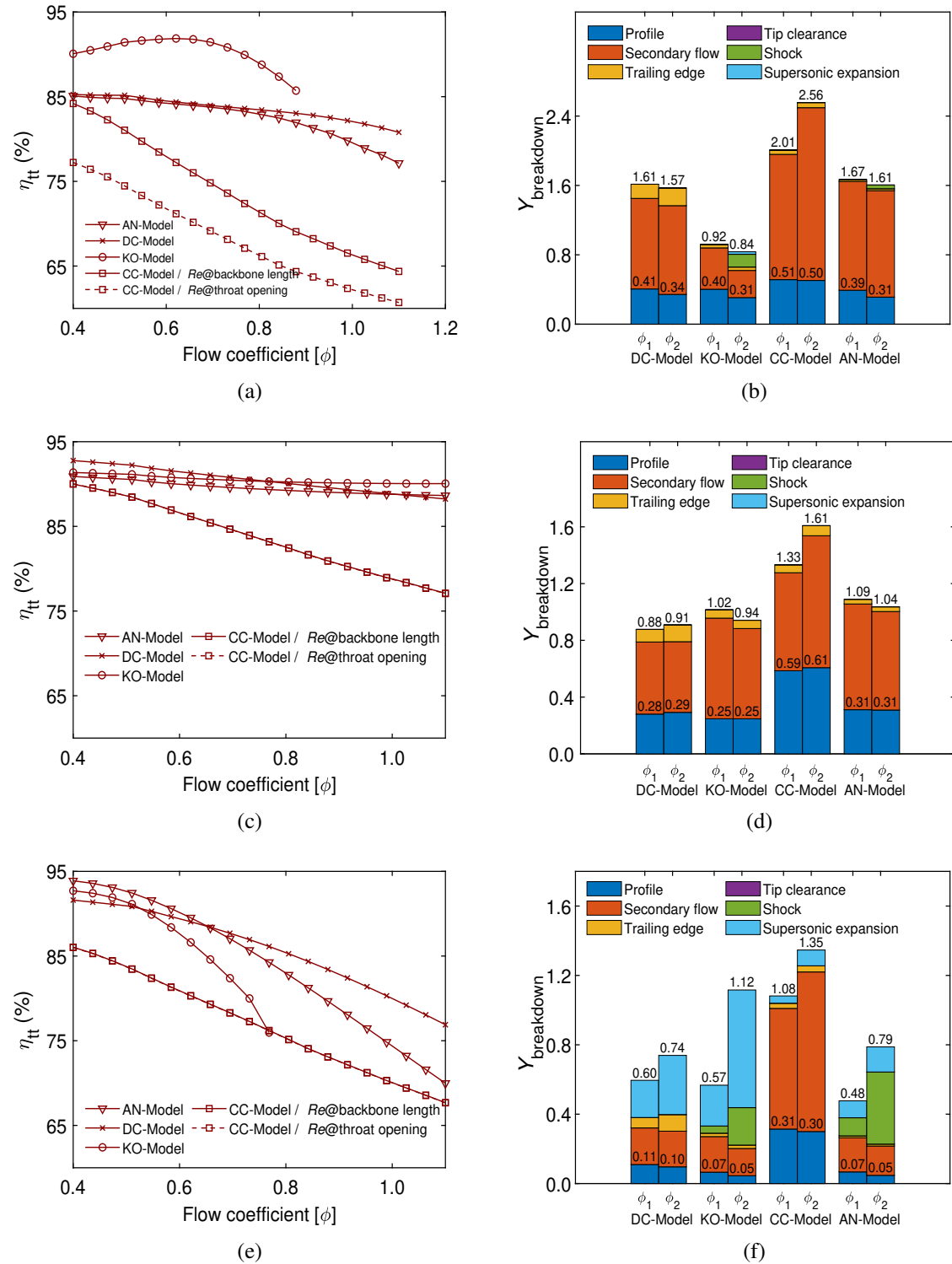
Figure 4.10: Flow coefficient $[\phi]$ versus total-to-total efficiency $[\eta_{tt}]$ and the pressure loss coefficient $[Y]$ breakdown at flow coefficients ϕ_1 and ϕ_2 of 0.5 and 0.7 respectively for **(a, b)** 100 kW air turbine **(c, d)** 300 kW sCO$_2$ turbine **(e, f)** 10 kW ORC turbine.

Despite the small geometry obtained for both the sCO_2 and ORC turbines, they both experience turbulent and transitional flow regimes owing to the high working fluid density. The CC model results in lower efficiencies compared to the other loss models for both ORC and sCO_2. The difference in the predictions of the CC model is due to the model over-predicting both the secondary flow and profile loss (as reported in Figures 4.2a and 4.2b. Although the CC model over predicts $\overline{Y_p}$ & $\overline{Y_s}$ for small scale turbine by the increment discussed in Section 4.3.1, the deviation between the CC model and the other loss models is larger in small scale designs. This is due to overestimating K_{Re} compared to the large-scale turbine (Figure 4.3) and hence, results in an increase in both profile and secondary by a larger factor.

For the characteristic of the flow regime effect, the small-scale ORC and sCO_2 turbines experience a similar behaviour to that experienced for the large-scale turbines, but with a greater effect of the surface roughness over the flow coefficient range from 0.4 to 1.1. The Reynolds number varies between 9.4×10^5 and 1.9×10^6 in the CC model, based on the backbone length, compared to 7.7×10^5 and 1.51×10^6 in the AN model as shown in Figure 4.11. Owing to the compact design geometries of small-scale turbines, the effect of the roughness is more pronounced than in large-scale turbines. Contrary to the large-scale turbine design case, the CC model over-predicts the Reynolds number correction factor compared to the AN model. A maximum K_{Re} of 1.65 is obtained for the small-scale sCO_2 turbine using the CC model, compared to 0.91 for the large-scale machine (Figure 4.3). In comparison, a maximum K_{Re} of 1.20 is obtained by the AN model for the small scale design. Given that the roughness effect is not considered in DC and KO models, both models resulted in small correction factors compared to both AN and CC models.

Compared to the small-scale sCO_2 turbine, the small-scale ORC turbine results in similar Reynolds number correction factors. Specifically, the Reynolds number varies between 3.7×10^5 and 7.9×10^5 in the CC model, based on the backbone length, compared to 3.1×10^5 and 5.1×10^5 in the AN model, and over the flow coefficient range the K_{Re} range between 1.56 and 1.77 for the CC model. The AN model results in a transition flow regime for the ORC turbine with a K_{Re} of 1.00 while in the CC model, the correction
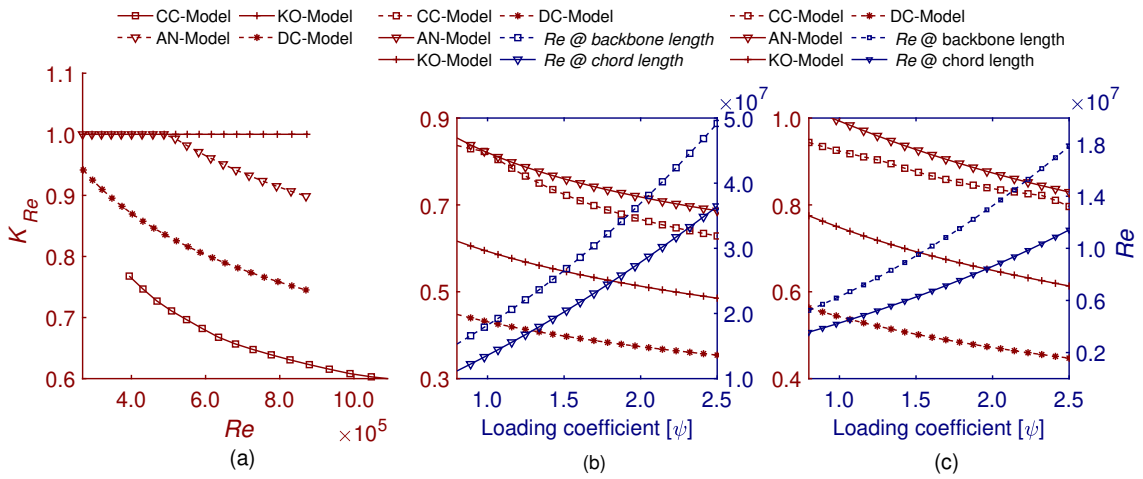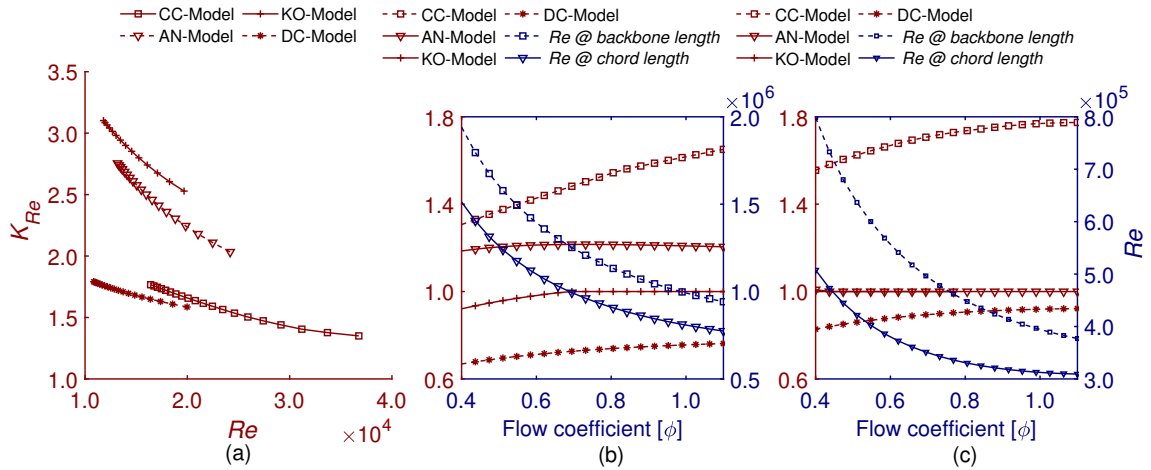
Figure 4.11: **(a)** Reynolds number $[Re]$ versus Reynolds number correction factor $[K_{Re}]$ for the 1st stage of the 100 kW air turbine, flow coefficient versus $[Re]$ and $[K_{Re}]$ for the 1st stage of **(b)** 300 kW sCO$_2$ turbine **(c)** 10 kW ORC turbine.

factor is higher due to the higher roughness effect. Given that shock losses are predominantly a function of expansion ratio and velocities, which are scale independent, similar conclusions are drawn for the shock and supersonic expansion losses experienced with the large-scale ORC turbine (Section.4.3.1).

The loss breakdown for each working fluid is presented in Figures 4.10b to 4.10f. For the air turbine, increasing the flow coefficient from 0.5 to 0.7 results in a total aerodynamic loss variation of 2%, 9%, 27% and 15% for the DC, KO, CC and AN models respectively. Likewise, the same increase in the flow coefficient for the sCO$_2$ turbine results in a total aerodynamic loss variation of 3%, 8%, 21% and4%, for the DC, KO, CC and AN models respectively. The ORC turbine experiences the highest sensitivity to changing the flow coefficient compared to both air and sCO$_2$ turbines due to the increasing shock and supersonic expansion losses; the total aerodynamic losses change by 23%, 96 %, 26% and 64% for the DC, KO, CC and AN models respectively.

4.3.5   Small scale designs across a range of loading coefficients

Similar to the large-scale turbines' analysis (Figures 4.5a to 4.5e), results are obtained for the small-scale turbines, at the same design conditions, over a loading coefficient range from 0.80 to 2.50. The total-to-total efficiency is predicted for over the loading coefficient

range for air, sCO$_2$ and ORC applications as shown in Figures 4.12a to 4.12e

Similar to the results presented in Section 4.3.4, the KO model predicts the highest efficiency for the 100 kW air turbine over the range, as shown in Figure 4.12a. This is due to the model ignoring the Reynolds number effect for the secondary flow loss where a laminar flow regime exists. Contrary to the large-scale designs, presented in Section 4.3.2, the CC model results in close efficiency predictions to the other loss models in the sCO$_2$ turbine and deviates significantly from the other loss models for the ORC turbine as shown in Figures 4.12c and 4.12e. Since the preliminary trends of both profile and secondary flow losses are independent of the machine scale, the same trends of both profile and secondary flow losses are obtained as in the large scale sCO$_2$ and ORC turbine presented in Figures 4.6 and 4.7. Therefore, the deviation in the CC model is due to the differences in predicting the Reynolds number effect. In the small-scale sCO$_2$ turbine design, the backbone length ranges from 2.6 to 8.3 mm in comparison to 33.0 to 106.5 mm for the large-scale turbine design. This results in higher surface roughness to backbone length ratio. Thus, the maximum Reynolds number correction factor increases from around 0.84, in the large-scale turbine design (Figure 4.8), to 1.43 in the CC model compared to an increase from 0.85, (Figure 4.8), to 1.20 in AN model. The Reynolds number ranges between 1.4×10^6 and 4.3×10^6 in the CC model compared to 1.0×10^6 and 3.4×10^6 in the AN model for the sCO$_2$ small scale turbine. Owing to the high Reynolds number in the sCO$_2$ turbine, the DC model predicts the highest efficiency as shown in Figure 4.12e.

Likewise, for the ORC turbine, the Reynolds number correction factor estimated by CC model reaches up to 1.7 owing to achieving a minimum backbone length of 1.4 mm while the AN model results in a lower effect for surface roughness due to the defined transition zone and the larger chord length. For the ORC turbine, the CC model predicts Reynolds number in the range of 5.4×10^5 to 1.8×10^6 compared to a range from 3.6×10^5 to 1.2×10^6 in AN model as shown in Figure 4.13. Based on AN surface roughness effect should be considered at Reynolds number greater than 5.0×10^5. Hence, the ORC turbine experiences transition flow at a low loading coefficient (< 1.2). Considering that the ORC turbine operates at Reynolds number less than the sCO$_2$ turbine, DC model results

in similar predictability to that obtained for the small-scale air turbine. This is due to
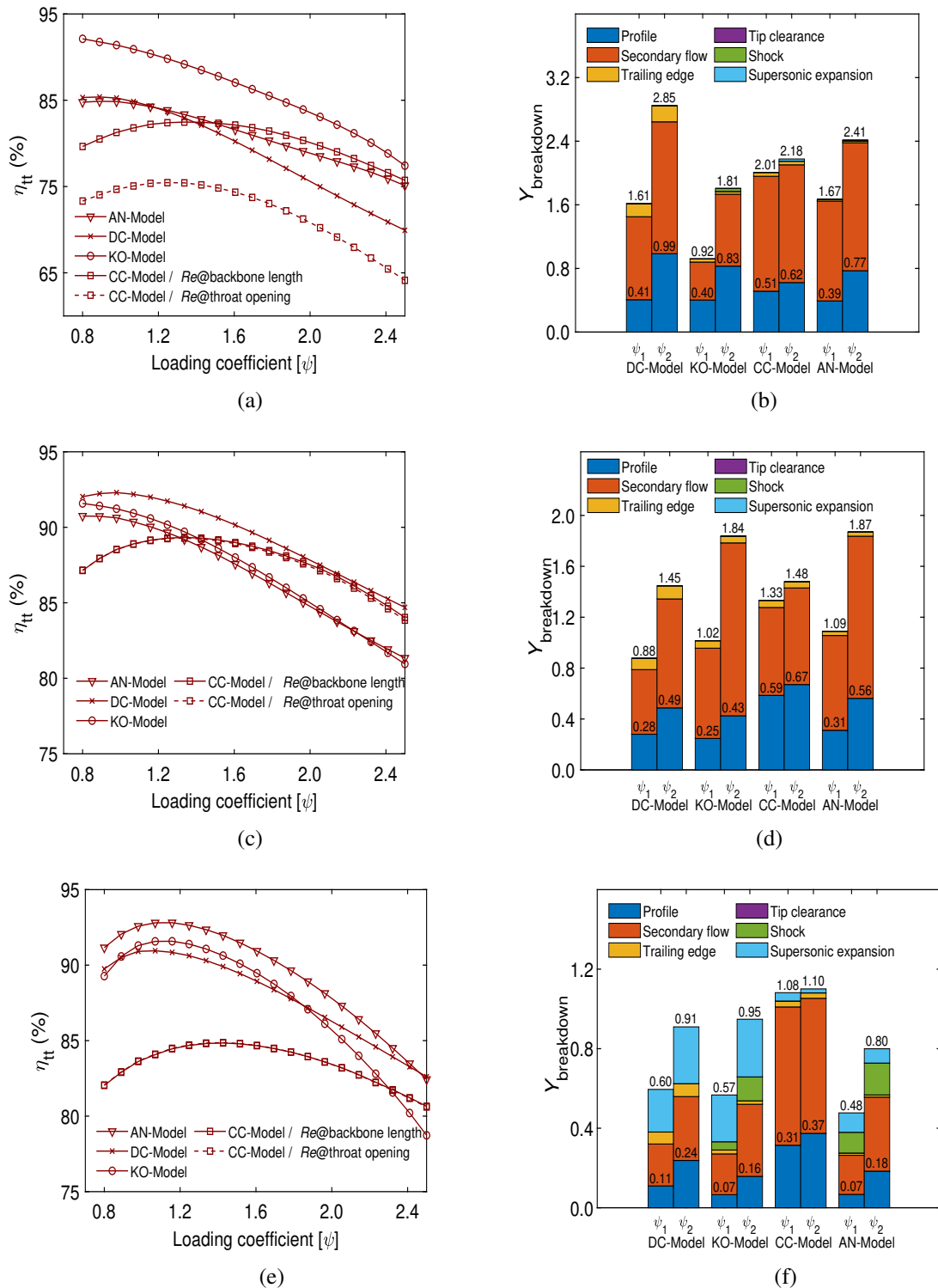
Figure 4.12: Loading coefficient $[\psi]$ versus total-to-total efficiency $[\eta_{tt}]$ and and the pressure loss coefficient $[Y]$ breakdown at loading coefficients ψ_1 and ψ_2 of 1 and 2 respectively for **(a, b)** 100 kW air turbine **(c, d)** 300 kW sCO$_2$ turbine **(e, f)** 10 kW ORC turbine.

operating at Reynolds numbers that are close to the average Reynolds number that the DC model was developed for. Furthermore, the diversity in the DC model predictions increases post to a loading coefficient of 1.7 due to ignoring the shock losses effect at the blade leading edge.
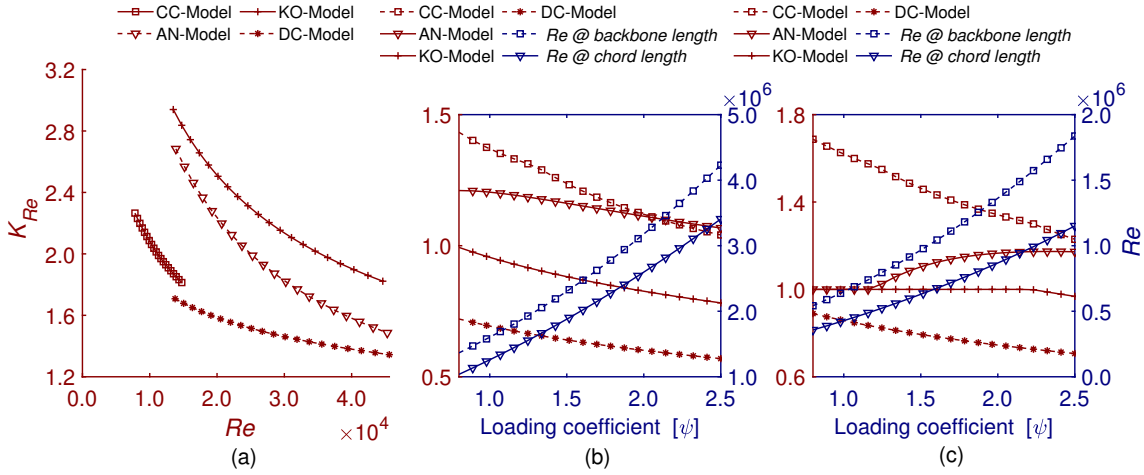
Figure 4.13: **(a)** Reynolds number $[Re]$ versus Reynolds number correction factor $[K_{Re}]$ for the 1st stage of the 100 kW air turbine, Loading coefficient versus $[Re]$ and $[K_{Re}]$ for the 1st stage of **(b)** 300 kW sCO$_2$ turbine **(c)** 10 kW ORC turbine.

Increasing the loading coefficient for the 100 kW air turbine from 1 to 2 results in a total aerodynamic loss variation of 77%, 98%, 8% and 49% for the DC, KO, CC and AN models respectively. Similarly, for sCO$_2$ turbine the same increase in the loading coefficient results in a total aerodynamic loss change of 65%, 80%, 11% and 72% for DC, KO, CC and AN models. The ORC turbine experiences a change in the aerodynamic loss of 52%, 67%, 2% and 66% for the DC, KO, CC and AN models respectively. Unlike the large-scale design, for all loss models, the air and sCO$_2$ turbines are highly sensitive to changing the loading coefficient compared to the ORC turbine.

4.3.6 Sensitivity analysis to key geometrical design parameters

The flow coefficient (ϕ) and loading coefficient (ψ) are known to be important design variables that affect aerodynamic performance, as indicated in the Smith chart [136], but this section focuses on investigating the sensitivity of loss models to other geometrical design parameters such as the pitch-to-chord (s/c) and aspect ratios (h/c). The sensitivity

is defined as the difference between the loss value at the examined condition and the design value in comparison to the design point; for example, the sensitivity of the profile loss to increasing the (s/c) ratio from 0.8 to 1.1 is equivalent to:

$$Y_{sensitivity(P)} = \frac{Y_{P@s/c=1.1} - Y_{P@s/c=0.8}}{Y_{P@s/c=0.8}} \times 100 \tag{4.1}$$

The sensitivity of the loss models is investigated at both high and low (s/c) ratios with respect to an optimum reference of $s/c = 0.8$. The following set of results has been obtained at a fixed ψ, ϕ and Λ of 1.0, 0.5 and 0.5 respectively. The blade s/c ratio influences turbine performance by affecting both profile and secondary flow losses as presented in Figures 4.14a and 4.14d. Decreasing s/c from 0.8 to 1.1 increases the profile losses for the 100 MW air turbine by 46%, 46% and 50% for the DC, KO and AN models respectively as presented in Figure 4.14a. On the contrary, decreasing s/c to 0.5 results in an increasing tread for all loss models with the least increase obtained by the CC model (39%) for the sCO$_2$ turbine compared to an increase by 53%, 53%, 58% for DC, KO and AN models respectively (Figure 4.14b).

For the secondary flow losses, the DC, KO and AN models showed no sensitivity to increasing or decreasing the s/c ratio. However, increasing s/c from 0.8 to 1.1 increases the secondary flow losses by around 25% for all fluids, while reducing the s/c to 0.5, results in a maximum reduction in the secondary flow loss of 34% as shown in Figures 4.14c and 4.14d. On this matter, increasing s/c was found to result in higher secondary flow losses in the literature [158, 159].

The blade aspect ratio influences the turbine performance by affecting both tip clearance and secondary flow losses. Thus, the sensitivity of the four loss models is investigated with respect to two extreme cases with aspect ratios of 3.0 and 0.5 respectively. As presented in Figure 4.15a, increasing the aspect ratio from 1.0 to 3.0 results in a reduction in the secondary flow losses for the 100 MW air turbine by 60%, 52%, 52% and 57% for the DC, KO, CC and AN models respectively. Similar results are obtained for the other working fluids, although the DC model is found to be more sensitive to the increase in

aspect ratio.
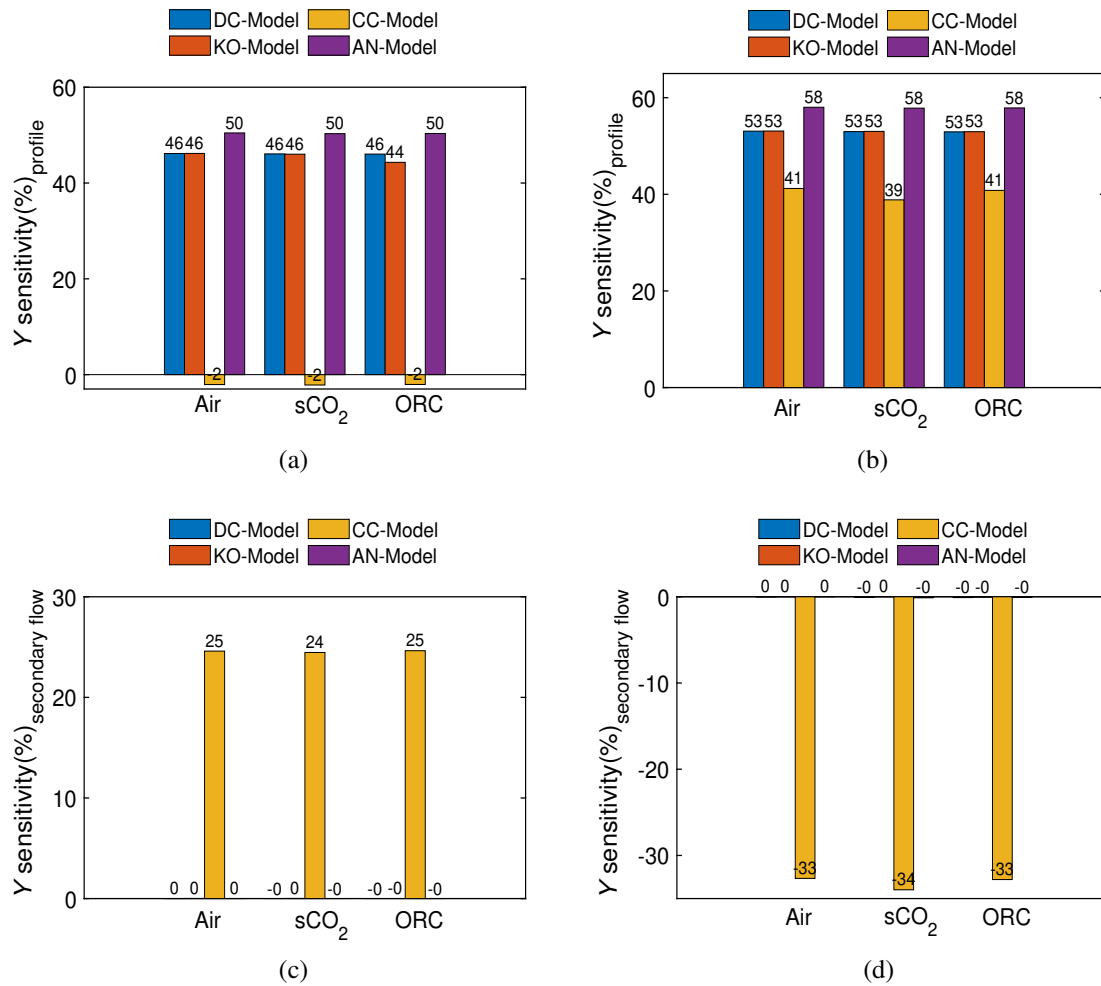
Figure 4.14: The sensitivity of profile pressure loss coefficient $[Y]$, of the 1st turbine stage of 100 MW air, 100 MW sCO_2 and 1 MW ORC turbines, to the pitch-to-chord ratio $[s/c]$ **(a)** increase from 0.8 to 1.1, **(b)** reduction from 0.8 to 0.5, the sensitivity of secondary flow pressure loss coefficient $[Y]$, of the 1st turbine stage of 100 MW air, 100 MW sCO_2 and 1 MW ORC turbines, to the s/c ratio **(c)** increase from 0.8 to 1.1 **(d)** reduction from 0.8 to 0.5.

On the other hand, larger differences are obtained when the aspect ratio is reduced from 1.0 to 0.5 as shown in Figure 4.15b. The AN and KO models predict lower secondary flow losses with respect to the DC and CC models; decreasing the h/c ratio from 1.0 to 0.5 for the air turbine results in an increase in the secondary flow loss by 33% and 45% in the KO and AN models, compared to 74% and 49% for the DC and CC models respectively. Although decreasing the h/c ratio results in higher secondary flow losses, both the KO and model results in a reduction in the secondary flow loss by 32% for the 1 MW ORC turbine as shown in Figure 4.15a. In principle, all the loss models result

in an increase in the preliminary secondary flow losses, excluding Reynolds number and compressibility correction factors, with reducing aspect ratio. Nevertheless, the KO model results in less overall secondary flow losses in the ORC turbine due to the deviation of the fluid compressibility correction factor with respect to the AN model. As noted by Aungier [66], the KO model compressibility factor was corrected to prevent excessive factor values for extreme cases where the axial chord-to-height ratio is very large.

(a)   (b)

(c)   (d)
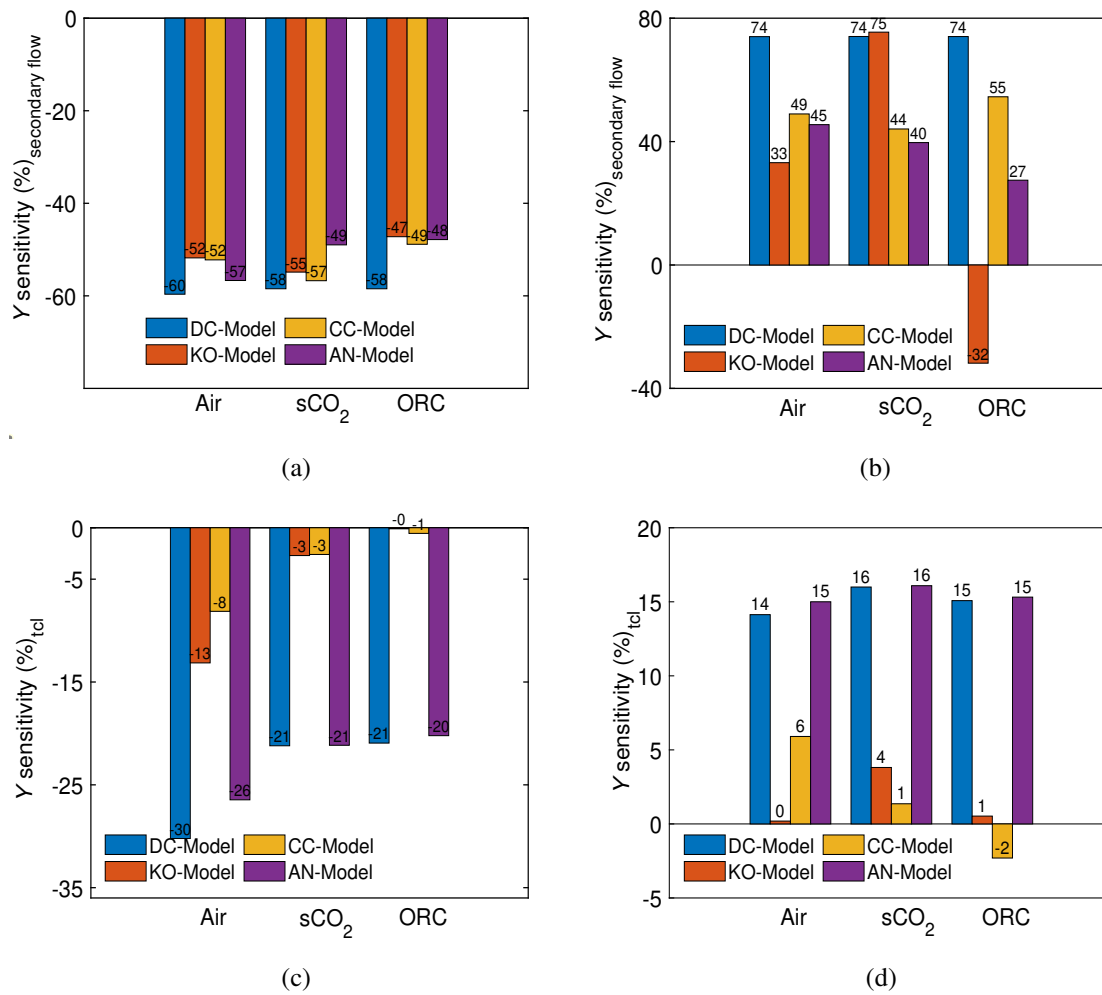
Figure 4.15: The sensitivity of secondary flow pressure loss coefficient $[Y]$, of the 1st turbine stage of 100 MW air, 100 MW sCO_2 and 1 MW ORC turbines, to the aspect ratio $[h/c]$ **(a)** increase from 1 to 3 **(b)** reduction from 1.0 to 0.5. Sensitivity of tip clearance pressure loss coefficient, of the 1st turbine stage of 100 MW air, 100 MW sCO_2 and 1 MW ORC turbines, to $[h/c]$ ratio **(c)** increase from 1.0 to 3.0 **(d)** reduction from 1.0 to 0.5.

For the ORC turbine, increasing the blade h/c ratio results in a reduction in the tip clearance loss by 21 and 20% for the DC and AN models respectively, as shown in Figure 4.15c; this is because both applied the same correlation which is a function of the

clearance gap to chord length. Furthermore, the clearance loss increases with a decreasing h/c ratio from 1.0 to 0.5 (Figure 4.15d) by 15% for the DC and AN models respectively. However, neither the CC nor KO models are found to be sensitive to a variation in the aspect ratio, with maximum changes of 5% being noted.

4.4 Remarks for small and large turbine designs

According to the previous analysis, it can be concluded that secondary flow losses appear to be the most dominant loss mechanism in large-scale air turbine design. Air turbines experience the highest profile and secondary flow losses compared to other turbines, whilst tip clearance losses have the smallest effect. However, for the small-scale air turbine, a higher percentage of losses is contributed to the tip clearance losses, because of the shorter blade heights and chord length.

For the large-scale sCO_2 and ORC turbines, clearance losses contribute by a larger extent to the total aerodynamic loss compared to the large-scale air turbine. Moreover, the large-scale air turbine mostly operates in the transitional region, while the ORC and sCO_2 turbines operate in the turbulent flow regime. Thus, the surface roughness effect on both profile and secondary flow losses is expected to be more significant in the sCO_2 and ORC turbines compared to air.

For small-scale turbines, the characteristics of the flow regime (laminar vs. turbulent flow) become more significant. For air turbines, a laminar flow regime exists where flow separation is expected to occur at the leading and trailing edges of the blade suction and pressure sides which increase the profile and secondary flow losses. For the sCO_2 and ORC turbines, the surface roughness effect, with respect to the characteristic length, is significant in turbulent flow regimes where this effect is highly pronounced in Craig and Cox model compared to the Aungier model. Due to the compactness of small-scale turbines, in addition to the larger losses predicted by the loss models, tip clearance loss deteriorates the turbine efficiency for all working fluids, with higher effects observed in the sCO_2 and ORC turbines.

In the off-optimum design cases, sCO$_2$ turbines are found to be less susceptible to high Mach numbers, and hence experience less shock and supersonic expansion losses. ORC turbines experience the highest shock and supersonic expansion losses due to the high-expansion ratios experienced in a turbine stage. Therefore, the ORC turbine is a lot more sensitive to increasing the flow coefficient compared to the air and sCO$_2$ turbines at both the small- and large scales. For large-scale turbine designs, changing the loading coefficient does not result in large discrepancies in the efficiencies predicted by the different loss models. However, the air turbine is found to be more sensitive to increasing the loading coefficient (ψ) compared to both the ORC and sCO$_2$ turbines. At the smaller scale, larger discrepancies are observed for all the turbine designs due to a more significant effect of the Reynolds number. For small-scale air turbines, the Reynolds number is typically around 10^4, resulting in a flow that is more prone to laminar boundary layer separations and developed secondary flows near the end walls. In contrast, the compact designs of both sCO$_2$ and ORC turbines lead to a higher surface roughness to chord ratio, which can cause changes in the boundary layer transition and affect the prediction capability of loss models.

Contrary to the large-scale designs, the air and sCO$_2$ turbines are more sensitive to increasing the loading coefficient compared to the ORC turbine. Furthermore, the Craig and Cox model appears to be the most sensitive to the flow coefficient change in the air turbine compared to the other loss models. However, a lower sensitivity was observed for the ORC turbine due to ignoring the shock loss effect at the leading edge and underestimating the supersonic expansion losses with respect to the other loss models. Also, Craig and Cox model shows higher sensitivity to increasing the pitch-to-chord ratios s/c.

Given that existing loss models were developed for air turbines, the transition Reynolds number is set based on the operating conditions of air turbines. Hence, this should be considered while dealing with non-conventional working fluids. Both the ORC and sCO$_2$ turbines are likely to operate at higher Reynolds number compared to air turbines; this is because both ORC and sCO$_2$ turbines often operate with higher fluid densities, resulting in higher Reynolds numbers. Additionally, the reduction in the critical Reynolds number, due

to the effect of both the high Mach number and surface roughness, is likely to affect the performance of ORC and sCO$_2$ turbines; considering that small transition Reynolds number would result in more significant surface roughness effect at smaller Reynolds number. Additionally, a lower critical Reynolds number can lead to earlier transition from laminar to turbulent flow, which can increase the skin friction and turbulence-induced losses. Therefore, the critical Reynolds number definition should be revised to allow for accurate Reynolds number correction factors' predictions. On a different note, applying the same Reynolds number correction factor for both profile and secondary flow losses for small-scale air turbine designs might penalise turbine performance as profile losses can be more affected by laminar flow than secondary flow losses [146].

Furthermore, fluid compressibility and surface roughness effects are found to be significant for ORC turbines. Therefore, it is recommended to select a loss model that accounts for both effects and hence, the AN model is the most suitable model in this regard. Though the KO model would result in less accuracy compared to the AN model for ORC turbines, due to ignoring surface roughness effects, it would be useful to use if a more accurate expression for supersonic expansion losses is integrated within the model instead of the one introduced by the DC model.

To conclude, both the KO and AN models are found to be suitable for sCO$_2$ turbines considering that supersonic expansion flow is less likely to happen. Nevertheless, the DC model would result in considerably less accurate results for both sCO$_2$ and ORC turbines due to ignoring surface roughness effects and underestimating Reynolds number effects; particularly when the flow regime operates at a high Reynolds number range compared to the used average of 2×10^5. Additionally, it ignores the compressibility effects and overestimates the supersonic expansion losses for the ORC turbines.

In principle, the CC model accounts for significant factors that affect turbine performance, such as the pitch-to-chord ratio and surface roughness effect, that are ignored in other models. However, both secondary and profile losses were found to be overly predicted by the CC model when tested using cascade experimental data [60]. Therefore, to the authors knowledge, the CC model is found to under-predict the efficiency for the

non-conventional working fluids compared to the other loss models, particularly for the off-optimum design conditions and small-scale turbine designs.

4.5   Conclusions

This chapter presented a comprehensive investigation into the performance predictions obtained using mean-line loss models that are commonly applied to the design of axial turbines, namely the Dunham and Came, Kacker and Okapuu, Craig and Cox and Aungier models. The models were evaluated over a wide range of boundary conditions and design variables. Three different case-studies were selected for air, ORC and sCO_2 turbines and each one was evaluated at two different scales (small and large scales).

According to the analysis results, it was found that large-scale air turbines experienced the highest profile and secondary flow losses compared to other turbines, whilst tip clearance losses have the smallest effect. For large-scale sCO_2 and ORC turbines, clearance losses contributed by a larger extent to the total aerodynamic loss compared to the large-scale air turbine. Moreover, the large-scale air turbine mostly operates in the transitional region, while the ORC and sCO_2 turbines operate in the turbulent flow regime. Thus, the surface roughness effect on both profile and secondary flow losses was found to be more significant in the sCO_2 and ORC turbines compared to air.

For the small-scale air turbines, it was found that a laminar flow regime existed where flow separation is expected to occur at the leading and trailing edges of the blade suction and pressure sides which increased both profile and secondary flow losses. As for small-scale sCO_2 and ORC turbines, the surface roughness effect, with respect to the characteristic length, was found to be significant in turbulent flow regimes. Due to the compactness of small-scale turbines, in addition to the larger losses predicted by the loss models, tip clearance loss deteriorated the turbine efficiency for all working fluids, with higher effects observed in the sCO_2 and ORC turbines.

Consequently, for the sCO_2 applications, it was recommended to implement both the Kacker and Okapuu and Aungier models taking into consideration that supersonic expan-

sion flow is less likely to happen; where Aungier should provide more accurate results due to considering surface roughness and Reynolds number effect for secondary flow losses. Dealing with smaller-scale sCO_2 and ORC turbines, it is recommended to implement a loss model that accounts for the effect of surface roughness. A higher surface roughness to the chord length ratio is experienced in those turbines and hence, the Aungier model was found to be better suited compared to Kacker and Okapuu where this effect is ignored.

This work provided a good insight into the diversity of the prediction capability of the commonly used loss models for air, sCO_2 and ORC turbines across a range of scales. Ultimately, the Aungier loss model was found to be the most suitable model for large-scale sCO_2 turbines. Therefore, the performance of CO_2 and CO_2 based blends will be evaluated in this work, covered in the next chapter, using the Aungier loss model.

This page is left intentionally blank

5 Flow path designs of axial turbines operating with CO_2 blends

5.1 Introduction

It is clear from the literature review that supercritical CO_2 (sCO_2) blends are promising for enhancing the performance of power cycles for concentrated solar power (CSP) applications. This anticipated potential should result in large reductions in the cost of CSP plants and increase its competitiveness with conventional power generation systems. To advance the state of the art of CO_2 cycle components, few studies in the literature have focused on developing aerodynamic designs of large-scale axial sCO_2 turbines. Nonetheless, none of the previous studies focused on evaluating the performance of turbines operating with CO_2 blends considering the rotor-dynamic and mechanical design aspects despite their significance for these applications.

This chapter presents an investigation of the impact of adopting different CO_2 blends, including CO_2/$TiCl_4$, CO_2/C_6F_6 and CO_2/SO_2, on the multi-stage axial turbine flow path design accounting for aerodynamic, mechanical and rotordynamic considerations. This includes assessing the sensitivity of the turbine design to selected working fluid and imposed optimal cycle conditions. The aim of this chapter extends to examining the differences in the turbine flow path designs generated for pure CO_2 compared to CO_2 blends taking into account aerodynamic, rotordynamic and mechanical design aspects, as assessed during the mean-line design process. Ultimately, the effects of changing turbine design variables, including loading coefficient, flow coefficient, degree of reaction and pitch-to-chord ratio, on the flow path design and overall aerodynamic performance are also investigated.

5.2 Cycle analysis

To investigate the effect of using the sCO_2 blends on the flow path design, a series of simulations have taken place by the SCARABEUS project partners at the University of Seville

to come up with the optimised cycle configurations for the candidate blends. At this point, three different blends have been identified by the SCARABEUS project consortium to be promising for the CSP plant. This includes Hexafluorobenzene (C_6F_6) [40], titanium Tetrachloride (TiCL$_4$) [160] and Sulphur Dioxide (SO_2) [20]. The three selected blends are found to be having different thermodynamic properties with a common feature of a high critical point compared to pure CO_2 allowing for working fluids condensation at 50 to 60°C. A brief overview of thermal stability issues, environmental and safety hazards for the three selected dopants was presented in Section 2.2.3. With regards to the cycle analysis, the selection of the best cycle configuration was found to be strongly dependent upon the used blend [13]. Therefore, simple recuperated (Figure 2.9a) cycle, precompression and recompression cycles have proven to be the most suitable for CO_2/TiCl$_4$, CO_2/C_6F_6 and CO_2/SO_2 blends as reported in Section 2.2.3.

The aim of this chapter is to study the impact of adopting different sCO$_2$ blends on the turbine flow path design and hence, to establish the sensitivity of the achievable turbine efficiency to the working fluid and the varying cycle conditions. Therefore, the effect of changing the molar fraction, the maximum pressure (ranging from 250 to 350 bar) and temperature (550 and 700°C) have been previously investigated with regard to the cycle analysis to proceed with the flow path sensitivity analysis. To achieve this aim, the upper and lower bounds of changing the molar fraction have been specified for each blend where the low bound is mainly dependent on the chemical composition of each compound. So, these ranges were specified based on a set criterion for the temperature difference between the minimum cycle temperature (T_{min}) and the critical temperature (T_{cr}). This difference was set to be equal to or higher than 30°C to allow for operating the compression in the immediate vicinity of the critical point. The minimum cycle temperature was set to 50°C and hence the molar fractions were selected to allow for critical blends temperature above 80°C. Therefore, a 10% molar fraction range was selected for the three dopants as follows: 10-20% for C_6F_6, 14-24% for TiCl$_4$ and 30-40% for SO_2.

Following the molar fraction specification, the efficiency trends have been investigated over the defined molar fraction range and the maximum cycle pressure for a maximum cy-

cle temperature of 550 and 700°C for the 100 MWe SCARABEUS CSP plant. $CO_2/TiCl_4$ was found to result in efficiency ranging from 41.5% up to 45.5% at turbine inlet temperature (TIT) of 550 °C and efficiency ranging from 48 to 51.5% for TIT of 700°C over the examined range of pressures. The Precompression cycle operating with CO_2/C_6F_6 was found to result in an efficiency range from 42.75 to 43.15% at 550°C and 49.6 to 50.05% at 700°C. Similarly, CO_2/SO_2 resulted in an efficiency ranging from 43.5 to 44.5% and 50.3 to 51.5% at 550°C and 700°C respectively.

According to these results, $CO_2/TiCl_4$ was found to experience the highest efficiency sensitivity to changing both the molar fraction and cycle maximum pressures followed by CO_2/SO_2 and CO_2/C_6F_6. For the $CO_2/TiCl_4$, the dopant molar fraction experienced significant changes, from 18% to 14%, to optimise cycle efficiency at a maximum cycle pressure of 350 bar compared to 250 bar. On the other hand, the optimum molar fraction was found to be 14.5-15% and 30% for the CO_2/C_6F_6 and CO_2/SO_2 blends, respectively, irrespective of the inlet pressure and temperature. Ultimately, the optimum pressure was found to change with the operating temperature (TIT) for both blends where it can reach up to 350 bar at 700°C. It is worth mentioning here that the Allam cycle operates at pressures and temperatures in excess of 320 bar and 950°C [118]. Further details of the cycle analysis results can be found in [43].

5.2.1 Definition of candidate boundary conditions for turbine design

According to the optimum molar fraction compositions and the maximum cycle pressure determined by the analysis results summarised in Section 5.2, the boundary conditions for the turbine are identified to allow for investigating the effects of changing the pressure and the molar fraction on the turbine design and performance. According to the cycle analysis results, the maximum pressure is defined to be 300 and 350 bar for CO_2/C_6F_6 and 310 and 350 bar for CO_2/SO_2 at 550°C and 700°C respectively. Five different molar fraction points are identified within a 10% range for all blends. This includes the optimum and minimum/maximum values at 250 bar and the optimum P_{max} pressure at temperatures of 550°C and 700°C. Accordingly, four different cases are generated and implemented for

the turbine design process as detailed in Tables 5.1 and 5.2; where *Case A*, *Case B*, *Case C* and *Case D* refer to a turbine inlet temperature and pressure of 550°C & 250 bar, 700°C & 250 bar, 550°C & the optimum P_{max} and 700°C & optimum P_{max} respectively.

Table 5.1: Operating conditions for turbine design: cases 'A' and 'B'

CO₂/TiCl₄

	Case A (TIT = 550°C, Pmax = 250 bar)					Case B (TIT = 700°C, Pmax = 250 bar)				
Thermal Efficiency [%]	44.35	44.92	**45.42**	44.13	42.71	50.28	50.84	**51.33**	50.21	48.89
TiCl$_4$ molar fraction [%]	14	15.5	**17**	20.5	24	14	15.5	**17**	20.5	24
Turbine mass flow [kg/s]	1485	1535	**1577**	1677	1756	1174	1210	**1241**	1312	1367
Turbine Inlet T [°C]	550	550	**550**	550	550	700	700	**700**	700	700
Turbine Inlet P [bar]	242.6	242.6	**242.6**	242.6	242.6	242.6	242.6	**242.6**	242.6	242.6
Turbine Outlet P [bar]	98.13	97.66	**97.14**	95.40	93.44	98.13	97.66	**97.14**	95.40	93.44
Total turbine isentropic enthalpy drop [kJ/kg]	90.36	87.65	85.14	80.24	76.08	109.80	106.68	103.80	98.25	93.59

CO₂/C₆F₆

	Case A (TIT = 550°C, Pmax = 250 bar)					Case B (TIT = 700°C, Pmax = 250 bar)				
Thermal Efficiency [%]	42.81	43.12	**43.17**	43.08	42.87	49.57	49.82	**49.90**	49.82	49.58
C$_6$F$_6$ molar fraction [%]	10	12.5	**14.5**	17.5	20	10	12	**14.5**	17	20
Turbine mass flow [kg/s]	1098	1129	**1152**	1186	1212	835.3	854.5	**877.3**	898.5	921.7
Turbine Inlet T [°C]	550	550	**550**	550	550	700	700	**700**	700	700
Turbine Inlet P [bar]	238.9	238.9	**238.9**	238.9	238.9	238.9	238.9	**238.9**	238.9	238.9
Turbine Outlet P [bar]	64.63	62.33	**61.48**	58.81	57.53	59.65	57.96	**56.28**	55.02	52.60
Total turbine isentropic enthalpy drop [kJ/kg]	143.38	139.01	134.47	130.29	125.94	182.97	178.48	172.66	166.71	162.00

CO₂/SO₂

	Case A (TIT = 550°C, Pmax = 250 bar)					Case B (TIT = 700°C, Pmax = 250 bar)				
Thermal Efficiency [%]	**44.32**	44.21	44.11	43.82	43.46	**50.87**	50.79	50.71	50.54	50.28
SO$_2$ molar fraction [%]	**30**	32.5	35	37.5	40	**30**	32.5	35	37.5	40
Turbine mass flow [kg/s]	**1016**	999.9	991.3	995.6	1004	**780.8**	772.8	760.4	760.0	761.8
Turbine Inlet T [°C]	**550**	550	550	550	550	**700**	700	700	700	700
Turbine Inlet P [bar]	**238.9**	238.9	238.9	238.9	238.9	**238.9**	238.9	238.9	238.9	238.9
Turbine Outlet P [bar]	**69.93**	67.75	65.60	63.47	61.35	**69.93**	67.75	65.60	63.47	61.35
Total turbine isentropic enthalpy drop [kJ/kg]	151.87	153.53	155.18	156.84	158.51	184.14	186.32	188.50	190.70	192.92

Table 5.2: Operating conditions for turbine design: cases 'C' and 'D'

$CO_2/TiCl_4$

Parameter	Case C (TIT = 550°C, Pmax = Popt)					Case D (TIT = 700°C, Pmax = Popt)				
Thermal Efficiency [%]	**45.55**	44.86	44.02	43.09	42.13	**51.57**	50.96	50.21	49.97	48.53
$TiCl_4$ molar fraction [%]	**14**	16.5	19	21.5	24	**14**	16.5	19	21.5	24
Turbine mass flow [kg/s]	**1316**	1387	1455	1521	1571	**1032**	1084	1132	1178	1212
Turbine Inlet T [°C]	**550**	550	550	550	550	**700**	700	700	700	700
Turbine Inlet P [bar]	**281.4**	281.4	281.4	281.4	281.4	**281.4**	281.4	281.4	281.4	281.4
Turbine Outlet P [bar]	**98.13**	97.33	96.22	94.79	93.44	**98.13**	97.33	96.22	94.79	93.44
Total turbine isentropic enthalpy drop [kJ/kg]	104.07	98.84	94.36	90.52	86.93	126.80	120.79	115.67	111.33	107.30

CO_2/C_6F_6

Parameter	Case C (TIT = 550°C, Pmax = Popt)					Case D (TIT = 700°C, Pmax = Popt)				
Thermal Efficiency [%]	42.80	43.10	**43.17**	43.07	42.89	49.68	49.96	**50.06**	50.01	49.86
C_6F_6 molar fraction [%]	10	12.5	**15**	17.5	20	10	12.5	**15.5**	17.5	20
Turbine mass flow [kg/s]	987.7	1016	**1046**	1073	1101	693.5	714.9	**740.1**	756.5	776.2
Turbine Inlet T [°C]	550	550	**550**	550	550	700	700	**700**	700	700
Turbine Inlet P [bar]	286.7	286.7	**286.7**	286.7	286.7	334.5	334.5	**334.5**	334.5	334.5
Turbine Outlet P [bar]	66.13	64.28	**63.47**	60.68	58.91	61.81	60.50	**57.33**	56.22	54.15
Total turbine isentropic enthalpy drop [kJ/kg]	159.57	153.64	146.93	143.49	139.15	220.38	211.43	204.69	199.00	193.70

CO_2/SO_2

Parameter	Case C (TIT = 550°C, Pmax = Popt)					Case D (TIT = 700°C, Pmax = Popt)				
Thermal Efficiency [%]	**44.53**	44.42	44.29	44.16	43.95	**51.52**	51.44	51.31	51.23	51.1
SO_2 molar fraction [%]	**30**	32.5	35	37.5	40	**30**	32.5	35	37.5	40
Turbine mass flow [kg/s]	**907.8**	903.0	892.0	888.8	879.9	**649.7**	645.9	639.2	636.2	634.7
Turbine Inlet T [°C]	**550**	550	550	550	550	**700**	700	700	700	700
Turbine Inlet P [bar]	**296.3**	296.3	296.3	296.3	296.3	**334.5**	334.5	334.5	334.5	334.5
Turbine Outlet P [bar]	**69.93**	67.75	65.60	63.47	61.35	**69.93**	67.75	65.60	63.47	61.35
Total turbine isentropic enthalpy drop [kJ/kg]	175.15	176.34	177.53	178.73	179.95	229.37	230.77	232.17	233.60	235.06

5.3   Turbine design methodology

Within the current work, a multi-stage mean-line design approach has been implemented, which was previously discussed and summarised in section 3.3.2; where the steady-state mass, energy, and momentum equations were solved at a constant hub diameter and hence, the blade geometry, velocity triangles and thermodynamic properties are obtained for all design stages. The flow paths are designed based on the design parameters specified in Table 5.3. In the current design methodology, the axial spacing between the turbine stages, and the radial tip clearance gap, have been specified as a percentage of the upstream pitch and tip diameter respectively.

Table 5.3: Decision variables for CO_2 blends designs.

Decision variables	Description	units	Value
N	Rotational speed	[kRPM]	3000 (50 Hz motor)
k_s	Surface roughness	[mm]	0.002
ϕ	Stage flow coefficient	[-]	1 [136]
ψ	Stage loading coefficient	[-]	0.5 [136]
Λ	Degree of reaction	[-]	0.5 [136]
t/o	Trailing edge thickness to throat ratio	[-]	0.05 [65]
s/c	Pitch-to-chord ratio	[-]	0.85 [63]

To evaluate the aerodynamic performance of the turbine, the design tool was integrated with Aungier [66] loss model to obtain the total pressure loss coefficients for the stator and the rotor; this loss model has been found to be the most suitable for sCO_2 turbine design according to the analysis carried out in Chapter 4. Within the used loss model, the effects of the profile, secondary flow, tip clearance and trailing edge losses are all considered throughout the aerodynamic performance analysis [66].

In addition to evaluating the aerodynamic turbine performance using the Aungier loss model, the mean-line aerodynamic design was integrated with mechanical and rotor-dynamic constraints that limit the maximum stress acting on the blades and the length of the shaft for rotordynamic stability to allow for a fair comparison of the achievable performance for the different geometrical and process parameters (dopant type and composition, pressures, temperatures and mass flow). Consequently, the main mechanical and rotor-dynamic con-

straints are summarised based on industrial experience as reported in Section 3.3.4.

The thermodynamic properties for the candidate blends namely, $CO_2/TiCl_4$, CO_2/C_6F_6 and CO_2/SO_2 are obtained using the Peng Robinson equation of state (EoS). To predict accurately the vapour-liquid equilibrium properties of the studied blends, the binary interaction parameters (K_{ij}) were used to tune the mixing model. The same binary interaction parameters used for cycle analysis have been implemented in the turbine design model to ensure consistency in the thermodynamic properties obtained by both models. The binary interaction parameters are reported in Table 5.4.

Table 5.4: Equations of state (EoS) and Binary Interaction parameter (K_{ij}) for the selected dopants.

Dopant	X_i [%]	EoS	K_{ij}
$TiCl_4$	14-24	Standard Peng-Robinson	0.0704
C_6F_6	10-20	Standard Peng-Robinson	0.16297 - 0.0003951 T[K]
SO_2	30-40	Standard Peng-Robinson	0.0242

5.4 Flow path designs and analysis

Based on the cycle analysis reported in Section 5.2 for the identified CO_2 blends, the turbine performance has been initially evaluated at a turbine inlet temperature and pressure of $550°C$ and 250 bar respectively, and at the minimum molar fraction for the three blends (14%, 10% and 30% for $CO_2/TiCL_4$, CO_2/C_6F_6 and CO_2/SO_2 blends respectively). These conditions were selected to allow for exploring the design space at initial design conditions and conducting further investigations for the sensitivity of the performance to increasing the pressure, temperature and molar fraction based on the same design methodology. The cycle conditions for the three candidate blends are summarised in Table 5.5.

Table 5.5: Operating conditions for the three candidate blends at $550°C$

Blend	X_i [%]	$\dot{m}$(kg/s)	P_{out} (MPa)	PR (–)	η_{th} (%)	Cycle configuration
$CO_2/TiCl_4$	14	1485	9.8	2.47	44.4	Recuperated
CO_2/C_6F_6	10	1098	6.5	3.69	42.8	Precompression
CO_2/SO_2	30	1016	6.9	3.42	44.3	Recompression

In this section, a comparison between the performance of the designed flow paths for each blend is presented for the axial turbine design for the 100 MWe CSP plant. In the following set of results, the turbine performance is investigated based on the operating conditions specified in Table 5.5. Initially, three flow paths have been designed for the promising blends that were selected to represent the goals of the study. During the initial design stage, four stage designs were selected for the three candidate blends based upon an industrial recommendation to limit the peripheral speed to 180 m/s where a constant enthalpy drop was assumed across each stage. The design results of the 1st and last turbine stages for the three candidate blends are summarised in Table 5.6.

Table 5.6: Flow path design details for the CO_2 blends for a fixed number of stages.

Parameter	$CO_2/TiCl_4$		CO_2/C_6F_6		CO_2/SO_2	
	1st stage	last stage	1st stage	last stage	1st stage	last stage
Number of stages [-]	4.0		4.0		4.0	
Hub diameter [mm]	879		1120		1152	
Bending stress [MPa]	126.9	126.7	88.4	129.3	77.7	128.0
Number of rotor blades	63	52	95	86	95	95
Radial tip clearance [mm]	0.67	0.71	0.81	0.86	0.83	0.87
Aspect ratio [-]	0.70	0.95	0.50	0.99	0.48	0.97
Slenderness ratio [-]	4.16	4.16	3.03	3.03	2.93	2.93
Total-to-total efficiency [%]	91.5		89.6		89.3	

Owing to the different thermodynamic properties of the candidate dopants, and also variations in the chosen cycle configuration, different values for the turbine stage specific work were obtained for each blend composition. As a result, large differences in the hub diameters and bending stresses were obtained. The 70%CO_2/30%SO_2 blend results in the largest hub diameter and the smallest gas bending stress as shown in Figure 5.1. On the contrary, the smallest hub diameter and the highest bending stresses are attributed to the 86%CO_2/14%$TiCl_4$ blend. For the $CO_2/TiCl_4$ flow path the blade count has been lowered to keep the bending stresses within the specified limit. Increasing the blade count for this flow path would result in bending stresses exceeding the 130 MPa static bending stress limit; although the same logic applies for the CO_2/C_6F_6 and CO_2/SO_2 designs. Concerning the aerodynamic performance, the turbine design for $CO_2/TiCl_4$ achieves the highest

efficiency compared to either the CO_2/C_6F_6 and CO_2/SO_2 designs, which is due to larger aspect ratio blades, smaller hub diameters and a smaller radial tip clearance gap. All three blends resulted in a slenderness ratio that is well within the specified design limit which indicates rotordynamic instability is of no concern. This also indicates there is scope to increase the flow path length, with the goal of increasing the number of stages and increasing efficiency.
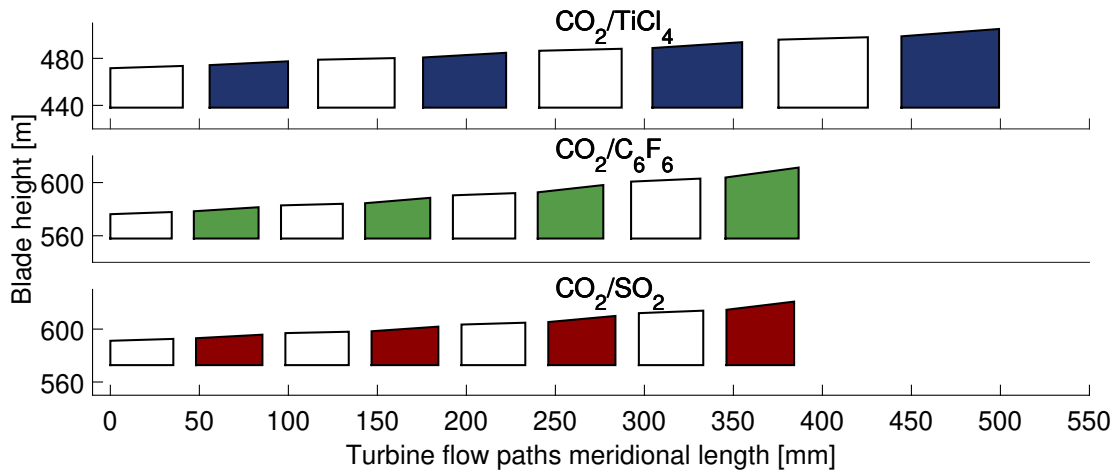
Figure 5.1: Turbine flow path meridional view for four-stage turbine designs for $CO_2/TiCL_4$, CO_2/C_6F_6 and CO_2/SO_2 blends.

To enable a fairer comparison between the three flow path designs, the effect of increasing the number of stages within the range of 4 to 14 stages was investigated for the three design cases. The analysis aims at examining the effect of a reduced hub diameter (D_{hub}), which is the result of increasing the number of design stages (n_{stages}), on the gas bending stress on the rotor blades ($\sigma_{bending}$), the isentropic efficiency (η_{tt}), and the slenderness ratio (*SR*). In this set of results, the designs are modified for each design case to keep the gas bending stress with the threshold limit, with the rotor blade count ranging between 35 and 95 . Given that the highest rotor bending stresses are experienced by the last turbine stage, which is due to the combination of a reduced density, enlarged flow area and increased blade heights, the bending stress values presented correspond to this specific stage. The results are summarised in Figures 5.2a to 5.2d.
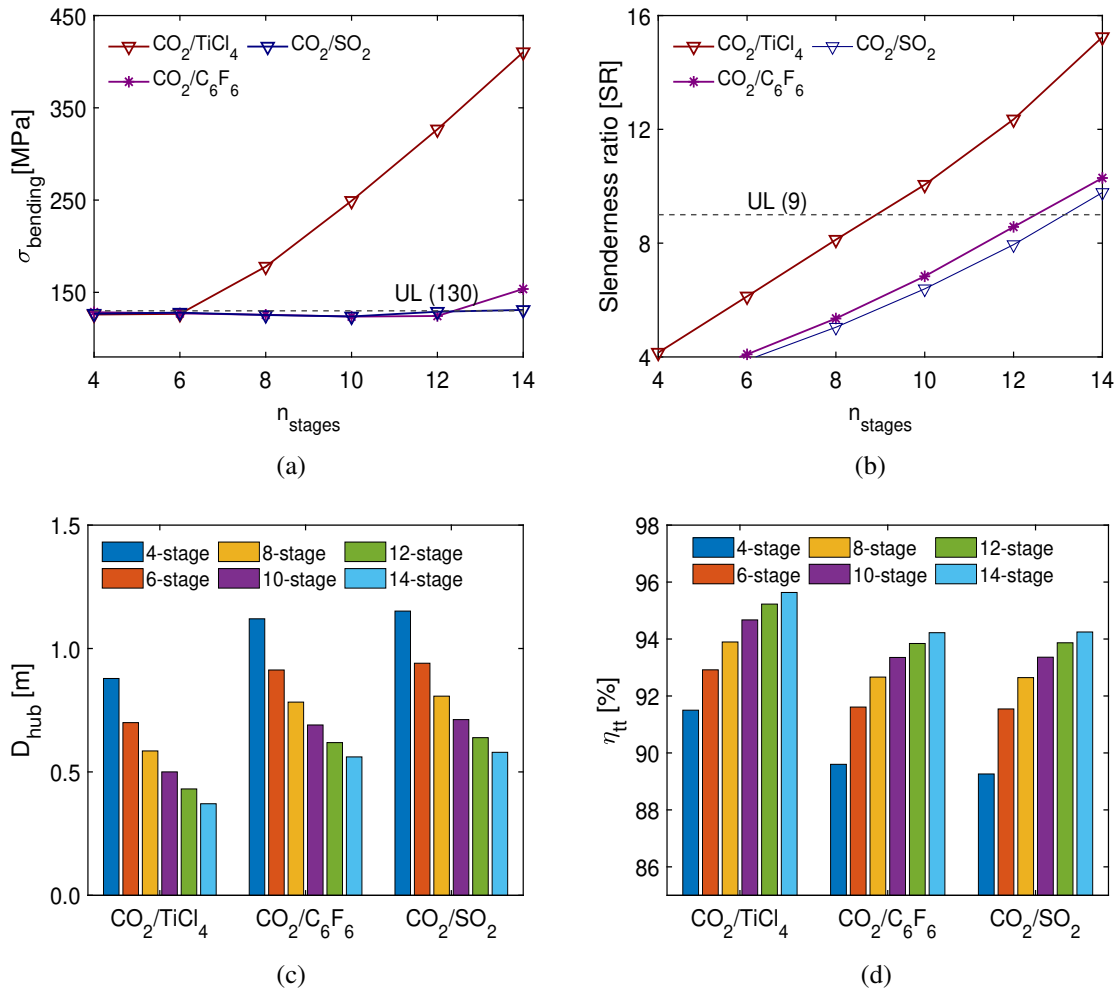
Figure 5.2: Number of stages [n_{stages}] versus (a) rotor bending stress [$\sigma_{bending}$] for the last turbine stage (b) Slenderness ratio [SR] (c) total-to-total efficiency [η_{tt}] (d) hub diameter [D_{hub}] for CO_2/$TiCl_4$, CO_2/C_6F_6 and CO_2/SO_2 blends at 4-14 turbine stages.

In view of the implemented design hypothesis, within which the designs are obtained at a constant rotational speed of 3000 RPM and loading coefficient of 1, the number of stages dictates that both the blade peripheral speed and the hub diameter, and this is a function of the specific isentropic enthalpy drop for a given blend and set of operating conditions. The smallest hub diameter is achieved for CO_2/$TiCl_4$ and the largest for CO_2/SO_2. Increasing the number of stages to 14 increases the overall total-to-total efficiency to 95.6% and 94.2% for CO_2/$TiCl_4$ and CO_2/SO_2 respectively. This is compared to initial respective efficiencies of 91.05% and 88.36% for the four-stage design. This increase in the number of stages is associated with a reduction in the hub diameter and the blade peripheral speed, which results in higher efficiency due to reducing the secondary flow losses. The reduction in the

blade peripheral speed enables to produce designs with longer blade heights and hence, this results in smaller chord length to blade height ratio and reduced secondary flow losses. Furthermore, less tip clearance losses are experienced with the long flow path designs as a results of the reduced the clearance gap size which is defined as a constant ratio of the tip diameter.

Increasing the number of stages also results in a higher slenderness ratio for all three-flow path designs, with the highest ratio obtained for the $CO_2/TiCl_4$ case. Moreover, to enhance the aerodynamic efficiency whilst achieving a design that complies with the rotor bending stress limit, it is necessary reduce the number of blades within the range of 95 to 35, as shown in Figure 5.3. Reducing the number of rotor blades results in a larger blade pitch, leads to longer chord lengths and smaller bending stress (both tangential and axial) on the blades. For the $CO_2/TiCl_4$ flow path, increasing the number of stages above six, whilst, at the same time, reducing the number of blades to 35 (the lower limit) results in bending stress that are above the threshold limit of 130 MPa. Therefore, the $CO_2/TiCl_4$ design should be limited to six stages in order to meet the constraints imposed on the slenderness ratio and bending stress. However, for both CO_2/C_6F_6 and CO_2/SO_2, the number of stages can be increased up to 12 stages without exceeding the maximum rotor bending stress of 130 MPa. Moreover, the slenderness ratio can be kept below 9 and the number of blades is above or equal to the minimum value of 35.
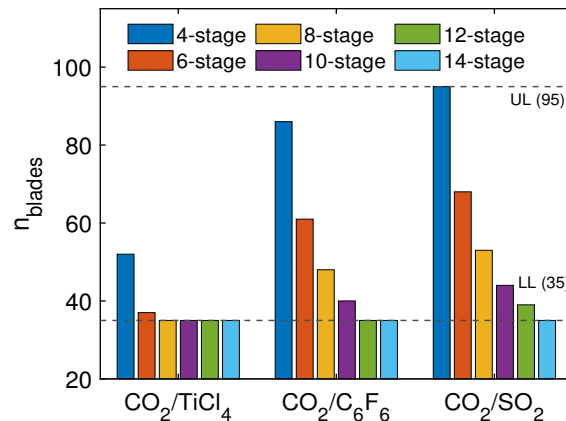
Figure 5.3: Number of rotor blades for the last turbine stages [n_{blades}] for CO_2/ $TiCl_4$, sCO_2/C_6F_6 and sCO_2/SO_2 blends at 4-14 turbine stages.

Based on the results presented in this subsection, it is possible to select the optimal number of stages, and hence hub diameter, that obtains the highest efficiency for a specified set of turbine boundary conditions. This number of stages provided the higher aerodynamic efficiency, whilst keeping the rotor bending stresses and slenderness ratio within the specified threshold limit. However, it should be noted that each pair of blend and boundary conditions results in an optimal flow path design with a different number of stages and a different number of rotor blades.

5.4.1   Sensitivity of turbine efficiency to cycle conditions

The previous analysis was completed at the minimum blend fraction (X_1) and at an inlet temperature and pressure of 550°C and 250 bar respectively. This section aims to investigate the effect of changing the thermodynamic boundary conditions, namely the turbine inlet temperature (T_{inlet}) and pressure (P_{inlet}) and dopant concentration (X_i) on the achievable turbine efficiency for a turbine design that meets the imposed mechanical and rotordynamic constraints. To do this, the remaining turbine design boundary conditions, namely the mass flow rate ($\dot{m}$), pressure ratio (PR) and molar fractions are taken from the results obtained from the thermodynamic cycle analysis. In the following set of results, as reported in Figures 5.4a to 5.4c, axial turbine designs are produced at a total inlet temperature and pressure of 550°C & 250 bar (*Case A*), 700°C & 250 bar (*Case B*), 550°C & P_{opt} (*Case C*) and 700°C & P_{opt} (*case D*). This is completed at different molar fractions ranging from 14 to 24%, 10 to 20%, and 30 to 40% for $CO_2/TiCl_4$, CO_2/C_6F_6 and CO_2/SO_2 respectively.

For the $CO_2/TiCl_4$ blend, changing the boundary conditions of turbine design by increasing the inlet temperature from 550 to 700°C results in a lower rotor bending stresses, and allows for a larger number of stages, smaller hub diameters and higher turbine efficiencies, whilst keeping the slenderness ratio within the defined limit as indicated in Figure 5.4a. On the other hand, less significant effects are obtained when turbine inlet pressure is increased from 25 *MPa* to P_{opt} for the same inlet temperature. As for the effect of molar fraction, increasing this from 14 to 24% results in a lower turbine efficiency (η_{tt}), which is
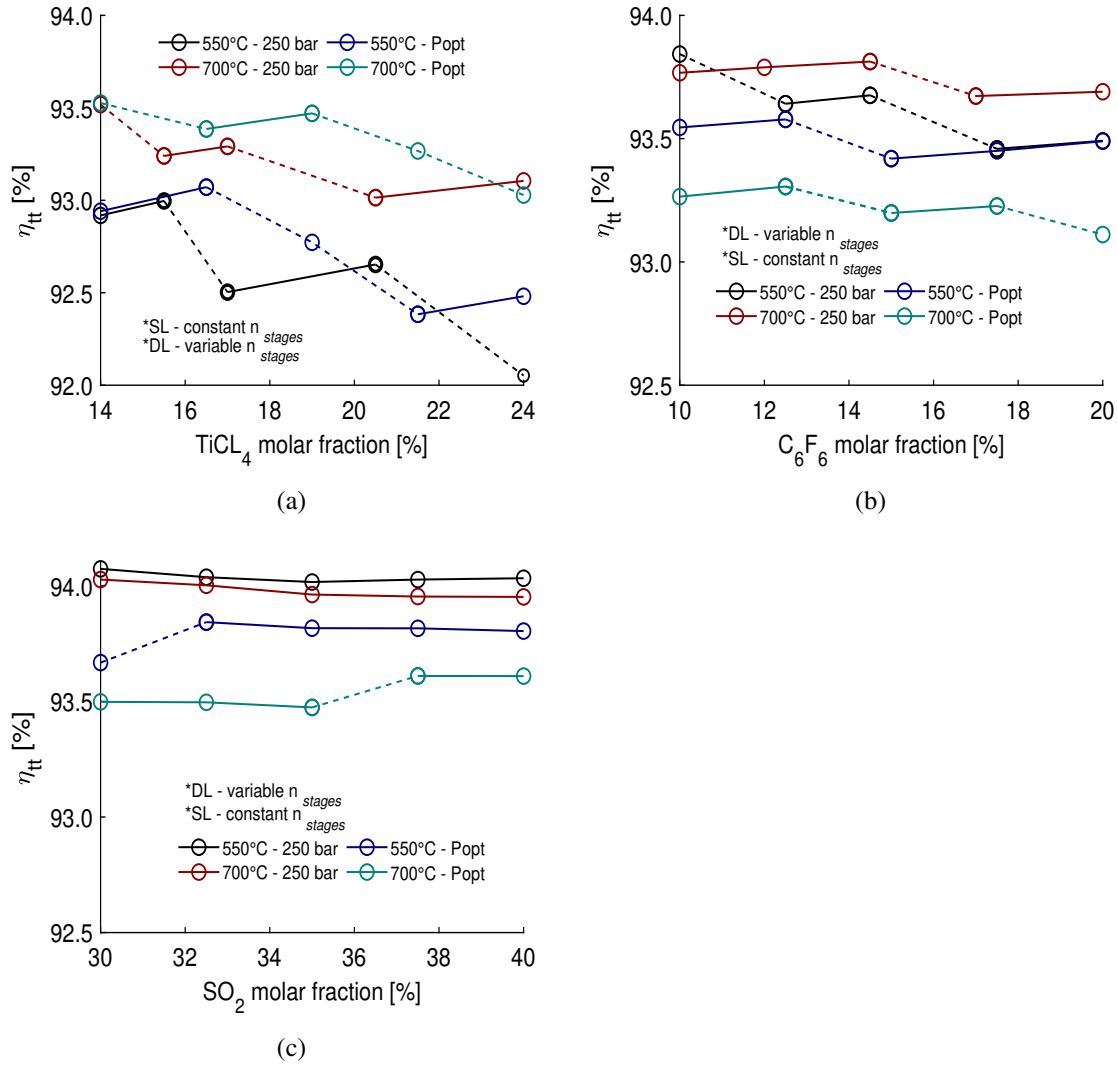
Figure 5.4: Total-to-total efficiency (η_{tt}) versus the molar fraction for (a) $CO_2/TiCL_4$ (b) CO_2/C_6F_6 (c) CO_2/SO_2 flow paths; where P_{opt} is the maximum optimum pressure for each cycle

due to the increased bending stresses; hence to keep $\sigma_{bending}$ within the specified limit, the stage number should be reduced or the number of blades should be reduced and the blade chord length increased. Increasing the dopant concentration results in a lower enthalpy drop across the turbine stage and thus a larger mass flow rate is needed to produce the same plant power output. This means that larger tangential stresses are applied on the rotor blades. Nevertheless, if increasing the dopant concentration $[X_i]$ allowed for producing designs with the same number of stages, a higher total-to-total efficiency would be obtained as experienced with X_1 & X_2 and X_3 & X_4 at 550°C & 250 bar (*Case A*). The feasibility of these designs is not addressed in this paper inasmuch as assessing the mechanical integrity of the flow path requires a more detailed analysis which is beyond the criteria identified for

screening purposes at the mean-line design stage. It is worth highlighting that the discontinuity experienced in the turbine efficiency with respect to the molar fraction is the result of integer decision variables, namely the number of stages and number of blades, which must be adjusted in order to comply with the specified mechanical and rotordynamic limits. For example, for the 550 °C and 250 bar case with CO_2/$TiCl_4$, the number of stages is equal to 6 for a molar fraction of 14 and 15.5%, but as the molar fraction is increased to 17 and 20.5% the number of stages must be decreased to 5 to comply with the imposed constraints.

For the CO_2/SO_2 flow paths, increasing the inlet temperature from 550 to 700°C has a less significant effect on turbine efficiency and results in trends that are contradictory to those observed for CO_2/$TiCl_4$. Specifically, a small increase in efficiency is obtained for the low pressure case compared to the reduction in efficiency for the P_{opt} case. Increasing the inlet temperature for the CO_2/SO_2 blend results in a lower slenderness ratio for the same number of stages, and allows for a larger number of stages (Figure 5.4c). However, as discussed in the previous section, the CO_2/SO_2 flow path design allows for a larger number of stages than the CO_2/$TiCl_4$ case, and as a result increasing the number of stages further, beyond a certain limit, results in a less significant efficiency enhancement. This is due to the small change in hub diameters that results from increasing the number of stages, which is due to the small change in blade peripheral speed that is experienced.

To analyse the effect of increasing the temperature from 550 to 700°C, and setting turbine inlet pressure to P_{opt} for the CO_2/SO_2 flow paths, the turbine size parameter and volumetric expansion ratio are introduced. This is done to highlight the effect of the working fluid properties, cycle parameters and turbine size on the achievable turbine efficiency. The turbine size parameter is defined as $SP = \sqrt{\dot{V}_{out}}/\Delta H_s^{0.25}$, where ΔH_s is the isentropic enthalpy drop and $\dot{V}_{out}$ is the volumetric flow rate at the outlet. The volumetric expansion ratio is defined as (ρ_{in}/ρ_{out}), where ρ_{in} and ρ_{out} are the fluid densities at the turbine inlet and outlet respectively. For the low pressure cases of all blends, the resulting size parameters obtained are rather similar, although there are some differences in the volumetric expansion ratio. Contrary to the CO_2/$TiCl_4$ case, increasing inlet temperature for

the high-pressure case results in lower turbine efficiencies for the CO_2/SO_2 flow paths due to the significant reduction in turbine size parameter (SP), alongside the increase in volumetric expansion ratio, as indicated in Figure 5.5. Similar conclusions regarding the effects of pressure and temperature are obtained for the CO_2/C_6F_6 flow paths as reported in Figure 5.4b. For the three blends examined, a maximum absolute efficiency difference of 0.88% is obtained due to changing the molar fraction in the $CO_2/TiCl_4$ flow path at 700°C and 250 bar. This confirms that high efficiency turbines can be designed within the SCARABEUS project for the three candidate working blends over the range of boundary conditions examined.
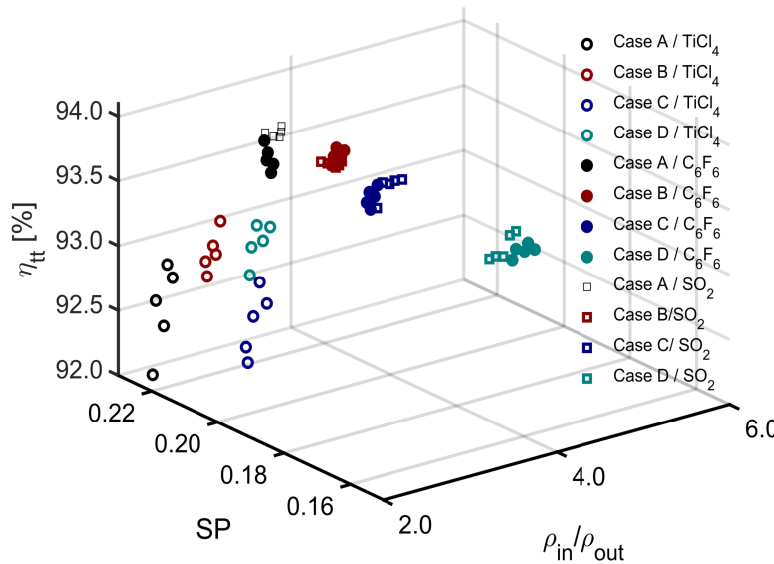
Figure 5.5: Turbine size parameter (SP) versus the volumetric expansion ratio (ρ_{in}/ρ_{out}) and the total-to-total efficiency (η_{tt})

In the cycle optimisation, the optimum dopant concentration was found to be 17, 14.5 and 30% for the 550°C and 250 bar inlet condition (*Case A*), for the $CO_2/TiCl_4$, CO_2/C_6F_6 and CO_2/SO_2 blends respectively. These values changed to 17 and 30% for 700°C and 250 bar (*Case B*) operating with $CO_2/TiCl_4$ and CO_2/SO_2 blends respectively. However, the turbine mean-line design indicates that optimal turbine efficiency is obtained at different molar fractions and this corresponds to 15.5, 10, 30% for *Case A*, and 14 and 30% for *Case B* for the same blends. Consequently, it can be observed that different optimum molar fractions are obtained from the perspective of cycle performance and turbine performance. For example, for the $CO_2/TiCl_4$ case, designing the turbine at the optimum cycle molar fraction

results in an absolute turbine efficiency drop of 0.52 and 0.23% compared to the optimum cycle design point for cases A and B, respectively. On the other hand, if the optimum cycle thermal efficiency is compared against the one calculated with the molar fraction that maximises the turbine efficiency, a drop of 0.5 and 1.05 percentage points is observed for cases A and B, respectively. A similar analysis for CO_2/C_6F_6 yields an absolute drop of 0.16$ in the turbine efficiency for *Case A*; the corresponding drop in cycle efficiency is 0.36 percentage points. Ideally, the optimal molar fraction should be identified through a coupled cycle-turbine design activity, whereby the cycle and turbine are simultaneously optimised. However, due to the complexity of the turbine design process, which includes multiple-stages and the need to manually iterate integer design variables to bring the turbine design within the imposed mechanical and rotordynamics, such an approach has not been adopted; such an approach could be explored in future research. Nonetheless, it is worth remembering that this behaviour exists. However, for the purposes of this current study, it is considered most suitable to design the turbine for the optimal molar fraction that maximises the thermal efficiency of the cycle.

Regarding turbine performance, the CO_2/SO_2 flow path designs achieve the highest efficiencies at an inlet temperature and pressure of 550°C and 250 bar and 700°C and 250 bar respectively. Similarly, the CO_2/C_6F_6 flow path designs achieve the highest efficiencies at an inlet temperature and pressure of 550°C and 250 bar. However, the $CO_2/TiCl_4$ flow path achieved the highest total-to-total efficiency (η_{tt}) at an inlet temperature and pressure of 700°C and P_{opt}. It is evident that increasing the inlet pressure for the CO_2/SO_2 blend at an inlet temperature of 700°C results in a smaller size parameter compared to the $CO_2/TiCl_4$ case. Therefore, the $CO_2/TiCl_4$ flow path is the best performing for the 700°C and P_{opt} case compared to the other flow paths, as indicated in Figures 5.5.

To further elaborate on the performance of the axial turbines operating with the different candidate blends, the change in specific work, blend molecular weight, bending stresses and mass-flow rate are presented in Figures 5.6a and 5.6b at the five different molar fractions. These figure are obtained at a turbine inlet temperature and pressure of 550°C and 250 bar respectively (case A).
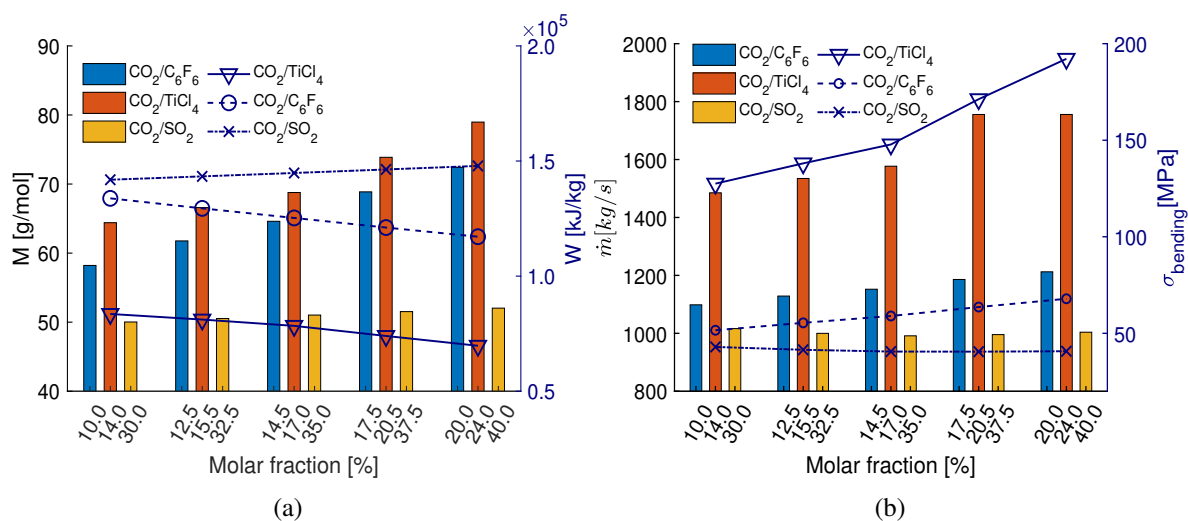
Figure 5.6: Molar fraction (X_i) versus (a) the molecular weight (M) and specific work (W), (b) mass flow rate ($\dot{m}$) and rotor bending stresses ($\sigma_{bending}$) for the same number of stages; the values on the right y-axis correspond to the line plot, while the values on the left y-axis correspond to the bar plot.

For the $CO_2/TiCl_4$ case, increasing the molar fraction of dopant (X_i) results in smaller hub diameters, taller blades and higher bending stress for the same number of stages (Figure 5.6b). This confirms the more significant reduction in the number of stages experienced by the $CO_2/TiCl_4$ case with the increasing concentration of dopant, compared to both CO_2/C_6F_6 and CO_2/SO_2. This is attributed to the significant increase in the mass-flow rate required to achieve the same net power output from the plant, which is due to the lower specific work of the $CO_2/TiCl_4$ blend compared to CO_2/C_6F_6 and CO_2/SO_2. The relative increase in mass flow rate with dopant concentration is much larger for $TiCl_4$ than for the other dopants. Although increasing the molar fraction of dopant, and hence the molecular weight of the blend, results in a lower specific work for CO_2/C_6F_6 and $CO_2/TiCl_4$, a slight increase is experienced in the CO_2/SO_2 case. Consequently, increasing the molar fraction results in designs with a lower number of stages for the $CO_2/TiCl_4$ and CO_2/C_6F_6 flow paths, which is necessary to allow for rotor bending stress and slenderness ratio within the specified limits; as a result more discontinuities are observed in the efficiency trends as shown in Figures 5.4a and 5.4b. However, for the CO_2/SO_2 case, increasing the molar fraction results in turbine designs with a larger number of stages, which is due to the larger enthalpy with increasing dopant concentrations, as indicated in Figure 5.6a.

166

5.4.2   Summary of flow path design details

Further to comparing the turbine aerodynamic performance, this section aims to summarise the flow path design details for the different blends at the optimum molar fraction. Tables 5.7 to 5.10 show the various design details for the $CO_2/TiCl_4$, CO_2/C_6F_6 and CO_2/SO_2 at different boundary conditions for *Case A*, *Case B*, *Case C* and *Case D*. This includes comparing the number of stages (n_{stage}), hub Diameter (D_{hub}), number of rotor blades (n), radial tip clearance (t_{cl}), chord length (c), blade height (h), diffusion angle (Δ), staggering angle (ζ), aspect ratio and total-to-total efficiency (η_{tt}).

The flow path designs at 550°C and 250 bar, *Case A*, experience the least number of stages, hence largest hub diameter, and the shortest flow path length with the smallest aspect ratio are obtained for the $CO_2/TiCl_4$ blend as shown in Figure 5.7a. The same conclusion can be deduced for the rest of the cases (Figures 5.7b, 5.8a and 5.8b); where the shortest flow path length is obtained for the $CO_2/TiCl_4$ as a result of the higher mass flow rate which constraints the number of stages to comply with the rotor bending stress limit. Furthermore, longer blade chords are obtained for the $CO_2/TiCl_4$ due to the smaller blade pitch resulting from the smaller number of blades specified for the design stages. This effect is highly experienced for the designs at 550°C and 250 bar (*Case D*). It is worth mentioning that all designs are produced with rotor chord size less than 100 mm based on the design methodology discussed in Section 3.3.2. It can be noticed that all designs operate with reduced number of rotor blades for the last stage. This is due to the increased rotor bending stresses resulting from the combination of a reduced density, enlarged flow area and increased blade heights. Compared to the other cases, the flow path designs at 550°C and 250 bar (*Case A*) experience the least number of stages, for all blends, with respect to the other cases operating at higher temperature and/or pressure (*Case B*, *Case C* and *Case D*).

Increasing the inlet temperature from 550 to 700°C, Figures 5.7a and 5.7b, results in longer flow path designs and hence, reduced hub diameter and better turbine performance. A maximum performance enhancement of approximately 1% is obtained for the $CO_2/TiCl_4$
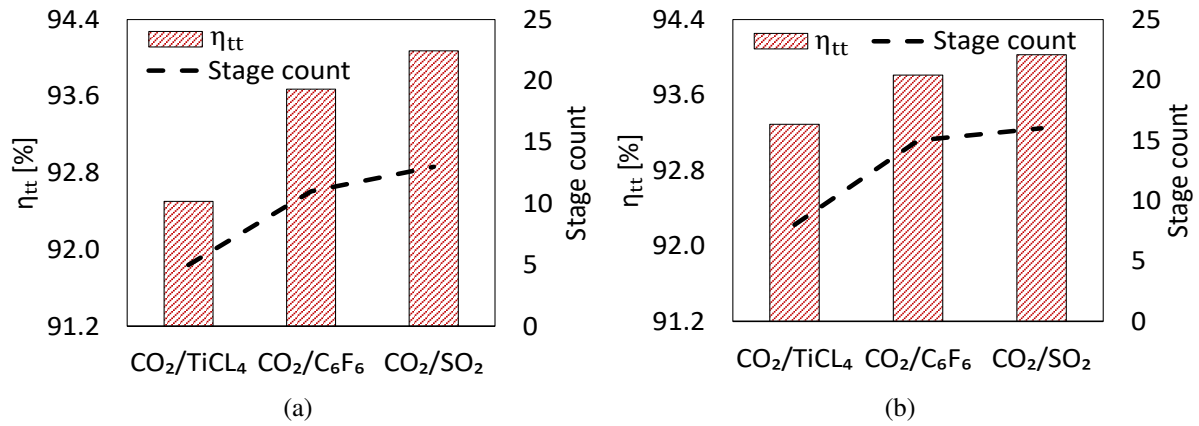
Figure 5.7: Stage count and total-to-total efficiency (η_{tt}) of $CO_2/TiCl_4$, CO_2-C_6F_6 and CO_2- SO_2 flow paths for (a) *Case A* and (b) *Case B*.

Table 5.7: Flow path design details for *Case A* the three candidate blends at optimum molar fractions.

Parameter	$CO_2/TiCl_4$		CO_2/C_6F_6		CO_2/SO_2	
	1st stage	last stage	1st stage	last stage	1st stage	last stage
Molar fraction [%]	17		14.5		30	
Number of stages [-]	5		11		13	
Hub diameter [m]	752		630		608	
Number of rotor blades	48	40	47	35	46	36
Radial tip clearance [mm]	0.59	0.65	0.51	0.63	0.51	0.61
Rotor chord length [mm]	61.65	77.80	53.67	81.89	53.70	77.22
Rotor blade height [mm]	47.55	82.68	50.72	130.32	58.10	129.92
Diffusion angle [°]	3.58	5.86	2.93	6.37	2.36	4.88
Staggering angle [°]	34.84	35.59	34.83	36.84	34.81	36.64
Aspect ratio [-]	0.77	1.06	0.94	1.59	1.08	1.68
Total-to-total efficiency [%]	92.50		93.68		94.07	

flow path. Whilst, an insignificant efficiency enhancement is observed for the other two flow path designs (CO_2/C_6F_6 and CO_2/SO_2).

Increasing the pressure at the same operating temperature (*Case A* versus *Case C* or from *Case B* versus *Case D*) results in a less significant performance enhancement or sensitivity in regards to the cycle analysis. For the turbine design, increasing the pressure results in longer flow path designs, and a larger number of stages, for all blends with a maximum increase and reduction in the total-to-total efficiency of 0.5% and 0.6% for the $CO_2/TiCl_4$ and CO_2/SO_2 blends respectively. Increasing the turbine inlet pressure for the 700°C case (*Case D*) results in up to 21-stage design for the CO_2/SO_2 case (Figure 5.8b). Therefore,

Table 5.8: Flow path design details for *Case B* the three candidate blends at optimum molar fractions

Parameter	$CO_2/TiCl_4$		CO_2/C_6F_6		CO_2/SO_2	
	1st stage	last stage	1st stage	last stage	1st stage	last stage
Molar fraction [%]	17		14.5		30	
Number of stages [-]	8		15		16	
Hub diameter [mm]	643		612		607	
Number of rotor blades	44	36	54	39	54	42
Radial tip clearance [mm]	0.53	0.60	0.50	0.62	0.50	0.60
Rotor chord length [mm]	58.94	77.52	45.34	72.51	45.38	65.47
Rotor blade height [mm]	56.64	102.54	48.49	136.98	53.95	124.23
Diffusion angle [°]	2.74	4.53	2.64	5.99	2.18	4.51
Staggering angle [°]	34.83	35.93	34.81	37.05	34.79	36.57
Aspect ratio [-]	0.96	1.32	1.07	1.89	1.19	1.90
Total-to-total efficiency [%]	93.29		93.81		94.03	

increasing the pressure results in more complicated designs with less overall efficiency. Hence, there is no benefit obtained for both the CO_2/SO_2 and CO_2/C_6F_6 flow paths from increasing the inlet pressure at 700°C. For all presented design cases, the CO_2/C_6F_6 & and CO_2/SO_2 flow paths experienced the longer blades in the later design stages with up to 137 mm rotor blade height for the CO_2/C_6F_6 flow path with an aspect ratio of 1.9 at 700°C and 250 bar. A maximum aspect ratio of 1.92 is obtained for the same blend operating at 700°C and P_{opt} with an efficiency of 93.2%. Given that the clearance gap is defined as a fixed percentage of the tip diameter, the clearance gap increases for the last turbine stages and a maximum clearance gap of 0.65 mm is obtained for the $CO_2/TiCL_4$ at 500°C and 250 bar.

For *Case A*, both the CO_2/C_6F_6 and CO_2/SO_2 flow paths experience similar velocity triangles due to accommodating a close number of design stages (11 versus 13). Nonetheless, the $CO_2/TiCL_4$ flow path operates with larger peripheral blade speed for the same loading coefficient due to accommodating less number of stages (5-stage) which resulted in larger axial velocity and hence, higher relative and absolute flow velocities (assuming constant axial velocities across the stages). The same can be concluded for *Case B*, *Case C* and *Case D*. According to the implemented design procedure where zero incidences have been assumed for the inlet flow angles, the absolute exit flow angle (α_3) is zero for the
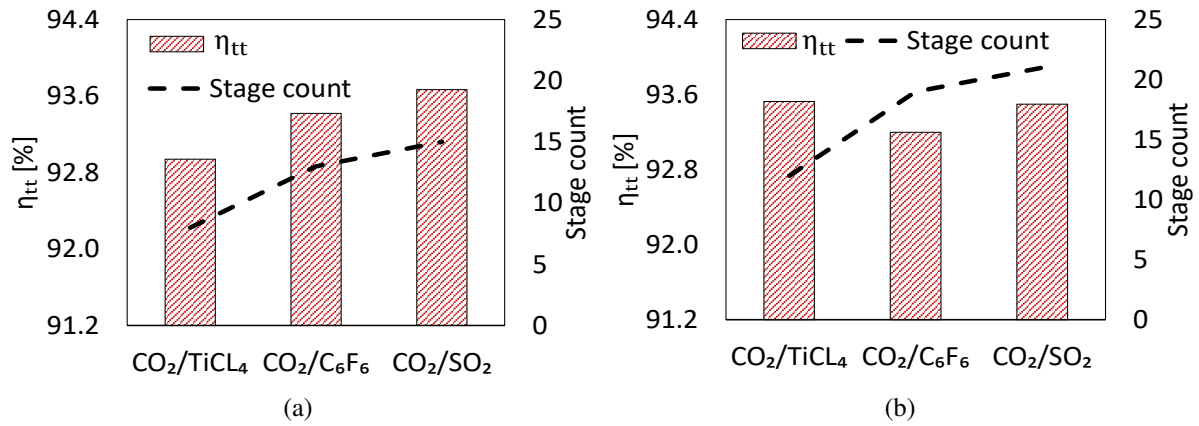
Figure 5.8: Stage count and total-to-total efficiency (η_{tt}) of $CO_2/TiCl_4$, CO_2-C_6F_6 and CO_2- SO_2 flow paths for (a) *Case C* and (b) *Case D*.

Table 5.9: Flow path design details for *Case C* the three candidate blends at optimum molar fractions

Parameter	$CO_2/TiCl_4$		CO_2/C_6F_6		CO_2/SO_2	
	1st stage	last stage	1st stage	last stage	1st stage	last stage
Molar fraction [%]	14		15		30	
Number of stages [-]	8		13		15	
Hub diameter [mm]	653		612		623	
Number of rotor blades	47	37	52	37	56	41
Radial tip clearance [mm]	0.52	0.59	0.49	0.60	0.50	0.60
Rotor chord length [mm]	55.13	75.23	46.56	74.53	43.99	67.23
Rotor blade height [mm]	46.69	91.74	41.45	120.26	42.48	111.88
Diffusion angle [°]	2.66	4.89	2.52	6.20	2.10	5.10
Staggering angle [°]	34.82	35.90	34.80	36.86	34.79	36.53
Aspect ratio [-]	0.85	1.22	0.89	1.61	0.97	1.66
Total-to-total efficiency [%]	92.94		93.42		93.67	

first design stages for all working fluids. However, it increases with the increased number of stages resulting in larger absolute outlet velocities (C_3). It is worth noting that all the flow paths are designed at constant loading and flow coefficient values of 1.0 and 0.5 and hence, the differences experienced in the velocity triangles are due to the differences in the peripheral blade speeds resulting from the difference in the enthalpy drop across the stages.

170

Table 5.10: Flow path design details for *Case D* the three candidate blends at optimum molar fractions

Parameter	$CO_2/TiCl_4$		CO_2/C_6F_6		CO_2/SO_2	
	1st stage	last stage	1st stage	last stage	1st stage	last stage
Molar fraction [%]	14		15.5		3	
Number of stages [-]	12		19		21	
Hub diameter [mm]	579		606		608	
Number of rotor blades	45	36	69	45	72	49
Radial tip clearance [mm]	0.48	0.56	0.47	0.59	0.47	0.57
Rotor chord length [mm]	52.05	71.43	34.20	60.30	33.05	54.38
Rotor blade height [mm]	52.81	106.53	31.53	115.82	34.58	103.2
Diffusion angle [°]	2.13 3.98	2.11	6.09	1.80	4.61	
Staggering angle [°]	34.80	36.22	34.78	36.97	34.77	36.52
Aspect ratio [-]	1.01	1.49	0.92	1.92	1.05	1.90
Total-to-total efficiency [%]	93.53		93.20		93.50	

5.4.3 Efficiency trends for the most technically feasible cycle

According to the thermal stability analysis and health and environmental considerations discussed in Section 2.2.3, alongside the current state-of-the-art in CSP power cycles, a precompression cycle operating with CO_2/C_6F_6 at 550°C could be considered to be one of the most technically feasible cycles. The analysis in this subsection focuses on this cycle in more detail, and aims to examine how the achievable turbine efficiency is influenced by the target inlet pressure and blend composition.

The contours of the optimal number of stages and the corresponding turbine isentropic efficiency are reported in Figures 5.9a and 5.9b for dopant concentrations ranging between 10 and 20% and turbine inlet pressures ranging between 240 and 300 bar. For the same molar fraction, increasing the inlet pressure results in a larger number of stages, and a lower turbine efficiency due to the increased pressure ratio and reduced mass flow rate. Similarly, for a fixed number of stages, increasing the molar fraction of dopant results in a lower turbine isentropic efficiency, where a molar fraction of 10% is found to yield highest overall turbine isentropic efficiency. Thus, for the CO_2/C_6F_6 blend, an increase in both the molar fraction and turbine inlet pressure results in a maximum drop in turbine efficiency of 0.4 points. Nonetheless, these results confirm that for the range of operating conditions considered, it is still possible to design a turbine flow path that can achieve a

171
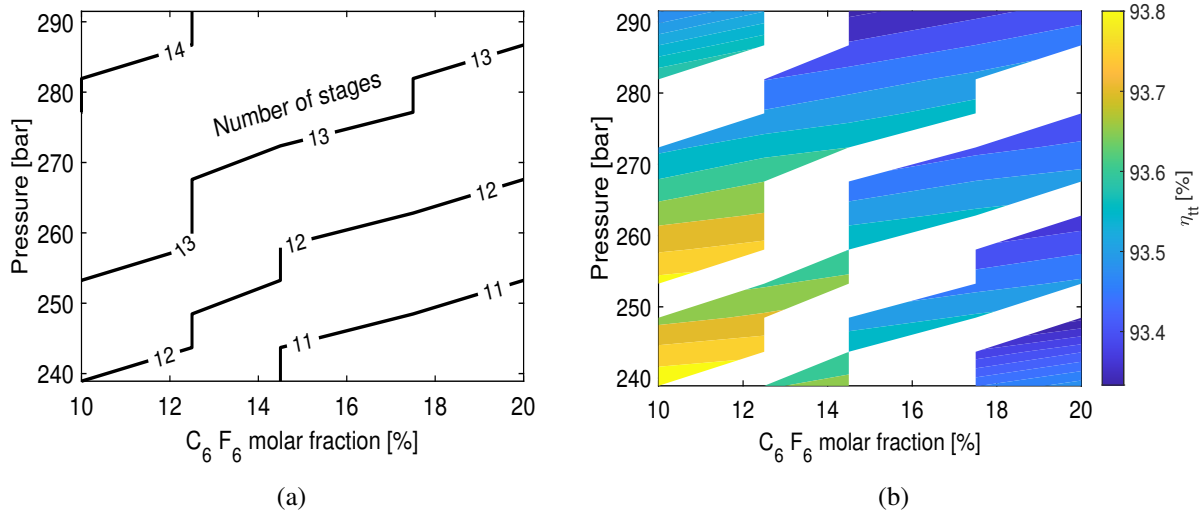
Figure 5.9: (a) Contour plot for the number of stages (b) contour surfaces for the total-to-total efficiency [%] of the CO_2/C_6F_6 flow path at 550°C and different pressures and molar fractions.

high isentropic efficiency.

5.5 Flow path designs for CO_2 blends compared to pure sCO_2

According to the aforementioned results, using sCO_2 blends resulted in a total-to-total turbine efficiency in excess of 92%. Nonetheless, the differences imposed by introducing CO_2 blends with respect to the pure CO_2 have not been discussed within the earlier analysis. Therefore, it is important to explore if any differences are imposed by introducing the CO_2 blends compared to the pure sCO_2 and also to highlight the impact of using CO_2 blends on the turbine performance compared to the pure CO_2.

This section aims to investigate the differences in the turbine flow path designed for pure CO_2 compared to CO_2 blends taking into account aerodynamic, rotordynamic and mechanical design aspects, as assessed during the mean-line design process. Multiple flow paths are designed for a large-scale axial turbine operating with $CO_2/TiCL_4$, CO_2/C_6F_6 and CO_2/C_6F_6 blends alongside pure CO_2. Given that the optimum cycle configuration was found to change with the selected blend, pre-compression and re-compression cycles were found to be optimum for the $CO_2/TiCL_4$, CO_2/C_6F_6 and CO_2/SO_2 blend. Consequently, the flow paths are firstly designed for the optimised cycle configurations and molar

172

fractions at a total inlet temperature of 973 K as presented in Section 5.4.

To have a fair comparison between the effect of the three-candidate blends on the flow path design with respect to the pure CO_2, recuperated cycle configurations are selected for all working fluids where the same power output is assumed for all designs. This is to overcome the differences in the turbine boundary conditions imposed by operating within pre-compression and re-compression cycle configurations for the CO_2/C_6F_6 and CO_2/SO_2 blends. The results of this analysis are discussed in Section 5.5.1. Furthermore, the comparison of the flow path designs is extended to address the axial turbine differences in the design dictated by the fluid properties by decoupling the turbine design from the cycle conditions. To achieve this aim, the flow paths are designed at a fixed volumetric flow rate and volumetric expansion ratio (Section 5.5.2).

5.5.1 Flow path comparison for fixed cycle configurations

Flow path designs are explained in this section for the three blends and the pure CO_2 at the boundary conditions summarised in Table 5.11 [16]. The boundary conditions for the CO_2 blends and pure CO_2 are obtained based on the cycle analysis conducted by Aqel et al. [16] and Manzolini et al.[18] respectively.

Table 5.11: Operating conditions for the pure sCO_2 and CO_2 blends for recuperated cycles.

Parameter	Pure CO_2 [18]	$CO_2/TiCl_4$ [16]	CO_2/C_6F_6 [16]	CO_2/SO_2 [16]
Mass flow rate [kg/s]	909	1393	1054	738
Inlet temperature [K]	973	973	973	973
Inlet pressure [MPa]	25	25	25	25
Outlet pressure[MPa]	10.52	10.10	7.74	7.40
Molar fraction [%]	-	17.4	16.7	26.4
Isentropic work[MW]	140	141	141	137.2

The flow paths design details for the 1st and last turbine stages are summarised in Table 5.12. It is evident from the presented results that pure CO_2 and CO_2 blends, operating with recuperative cycles, result in flow path designs with efficiency in excess of 92.5%. Though similar performance is predicted for all working fluids, there exist some differences between the flow path designs of the CO_2 blends with respect to the pure CO_2.

The CO_2/SO_2 results in the longest flow path design while $CO_2/TiCL_4$ results in the shortest flow path with the least number of stages due to experiencing the highest bending stresses. This is due to the thermo-physical properties of $CO_2/TiCL_4$ where the smallest specific work is obtained for the $CO_2/TiCL_4$ compared to the other working fluids. Therefore, a higher mass flow rate is needed to produce the same turbine power; a 89% mass flow rate higher than the CO_2/SO_2 case. Hence, larger tangential stress is applied to the rotor blades. Sixteen design stages are required for the CO_2/SO_2 compared to thirteen, twelve and seven stages for pure CO_2, CO_2/C_6F_6 and $CO_2/TiCL_4$ respectively.

It can be noticed that the design of CO_2/C_6F_6, CO_2/SO_2 and pure CO_2 are very similar with regards to the hub diameter (approximately 600 mm as shown in Figure 5.10) and chord length with the shortest chord length is obtained by the CO_2/SO_2 flow path. On the other hand, due to the high stresses experienced in $CO_2/TiCL_4$, a shorter flow path length and hence a larger hub diameter of 686 mm are obtained. Additionally, the highest aspect ratio is experienced in the last stage of CO_2/SO_2 flow path design followed by pure CO_2, CO_2/C_6F_6 and CO_2/SO_2.

Regarding the turbine performance, unlike the cycle analysis, where up to 6% enhancement is achieved by operating with pre-compression and re-compression cycles compared to a simple recuperated CO_2 cycle, a lower turbine efficiency is obtained by using CO_2 blends compared to the pure CO_2 case; where a maximum and minimum efficiency reduction of 1% and 0.2% are achieved for the $CO_2/TiCL_4$ and CO_2/C_6F_6 respectively.

Contrary to the results obtained by operating with pre-compression and re-compression cycles, designing the turbine flow paths within recuperated cycles resulted in different flow path designs for the CO_2/C_6F_6 and CO_2/SO_2; where the CO_2/C_6F_6 flow path is associated with less number of stages compared to the CO_2/SO_2 (12 versus 16 stages). For recuperated cycles with the same power output, a greater mass flow rate is required for the CO_2/C_6F_6, 1054 compared to 877 kg/s in the pre-compression cycle, based on the specific work obtained using the imposed boundary conditions. Hence, operating within a recuperated cycle results in higher bending stress and the number of stages is reduced for the CO_2/C_6F_6 from fifteen, for the pre-compression cycle (Figure 5.7b), to twelve stages to

comply with the mechanical and rotodynamic design criteria.
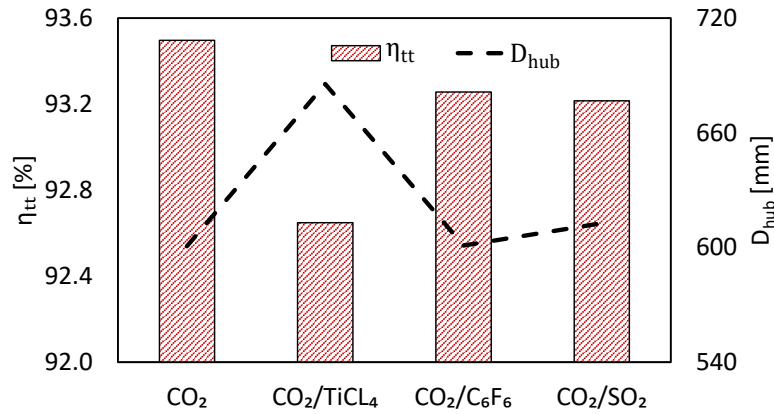
Figure 5.10: Hub diameter (D_{hub}) and total-to-total efficiency (η_{tt}) for the three blends for recuperated cycle configurations.

Table 5.12: Flow path design details for pure CO_2 turbine design compared to CO_2 blends for recuperated cycles.

Parameter	Pure CO_2		$CO_2/$ TiCl$_4$		CO_2/C_6F_6		CO_2/SO_2	
	1st stage	last stage	1st stage	last stage	1st stage	last stage	1st stage	last stage
Number of stages [-]	13		7		12		16	
Hub diameter [mm]	601		686		601		613	
Number of rotor blades	46	39	44	37	46	36	59	45
Radial tip clearance [mm]	0.52	0.59	0.56	0.62	0.50	0.60	0.50	0.60
Rotor chord length [mm]	54	69	62	79	53	76	42	61
Rotor blade height [mm]	67	118	55	99	54	123	49	113
Diffusion angle [°]	1.98	3.29	2.88	4.82	2.56	5.04	2.16	4.39
Staggering angle [°]	35	36	35	36	35	37	35	36
Aspect ratio [-]	1.24	1.71	0.88	1.24	1.03	1.63	1.19	1.87
Total-to-total efficiency [%]	93.50		92.65		93.26		93.22	

5.5.2 Fixed volumetric flow rate and expansion ratio

This section aims to explore if any differences in the design are introduced due to differences in the thermo-physical properties of the working fluids. To do this, the cycle and turbine are decoupled and the flow paths are designed at a fixed volumetric flow rate and volumetric expansion ratio; where the mass flow rate and outlet pressure for each blend are set to allow for a constant volumetric flow rate ($\dot{V}$) and expansion ratio (VR) of 9.4 m^3/s and 2.0, respectively, for all designs. The volumetric flow rate and expansion ratio are obtained at the average fluid density and specific heat ratio between the inlet and outlet conditions. Finally, an inlet pressure of 25 MPa and a molar fraction of 20% have been

set for all working fluids. A summary of the turbine boundary conditions is presented in Table 5.13.

Table 5.13: Operating conditions of pure sCO_2 and CO_2 blends at a constant VR and $\dot{V}$.

Parameter	Pure CO_2 [18]	CO_2/TiCl$_4$ [16]	CO_2/C$_6$F$_6$ [16]	CO_2/ SO$_2$ [16]
Mass flow rate [kg/s]	909	1514	1479	995
Inlet temperature [K]	973	973	973	973
Inlet pressure [MPa]	25	25	25	25
Outlet pressure[MPa]	10.52	10.65	11.2	10.49
Molar fraction [%]	-	20	20	20
Volume flow rate [m^3/s]	9.42	9.42	9.42	9.42
Volume expansion ratio	0.49	0.49	0.49	0.49
Average specific heat ratio [-]	1.212	1.197	1.23	1.22
Average density [kg/m^3]	96.4	160.65	159.97	105.56

For a volumetric flow rate and expansion ratio of 9.4 m^3/s and 2.0, respectively, thirteen and twelve turbine stages are obtained for the CO_2/SO$_2$ and pure CO_2 compared to six stages for CO_2/C$_6$F$_6$ and CO_2/TiCL$_4$ blends. Therefore, the CO_2/SO$_2$ design showed a similar hub diameter to the pure CO_2 blend, of approximately 600 mm (Figure 5.11), with a similar total-total efficiency of 93.9%. This is due to the similar density and specific heat ratio values for the CO_2/SO$_2$ at 20% molar fraction with respect to the pure CO_2. This results in similar mass flow rates, for the same volumetric flow rate and expansion ratio, and hence, similar number of stages are assigned for both designs (12 and 13). These design details are summarised in Table 5.14.

On the contrary, the CO_2/C$_6$F$_6$ results in the lowest total-to-total efficiency with respect to the pure CO_2 case; this is mainly due to designing the flow path with approximately half the number of stages of the pure CO_2 flow path which results in a larger hub diameter of approximately 700 mm. For the CO_2/C$_6$F$_6$ blend, a greater mass flow rate is needed compared to the pure CO_2 (in excess of 62%) to operate at the same volumetric flow rate and ratio. This results in much higher bending stresses acting on the rotor blades, and hence less stages are required to comply with the mechanical and rotor-dyanmic design criteria. Similar conclusions can be retrieved for the CO_2/TiCL$_4$ case which has a similar density with respect to the CO_2/C$_6$F$_6$. Therefore, similar turbine designs are obtained for
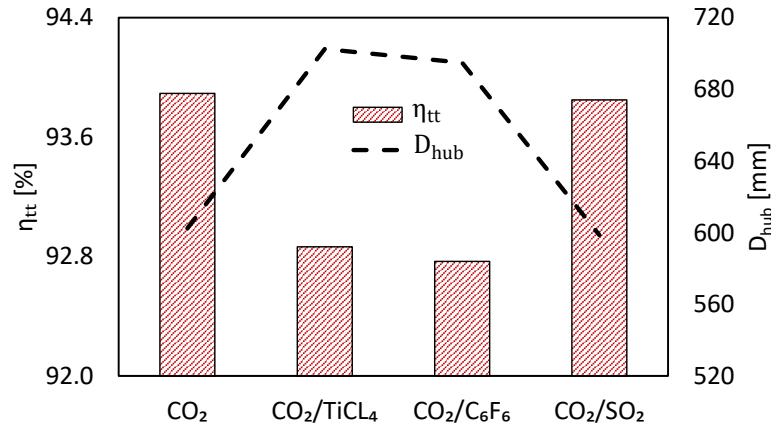
Figure 5.11: Hub diameter (D_{hub}) and total-to-total efficiency (η_{tt}) for the three blends at a fixed volumetric expansion ratio and flow rate.

both CO_2/C_6F_6 and $CO_2/TiCL_4$ blends.

Table 5.14: Flow path design details for pure CO_2 turbine design compared to CO_2 blends at constant VR and $\dot{V}$.

Parameter	Pure CO_2		CO_2/ $TiCl_4$		CO_2/C_6F_6		CO_2/SO_2	
	1st stage	last stage	1st stage	last stage	1st stage	last stage	1st stage	last stage
Number of stages [-]	13		6		6		12	
Hub diameter [m]	602		702		695		599	
Number of rotor blades	46	39	44	37	43	37	41	36
Radial tip clearance [mm]	0.52	0.59	0.57	0.63	0.57	0.62	0.51	0.59
Rotor chord length [mm]	54.02	69.35	63.78	80.37	64.71	79.69	60.36	74.88
Rotor blade height [mm]	66.65	117.95	54.84	93.50	55.94	94.24	67.47	118.91
Diffusion angle [°]	1.98	3.30	3.10	4.94	3.09	4.83	1.94	3.34
Staggering angle [°]	34.80	36.06	34.84	35.70	34.84	35.70	34.81	36.09
Aspect ratio [-]	1.23	1.70	0.86	1.16	0.86	1.18	1.12	1.59
Total-to-total efficiency [%]	93.89		92.86		92.77		93.85	

Ultimately, designing the turbine to operate within different cycle configurations results in similar flow path designs for both CO_2/C_6F_6 and CO_2/SO_2 blends. Whilst, designing the turbine to operate within fixed cycle configurations (recuperated) results in different designs for both blends and similar designs between the CO_2/C_6F_6 and pure CO_2. Decoupling the cycle conditions results in significant differences between the flow path designs of both CO_2/C_6F_6 and CO_2/SO_2 blends and similar flow path designs for the CO_2/SO_2 and pure CO_2. It can be noted that regardless of the cycle configuration, for all design cases, the $CO_2/TiCL_4$ blend results in designs with the shortest flow path length (with 6 to

8 design stages).

5.6   Design details of the selected flow paths

Further to considering the CO_2/C_6F_6 flow path at 550 $^\circ C$, as discussed in Section 5.4.3, CO_2/SO_2 at 700 $^\circ C$. It is worth mentioning here that the CO_2/C_6F_6 blends showed signs of thermal degradation at temperature above 600 $^\circ C$ [44] and hence, the CO_2/SO_2 is selected to operate at 700 $^\circ C$ due to its thermal stability at high temperatures. The SO_2 can be principally produced from different processes that allow for its operation at high temperatures; this includes the production during the combustion of coal in coal-fired power plants and volcanic eruptions [42]. Furthermore, it is not a flammable gas and does not react with air, water nor CO_2 and its ozone depletion potential is completely negligible. This conclusion should be confirmed with experimental results to verify the compatibility of the SO_2 with the material of the various power block components (stainless steel or Inconel) [42]. Nonetheless, the high toxicity level is one of the main drawbacks of using this compound. However, since it is to be implemented for closed cycles developed for CSP applications, the plants are located in dry regions and the power block is placed in a controlled ventilated environment, reducing its severe threats. Hence, the CO_2/SO_2 is considered in the current analysis at a lower molar fraction, of 20%, for reduced environmental hazards. A summary of the boundary conditions of the selected cases is reported in Table 5.15.

Table 5.15: Operating conditions for the CO_2/C_6F_6 and CO_2/SO_2 blends at 550 and 700 $^\circ C$ respectively.

Parameter	Unite	CO_2/C_6F_6	CO_2/SO_2
Inlet Temperature [T_{01}]	$^\circ C$	550	700
Inlet Pressure [P_{01}]	MPa	23.89	23.9
Outlet pressure [P_{03}]	MPa	6.1	8.15
Mass flow rate [$\dot{m}$]	kg/s	1152.22	827.06
Optimum molar fraction X_i	%	14.5	20

The flow path designs are produced for the $80\%CO_2/20\%SO_2$ and $85.5\%CO_2/14.5\%C_6F_6$ blends and the design details of both flow paths are summarised in Table 5.16. The optimum aerodynamic performance for the CO_2/SO_2 is achieved at a 14-stage flow path with a hub diameter of 624 mm and a total shaft length of 1.8 m. The meridional cross-section

of the 80%CO_2/20%SO_2 turbine flow path is shown in Figure 5.13, where the unfilled and filled shapes represent the stator and rotor blades respectively. Similarly, eleven stage design with a hub diameter of 630 mm and axial flow path length of 1.5 m is obtained for the CO_2/C_6F_6 flow path (Figure 5.12).
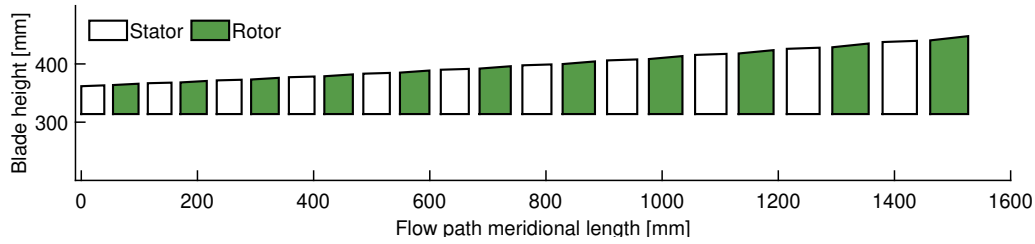
Figure 5.12: Turbine flow path meridional view for the CO_2/C_6F_6 blend.
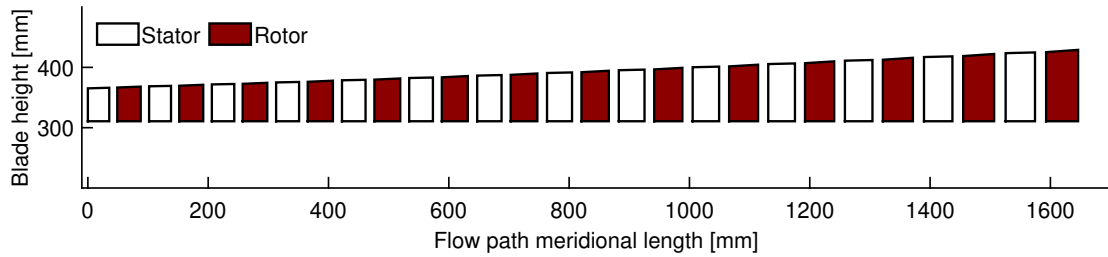
Figure 5.13: Turbine flow path meridional view for the CO_2/SO_2 blend.

Table 5.16: Flow path design details for the CO_2/C_6F_6 and CO_2/SO_2 blends.

Parameter	CO_2-C_6F_6		CO_2- SO_2	
	1st stage	last stage	1st stage	last stage
Molar fraction [%]	14.5		20	
Number of stages [-]	11.00		14.00	
Hub diameter [m]	630		624	
Number of rotor blades	47.00	35.00	53	42
Radial tip clearance [mm]	0.51	0.63	0.52	0.60
Rotor chord length [mm]	53.67	81.89	47.58	66.11
Rotor blade height [mm]	50.72	130.32	56.37	116.43
Diffusion angle [°]	2.94	6.31	2.2	4.1
Staggering angle [°]	34.83	36.84	34.80	36.26
Aspect ratio [-]	0.95	1.60	1.19	1.77
Total-to-total efficiency [%]	93.68		93.86	

179

The velocity triangles of both designs are obtained; where the triangles for CO_2/SO_2 and CO_2/C_6F_6 are quite similar owing to the fact that both flow paths are designed at constant flow coefficient, loading coefficient and degree of reaction of 0.5, 1.0 and 0.5 respectively. The CO_2/SO_2 enter the stator blade row at a zero incidence angle with $\alpha_1 = 0$ where it expands and hence, speeds up in the stator blades till reaching an absolute flow velocity of 120 m/s and exits at an absolute angle $\alpha_2 = 63.4°$. Then the fluid enters the rotor blades with the same velocity and continues to expand in the rotor blades with a specified degree of reaction of 0.5. As a result, the working fluid leaves the rotor blades with a relative flow angle of $\beta_3 = 63.4°$ and a relative flow velocity $w_3 = 53.5 m/s$.

The turbine design has an inlet stator annulus area of 0.12 m^2 and an outlet annulus area of 0.28 m^2 and stator inlet blade height of 55 mm and a rotor outlet blade height of 116 mm. As a consequence of the increased blade heights at the last turbine stage, higher bending stresses are experienced with the later design stages in comparison with the earlier stages. It is worth mentioning that all the flow path designs presented in the current study have similar velocity triangles to the CO_2/SO_2 blend (Figure 5.14) due to designing them at a constant loading coefficient, flow coefficient and degree of reaction of 1.0, 0.5 and 0.5 respectively.
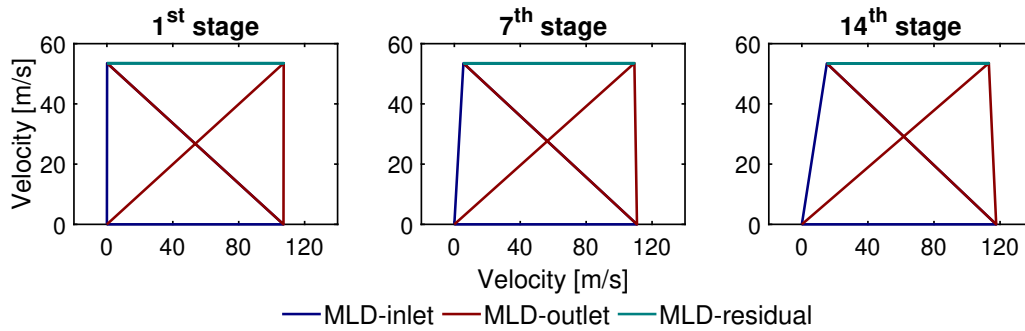
Figure 5.14: Velocity triangles the CO_2/SO_2 flow path.

5.6.1 Parametric study

In view of the fact that the previous flow paths were designed at fixed design parameters, further analysis has been conducted to investigate the effect of aerodynamic design vari-

ables such as the flow coefficient (ϕ), loading coefficient (ψ), degree of reaction (Λ) and pitch-to-chord ratio (s/c) on the performance of axial turbines operating with CO_2 blends.

A parametric study is presented in this section to investigate the effect of the design variables on the performance and flow path designs of both CO_2/C_6F_6 and CO_2/SO_2 blends operating within precompression and recompression cycles respectively. The goal of this section is to explore whether there is any advantage in further modifying the design parameters with the goal of further improving the efficiency of the turbine. A summary of the boundary conditions for the CO_2/C_6F_6 and CO_2/SO_2 flow paths is shown in Table 5.16.

Within this analysis, the effect of changing these design parameters on the aerodynamic turbine performance and flow path design was investigated considering constrained (CD) and non-constrained (NCD) design criteria. This is to highlight the effect of changing those parameters from a purely aerodynamic standpoint compared to considering both rotordynamic and mechanical design considerations throughout the design process.

For the non-constrained criteria, the turbine aerodynamic performance is investigated for a given number of stages and number of rotor blades, over a wide range of design variables, and the constraints imposed on the rotor bending stress and slenderness ratio are removed. Whilst, in the constrained criteria, new turbines are designed over a range of design variables ϕ, ψ, Λ, s/c considering the rotordynamic and mechanical design criteria. This means that for the non-contained criteria, the aerodynamic performance is investigated for a fixed design (with a fixed number of stages and rotor blades) at variable design parameters. However, different turbine flow paths with different numbers of stages and blades are designed for the constrained design criteria (Section 3.3.4).

Figure 5.15 shows the parametric analysis results for the CO_2/C_6F_6 flow path where both constrained (CD) and non-constrained (NCD) design cases are considered. Considering that ϕ, ψ, Λ vary across the stages, the plotted values in Figures 5.15a to 5.15d are the arithmetic averages of the properties across the stages.

To investigate the effect of changing the loading coefficient (ψ) on the performance of the CO_2/C_6F_6 flow path, ψ was varied between 0.8 and 1.5 while fixing the flow co-

181

Figure 5.15: The (a) loading coefficient [ψ], (b) flow coefficient [ϕ], (c) degree of reaction [Λ],and (d) pitch-to-chord ratio [s/c] effect on total-to-total efficiency [η_{tt}] for constrained (CD) and non-constrained designs (NCD) operating with CO_2/C_6F_6 blend.

efficient, degree of reaction and pitch to chord ratio to 0.5, 0.5 and 0.85 respectively. For the non-constrained case, denoted by the red line, the loading coefficient was varied between 0.8 and 1.5 for the flow path designed at a loading coefficient of 0.8; where fourteen stages are required to comply with the design criteria. Increasing the ψ results in lower blade velocities hence smaller hub diameter and higher total-to-total efficiency (η_{tt}). The increase in the loading coefficient from 0.8 results in an efficiency increase until a loading coefficient of 1.2 then the efficiency decreases slightly. Further increase in the loading coefficient results in efficiency reduction as shown in Figure 5.15a.

Increasing the loading coefficient over the range from 0.8 to 1.5 for the constrained turbine design, denoted by the black line, results in higher static bending stresses on the rotor

blades and hence, designs accommodate a small number of stages. Reducing the number of stages results in higher peripheral blade speeds, larger hub diameters and hence reduced total-to-total efficiency. From a pure aerodynamic standpoint, increasing the loading coefficient from 0.8 to 1.5 results in an efficiency enhancement of almost 1.1 percentage points. Nonetheless considering the rotor-dynamic and mechanical design constraints, increasing the loading coefficient over the examined range results in efficiency reduction by around 4 percentage points. This significant reduction in the total-to-total turbine (η_{tt}) efficiency is a result of the number of stages reducing from fourteen to five stages to keep the bending stresses within the threshold limit (130 MPa).

To investigate the effect of the flow coefficient (ϕ) on the turbine performance, the analysis has been repeated at a fixed loading coefficient, degree of reaction and pitch-to-chord ratio of 1.0, 0.5 and 0.85 respectively and the flow coefficient was varied between 0.3 and 0.7. For the non-constrained case, denoted by the red line, the flow coefficient was varied between 0.3 and 0.7 for the turbine design developed at a flow coefficient of 0.3; where six stages are required to comply with the design criteria. Increasing ϕ for the same turbine design, for the same number of stages and rotor blades, at the same boundary conditions results in a lower turbine efficiency (Figure 5.15b) owing to the increase experienced in the flow velocities and hence, flow losses.

For the constrained turbine design, donated by the black line, increasing the flow coefficient results in lower bending stresses, and hence allows to accommodate more stages. This results in smaller hub diameters, and enhanced turbine performance (η_{tt}). This effect is experienced up to an optimum ϕ of 0.5 for a constrained design where afterwards the efficiency deteriorates. Increasing the flow coefficient (ϕ) over the specified range, from 0.3 to 0.7, results in efficiency reduction by up to 2.6%. Nonetheless, taking into account the mechanical and rotor-dyanmic design constraints allows for efficiency enhanced by up to 2.0 percentage points; where the number of stages increases from six to thirteen stages for the C_6F_6 flow path.

As for the effect of the degree of reaction (Figure 5.15c), the non-constrained and constrained designs experience the same effects for increasing the degree of reaction from

0.3 to 0.45; where an efficiency increase is achieved. It is worth noting the constrained design analysis was carried out for twelve-stage design operating with a degree of reaction of 0.3. Increasing the degree of reaction beyond 0.45, for the constrained design, results in higher stresses on the turbine blades due to the higher pressure drop across the rotor blades and hence, less number of design stages and less turbine performance. Increasing the degree of reaction over the specified range results in total-to-total efficiency (η_{tt}) increase by approximately 0.5 percentage points for the constrained turbine design.

Furthermore, increasing pitch to chord ratio (s/c) from 0.80 to 0.85 results in better turbine efficiency as indicated in Figure 5.15d for the non-constrained turbine design due to reducing the blade chord size and hence less tip clearance losses; less chord to blade height ratio and less clearance losses. The effect of changing the pitch-to-chord ratio was investigated for a twelve-stage design generated at a pitch-to-chord ratio of 0.8. The opposite effect is obtained for the constrained turbine design where increasing s/c results in higher bending stress and therefore the design should accommodate less stages. Ultimately, the effect of changing the pitch-to-chord ratio does not have a significant effect on the turbine performance as noticed from the parametric study results due to the narrow range considered for this analysis. Nonetheless, considering a wider range would result in more significant effects.

Given that the effect of changing both the flow and loading coefficients is found to be significantly affecting the performance of the turbine compared to the rest of the parameters, new flow paths are designed for the CO_2/C_6F_6 blend at different loading and flow coefficients (ψ and ϕ) and at a constant degree of reaction and pitch-to-chord ratio of 0.5 and 0.85 respectively. Figure 5.16a and 5.16b shows the stage count and the total efficiency obtained at different ψ and ϕ for constrained turbine designs. Increasing the flow coefficient, while keeping the rest of the parameters fixed, allows for accommodating more stages and hence, the efficiency increases (as indicated in Figure 5.15b). Whilst, increasing the loading coefficient, while keeping the rest of the parameters fixed, results in less turbine stages and hence, less efficiency (as indicated in Figure 5.15a). Combining both effects together, by allowing the flow and loading coefficients to vary simultaneously at a

fixed degree of reaction and picth-to-chord ratio of 0.5 and 0.85 respectively, results in an increase in the number of stages in some designs. However, in other cases, the slenderness ratio limits the design stages as shown in Figures 5.16a and 5.16b.

By comparing the results obtained at different values of ψ & ϕ to the baseline flow path designed at $\psi = 1.0$ and $\phi = 0.5$, it is observed that the maximum efficiency of 93.8% can be obtained at $\psi = 0.8$ and $\phi = 0.6$. This corresponds to an efficiency enhancement of 0.2%, where the number of stages is increased from fifteen stages compared to eleven stages for the baseline design case. Bearing in mind that increasing the number of stages adds challenges related to the complexity and the cost of the turbine, some consideration of stage number and efficiency enhancement should be should be taken into account. In this capacity, the maps reported in Figures 5.16a and 5.16b give an indication of the number of stages needed to achieve high turbine performance. In this regard, to achieve an efficiency greater than 93% (i.e., the yellow area in Figure 5.16b), the turbine should be designed with the number of stages ranging from nine to fifteen; in this range efficiencies of 93.1 and 93.8% are obtained for the designs with nine and fifteen stages designs respectively, with an efficiency difference of 0.69 percentage points).

(a)   (b)
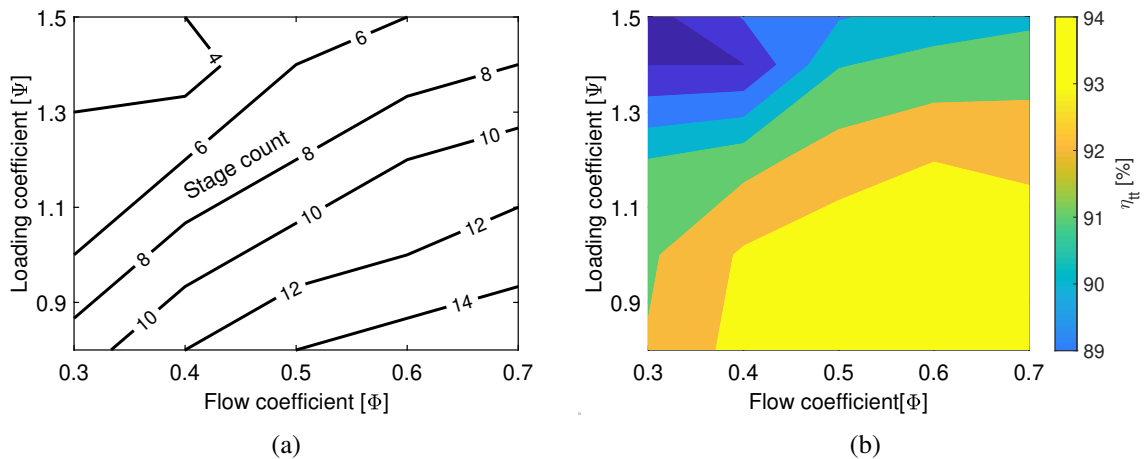
Figure 5.16: (a) Stage count at different loading (ψ) and flow coefficients (ϕ) (b) Total-to-total turbine efficiency η_{tt} at different loading (ψ) and flow coefficients (ϕ).

It is worth mentioning that the same analysis is carried out for the CO_2/sCO_2 flow path and the same conclusions are drawn (Figures 5.17a to 5.17d). However, some differences are observed in the trends of efficiency with varying flow coefficients. This is due to a lower

sensitivity of the CO_2/sCO_2 bending stress to the flow coefficient compared to CO_2/C_6F_6. This behaviour is due to the differences in the thermo-physical properties of both working fluids.
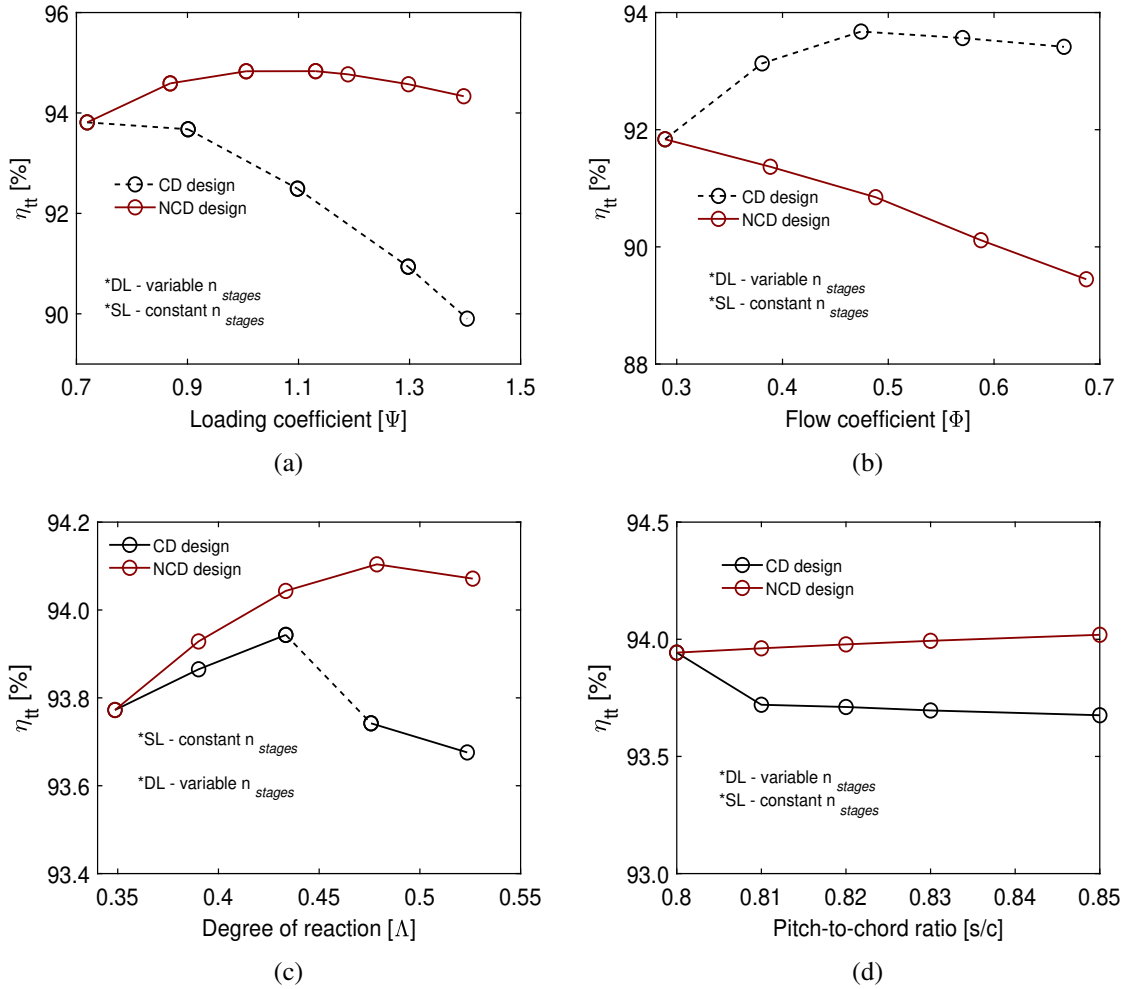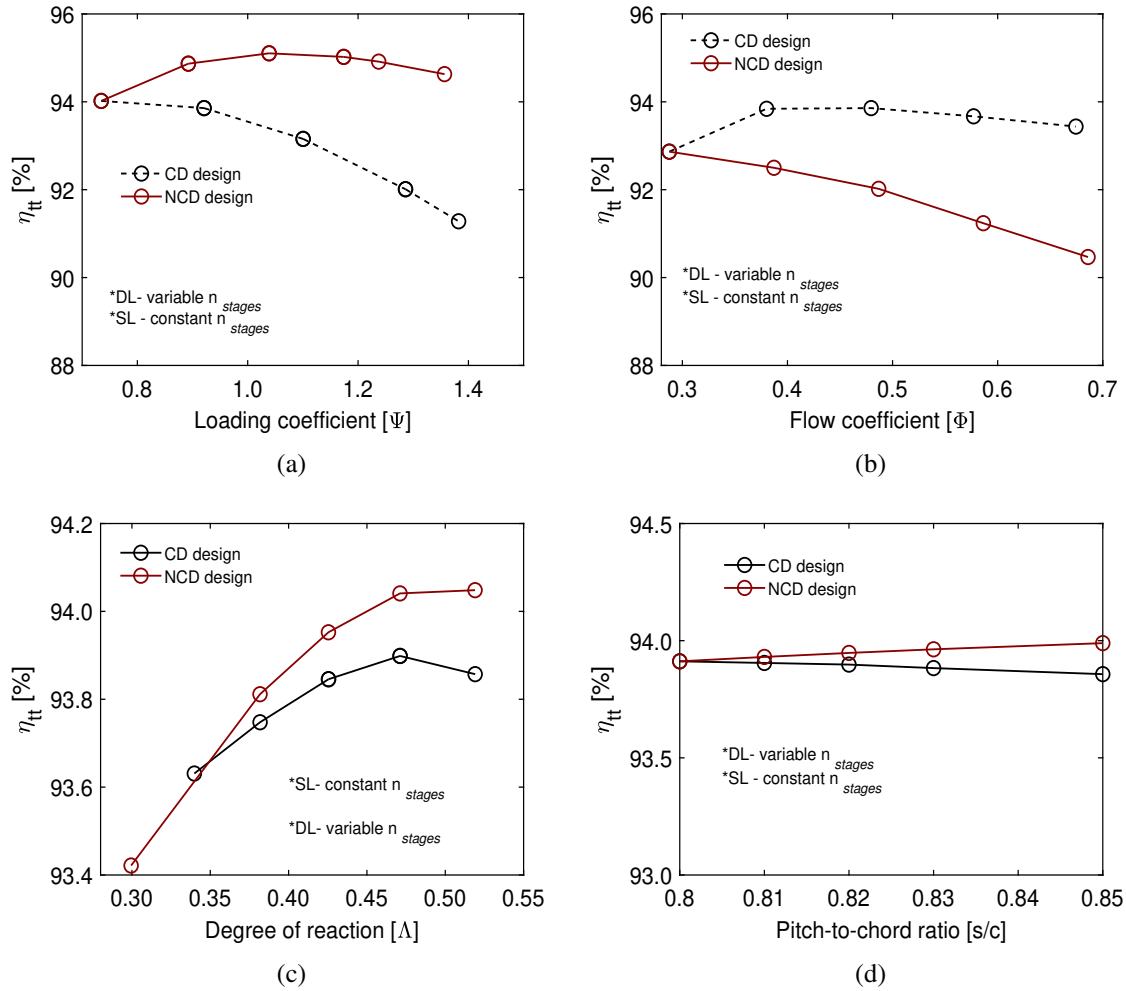

Figure 5.17: The (a) loading coefficient $[\psi]$, (b) flow coefficient $[\phi]$, (c) degree of reaction $[\Lambda]$, and (d) pitch-to-chord ratio $[s/c]$ effect on total-to-total efficiency $[\eta_{tt}]$ for constrained (CD) and non-constrained designs (NCD) operating with CO_2/SO_2 blend.

5.6.2 Preliminary cost assessment

Though the preliminary 1D design methodology, presented in Chapter 3, is integrated with mechanical and rotordynamic design criteria to limit the mechanical bending stress and the axial length of the flow path, a detailed analysis should be carried out to assess the mechanical integrity of the 3D turbine design. Consequently, within the context of the SCARABEUS project, following the preliminary flow path design, the 3D blades were

generated and optimised in a different research framework using CFD simulations. Subsequently, ongoing activities are being carried out by the project industrial partners to proceed further with the generated 3D blades and finalise the detailed turbine design; this includes designing the inner/outer turbine casings considering the manufacturability constraints, designing the main cooling streams, selecting the bearing, seals, and coupling and finally conducting a detailed mechanical integrity and rotordynamic stability analysis for the shaft arrangement. Furthermore, this task extends to material selection considering investigating the material compatibility with the working fluids. Moving onwards with the material selection should allow for providing an overall cost assessment of turbine components. It is worth mentioning that a test loop is constructed to validate the SCARABEUS technology through a 300-hour testing period, which includes the manufacturing and demonstration of components such as the air-cooled condenser and recuperator. The test loop will be utilised to validate the heat exchanger design as well as certain properties of the working fluids, including vapour liquid equilibrium. Nonetheless, a turbine prototype is not considered within the project test loop; it is rather replaced by a throttling valve to model the expansion process. Therefore, experimental data will not be available to validate the turbine design results.Ultimately, Life Cycle Assessment (LCA) and natural capital assessment will be performed within the project work packages to understand and evaluate the environmental and social impacts of the SCARABEUS technology.

In view of the fact that longer flow path designs were found to be optimum from an aerodynamic standpoint with respect to other designs with shorter axial lengths, a cost assessment should be carried out to investigate the financial feasibility of the 14-stage turbine design operating within $80\%CO_2/20\%SO_2$ in a recompression cycle. Consequently, alongside the detailed cost assessment being conducted by the project industrial partners, this section presents a preliminary cost assessment for the different flow path designs; this includes comparing the overall machine cost for designs accommodating a small number of stages versus a large number of stages over the range from 4 to 14 stages. The cost analysis assumptions and steps are summarised based on Baker Hughes [161] experience in a few parameters that can be easily evaluated using the mean-line design flow path parameters:

- The overall machine cost is the sum of two main components: the direct material cost and labour cost. The direct material cost is the cost associated with the material required for each turbine component, whereas the labour cost covers the machining cost of the different turbine components and the assembly cost of the whole machine

- The direct material cost is associated with the bulk cost of the inner casing, outer casing, shaft, blading, balancing drum, and shaft ends that include dry gas seals, coupling and bearings. The direct cost is evaluated based on the volume and weight of the different turbine components.

- Machining cost is the cost estimated for the manufacturing of the different machine parts such as casing and blading. Hence, this cost is calculated based on the machined surface areas. It is not feasible to quantify the machining cost associated with the different parts. As such, only the direct material cost is considered owing in this preliminary analysis.

- The coating (cladding) cost is considered within the estimated expenses. This is related to the inner surface of the outer casing of the machine to avoid direct contact between the stainless steel and working fluid.

- Assembly cost of the whole machine is considered to be similar for all designs. Since the same architecture is applied for all designs, with differences only in the axial and radial dimensions of the machine, the overall assembly cost of the turbine is not expected to be vary significantly. Nonetheless, some differences are expected in the assembly cost of the inner casing and rotor for the different designs. Unfortunately due to the simplified nature of this analysis, it is not manageable to address those differences.

- The cost associated with other sub-components, such as valves, is excluded from the analysis. Principally, valve selection is a function of the volume flow rate of the working fluid flowing through the machine. Since all machines are designed at a similar volumetric flow rate, the cost is assumed to be similar for each design.

- Although the cost associated with the shaft ends may have significant impact on the machine cost, it is not taken into account within this preliminary cost assessment. It is worth mentioning that the cost associated with the shaft end dimensioning is

with certainty larger for large machines with less number of stages. Thus, if the machine with a longer flow path resulted in less overall cost without considering the shaft end dimensioning costs, it would be evident that the calculated cost saving is underestimated in the current procedure compared to the actual savings.

- The suction and discharge nozzles are not functions of the machine size (i.e., axial and radial dimensions), and therefore their costs are not included in the analysis.

- Maintenance and running costs can be rationally assumed similar for all design cases.

5.6.3   Cost estimation methodology

5.6.3.1   Direct Material Cost

The direct material cost is associated with the bulk cost of the different machine components and hence, it is estimated using the components weight. The weight can be expressed as a function of the component volume and density of the manufacturing material as follows:

$$m = \rho V \tag{5.1}$$

The inner and outer casings are exposed to circumferential stresses due to the pressure gradient applied at the inner surface of the casing. Therefore, the thickness of the casing should be scaled for all designs according to the operating diameter to keep conservative hoop stresses. Circumferential stresses applied to the casings can be expressed as follows:

$$\sigma = \frac{PD}{2t} \tag{5.2}$$

where P is the applied pressure, t is the thickness, σ: is the hoop stress, and D is the inner diameter. For conservative stresses, σ should be the same for all examined designs as the inner and outer casing are assumed to be manufactured using nickel-based alloys and stainless steel, respectively, for all designs. Thus:

$$\left[\frac{D_{tip}}{2t}\right]_D = \left[\frac{D_{tip}}{2t}\right]_{ref} \tag{5.3}$$

189

Hence:

$$\frac{[D_{tip}]_D}{[D_{tip}]_{ref}} = \left[\frac{t_D}{t_{ref}}\right] \tag{5.4}$$

Using the above relation, the scaling factor of the radial dimensions of the machine is defined as a ratio of the tip diameters for each design. Hence, Radial Scale Factor (RSF) can be expressed as:

$$RSF = \frac{[D_{tip}]_D}{[D_{tip}]_{ref}} \tag{5.5}$$

where the subscript D and ref corresponds to the investigated design & the the reference design (14-stage) respectively.

To evaluate the overall axial length of the machine, the axial dimension of the machine is scaled using a defined axial scaling factor. The axial length of the machine is composed of the flow path axial length and the axial length of the balancing drum. Principally, the balancing drum is mounted on the rotor to balance the axial thrust force acting on the blades, where the total axial thrust is obtained as the sum of forces acting on an individual rotor. Whereas thrust bearings are used to withstand the residual thrust which is not compensated by the balancing drum. To account for the axial and radial dimensions of the balancing drum in the current analysis, it has been found based on industrial experience that a balancing drum with a diameter equal to the hub diameter of the machine is required to balance the axial thrust forces acting on the blades. Whilst, a constant aspect ratio for the drum is assumed to obtain the axial length of the drum. The drum aspect ratio of the 14-stage design is used as the reference point for the rest of the designs. Hence, the Axial Scale Factor (ASF) can be expressed as:

$$ASF = \frac{[l_f + l_b]_D}{[l_f + l_b]_{ref}} \tag{5.6}$$

where l_b the axial length of the balancing drum and l_f is the flow path axial length. The flow path axial length and can be obtained as follows:

$$l_f = \sum_{[stages)} [(b_x)_R + (b_x)_S + 2\ ss] \tag{5.7}$$

190

where $(b_x)_R$ and $(b_x)_S$ are the axial chord lengths of the rotor and stator respectively and *ss* is the axial spacing between the stator and rotor.

With the known RSF and ASF, the Weight Scale Factor (WSF) for the casing and the rotor shaft can be expressed as:

$$WSF = \frac{m_D}{m_{ref}} = \frac{[\rho V]_D}{[\rho V]_{ref}} \tag{5.8}$$

For the same manufacturing material, and hence the same density, the Weight Scale Factor (WSF) can be expressed as:

$$WSF = \frac{[D_{tip}]_D \left[l_f + l_b\right]_D}{[D_{tip}]_{ref} \left[l_f + l_b\right]_{ref}} = RSF^2 ASF \tag{5.9}$$

For the turbine blades, the WSF is defined as the ratio of the total blade volume between two different designs. In addition to accounting for the weight of the stator and rotor blades, the weights of the rotor shroud and roots are also considered within the analysis. The weight of the rotor shroud and roots are specified as a percentage of the weight of the airfoil. This percentage is specified based on the rotor design for the 14-stage turbine, where two different root and shroud sizes are set for the airfoils based on their chord size. With the known total weight of the rotor, the cost is calculated as a function of the weight ratio of the rotor design with respect to the reference 14-stage design. The WSF for the blades can be expressed as a function of the blade volume (V) as follows:

$$WSF_{blades} = \frac{V_D}{V_{ref}} \tag{5.10}$$

5.6.3.2 Machining and labour cost

Principally, machining cost is associated with the machining of the different parts that can be quantified based on the machined area to several categories (A, B, C &D):

$$ASF\left[A\right] = RSF^2 \tag{5.11}$$

$$ASF\,[B] = RSF \times ASF \tag{5.12}$$

$$ASF\,[C] = STSF \tag{5.13}$$

where $ASF\,[A]$, $ASF\,[B]$ and $ASF\,[C]$ are the scale factors for machining area categories 'A', 'B', 'C' respectively and STSF is the stage number scaling factor.

To quantify the total machining cost, the cost for categories 'A', 'B', 'C' should be added in addition to considering category 'D' cost which is associated with bolting at the inlet and exhaust nozzles for all machines (which is the same). Nonetheless, doing so is not feasible to be carried out for the current analysis stage which is a limitation of this simplified analysis.

As for the cladding cost, the area scale factor is used to scale the cladding cost with respect to the 14-stage turbine design which is defined as:

$$[ASF]_{cladding} = RSF \times ASF \tag{5.14}$$

5.6.4   Cost analysis

Using the different scale factors, as defined in the cost estimation methodology, Section 5.6.3, allows for a comparison between the cost of the different machine sizes (from 4 up to 14 stage designs). To proceed with the cost analysis, the material should be first selected for the different machine components. On this matter, preliminary test results are used as a reference for the material selection process. However, due to the confidentiality of these tests, the results are not disclosed in the current analysis. Different nickel-based alloys are selected for the machine shaft, blading and inner casing, whilst stainless steel is selected, with the inner coating (cladding), for the outer casing of the machine. Despite the different materials selected for the components, a fixed cost of nickel-based alloys is considered for all mentioned parts for the sake of simplicity and confidentiality. In this regard, nickel-based alloys are assumed to be at an order of magnitude of the stainless steel. Whilst, the cladding material is considered to be two orders of magnitude of the nickel-based alloy material cost per square meter.

Given that the analysis is carried out with respect to a reference case, the 14-stage design, the weight of the inner casing, outer casing and shaft are specified based on the machine design shared by the project industrial partners (Table 5.17). Further to the specified weights, the cost of nickel-based alloys, stainless steel and cladding are specified as shown in Table 5.17. Two different costs are considered in this analysis which are defined as cost 'A' and cost 'B'. Then the overall machine cost is estimated with respect to the 14-stage design to compare the cost of designing a turbine with a shorter axial length and larger radial dimension with respect to designs with longer axial length and smaller radial dimensions.

Table 5.17: Components weight for the 14-stage machine and cost per kg of material.

Component	Weight [kg]	Cost 'A'	Cost 'B'
Inner casing	22700	60 €/Kg	100 €/Kg
Outer casing	48000	10 €/Kg	10 €/Kg
Shaft	7700	60 €/Kg	100 €/Kg
Stator blades	188	60 €/Kg	100 €/Kg
Rotor blades	504	60 €/Kg	100 €/Kg
Outer casing cladding	-	20 k €/m^2	20 k€/m^2

The total weight of the machine (W_T) can be expressed using the different scale factors as:

$$W_T = WSF\left[W_{ref \cdot IC} + W_{ref \cdot OC} + W_{ref \cdot S}\right] + WSF_{blades}\left[W_{ref \cdot BR} + W_{ref \cdot BS}\right] \quad (5.15)$$

where $W_{ref \cdot}$ is the weight of the reference machine (14-stage), and OC, IC, S, BR and BS subscripts stand for the outer casing, inner casing, shaft, rotor blades and stator blades respectively. The difference in weight (ΔW) can be expressed as:

$$\Delta W = W_D - W_{ref \cdot} \quad (5.16)$$

Then, the difference in machine cost Δ DMC in euros can be defined for cost 'A' as:

$$\Delta \text{DMC} = 60\left[\Delta W_{IC} + \Delta W_S + \Delta W_{BR} + \Delta W_{BS}\right] + 10\left[\Delta W\right]_{OC} + 200\left[\Delta ASF\right]_{cladding} \quad (5.17)$$

The four, six, eight, ten and twelve-stage machines are designed using the same design methodology as the fourteen-stage machine for the CO_2/SO_2 blend (Section 3.3.2). Consequently, the scale factors are expressed with respect to the 14-stage turbine dimensions as shown in Table 5.18. For the largest machine (4-stage design), the highest radial scale factor (RSF) is obtained. Nonetheless, the axial scale factor is not the smallest despite that 4-stage design is having the shortest flow path length. This is due to assuming a constant aspect ratio (length$_{drum}$/D_{hub}) of 1.3 for the balancing drum based on the 14-stage design. Hence, a longer balancing drum length is obtained for the 4-stage (largest diameter) compared to the rest of the designs. As a result of the large RSF, the 4-stage design has the largest weight and area scale factors among all designs.

Table 5.18: Scale factors for the different turbine designs

Factors	Turbine designs (number of stages)				
	4	6	8	10	12
Axial scale factor (ASF)	0.81	0.747	0.76	0.82	0.90
Radial scale factor (RSF)	1.490	1.29	1.17	1.09	1.04
Weight scale factor (WSF)	1.80	1.24	1.04	0.97	0.97
Area scale factor (ASF)	1.21	0.96	0.886	0.89	0.93

Tables 5.19 to 5.23 show the costs for the four, six, eight, ten and twelve-stage designs with reference to the fourteen-stage case respectively; these tables are further explained with Figure 5.18. The weight of each component is calculated with respect to the reference case (14-stage design) as explained in Equation 5.15. Whilst, the difference in weight of the different components, including the inner casing, outer casing, shaft, stator blades and rotor blades is calculated using Equation 5.16.

The difference in cost for categories 'A' and 'B' (Δ cost 'A' & Δ cost 'B') is calculated based on the price list defined for all materials as summarised in Table 5.17. It can be concluded that the highest cost difference for all machines, with respect to the reference case, is contributed to the inner casing; which accounts for almost 65%, 66% and 72% of the total Δ*cost* of the 4, 6 and 8-stage machines respectively. This is followed by the shaft cost which accounts for almost 22%, 24%, and 22% of the total cost difference,

Table 5.19: Preliminary cost assessment results for the 4-stage machine compared to the 14-stage machine.

Total weight	Reference	4-stage	Δ weight [kg]	Δ cost 'A' (€)	Δ cost 'B' (€)
Inner casing	22700.0	40903.5	18203.5	1092212.6	1820354.3
Outer casing	48000.0	86492.1 3	8492.1	384920.7	384920.7
Shaft	7700.0	13874.8	6174.8	370486.2	617477.0
Stator blades	187.9	67.4	-120.5	-7232.9	-12054.9
Rotor blades	503.5	198.6	-304.9	-18296.1	-30493.5
Outer casing cladding	1.0	1.2	-	4176.3	4176.3
Total savings [cost 'A']			1.8 M€		
Total savings [cost 'B']			2.8 M€		

for the 4, 6 and 8-stage machines respectively. Though of the significant increase in the number of stages from 4 to 14 stages, the stator and rotor blading weight and their DM cost contribution are not highly significant compared to the inner casing and shaft direct material cost. Ultimately, the 14-stage machine results in savings of almost 1.8 M€ with respect to the 4-stage machine. Whilst, it results in savings of 0.5 and 0.6 M€ with respect to the 6 and 8-stage machines respectively.

Table 5.20: Preliminary cost assessment results for the 6-stage machine compared to the 14-stage machine.

Total weight	Reference	6-stage	Δ weight [kg]	Δ cost 'A' (€)	Δ cost 'B' (€)
Inner casing	22700.0	28109.7	5409.7	324582.6	540971.0
Outer casing	48000.0	59439.0	11439.0	114390.3	114390.3
Shaft	7700.0	9535.0	1835.0	110100.7	183501.2
Stator blades	187.9	75.7	-112.2	-6731.3	-11218.9
Rotor blades	503.5	225.9	-277.7	-16659.8	-27766.3
Outer casing cladding	1.00	0.96	-797.6	-797.6	
Total savings [cost 'A']			0.5 M€		
Total savings [cost 'B']			0.8 M€		

Designing the turbine for a larger number of stages beyond 8-stages (10 and 12-stages) compared to the 14-stages results in less direct material cost by around 0.1 M€. This is due to the similar radial dimensions of the machines (hub diameter) compared to the increase in the axial dimension obtained by the 14-stage design. Nonetheless, this increase in the DM cost is considered insignificant considering that cost 'A' and 'B' pricing are set based on a conservative criterion; where in reality some of the nickel-based alloys are

Table 5.21: Preliminary cost assessment results for the 8-stage machine compared to the 14-stage machine.

Total weight	Reference	8-stage	Δ weight [kg]	Δ cost 'A' (€)	Δ cost 'B' (€)
Inner casing	22700.0	23462.6	762.6	45755.3	76258.8
Outer casing	48000.0	49612.5	1612.5	16125.2	16125.2
Shaft	7700.0	7958.7	258.7	15520.5	25867.5
Stator blades	187.9	97.6	-90.3	-5420.1	-9033.5
Rotor blades	503.5	297.0	-206.6	-12393.0	-20655.0
Outer casing cladding	1.00	0.9	-2289.3	-2289.3	
Total savings [cost 'A']			0.06 M€		
Total savings [cost 'B']			0.11 M€		

expected to be more expensive than the considered costs. It is worth mentioning that due to the simple nature of the current analysis, the same material price is set for the blading, shaft and inner casing. However, the cost differences associated with the used materials should be taken into account in the detailed cost analysis, and this would affect the overall machine cost. Ultimately, this insignificant increase in the direct material cost is expected to be overturned by the higher operating expenditure and shaft end costs associated with the large machines (which will be discussed in the following sub-sections).

Table 5.22: Preliminary cost assessment results for the 10-stage machine compared to the 14-stage machine.

Total weight	Reference	10-stage	Δ weight [kg]	Δ cost 'A' (€)	Δ cost 'B' (€)
Inner casing	22700.0	22081.4	-618.6	-37118.2	-61863.6
Outer casing	48000.0	46691.9	-1308.1	-13081.3	-13081.3
Shaft	7700.0	7490.2	-209.8	-12590.7	-20984.6
Stator blades	187.9	125.7	-62.2	-3734.6	-6224.3
Rotor blades	503.5	384.3	-119.2	-7152.2	-11920.4
Outer casing cladding	1.00	0.9	-2138.2	-2138.2	
Total savings [cost 'A']			-0.08 M€		
Total savings [cost 'B']			-0.1 M€		

This preliminary direct material cost analysis indicates that machines with a large number of stages are financially feasible compared to the machines with a small number of stages. Although it is worth noting that the operating expenditure (OPEX) should be added to the overall machine cost to quantify the effect of efficiency differences of the machine over the lifespan of the entire plant. In this regard, the four-stage machine results in a total-

196

Table 5.23: Preliminary cost assessment results for the 12-stage machine compared to the 14-stage machine.

Total mass	Reference	12-stage	Δ weight [kg]	Δ cost 'A' (€)	Δ cost 'B'(€)
Inner casing	22700.0	21949.5	-750.5	-45032.3	-75053.8
Outer casing	48000.0	46413.0	-1587.0	-15870.4	-15870.4
Shaft	7700.0	7445.4	-254.6	-15275.3	-25458.8
Stator blades	187.9	154.8	-33.1	-1988.1	-3313.6
Rotor blades	503.5	472.6	-30.9	-1853.8	-3089.6
Outer casing cladding	1.00	0.9	-1346.4	-1346.4	
Total savings [cost 'A']			-0.08 M€		
Total savings [cost 'B']			-0.1 M€		

to-total efficiency (η_{tt}) that is almost 6% less than the 14-stage machine, and assuming the same thermal input into the cycle, would reduce power output by around 9 MW. Similarly, the 6-stage machine results in a reduction in η_{tt} by 4% and a drop in power of around 4.6 MW. A lower reduction in efficiency is obtained for the 8, 10, and 12 stage designs, where a 2%, 1% and 0.4% reduction is obtained compared to the 14-stage design. This accounts to a drop in power of around 2.6, 1.5, 0.6 MW respectively. By considering the operating expenditure (OPEX) for all machines, the machines with less number of stages, and a lower η_{tt}, are expected to result in higher OPEX compared to the machines with a larger number of stages.
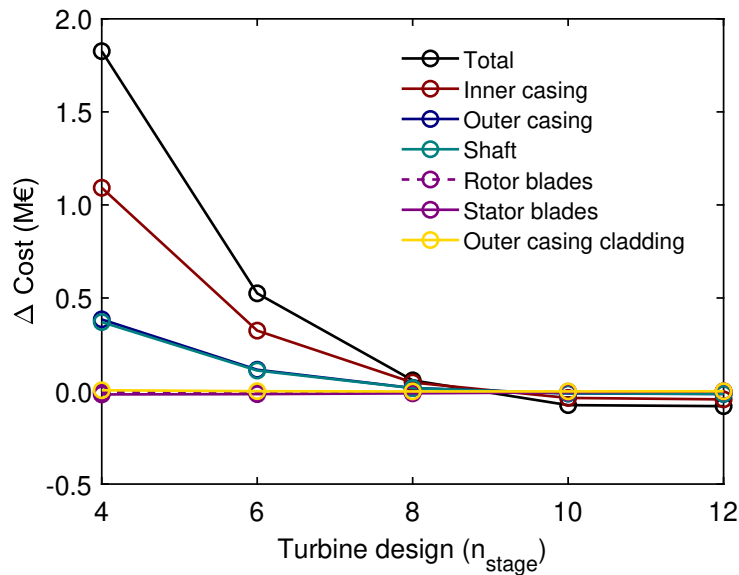
Figure 5.18: Direct material cost differences (cost 'A') associated with the different turbine designs with respect to the CO_2/SO_2 14-stage design.

5.6.4.1   Additional cost considerations

Synchronising a turbine generator to the transmission network during start-up can cause torsional disturbances, including impulsive step changes and 50/60 Hz torque components. Synchronised machines are subjected to short-circuit faults at the generator terminals and the occurrence of self-oscillations in the grid–generator–shaft system. This can lead ton high transient torques and torsional vibration excitation in the machine shafts, which cause additional stresses that may damage the shaft system. Therefore, shaft ends should be designed to ensure safe operation under such conditions [141].

Given the fact that the sizing of the shaft ends is driven by the need to withstand the electrical malfunctioning torques (short circuit and out-of-phase synchronisation), the amplitude of these alternate transient torques is primarily influenced by the ratio of the inertia of the expander rotor to that of the generator rotor. Hence, the cost associated with the shaft end dimensioning is with certainty larger for large machines with less number of stages. This proves the feasibility of small machines (designed with a large number of stages). On a different note, the adoption of dry gas seals (DGS) is mandatory to have leakages affordable machine for this application. However, the current DGS technology has limitations in terms of the maximum available diameter, which is in the order of 350-400 mm. This adds more constraints to the feasibility of the design of the large machines (designed with a small number of stages) [141].

According to the presented cost analysis, it can be concluded that a machine designed for a smaller hub diameter and a larger axial length should be cheaper compared to a machine designed for a larger hub diameter and a smaller axial length (low number of stages). This conclusion will be further confirmed by the detailed cost analysis taking place by the project industrial partners.

5.6.5   Remarks about the turbine design for CO_2 blends

In summary, for the sCO_2 blends considered, a total-to-total turbine isentropic efficiency above 92% can be achieved at two different turbine inlet pressure and temperature levels of

250 & 350 bar and 550 & 700°C respectively. This is considered an important milestone within the SCARA-

BEUS project, and is a promising result for developing the technology further. Moreover, it is worth reiterating that, in comparison with the reference cycle design, where an overall turbine efficiency was assumed to be equivalent to 92%, better cycle performance can be obtained for the updated flow path efficiency. On this point it should however be noted that the current study is concerned with providing an assessment for the flow path performance and does not account for the additional losses experienced with the turbine, such as inlet, bearing, balancing drum, and throttle and discharge losses that would further reduce the turbine efficiency below the results obtained here. Having said this, it is worth noting that most of these losses scale with the same parameters that influence turbine efficiency; for example, balancing drum and bearing losses are expected to be higher with larger hub diameters. On the contrary, throttle losses can be safely assumed to be low regardless of the specific flow path designs given that the size of the valves is typically chosen targeting fluid velocities that yield similar losses. Nevertheless, these losses will have to be quantified in later design stages.

It is evident that high turbine efficiency is achieved for designs that are able to accommodate a large number of stages; for example 10 to 12 stages can be accommodated for the CO_2/C_6F_6 flow path design at 550°C and 250 bar over a molar fraction range from 10 to 20%. However, it is also important to consider the effect that increased number of stages may have on the cost of the turbine. This is another essential criterion for the development of sCO_2 power blocks for CSP plants technologies. According to the preliminary cost analysis, it has been concluded that a turbine designed with a smaller hub diameter and a larger axial length should be cheaper compared to a turbine designed with a larger hub diameter and a smaller axial length (small number of stages). Nonetheless, this conclusion should be further confirmed by the detailed cost analysis taking place by the project industrial partners.

5.7 Conclusions

Mean-line flow path designs for a large-scale axial turbine, for installation in a 100 MW$_e$ CSP plant, were presented for different blends based on carbon dioxide, namely $CO_2/TiCl_4$, CO_2/C_6F_6 and CO_2/SO_2, and for different boundary conditions. The mean-line aerodynamic design was integrated with mechanical and rotordynamic constraints to limit the maximum stress acting on the blades and the length of the shaft for rotordynamic stability.

To study the impact of adopting different sCO_2 blends on the turbine flow path design, multiple flow path designs were produced for different cycle operating conditions, where different turbine inlet temperatures, turbine inlet pressures and molar fraction were considered. The turbine flow paths were designed with the goal of achieving maximum aerodynamic efficiency, while meeting imposed mechanical and rotordynamic considerations. Designs with a large number of stages were found to result in higher turbine efficiencies; this corresponds to designs with reduced hub diameters due to keeping a fixed synchronous rotational speed. These designs showed to be financially feasible compared to short flow path designs based on the conducted preliminary cost analysis results. Among the examined blends, it was found that using the $CO_2/TiCl_4$ blend resulted in the shortest flow-path length compared to both CO_2/C_6F_6 and CO_2/SO_2. Furthermore, for the three CO_2 blends investigated it was possible to obtain a flow path with an overall total-to-total efficiency in excess of 92%. This is considered promising for the future of CO_2 plants. This proves that using CO_2 blends can result in high efficiencies across the range of the boundary conditions and molar fractions considered. Hence, a high component efficiency is achievable, which will help realise the thermodynamic potential of the proposed cycle designs.

The sensitivity of the turbine design to the three blends was assessed for optimised cycle conditions. This was completed for two different turbine inlet pressure and temperature levels, ranging between 250 & 350 bar and defined at 550 & 700°C respectively, and for five different molar fractions for each blend. Despite each blend showing a different level of sensitivity to the inlet temperature, pressure and molar fraction, all the flow path designs obtained were found to achieve a high aerodynamic efficiency, which is in excess of 92%,

whilst meeting the rotordynamic and mechanical constraints. Moreover, a cycle efficiency greater than 50% was achieved for all the investigated blends at an inlet temperature of 700°C. Ultimately, it is concluded that designing the turbine for the optimal molar fraction that maximises the thermal efficiency of the cycle is a worthwhile endeavour.

Further to the sensitivity analysis, a parametric study was conducted to investigate the effects of changing the aerodynamic design variables including pith-to-chord ratio, flow coefficient, loading coefficient and degree of reaction on the turbine design and performance considering both the mechanical and rotordynamic design aspects. Increasing the flow coefficient from 0.3 to 0.7, while keeping constant loading coefficient, pitch-to-chord ratio and degree of reaction of 1.0, 0.85 and 0.5 respectively, results in an efficiency increase of up to 2.0 percentage points due to increasing the number of stages from six to thirteen. Whilst increasing the loading coefficient from 0.8 to 1.5, at constant flow coefficient, pitch-to-chord ratio and degree of reaction of 0.5, 0.85 and 0.5 respectively, results in an efficiency reduction by around four percentage points as a result of the number of stages reduction from fourteen to five stages to comply with the rotordynamic and mechanical design constraints. Changing the flow and loading coefficients simultaneously, at a constant degree of reaction and pitch-to-chord ratio of 0.5 and 0.85 respectively, resulted in an efficiency enhancement of 0.2% with respect to the baseline design produced at loading and flow coefficients of 1.0 and 0.5 respectively.

The flow path designs for the pure CO_2 and CO_2 blends were compared in this chapter for different cycle operating conditions; this includes designing flow paths for the same cycle configuration and power output alongside comparing flow paths designed at the same volumetric flow rate and expansion ratio. It was found that turbines operating with either pure CO_2 and CO_2 blends, at turbine inlet temperature of 700°C, result in overall total-to-total efficiencies in excess of 92.5%; where the highest turbine efficiency is achieved for the turbine operating with a pure CO_2 with a maximum efficiency difference of 1.1 percentage points obtained with respect to the CO_2/$TiCL_4$ blend; where the CO_2/$TiCL_4$ blend allows for accommodating six design stages compared to thirteen-stages in the case of pure CO_2 due to experiencing high rotor bending stresses associated with the high mass

flow rate. Meanwhile, differences are experienced within the flow path length (number of stages) and turbine geometry based on both the imposed boundary conditions and the properties of the working fluids.

Finally, the 14-stage $80\%CO_2/20\%SO_2$ flow path has been selected for the SCARABEUS project based on blend selection criteria and cycle optimisation results. Hence, the rest of the work in this thesis will be carried out for the $80\%CO_2/20\%SO_2$ flow path.

This page is left intentionally blank

6 Off-design Performance analysis

6.1   Introduction

In chapter 5 detailed turbine designs were presented for a 100 MWe CSP plant operating with pure CO_2 and CO_2 blends. Turbines operating with CO_2 and CO_2 blends have proven to achieve a total-to-total efficiency in excess of 92%. Given that one of the objectives of this thesis is to enable the mean-line flow-path design of a multi-stage axial turbine operating with CO_2 blends, it is important to assess the turbine performance at off-design conditions. Turbines principally operate at conditions away from the design point at starting, idling, variable power and speed conditions. Deviating from the design point results in an increase in the aerodynamic losses which deteriorates the overall turbine performance. Thus, the aim of this chapter is to investigate the performance of the selected flow path (14-stage 80%CO_2/20%SO_2) over a range of off-design conditions.

6.2   Dimensional analysis: similitude

Dimensional analysis is extensively used to obtain the general behaviour of all turbomachinery. Within the dimensional analysis, a small group of variables are introduced to represent some physical characterises of the flow in turbomachinery. Principally, dimensional analysis is used to predict a prototype's performance based on tests conducted on a scale model (similitude). Also, it is used to determine and select the suitable machine type based on the predicted performance for the specified conditions [162].

The performance of turbomachinery is expressed in terms of control variables, geometric variables, and fluid properties. For non-compressible working fluids, the volume flow rate Q, rotational speeds (N), diameter (D), length (l), viscosity(μ) and density (ρ) are used to express the performance of the machine. Dealing with compressible fluid requires considering additional parameters such as the stagnation speed of sound at the entry of the machine (a_{01}) and the specific heat ratio ($\gamma = C_p/C_v$). Additionally,dealing with density changes required considering the mass flow rate ($\dot{m}$) instead of the volume flow rate (Q).

Given the fact that the heat transfer from the casing can be considered negligible for tur-
bomachinery, the temperature on its own can be excluded from the analysis. Therefore,
the performance parameters for a turbomachinery, a turbine, handling a compressible flow,
can be expressed as:

$$[\Delta h_{0s}, P, \eta] = f(\mu, N, D, \dot{m}, \rho_{01}, a_{01}, \gamma) \tag{6.1}$$

where h_{0s} is the work done per unit mass of fluid, P is the power, η is the efficiency, (ρ) is
the fluid density, a is the speed of sound, D is the characteristic diameter, μ is the dynamic
viscosity and γ is the specific heat ratio.

As the density (ρ) and speed of sound (a) change through the machine, they are selected
at the inlet conditions (station 1). By taking the ρ, D and N as common factors, the
relationship can be reduced to five dimensionless groups:

$$\left[\frac{\Delta h_{0s}}{N^2 D^2}, \ \eta, \ \frac{P}{\rho_{01} N^3 D^5} \right] = f\left(\frac{\dot{m}}{\rho_{01} N D^3}, \ \frac{\rho_{01} N D^2}{\mu}, \ \frac{ND}{a_{01}}, \gamma \right) \tag{6.2}$$

Given that ND is proportional to the blade speed, $\frac{ND}{a_{01}}$ can be regarded as the blade Mach
number and the equation can be written as:

$$\left[\frac{\Delta h_{0s}}{a_{01}^2}, \ \eta, \ \frac{P}{\rho_{01} a_{01}^3 D^2} \right] = f\left(\frac{\dot{m}}{\rho_{01} a_{01} D^2}, \ \frac{\rho_{01} a_{01} D}{\mu}, \ \frac{ND}{a_{01}}, \gamma \right) \tag{6.3}$$

The isentropic relationship for perfect gases can be used for machines operating with work-
ing fluids that behave close to the ideal gas behaviour, which can be expressed as:

$$\frac{T_{0s}}{T_{01}} = \frac{P_{02}}{P_{01}}^{\frac{(\gamma-1)}{\gamma}} \tag{6.4}$$

hence, Δh_{0s} can be expressed as:

$$\Delta h_{0s} = C_p T_{01} \left[(P_{02}/P_{01})^{\frac{(\gamma-1)}{\gamma}} - 1 \right] \tag{6.5}$$

since

$$C_p = \gamma R / (\gamma - 1), (a_{01})^2 = \gamma R T_{01} \tag{6.6}$$

then,

$$(a_{01})^2 = (\gamma - 1) C_p T_{01} \tag{6.7}$$

Thus:

$$\frac{\Delta h_{0s}}{(a_{01})^2} = \frac{\Delta h_{0s}}{(\gamma - 1) C_p T_{01}} = \frac{1}{(\gamma - 1)} \left[\frac{P_{02}}{P_{01}}^{\frac{(\gamma - 1)}{\gamma}} - 1 \right] = f(P_{02}/P_{01}, \gamma) \tag{6.8}$$

The dimensionless groups can be formed using mass, length and time as three primary dimensions. Hence, the non-dimensional mass flow can be more conveniently expressed as:

$$\hat{m} = \frac{\dot{m}}{\rho_{01} a_{01} D^2} = \frac{\dot{m} R T_{01}}{P_{01} \sqrt{\gamma R T_{01}} D^2} = \frac{\dot{m} \sqrt{\gamma R T_{01}}}{D^2 P_{01} \gamma} \tag{6.9}$$

Similarly the power coefficient can also be re-written as:

$$\hat{P} = \frac{P}{\rho_{01} a_{01}^3 D^2} = \frac{\dot{m} C_p \Delta T_0}{\rho_{01} a_{01} D^2} a_{01}^2 = \hat{m} \frac{C_p \Delta T_0}{a_{01}^2} = \frac{\dot{m}}{\gamma - 1} \frac{\Delta T_0}{T_{01}} \tag{6.10}$$

Using the newly defined non-dimensional groups and integrating them with Equation 6.3 reduces Equation 6.2 to:

$$\left[\frac{P_{02}}{P_{01}}, \eta, \frac{T_{02}}{T_{01}} \right] = f \left(\frac{\dot{m} \sqrt{\gamma R T_{01}}}{P_{01} D^2}, \frac{ND}{\sqrt{\gamma R T_{01}}}, Re, \gamma \right) \tag{6.11}$$

Specific heat ratio (γ) can be considered as an independent variable for machines handling a single working fluid. Similarly, the Re number can be droppedfor machines operating at a high Reynolds number. For a known machine size and fixed working fluid C_p and D can be dropped and the equation reduces to:

$$\left[\frac{P_{02}}{P_{01}}, \eta, \frac{T_{02}}{T_{01}} \right] = f \left(\frac{\dot{m} \sqrt{T_{01}}}{P_{01}}, \frac{N}{\sqrt{T_{01}}} \right) \tag{6.12}$$

It is worth mentioning that after omitting the diameter D and gas constant R, the independent variables in Equation 6.11 are no longer dimensionless. The performance of

a turbomachinery, operating with compressible working fluids, can be evaluated by constructing maps function of the previously presented non-dimensional parameters that can be summarised as follows:

$$\frac{P_{01}}{P_{02}} : Total\text{-}to\text{-}total\ \ pressure\ \ ratio \tag{6.13}$$

$$\frac{T_{01}}{T_{02}} : Total\text{-}to\text{-}total\ \ temperature\ \ ratio \tag{6.14}$$

$$\frac{\dot{m}\sqrt{\gamma R T_{01}}}{D^2 P_{01}} : Mass\ \ flow\ \ function \tag{6.15}$$

$$\frac{ND}{\gamma R T_{01}} : Corrected\ \ rotational\ \ speed \tag{6.16}$$

6.3 Performance analysis methodology

An iterative mean-line approach is adopted to predict the performance of sCO$_2$ turbines at off-design conditions. Initially, the turbine geometry is introduced into the performance model based on the results presented in Chapter 5. This includes blade heights (h), chord length (c), stagger angle (ζ), blade speeds (U), blade areas (A), blade angles (α' & β'), hub diameter (D_{hub}) and the number of blades (n_{blades}). Alongside the defined geometry, the model is supported with turbine boundary conditions to evaluate the off-design turbine performance. In this regard, two different approaches can be implemented. The first approach includes defining the inlet stagnation temperature and pressure, the total-to-static pressure ratio, and the rotational speed as the system inputs and solving for the turbine performance and the mass flow (system outputs). Alternatively, the mass flow rate can replace the pressure ratio in the system inputs. In this case, the corresponding pressure ratio and system performance (efficiency) are the system outputs.

In this thesis, the mass flow rate ($\dot{m}$), static outlet pressure (P_3), total inlet temperature (T_{01}) and fluid molar fraction (X_i) are introduced in the off-design model as summarised in Table 6.1. Hence, the mass flow rate is considered as the input to the performance model whereas the pressure ratio and total-to-total efficiency are the outputs of the model (2nd approach). As discussed in Chapter 5, fluid properties are obtained using the Peng Robinson

equation due to its simplicity and accuracy to obtain the thermodynamic properties of the selected working fluids; where the binary interaction parameters presented in Table 5.4 are used.

<div align="center">Table 6.1: Input parameters for the off-design performance model.</div>

Input geometry	Symbol	Input geometry	Symbol
Number of blades	n	Diffusion angles	Δ
Inlet/Outlet blade angles	$\alpha' \& \beta'$	Inlet/Outlet areas	A
Stagger angles	γ	Inlet/Outlet blade heights	h
Hub/tip Radii	$R_h \& R_t$	Blade pitch	s
Axial chord length	c	Clearance gap	t_{cl}
Axial spacing	ss	Blade peripheral speed	U
Throat to pitch ratio	o/s		

Following the definition of the turbine boundary conditions and geometry, the flow velocity (C_1) is assumed at the inlet of the stator blades (station 1) (Figures 3.4a and 3.4b), for the first turbine stage, and hence, the static pressure (P_1) and temperature (T_1) are calculated at the stator inlet conditions. Accordingly, the flow density (ρ_1) and the axial velocity (Ca_1) are obtained using the following continuity equation:

$$C_1 = f(C_{a1}, \alpha_1) \tag{6.17}$$

$$h_1 = f(h_{01}, C_1) \tag{6.18}$$

$$\rho_1 = f(P_1, h_1) \tag{6.19}$$

where α_1 is defined based on the turbine geometry and h_{01} is obtained from the introduced cycle boundary conditions $f(P_{01}, T_{01})$. At this stage, Ca$_1$ can be obtained using the continuity equation.

$$Ca_1 = \frac{\dot{m}}{\rho_1 \times A_1} \tag{6.20}$$

Using the calculated axial velocity and the inlet blade angle (α_1), the velocity assumption (C_1) is updated till convergence; a convergence criterion less than 10^{-6} is used for all iterative solutions. Then, the stator loss coefficient (ζ_S) is assumed alongside the ax-

ial velocity (Ca_2) at the rotor inlet conditions (station 2). Hence, the relative outlet flow angle (β_2), the flow velocities and the thermodynamic properties are all obtained. This is followed by obtaining the outlet static pressure, temperature (P_2, T_2) and flow density (ρ_2) as follows:

$$C_2 = f(C_{a2}, \alpha_2) \tag{6.21}$$

$$\beta_2 = f(C_{a2}, \alpha_2) \tag{6.22}$$

$$V_2 = f(C_{a2}, \beta_2) \tag{6.23}$$

$$h_2 = f(h_{02}, C_2) \tag{6.24}$$

$$h_{2s} = f(h_2, \zeta_N) \tag{6.25}$$

$$T_2 = f(h_2, P_2) \tag{6.26}$$

$$\rho_2 = f(T_2, P_2) \tag{6.27}$$

Using the continuity equation and the thermodynamic properties at the rotor inlet, the axial velocity can be obtained and hence, Ca_2 can be updated in the iteration loop. By integrating the performance model with the loss model, ζ_S is obtained and the initial assumption at this stage is updated. This loop runs till meeting the convergence criteria for both axial velocity and stator loss coefficient.

$$Ca_2 = \frac{\dot{m}}{\rho_2 \times A_2} \tag{6.28}$$

At the rotor outlet, the iterative solution starts by assuming axial velocity (Ca_3) and the rotor loss coefficient (ζ_R) at the rotor outlet (station 3) and hence, absolute and relative flow velocities can be obtained as:

$$V3 = f(C_{a3}, \beta_3) \tag{6.29}$$

$$\alpha_3 = f(C_{a3}, \beta_3) \tag{6.30}$$

$$C_3 = f(C_{a3}, \alpha_3) \tag{6.31}$$

Using the conservation of rothalpy indicated in equation 6.32, the enthalpy drop across the stage is obtained and hence, corresponding pressure (P_3), temperature (T_3) and density (ρ_3) are all obtained.

$$I_2 = h_2 + 0.5\ V_2^2 - 0.5\ U_2^2$$
$$I_3 = h_3 + 0.5\ V_3^2 - 0.5\ U_3^2 \tag{6.32}$$

$$h_{03s} = f(h_3, s_3) \tag{6.33}$$

$$P_3 = f(h_3, s_3) \tag{6.34}$$

$$\rho_3 = f(T_3, P_3) \tag{6.35}$$

With the known density (ρ_3), the axial velocity (Ca_3) at the rotor exit can be obtained and hence, the assumed value is updated.

$$Ca_3 = \frac{\dot{m}}{\rho_3 \times A_3} \tag{6.36}$$

After obtaining the axial velocities across the last turbine station (Ca_3), ζ_R is obtained using the loss models correlations for the rotor outlet and hence the initial assumption at this stage is updated till convergence. Ultimately, the total-to-total efficiency (η_{tt}) is obtained using the following definition:

$$\eta_{tt} = \left[1 + \left(\frac{\zeta_R \frac{w_3^3}{2} + \frac{C_2^2}{2} \zeta_N \frac{T_3}{T_2}}{h_{01} - h_{03}} \right) \right]^{-1} \tag{6.37}$$

where C_2 and w_3 are the absolute and relative velocities at the rotor inlet and exit respectively, T_2 and T_3 are the static temperatures at the rotor inlet and exit respectively and $(h_{01} - h_{03})$ is the stage total enthalpy drop across the stage. The whole performance model is presented in the schematic drawing shown in Figure 6.1.
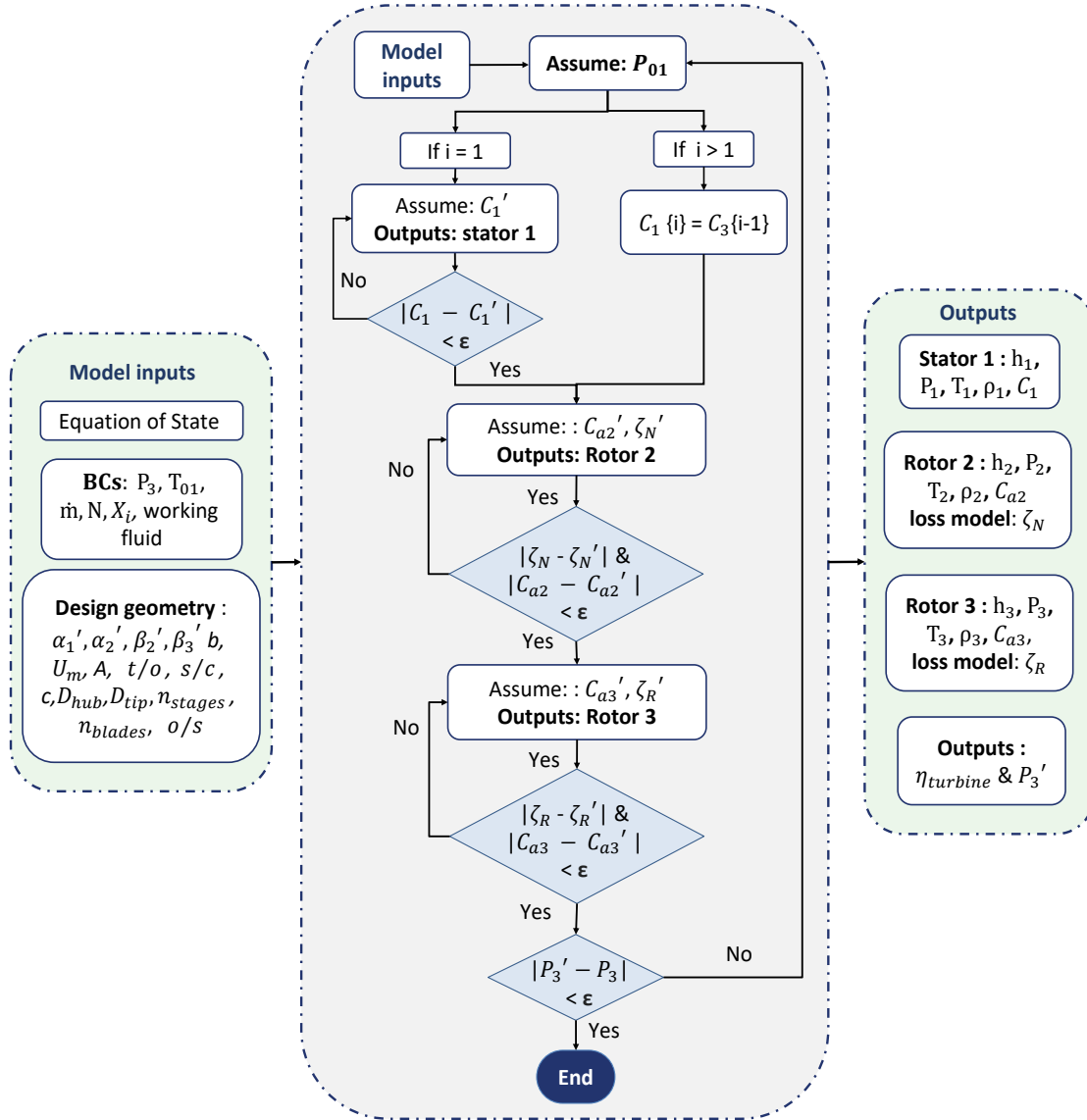
Figure 6.1: Flow chart of off-design performance analysis methodology.

6.3.1   Incidence losses

To assess the turbine performance at off-design operating conditions, incidence effects should be considered in addition to the profile, secondary flow, trailing edge and tip clearance losses. Incidence losses occur due to the presence of incidence (mismatch) between the design blade angle (α_1') and the inlet flow angle (α_1) as indicated in Figure 2.13.

In this context, the Aungier model [66] used the same correction factor introduced by Ainley and Mathieson [63]. Ainley and Mathieson [63] firstly estimated the profile losses

at zero incidence. Afterwards, the stalling incidence (i_s), the incidence at which the profile loss is twice the loss achieved at zero incidence, is obtained and hence, the incidence and profile losses at non-zero incidence are determined. This has been done assuming that the profile losses ratio at non-zero incidence with respect to the zero incidence is a function of a ratio of incidence to the defined stalling incidence (i/i_s). Stalling incidence is assumed to be a function of the inlet blade, exit flow angle and pitch-to-chord ratio as shown in Figure 6.2a. Once the stalling incidence is obtained from Figures 6.2a and 6.2b, the profile loss correction can be obtained using Figure 6.3. Aungier [66] provided empirical correlations to replace those figures and provide a wider range of applications.

| (a) | (b) |
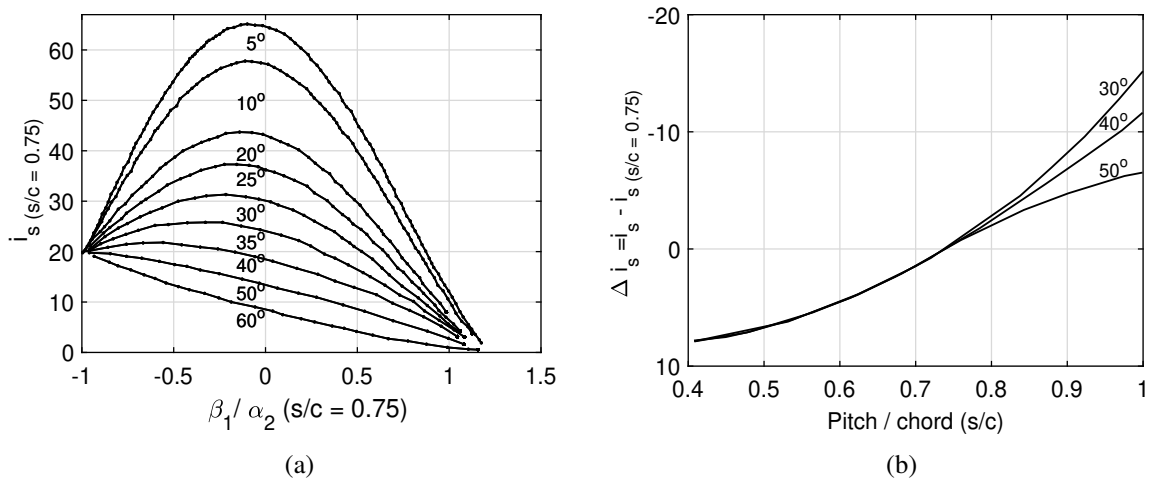
Figure 6.2: (a) Positive stalling incidence (b) incidence correction for the turbine blades at different pitch to chord ratio by the AN loss model [66].
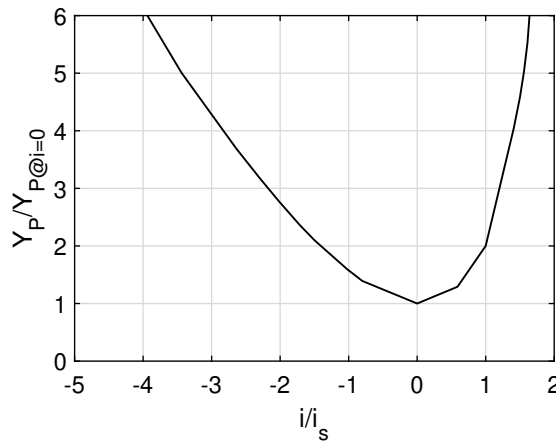
Figure 6.3: Variation of profile loss with incidence for typical turbine blading

6.3.2 Methodology verification

There is a scarcity of published work for verification purposes, particularly for turbines operating with novel working fluids such as blended sCO_2 at design and off-design conditions. In particular, few cases were provided in the literature to evaluate the off-design performance analysis for turbines operating with sCO_2 working fluids. To support this analysis, the off-design performance tool has been verified against multiple cases from the literature operating with air and pure sCO_2. The cases have been selected from the literature to allow for initially mapping the design using the in-house design tool and then evaluating their performance at off-design conditions.

The first verification case relates to the mean-line results for a single-stage 6.5 MW sCO_2 turbine where the Aungier loss model was used to evaluate the performance at the off-design conditions [104]. The second verification case relates to the experimental data for the off-design performance analysis of a 4-stage 700 kW air turbine [163]. Finally, the off-design performance model is verified against CFD presented in the literature for a 3-stage 10 MW sCO_2 turbine [80]. To proceed with the off-design performance model verification, turbines were designed initially using the mean-line design tool, presented in Chapter 2, for the selected verification cases using the boundary conditions specified in Table 6.2.

Table 6.2: Boundary conditions for the selected verification cases.

Parameter	Description	Unit	Literature cases		
			[104]	[80]	[163]
-	Working fluid	[-]	sCO_2	sCO_2	Air
T_{01}	Stator total inlet temperature	[K]	773.15	385	413
P_{01}	Stator total inlet Pressure	[MPa]	15.00	12.86	0.26
PR	Pressure ratio	[-]	1.55	2	2.54
n	Number of stages	[-]	3.00	1	4
$\dot{m}$	Mass flow rate	[kg/s]	184.00	213.42	7.8
t_{cl}	Clearance gap	[mm]	0.00		0.24
N	Rotational speed	[kRPM]	10.00	20.3	7.5
$\dot{W}$	Power output	[MW]	10.00	6.5	0.7

Figures 6.4a-6.4d show the verification results of a single-stage sCO_2 and 4-stage air

212

turbine. The performance maps are presented in the form of curves of mass flow function, defined as $\frac{\dot{m}\sqrt{T_{01}}}{P_{01}}$, plotted against the operating pressure ratio *PR* and total-to-static stage η_{ts} efficiency plotted against the total-to-static pressure ratio across a range of off-design conditions. A good agreement is achieved between the results of the performance model, developed in this study, and the mean-line results presented in the literature for the 6.5 MW sCO$_2$ turbine as shown in Figures 6.4a and 6.4b.
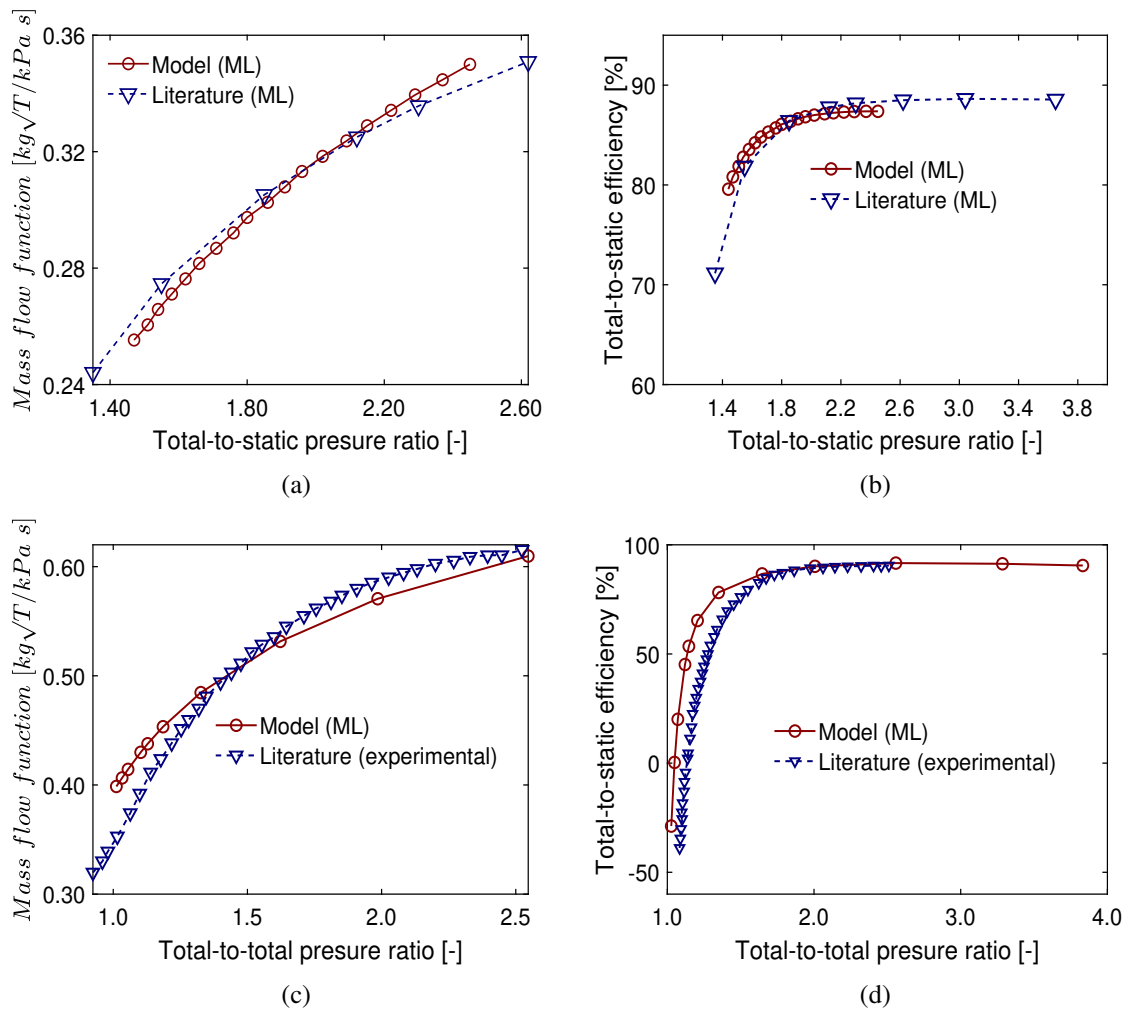
Figure 6.4: Verification results of the off-design performance model against (a,b) 6.5 MW SCO$_2$ turbine (c,d) 0.7MW air turbine.

Similarly, the mass flow function and the total-to-static efficiency for the 4-stage air turbine are plotted versus the total pressure ratio as shown in Figures 6.4c & 6.4d. A good agreement is obtained in the pressure ratio change with respect to the mass flow function. Nevertheless, differences are realised in the efficiencies obtained by the mean-line

model compared to the experimental data which is potentially due to the separation effects and losses that have not been considered within the mean-line design model (for example windage losses). Finally, the off-design performance results of a 10 MW turbine predicted by CFD simulations [80] are used to further verify the off-design performance model as shown in Figure 6.5. A good agreement is achieved in the predicted turbine efficiency versus the corresponding mass flow rate. Overall, a good agreement is realised for the pressure ratio and efficiency change with respect to the mass flow function compared to the cases from the literature. This confirms the right implementation of the off-design performance analysis methodology and the loss model.
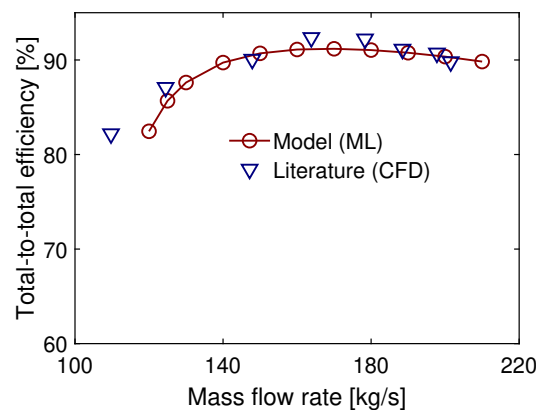
Figure 6.5: Verification results of the off-design performance model against 10 MW SCO$_2$ turbine.

6.3.3 Performance analysis for the 14-stage CO$_2$/SO$_2$ turbine

Following the performance model verification, the off-design performance of the 14-stage CO$_2$/SO$_2$ turbine flow path design is evaluated by the mean-line tool and the CFD simulations. The detailed flow path design of the turbine operating with the 80%CO$_2$/20%SO$_2$ blend is presented in Section 5.6. Whilst, further details of the CFD numerical simulation results can be found in Abdeldayem et al. [142]. A brief summary of the main ML design aspects can be found in Table 5.16. It is worth noting that the CFD results are obtained by a research fellow working on the numerical analysis studies within the context of the SCARABESU project. Within the CFD framework, the off-design CFD model is set up to evaluate the turbine off-design performance by changing the total inlet turbine pressure while keeping a fixed total inlet turbine temperature and static outlet pressure. Further

details about the off-design performance model can be found in [142].
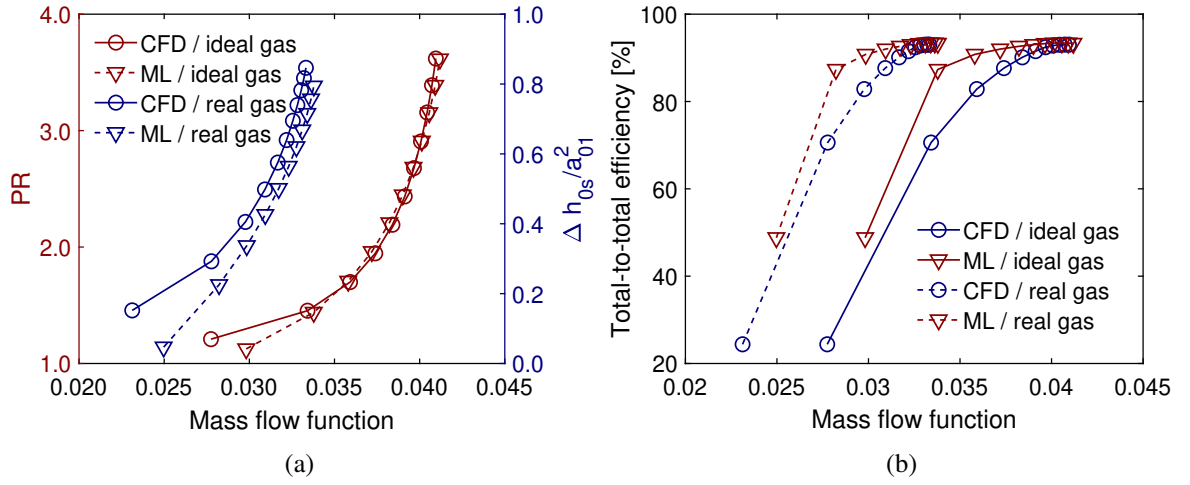
Figure 6.6: Performance maps of the 14-stage CO_2/SO_2 flow path using CFD and ML models; mass flow function versus (a) $\Delta h_{0s}/a_{01}^2$ and pressure ratio (b) total-to-total efficiency.

Given that the 14-stage turbine design is operating with CO_2/SO_2 blend where the fluid might deviate from the ideal gas behaviour, the mass flow function is defined using both the ideal gas assumptions ($\dot{m}\sqrt{\gamma R T_{01}/D^2 P_{01}}$) and real gas form ($\dot{m}/\rho_{01}a_{01}D^2$) to examine the accuracy of ideal gas approximation for the CO_2/SO_2 blend. It is evident that using the mass flow function definition based on ideal gas assumptions results in deviations with respect to the results obtained using the real gas form as shown in Figures 6.6a and 6.6b.

Figures 6.7a and 6.7b show the maps of the 14-stage CO_2/SO_2 turbine considering the real gas behaviour for the CO_2/SO_2 blend. Though a good agreement is obtained with the performance model with the selected cases from the literature, the results for the 14-stage design of the CO_2/SO_2 resulted in noticeable deviations in the predicted total-to-total flow path efficiency. A good agreement is obtained in the predicted $\Delta h_{0s}/a_{01}^2$ with respect to the mass flow function which is investigated over mass flow rates ranging from 52 to 130% of the design point. Nonetheless, large deviations are obtained in the total-tot-total efficiency (η_{tt}) predicted by the ML model compared to the CFD results.

Varying the mass flow rate over the examined range, from 52 to 130% of the design mass flow rate, results in an increase in $\Delta h_{0s}/a_{01}^2$ from almost 0.2 to 0.8 (as predicted by both ML and CFD models). The total-to-total efficiency is almost constant between
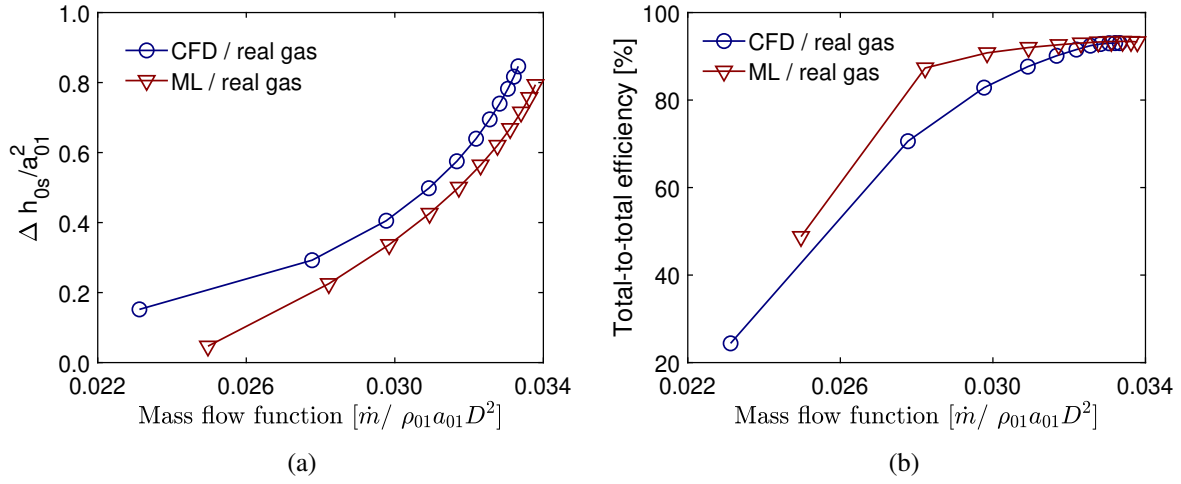
Figure 6.7: Performance maps of the 14-stage CO_2/SO_2 flow path using CFD and ML models; mass flow function versus (a) $\Delta h_{0s}/a_{01}^2$ (b) total-to-total efficiency.

90% and 130% of the design mass flow rate but it decreases significantly at lower mass flow rates. Based on the CFD results, this turbine can operate down to 52% of the design mass flow rate with a total-to-total efficiency of over 80%. Nonetheless, based on the ML predictions the turbine can operate down to 52% with total-to-total efficiency over 90%. These deviations in the total-to-total efficiency confirm that some of the flow features and losses are not well captured within the mean-line performance evaluation which resulted in over-predicting the total-tot-total efficiency compared to the CFD results, particularly at very low mass flow rates.

Axial velocities and outlet flow angles deviate from the design point at off-design operation due to changing the turbine inlet mass flow rate. This results in deviations in the inlet flow angles from the blade angles of the downstream stages. Consequently, incidence losses occur and the turbine performance deteriorates. Furthermore, the off-design operation affects the loss contribution of the different loss mechanisms in the blade row due to changing the operating conditions. This section focuses on comparing turbine performance at off-design conditions as predicted by the ML model with respect to the CFD results to address the main reasons behind the deviations between both techniques. This includes investigating the differences in the predicted efficiencies, loss coefficients, entropy change, incidence angles, deviation angles, velocity triangles and produced power across each turbine stage. The total-to-total efficiency predicted by both techniques is compared across

each design stage for the 14-stage CO_2/SO_2 design. Additionally, the stator and rotor loss coefficients are compared across the stages for both techniques at different percentages of mass flow rate covering 52%, 82%, 100% and 130% of the design flow rate.

Figures 6.8a to 6.8d show the total loss coefficient, a summation of the stator and rotor loss coefficients, and flow path total-to-total efficiency (η_{tt}) plotted against the number of stages over the mass flow rate ranging from 52 to 130% of the design flow rate. Slight differences are obtained in the loss coefficients and stage efficiency, as predicted by both the ML and CFD models, over the first seven design stages (from the 1st to the 7th stage) at a mass flow rate of 52% of the design ṁ. Afterwards, the mean-line results deviate significantly from the CFD results across the turbine stages; where the maximum deviation is evident at the last turbine stage (14th) as shown in Figure 6.8a. The efficiency difference between the ML and CFD models reaches a maximum of 4% across the first seven stages, whilst moving downstream resulted in an efficiency difference ranging from 7 to 46% at the 7th and 14th stage respectively. This is corresponding to a η_{tt} of 81% (ML) compared to 43% as predicted by the CFD model. The 46% difference in the total-to-total efficiency is due to the deviation in the predicted loss coefficients by 380% with respect to the CFD results.

Increasing the mass flow from 52% to 82%, and beyond, results in a better agreement across a larger number of stages; where the ML and CFD models start to deviate after the 12th design stage as shown in Figure 6.8b. Operating at 82% of the design mass flow rate results in a maximum efficiency difference of 2.6% over the first twelve stages, whilst the efficiency difference increases till reaching 7.3% at the last turbine stage (14th); this corresponds to an increase in the loss coefficient by 100%. Increasing the mass flow rate beyond the design point, till reaching up to 130% of the mass flow rate, results in a good agreement between the ML and CFD results across all the stages. The efficiency difference between the ML and CFD results reaches a maximum of 2.6% as shown in Figures 6.8c and 6.8d.

In view of the fact that the off-design operation results in non-zero incidence and deviation angles, it is important to quantify those angles with respect to both ML and CFD models. This should help in understanding the reasons behind the discrepancies in the
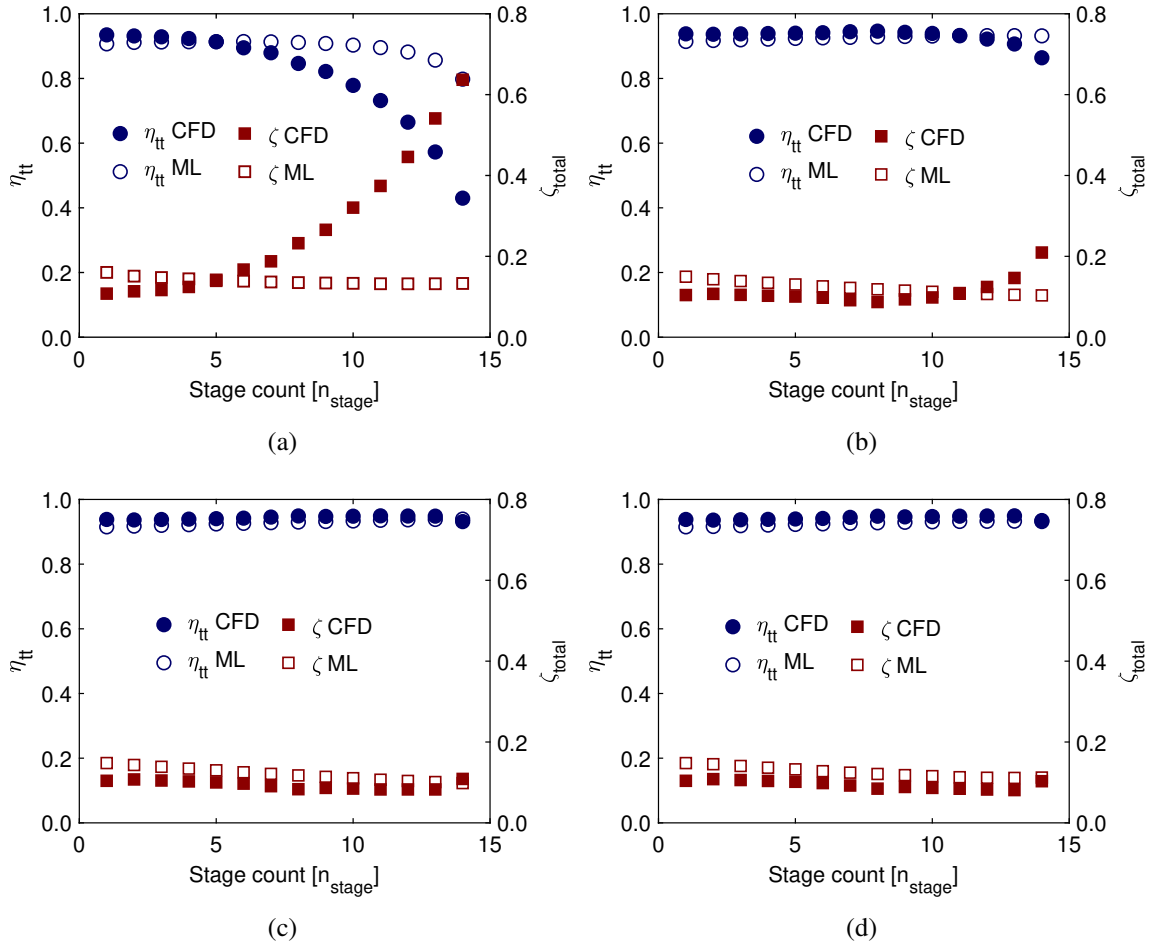
Figure 6.8: The total-to-total turbine efficiency (η_{tt}) and loss coefficient (ζ_{total}) change versus the different turbine stages (n_{stage}) at (a) 52% (b) 82% (c) 100% (c) 130% of the design mass flow rate.

predicted total-to-total efficiency by both techniques, particularly at low mass rates.

Figures 6.9a to 6.9b present the incidence angles estimated by both ML and CFD techniques at 52% and 130% of the design mass flow rate; which are equivalent to 434 and 1053 kg/s respectively. These two cases are selected to address the main difference between the ML and CFD results at two extreme conditions where the turbine is operating at a very low and high mass flow rates. Operating at a low mass flow rate with respect to the design point results in a negative incidence. The incidence angle increases from -17° to -53° across the turbine stages, from the 1st till the last stage, in the stator blade row whereas less incidence is experienced in the rotor blade row with a maximum increase from -16 to -42 ° across the stages as predicted by the ML model. Both the CFD and ML models result in similar incidence angles across the stages with a maximum difference of 6

$^\circ$ at the 7$^{\text{th}}$ stage and 2.2° at the 1$^{\text{st}}$ stage of the stator and rotor blades respectively. On the contrary, a positive incidence is experienced with operating at a 130% of the design mass flow rate due to the increased axial velocity with respect to the design point. A maximum difference in the incidence angle of 4.8% is obtained between ML and CFD models for the last turbine stage.
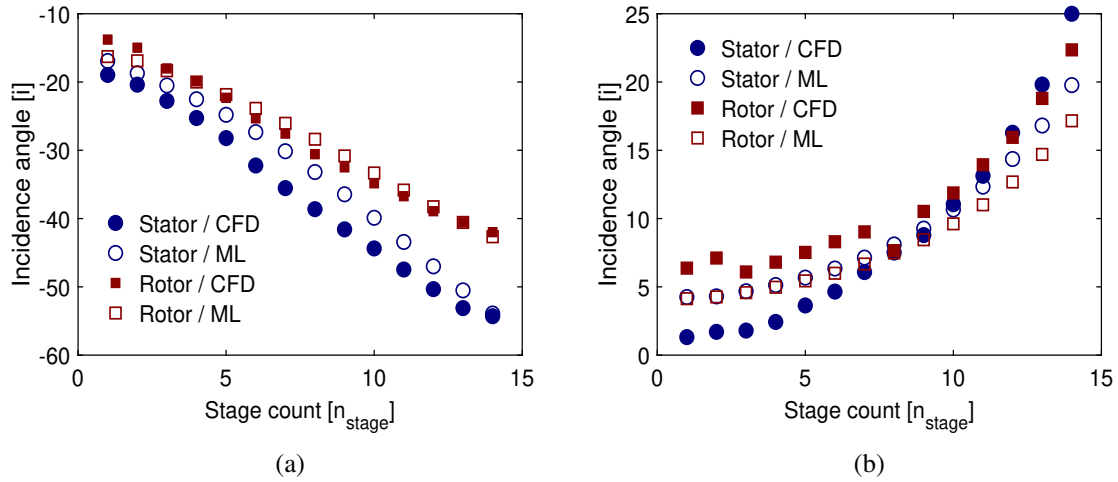
Figure 6.9: Incidence angle (i) versus the stage count (n_{stage}) at (a) 52% (b) 130% of the design mass flow rate.

Similarly, the deviation angle, defined as the difference between the outlet flow and blade angle ($\delta = \beta_3 - \beta_3'$), is obtained by both ML and CFD models at 52% and 130% of the design mass flow rate as shown in Figures 6.10a and 6.10b. According to the ML results, the deviation angle increases and decreases across the rotor and stator blades, respectively, at 52 and 130% of the design mass flow rate. A maximum deviation angle (δ) of -1.8° is obtained at 130% of the mass flow rate as shown in Figure 6.10b. The specific trend predicted by the ML model is a result of keeping a fixed outlet flow angle (α_2 & β_3) that is dictated by the blade throat-to-pitch ratio. Nonetheless, no specific trend governs the change of the deviation angle along the turbine design stages with respect to the CFD results. A maximum difference in the predicted deviation angle between ML and CFD of 1.86 $^\circ$ is obtained at the last turbine stage of the rotor blades at 52% of the design mass flow rate.

Further to comparing the incidence and deviation angles, the velocity triangles obtained by the ML and CFD models are compared against each other. Figure 6.11 show the velocity

219
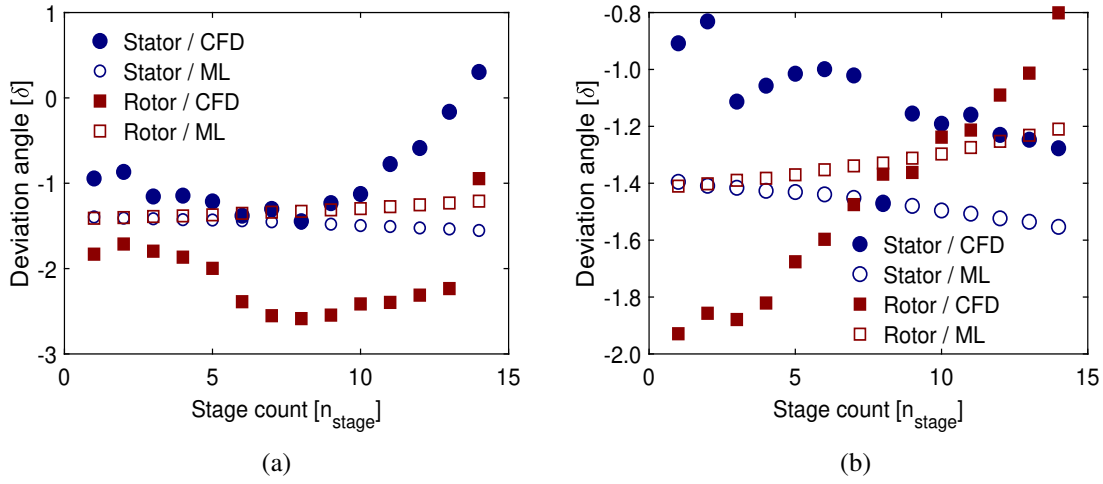
Figure 6.10: Deviation angle (δ) versus the stage count (n_{stage}) at (a) 52% (b) 130% of the design mass flow rate.

triangles obtained by both models at 52%, 100% and 130% of the design mass flow rate for the 1st, 7th and 14th stage. The solid lines represent the velocities predicted by the ML model whilst the dashed lines represent the velocities obtained by the CFD model. At the design point, similar velocities triangles are obtained across the stages resulting in the same power across the stages (see Figure 6.11). However, at 52% of the design mass flow rate the axial velocities of the flow decrease from the 1st to the 14th stage resulting in less whirl velocity difference and power generation across the turbine stages. Owing to this, a negative power output is obtained for the extremely reduced mass flow rate cases. It can be noticed that small changes in the flow angles can cause the velocity triangle to shift significantly away from the design point. Increasing the mass flow rates across the turbine blades results in an increase in axial the velocity component downstream and hence, an increase in the whirl velocity difference and power generated across the stages. It is worth concluding here that both the ML and CFD models resulted in significantly similar velocity triangles at the off-design conditions operating with 52% and 130% of the design mass flow rates.

It is evident from the previous results that the ML and CFD models predict similar flow angles and velocity triangles. However, the efficiency predicted by the ML model deviates significantly from the CFD results at lower mass flow rates whilst showing a good agreement at high mass flow rates. Even though both models predict similar flow angles,

220

small deviations in flow angles can significantly affect the predicted efficiency. This is because small deviations in flow angles can affect the flow at the blade inlet, which in turn can lower the efficiency. An increase in this deviation at lower mass flow rates reduces the effective flow area, which results in an increase in the flow velocity and secondary flow losses. Furthermore, large deviations in flow angles cause the boundary layer to separate and hence, this reduces the overall efficiency of the turbine; where flow separations are 3D phenomena captured using CFD simulations and are not well captured in the loss models.
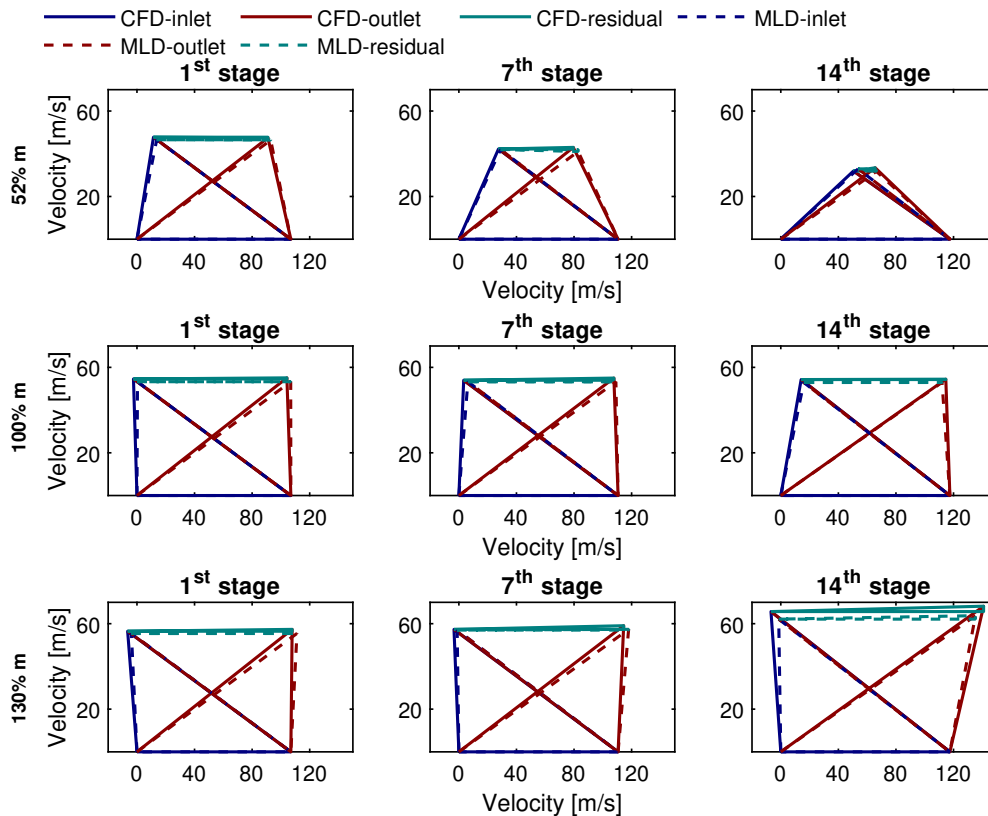
Figure 6.11: Comparison between the velocity triangles of the CO_2/SO_2 flow path at 52%, 100% and 130% of the design mass flow rate.

To further explain the flow separations, the flow structures, captured by the CFD model at 52% and 100% of the design mass flow rate, are presented in Figure 6.12. At the design point, the flow passes through each turbine stage without generating any excessive vortices. On the contrary, at the low mass flow rate case (52% of the design mass flow rate) there is an indication of flow separation towards the final turbine stages as a result of the increased incidence. By investigating the off-design operation over a range of mass flow rates, it is

found that the location where flow separation starts moves further upstream with reducing the mass flow rate. Therefore, flow separations are experienced over a larger number of stages at low mass flow rates. This explains the high drop in efficiency predicted by the CFD model with respect to the ML model at lower mass flow rates in addition to confirming the similar performance obtained by both models at higher mass flow rates. It is worth mentioning that flow separations similar to those observed at the mid-span are also present at the blade hub. However, significantly larger flow separations occur at the blade tip compared to the blade hub and mid-span due to the clearance gap effect near the tip.

It can be concluded that the difference in flow angles between the mean-line and CFD simulations, with a maximum difference of $6°$ in the incidence angle, results in passage blockage (reducing the effective flow area) and separation effects at lower mass flow rates, leading to differences in the predicted total-to-total efficiency.
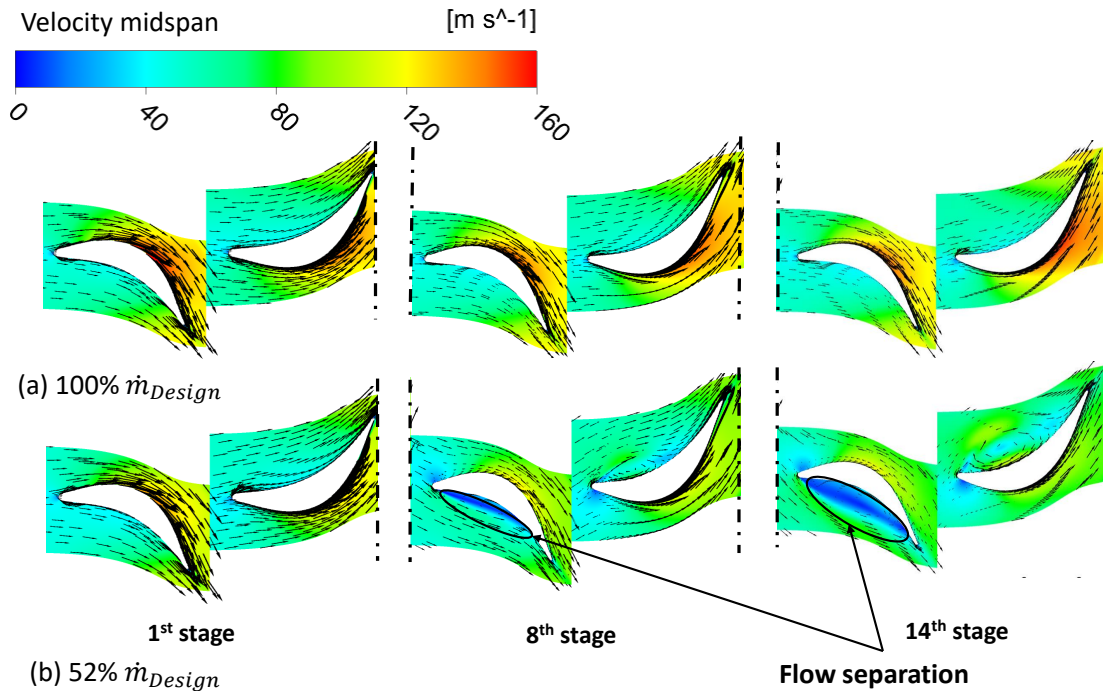
Figure 6.12: Flow field obtained for the 1st, 7th and 14th design stage (a) at the design point (b) 52 % of the design mass flow rate at the blade mid-span.

The separation effects are further elaborated with the enthalpy-entropy change across the turbine stages as presented in Figure 6.13a. The deviation between the ML and the

CFD results is more evident at the lowest mass flow rate (52% of $\dot{m}_{design}$) as shown in Figure 6.13a. Therefore, the entropy change estimated by the CFD results is different from the ML results at lower mass flow rates due to capturing the secondary flows and vortices within 3D flow. Similarly, the power produced per stage is presented by both the ML and CFD results in Figure 6.13b.

In summary, it is evident that the ML model under-predicts the turbine off-design performance at low mass flow rates with respect to the CFD result. This is due to the flow separation effects captured in the 3D flow which results in entropy change and hence, less turbine efficiency; where the ML loss model does not accurately predict the turbine performance in the presence of flow separations. Having said this, Moustapha et al. [75] reviewed the Ainley model, on which the Aungier off-correlations are based, and they concluded that this model is under-predicting the profile losses at high negative incidence. Additionally, the incidence effect is not considered in the secondary flow losses and hence, it also under-predicts the secondary flow losses. On this matter, a preliminary investigation for Moustapha et al. [75] correlations are conducted for the same design case and similar results are found.
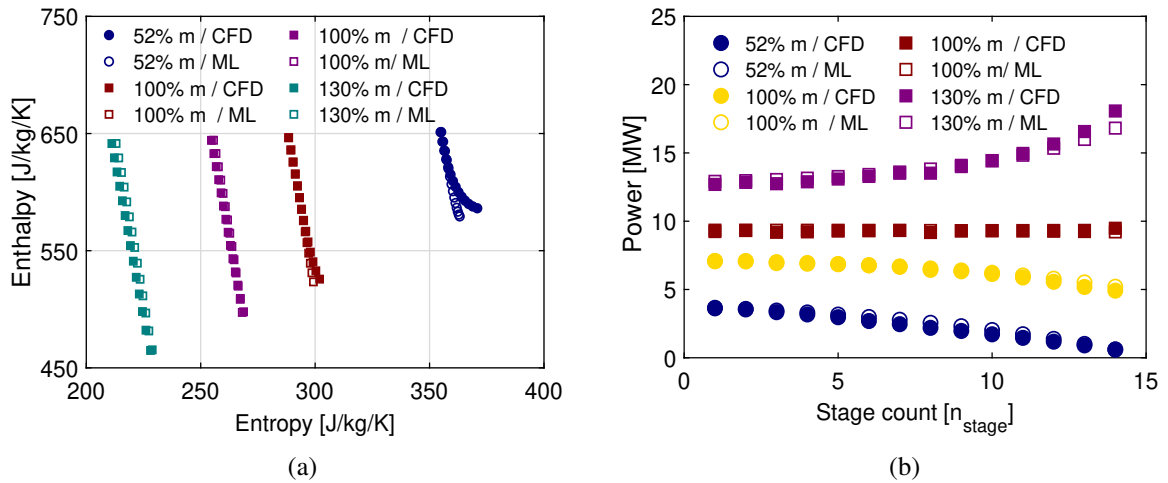
Figure 6.13: Entropy-Enthalpy (h-s) diagram (b) power generated versus the number of stages for the CO_2/SO_2 flow path at 52%, 82% 100% and 130% of the design mass flow rate.

6.4 Conclusions

In this chapter, the different aspects of off-design mean-line performance methodology were discussed. This includes a description of the implemented mean-line performance approach alongside a discussion about the implemented loss model in the current work. The mean-line performance approach was verified against multiple cases from the literature that includes a single-stage CO_2 turbine, a four-stage air turbine and a three-stage CO_2 turbine. A good agreement was obtained between the used methodology and the cases from the literature. Nonetheless, some differences in the predicted efficiencies for the air turbine case were obtained; which was expected to happen due to the losses that are not well captured within the mean-line model.

Furthermore, the off-design performance maps were presented for the CO_2/SO_2 turbine. The maps generated by the mean-line mode were compared with respect to the CFD results and a good agreement was achieved between the ratio of the isentropic stagnation enthalpy change to the square of speed of sound ($\Delta h_{0s}/a_{01}^2$), which is directly related to the turbine pressure ratio, predicted by both mean-line and CFD models across a wide range of mass flow rates (from 52 to 130% of the design value). Nevertheless, large deviations were found in the total-to-total efficiency. Therefore, this chapter presented a comprehensive investigation into the performance predictions obtained by the mean-line model in comparison to the CFD results. This includes comparing and investigating the differences in incidence and deviation angles, velocity triangles, produced power and entropy change. It was found that deviations occur due to flow separation in the flow field, which is not well captured in the loss model that assumes attached flows. This separation is caused by the deviation in the predicted flow angles between the mean-line and computational fluid dynamics models.

This page is left intentionally blank

7 Conclusions and recommendations for further work

7.1 Conclusions

The aim of this study is to apply the existing design methodologies and enable the conceptual mean-line flow-path design for a multi-stage axial turbine operating with CO_2 blends for installation in a 100 MWe CSP plant. Within the context of this research framework, the predictive capability of existing loss models were investigated for non-conventional working fluids across a range of scales. Multiple mean-line flow paths were designed to operate with pure CO_2 and CO_2 blends. Ultimately, a performance analysis was carried out for the final selected flow path over a range of off-design conditions. The main objectives of this research were specified in Chapter 1.

In the following sub-sections, the outcomes of this thesis are evaluated against the research objectives and gaps specified in the literature.

7.1.1 Develop a mean-line tool for supercritical CO_2 axial turbine design

Supercritical CO_2 (sCO_2) turbines experience several operation challenges due to the compact geometries, high density and low kinematic viscosity of the working fluid compared to air turbines as reported in the literature (Chapter 2). Particularly, structural and mechanical considerations were found to be highly significant while dealing with dense working fluids such as sCO_2. Therefore, the first objective of this study is to explore the existing design methodologies for multistage axial turbine design for sCO_2 blends considering both mechanical and rotordynamic design constraints. The design constraints were specified based on industrial experience to ensure technically feasible solutions with maximum aerodynamic efficiency. It is worth mentioning that these constraints were not considered within the earlier studies presented in the literature which adds to the novelty of the pre-

sented work.

In this thesis, the mean-line model was developed to design the turbine under two different assumptions; constant mean diameter and constant hub diameter. The constant hub diameter assumption was considered to avoid the potential rotordynamic and mechanical challenges associated with turbines designed at a constant mean diameter. To ensure the suitability of the design tool for different working fluids, the design methodology was verified against multiple case-studies from the literature for air, sCO_2 and organic Rankine cycle (ORC) turbines. A maximum percentage difference of 1.5% and 3.7% in the total-to-total and total-to-static efficiency, respectively, was obtained between the developed model and the verification cases.

The design tool was verified for the Smith chart and a good qualitative agreement was obtained. Comparing the result to the Smith chart provided credibility for the developed design tool over a range of operating conditions. The model was verified against CFD simulation results for the 14-stage CO_2/SO_2 turbine. A good agreement was obtained between the mean-line design model and CFD results with a maximum difference in a mass flow rate and total-to-total efficiency of 0.5% and 1.0%, respectively. In summary, the verification results presented in Chapter 3 provided a good credibility for the mean-line design tool over a range of operating conditions for sCO_2 turbine design.

7.1.2   Comparison of the predictive capability of classical loss models

As demonstrated in the literature review (Chapter 2), the first loss model for axial turbine design was developed back in 1949 by Soderberg [62] and one of the latest model updates was presented in 2006 by Aungier [66]. However, these models are still being used as part of the mean-line design procedure in recent studies. Specially, these models have been implemented in the design process of sCO_2 and ORC axial turbines within which each study has applied a single loss model and considered a single working fluid, turbine scale or operating condition. None of the previous studies attempted to highlight the discrepancies between the different models in predicting the turbine performance for non-conventional working fluids. Therefore, a mean-line approach was adopted to investigate the predic-

tive capability of all the common loss models employed within the literature for different working fluids and turbine scales as a part of this thesis.

In Chapter 4 the predictive capability of Dunham and Came, Kacker and Okapuu, Craig and Cox and Aungier loss models were investigated for non-conventional working fluids, thus achieving the second and third objectives of this thesis. Three different case-studies were defined for air, organic Rankine cycle (ORC) and sCO$_2$ turbines within the loss analysis at two different scales. This due to the growing research interest in ORC and closed loop sCO$_2$ cycles for low-to-medium temperature applications ($< 400\,^{\circ}$C) and at heat-source temperatures in the range of 400 to 800 $^{\circ}$C respectively. Small and large-scale turbines of 100 kW & 100 MW, 300 kW & 100 MW and 10 kW & 1 MW were considered for air, sCO$_2$ and ORC systems, respectively, to examine the effect of turbine scale on the predictive capability of the loss models. This allows for examining the effect of some loss contributors such as clearance gap to blade height and surface roughness to chord length ratios with respect to the different turbine scales.

It was found that large-scale air turbines experience the highest profile and secondary flow losses compared to sCO$_2$ and ORC turbines, whilst tip clearance losses were found to have the smallest effect on the turbine performance. For large-scale sCO$_2$ and ORC turbines, clearance losses contributed by a larger extent to the total aerodynamic loss compared to the large-scale air turbine. The large-scale air turbine mostly operates in the transitional region, while the ORC and sCO$_2$ turbines operate in the turbulent flow regime. Thus, the surface roughness effect on both profile and secondary flow losses was found to be more significant in the sCO$_2$ and ORC turbines compared to the air turbine.

For the small-scale air turbines, it was found that the flow is subjected to laminar boundary layer separations and hence, high profile and secondary flow losses were observed. For small-scale sCO$_2$ and ORC turbines, the fluid compressibility and surface roughness effect were found to be significant in turbulent flow regimes. Tip clearance loss was found to significantly reduce the turbine efficiency for all working fluids, particularly for the sCO$_2$ and ORC turbines, due to the compactness of small machines and the over-estimated clearance losses by the mean-line models.

Therefore, it is recommended to implement both the Kacker and Okapuu and Aungier loss models for the large-scale sCO_2 applications taking into consideration that supersonic flow is less likely to happen. Meanwhile, the Aungier model should provide more accurate results due to considering surface roughness and Reynolds number effects for the secondary flow losses. As for the ORC turbines, the Aungier model was found to be the most suitable model due to the accurate predictions of the supersonic flow losses. It is recommended to implement a loss model that accounts for the effect of surface roughness for small-scale sCO_2 and ORC turbines, where higher surface roughness to the chord length ratio is experienced. Thus, the Aungier model was found to be more accurate compared to the Kacker and Okapuu model where this effect is ignored.

The Dunham and Came model was found to provide considerably less accurate results for both sCO_2 and ORC turbines, for large and small-scale turbines, due to ignoring surface roughness and compressibility effects, overestimating the supersonic expansion losses and underestimating the Reynolds number effects. To the authors' knowledge, the Craig and Cox model was found to under-predict the efficiency of the non-conventional working fluids compared to the rest of the models, particularly for the off-optimum design conditions and small-scale turbine designs. To conclude, the Aungier model was found to be the most suitable loss model for the SCARABEUS turbine scale.

The findings of this analysis are considered important contributions to the field by providing clarity on the selection of axial turbine loss models for application areas that are becoming increasingly important for future sustainable power production. It is worth noting here that these conclusions should be validated against experimental data. Unfortunately, most of the existing experimental work considers turbines operating with air and steam with limited experimental data available for axial sCO_2 and ORC turbines. Therefore, experimental data for the validation of turbomachinery loss models and loss breakdown is scarce. In view of this, the next step would be to conduct 3D CFD simulations to further validate the results.

7.1.3   Flow path designs for axial turbines operating with CO_2 based working fluids

The utilisation of certain supercritical CO_2 (sCO_2) blends, namely CO_2/TiCl$_4$, CO_2/C$_6$F$_6$ and CO_2/SO$_2$, have been found to be promising for enhancing the performance of power cycles for Concentrated Solar Power (CSP) applications; allowing for up to 6 percentage points enhancement in cycle efficiency with respect to a simple recuperated CO_2 cycle, depending upon the nature of the used mixture and the choice of cycle configuration. This efficiency gain is primarily due to the reduction in compression work realised by operating with a condensing CO_2 cycle. The fourth objective of this study is concerned with applying the existing design methodologies for a multi-stage axial turbine operating with CO_2 blends for installation in a 100 MWe CSP plant. Within this objective, the sensitivity of the turbine design to the selected working fluids and imposed optimal cycle conditions was assessed. Furthermore, a parametric study was conducted to investigate the effect of changing multiple turbine design parameters, including the loading and flow coefficients, degree of reaction and pitch-to-chord ratio, on the flow path design and overall aerodynamic performance. Ultimately, the performance of turbines operating with CO_2 blends was compared to pure CO_2 alongside exploring the differences in the flow path design imposed by introducing the different working fluids.

To achieve this objective, several flow paths were designed for the three sCO_2 blends under different cycle boundary conditions. Five different molar fractions and two different turbine inlet pressure and temperature levels were considered, between 250 & 350 bar and at 550 & 700°C respectively, to develop turbine designs for optimised cycle configurations. Despite the different degrees of sensitivity of each blend to the inlet temperature, pressure and molar fraction, all the designs were capable of achieving high aerodynamic efficiency. A total-to-total efficiency in excess of 92% was obtained for all designs considering both rotor-dynamic and mechanical design constraints. However, a cycle efficiency greater than 50% was achieved for all the investigated blends at an inlet temperature of 700°C only. As for the molar fraction effect, different optimum molar fractions were obtained for the best cycle and turbine performance; for example, 17% and 14.5% were found to be the optimum

molar fractions of the CO_2/$TiCl_4$ blend, at an inlet 700°C and 250 bar, for the optimum cycle and turbine performance, respectively. In this regard, designing the turbine, for the CO_2-$TiCl_4$ blend, at the optimum cycle molar fraction resulted in a turbine efficiency drop of 0.23 percentage points compared to the optimum (cycle) design point at 250 bar 700°C. On the other hand, if the optimum cycle thermal efficiency is compared against the one calculated with the molar fraction maximising turbine efficiency, a drop of 1.05 percentage points would be obtained at 700°C and 250 bar, respectively. It is worth mentioning that the 0.23 percentage points drop in the turbine efficiency is considered within the margin of accuracy of mean-line flow path design. Therefore, it is worthwhile in any case to design the turbine for the optimal molar fraction capable of maximising the thermal efficiency of the cycle.

This work was extended to cover a parametric study to investigate the effect of changing turbine design variables, including loading and flow coefficients, degree of reaction and pitch-to-chord ratio, on the flow path design and overall aerodynamic performance. It was found that changing the loading coefficient from 0.8 to 1.5 resulted in a reduction in the number of stages from fourteen to five stages for the CO_2/C_6F_6 flow path operating at 700°C and 250 bar. Hence, the total-to-total efficiency decreased by approximately 4 percentage points. Increasing the flow coefficient from 0.3 to 0.7 resulted in an increase in the number of stages from six to thirteen stages and a total-to-total efficiency enhancement by up to 2 percentage points. A less significant effect was found in the case of changing the degree of reaction and pitch-to-chord ratio.

To address the differences in the flow path design imposed by introducing the CO_2 blends compared to the pure CO_2 case, multiple flow paths were designed to operate with the selected working fluids. This includes designing flow paths for the same cycle configuration and power output alongside comparing flow paths designed at the same volumetric flow rate and expansion ratio. It was found that turbines operating with both pure CO_2 and CO_2 blends resulted in overall total-to-total efficiencies in excess of 92.5%. The highest turbine efficiency was obtained by using the pure CO_2 with a maximum efficiency difference of 1.1 percentage points obtained with respect to CO_2/$TiCL_4$ blend; where the

CO_2/TiCL$_4$ mixture allows for accommodating six design stages compared to thirteen-stages in the case of pure CO_2 due to experiencing high rotor bending stresses associate with the high mass flow rate. Meanwhile, differences are experienced within the flow path length (number of stages) and turbine geometry based on both the imposed boundary conditions and the properties of the working fluids.

This performance is considered promising for the pure CO_2 and CO_2 blends in terms of the high aerodynamic performance and compactness of the machine. A hub diameter in the order of 600- 700 mm was obtained which is a significantly compact design compared to conventional steam and air turbines. However, the number of stages is significantly high which is uncommon with respect to the conventional design of air and steam turbine (with a few stages). This is due to the low specific speeds of turbines operating with CO_2 and CO_2 blends of the same size as an air turbine (almost half) for synchronous machines spinning at 3000 RPM. Hence, large number of stages is needed to achieve high aerodynamic performance. It is worth noting that the long flow path proved to be technically feasible based on the preliminary cost analysis presented in Chapter¬5. Designing the CO_2/SO$_2$ flow path with fourteen stages resulted in cost savings (considering the direct material only) of around 1.8 M€with respect to the four-stage design. It can be concluded that turbine designs with large number of stages are needed for real scale CSP plants to achieve a high aerodynamic performance which is contrary to the existing sCO$_2$ turbines prototypes. Accommodating large number of stages for the CO_2 turbines resulted in compact machines with significantly reduced radial dimensions which proved to be economically feasible.

7.1.4 Off-design performance analysis

The last objective of this thesis is concerned with predicting the off-design performance of sCO$_2$ turbines; particularly the turbine performance of the SCARABEUS plant. To achieve this objective, the mean-line off-design approach was applied to the selected flow path design operating with CO_2/SO$_2$ blend. Within the off-design performance model, the Aungier loss correlations were updated to allow for predicting the incidence losses

resulting from the off-design operation. Prior to predicting the turbine performance, the developed off-design methodology was verified against multiple cases from the literature including a single-stage CO_2 and four-stage air turbine cases. Initially, the turbines were designed for the selected cases using the in-house design tool and hence, the off-design performance was predicted. A good agreement was obtained in the predicted performance maps and the literature results which gives a credibility to the performance methodology and the implemented loss model.

The off-design performance maps were generated for the CO_2/SO_2 flow path using the mean-line tool and were compared to the CFD results. A good agreement was obtained between the ratio of the isentropic stagnation enthalpy change to the square of speed of sound $(\Delta h_{0s}/a_{01}^2)$, which is directly related to the turbine pressure ratio, predicted by the mean-line and CFD models across a wide range of mass flow rates ranging from 52 to 130% of the design value. Nonetheless, large deviations were obtained between both models in the predicted total-to-total efficiency. Therefore, a comprehensive comparison between incidence and deviation angles, velocity triangles, produced power and entropy change estimated by the mean-line and CFD models was presented within this analysis. A good agreement was obtained between both models in estimating the incidence, deviation angles and velocity triangles. A maximum difference in the incidence and deviation angles of 6.0% and 1.86 $^\circ$ was obtained between the models at 52% of the design mass flow rate. Nonetheless, small deviations in flow angles can significantly affect the predicted efficiency; where these deviations result in reducing the effective flow area and the presence of flow separations within the flow field. These effects are captured by the CFD model and disregarded within the mean-line tool and hence, efficiencies tend to deviate significantly at low mass flow rates between both models. In conclusion, it is suggested to modify the mean-line loss model to predict the turbine performance at operating conditions where flow separations occur. This requires carrying out extensive investigations for the predicted losses over a range of operating conditions for different working fluids.

7.2   SCARABEUS project on-going activities

As discussed in Chapter 5, ongoing activities are being carried out by the project indus-trial partners to finalise the detailed turbine design for the selected flow path operating with CO_2/SO_2 blend. This includes designing the inner casing, and main cooling streams, selecting the bearing, seals, and coupling and finally conducting a detailed mechanical in-tegrity and rotordynamic stability analysis for the shaft arrangement.

Following, a detailed material selection will take place as a part of this work to identify the final materials selected for each turbine component. Hence, a detailed cost assessment of turbomachinery components, including mechanical and electrical design considerations will be carried out. The detailed mechanical integrity and cost analysis should support the preliminary cost analysis results presented in Chapter 5 and provide a confirmation for the validity of the proposed design hypothesis (long flow path with small hub diameter), with respect to the less number of stages, from a manufacturability and stability standpoint.

7.3   Future work

Here is a list of some recommendations that can be made for future work with respect to the mean-line design methodology and off-design performance model and loss models.

7.3.1   Improvements to the mean-line design model

The in-house design tool developed in the current work (presented in Chapter 3) could be further improved in different ways. The design methodology was developed to allow for considering mechanical and rotordynamic design constraints for a specific turbine scale for the SCARABEUS 100 MWe plant. Hence, the flow paths were designed at specific design parameters (such as the loading and flow coefficients) and a rotational speed of 3000 RPM for large-scale applications. Therefore, the design methodology could be further improved by extending the constraints criteria to be suitable for multiple turbine scales operating over a range of rotational speeds. Within this improvement, additional design considerations should be taken into account to allow for designing feasible sCO_2 turbines at different

scales.

The flow paths were designed in this thesis using a manual process that involves tuning and adjusting the number of stages and number of blades to meet the set design criteria. This allowed for designing multiple flow paths with a high aerodynamic performance alongside complying with the specified mechanical and rotordynamic design criteria. In this regard, the design process should be automated to allow for a faster and more efficient process.

Ultimately, the design methodology did not consider the optimisation of the various design parameters, including flow and loading coefficients, degree of reaction and pitch-to-chord ratio. A specific point was defined within the design space, for the chosen turbine scale, to provide an optimised turbine design from an aerodynamic standpoint considering the different design constraints. On a different note, ideally the optimal molar fraction should be identified through a coupled cycle-turbine design activity, whereby the cycle boundary conditions and turbine are simultaneously optimised. However, due to the complexity of the turbine design process, which includes multiple-stages and the need to manually iterate integer design variables to bring the turbine design within the imposed mechanical and rotordynamics, such an approach has not been adopted. To support the proposed design hypothesis, a simplified cost analysis was carried out for the designed flow paths without being considered throughout the turbine design process.

On this matter, a multi-objective optimisation (i.e., Pareto front) should be applied taking into account the thermodynamic cycle performance, turbine performance and cost as the three objectives of the problem. An optimisation methodology of machine learning and design of experiments (DOE) could be effectively utilised to enhance the tool optimisation capabilities. This is to develop a mathematical model capable of optimising the molar fraction composition of the working fluid, cycle boundary conditions, and configurations to enhance the thermodynamic cycle performance. Additionally, the model should optimise the turbine for both aerodynamic performance and cost. This hybrid approach of machine learning and DOE will depend on the foundations and outcomes resulting from the current work to establish a useful data basis that can be updated to nourish the algorithms of this

optimisation technique. In other words, this method should take benefits of the design of the experiments technique in defining/constraining the significant design variables and the accuracy of the machine learning tool in optimising the performance with respect to the two main areas of interest (efficiency and cost).

7.3.2   Calibration of existing loss models

In Chapter 4 an extensive comparison of the predictive capability of the classical loss models was carried out from the preliminary design standpoint. As per the findings of Chapter 4, the loss models were found to provide discrepancies in the obtained performance and hence, the estimated loss breakdown. Therefore, numerical CFD simulations are being carried out within a different research framework to compare the predictive capability of the loss models against the CFD results. However, both the mean-line design and CFD results were validated for different cases and working fluids from the literature. In this regard, it would be helpful and credible to validate the loss models against experimental measured data for different working fluids. This would enhance the credibility of mean-line design tool and provide a more accurate assessment of the suitability of the existing loss correlations for different working fluids and turbine scales.

Finally, the experimental data should be used to provide some modifications for the empirical constants and correction factors implemented in the loss models, whenever needed, to enhance the accuracy of the models for both ORC and sCO_2 turbines.

7.3.3   Improvements to the off-design performance model

The performance maps were generated and presented for the CO_2/SO_2 flow path using the mean-line performance model over a range of mass flow rates. The Aungier loss model was found to over-predict the turbine aerodynamic performance at off-design conditions compared to the CFD results particularly at a very low mass flow rate (at high negative incidence) as discussed in Chapter 6. This is due to the inability of the loss model to capture some flow effects that existed in the 3D flow path. Therefore, to develop this work further, it will be interesting to compare the predictive capability of the Aungier loss model against

other existing loss models. This should include introducing some modifications to the Aungier loss model to allow for accurate performance predictions at off-design conditions. To do so, an extensive analysis should be carried out to examine the stability of those loss models at different off-design conditions and for different turbine designs. This could be extended to consider different working fluids such as the pure sCO_2 and multiple sCO_2 blends. Consequently, modified mathematical correlations can be imposed on the existing model to allow for predicting the separations that occur in the turbine blade row at very low mass flow rates.

The turbine design presented in Chapter 3 was found to operate with an efficiency of around 93% at design conditions. Nonetheless, the turbine performance was found to decrease at off-design conditions, particularly at very low mass flow rates. Therefore, the machine learning and design of experiments optimisation methodology should be integrated with off-design performance maps to select the best performing turbine design taking into account the performance obtained at design and off-design conditions.

This page is left intentionally blank

Bibliography

[1] G. Kjaerheim, "Cleaner production and sustainability," *Journal of cleaner production*, vol. 13, no. 4, pp. 329–339, 2005.

[2] R. E. S. IRENA, "Renewable Energy Outlook:Egypt, International Renewable Energy Agency," tech. rep., Abu Dhabi, 2018.

[3] T. J. Held, "Supercritical CO_2 cycles for gas turbine combined cycle power plants," Power Gen International December 8-10, Las Vegas, Nevada.

[4] M. T. Islam, N. Huda, A. Abdullah, and R. Saidur, "A comprehensive review of state-of-the-art concentrating solar power (CSP) technologies: Current status and research trends," *Renewable and Sustainable Energy Reviews*, vol. 91, pp. 987 – 1018, 2018.

[5] S. Polimeni, M. Binotti, L. Moretti, and G. Manzolini, "Comparison of sodium and kcl-mgcl$_2$ as heat transfer fluids in csp solar tower with sCO$_2$ power cycles," *Solar Energy*, vol. 162, pp. 510–524, 2018.

[6] D. A. Baharoon, H. A. Rahman, W. Z. W. Omar, and S. O. Fadhl, "Historical development of concentrating solar power technologies to generate clean electricity efficiently – a review," *Renewable and Sustainable Energy Reviews*, vol. 41, pp. 996 – 1027, 2015.

[7] REN21, "Renewables 2019 global status report," *available online: http://www.ren21.net/gsr-2019/ [accessed on 26 July 2019]*.

[8] B. D. Iverson, T. M. Conboy, J. J. Pasch, and A. M. Kruizenga, "Supercritical CO_2 brayton cycles for solar-thermal energy," *Applied Energy*, vol. 111, pp. 957 – 970, 2013.

[9] U. department of energy, "The Year of Concentrating Solar Power," tech. rep., 2014.

[10] C. S. Turchi, Z. Ma, T. W. Neises, and M. J. Wagner, "Thermodynamic Study of Advanced Supercritical Carbon Dioxide Power Cycles for Concentrating Solar Power Systems," *Journal of Solar Energy Engineering*, vol. 135, 06 2013.

[11] S. Besarati and D. Goswami, "Chapter8 - supercritical CO_2 and other advanced power cycles for concentrating solar thermal (cst) systems," in *Advances in Concentrating Solar Thermal Research and Technology* (M. J. Blanco and L. R. Santigosa, eds.), Woodhead Publishing Series in Energy, pp. 157 – 178, Woodhead Publishing, 2017.

[12] F. Crespi, D. Sánchez, G. S. Martínez, T. Sánchez-Lencero, and F. Jiménez-Espadafor, "Potential of supercritical carbon dioxide power cycles to reduce the levelised cost of electricity of contemporary concentrated solar power plants," *Applied Sciences*, vol. 10, no. 15, p. 5049, 2020.

[13] F. Crespi, P. R. de Arriba, D. Sánchez, A. Ayub, G. Di Marcoberardino, C. M. Invernizzi, G. Martínez, P. Iora, D. Di Bona, M. Binotti, *et al.*, "Thermal efficiency gains enabled by using CO_2 mixtures in supercritical power cycles," *Energy*, vol. 238, p. 121899, 2022.

[14] M. T. White, G. Bianchi, L. Chai, S. A. Tassou, and A. I. Sayma, "Review of supercritical CO_2 technologies and systems for power generation," *Applied Thermal Engineering*, vol. 185, p. 116447, 2021.

[15] Z. Ma and C. S. Turchi, "Advanced supercritical carbon dioxide power cycle configurations for use in concentrating solar power systems," tech. rep., National Renewable Energy Lab.(NREL), Golden, CO (United States), 2011.

[16] O. A. Aqel, M. T. White, M. Khader, and A. Sayma, "Sensitivity of transcritical cycle and turbine design to dopant fraction in CO_2-based working fluids," *Applied Thermal Engineering*, vol. 190, p. 116796, 2021.

[17] M. Binotti, C. M. Invernizzi, P. Iora, and G. Manzolini, "Dinitrogen tetroxide and carbon dioxide mixtures as working fluids in solar tower plants," *Solar Energy*, vol. 181, pp. 203 – 213, 2019.

[18] G. Manzolini, M. Binotti, D. Bonalumi, C. Invernizzi, and P. Iora, "CO_2 mixtures as innovative working fluid in power cycles applied to solar plants. techno-economic assessment," *Solar Energy*, vol. 181, pp. 530 – 544, 2019.

[19] "Scarabeus project home page," Available online: http://www.scarabeusproject.eu/ [Accessed: 26/11/2015].

[20] F. Crespi, P. R. de Arriba, D. Sánchez, and A. Muñoz, "Preliminary investigation on the adoption of CO_2-SO_2 working mixtures in a transcritical Recompression cycle," *Applied Thermal Engineering*, vol. 211, p. 118384, 2022.

[21] G. Musgrove and S. Wright, "Chapter 1 - introduction and background," in *Fundamentals and Applications of Supercritical Carbon Dioxide(sCO_2) Based Power Cycles* (K. Brun, P. Friedman, and R. Dennis, eds.), pp. 1 – 22, Woodhead Publishing, 2017.

[22] H. Saravanamuttoo, G. Rogers, and H. Cohen, *Gas Turbine Theory*. Prentice Hall, 2001.

[23] S. Dixon and C. Hall, "Chapter 4 - axial-flow turbines: Mean-line analysis and design," in *Fluid Mechanics and Thermodynamics of Turbomachinery* (S. Dixon and C. Hall, eds.), pp. 97 – 141, Boston: Butterworth-Heinemann, sixth edition ed., 2010.

[24] Y. Cengel and M. Boles, "Chapter 6 - the second law of thermodynamics," in *Thermodynamics : An Engineering Approach*, pp. 279 – 330, McGraw-Hill, 2010.

[25] F. Crespi, G. Gavagnin, D. Sánchez, and G. S. Martínez, "Supercritical carbon dioxide cycles for power generation: A review," *Applied Energy*, vol. 195, pp. 152 – 183, 2017.

[26] Y. Liu, Y. Wang, and D. Huang, "Supercritical CO_2 brayton cycle: A state-of-the-art review," *Energy*, vol. 189, p. 115900, 2019.

[27] G. Angelino, "Carbon Dioxide Condensation Cycles For Power Production," *Journal of Engineering for Power*, vol. 90, pp. 287–295, 07 1968.

[28] E. Feher, "The supercritical thermodynamic power cycle," *Energy Conversion*, vol. 8, no. 2, pp. 85 – 90, 1968.

[29] V. Dostal, M. Driscoll, and P. Hejzlar, *A supercritical carbon dioxide cycle for next generation nuclear reactors*. Massachusetts Institute of Technology, Boston, MA., 2004.

[30] N. Weiland, R. Dennis, R. Ames, S. Lawson, and P. Strakey, "Chapter 12 - fossil energy," in *Fundamentals and Applications of Supercritical Carbon Dioxide (sCO_2) Based Power Cycles* (K. Brun, P. Friedman, and R. Dennis, eds.), pp. 293 – 338, Woodhead Publishing, 2017.

[31] C. S. Turchi, Z. Ma, and J. Dyreby, "Supercritical CO_2 for application in concentrating solar power systems," in *Proceedings of SCCO$_2$ power cycle symposium*, pp. 29–30, 2009.

[32] T. Neises and C. Turchi, "A comparison of supercritical carbon dioxide power cycle configurations with an emphasis on csp applications," *Energy Procedia*, vol. 49, pp. 1187–1196, 2014.

[33] F. A. Al-Sulaiman and M. Atif, "Performance comparison of different supercritical carbon dioxide brayton cycles integrated with a solar power tower," *Energy*, vol. 82, pp. 61–71, 2015.

[34] K. Wang, Y.-L. He, and H.-H. Zhu, "Integration between supercritical CO_2 brayton cycles and molten salt solar power towers: A review and a comprehensive comparison of different cycle layouts," *Applied energy*, vol. 195, pp. 819–836, 2017.

[35] G. Di Marcoberardino, C. Invernizzi, P. Iora, A. Ayub, D. Di Bona, P. Chiesa, M. Binotti, and G. Manzolini, "Experimental and analytical procedure for the characterization of innovative working fluids for power plants applications," *Applied Thermal Engineering*, vol. 178, p. 115513, 2020.

[36] W. S. Jeong, J. I. Lee, and Y. H. Jeong, "Potential improvements of supercritical recompression CO_2 brayton cycle by mixing other gases for power conversion system of a SFR," *Nuclear Engineering and Design*, vol. 241, no. 6, pp. 2128–2137, 2011.

[37] W. S. Jeong and Y. H. Jeong, "Performance of supercritical brayton cycle using CO_2-based binary mixture at varying critical points for sfr applications," *Nuclear Engineering and Design*, vol. 262, pp. 12–20, 2013.

[38] R. Valencia-Chapi, L. Coco-Enríquez, and J. Muñoz-Antón, "Supercritical CO_2 mixtures for advanced brayton power cycles in line-focusing solar power plants," *Appl. Sci.*, vol. 10, 2020.

[39] E. Morosini, G. Manzolini, G. Di Marcoberardino, C. Invernizzi, and P. Iora, "Investigation of CO_2 mixtures to overcome the limits of sCO2 cycles," in *76th Italian National Congress ATI (ATI 2021)*, vol. 312, pp. 08010–08019, 2021.

[40] G. Manzolini, M. Binotti, E. Morosini, D. Sánchez, F. Crespi, G. Di Marcoberardino, P. Iora, and C. Invernizzi, "Adoption of CO_2 blended with C_6F_6 as working fluid in CSP plants," in *AIP Conference Proceedings*, vol. 2445, p. 090005, AIP Publishing LLC, 2022.

[41] P. Rodríguez-deArriba, F. Crespi, D. Sánchez, A. Muñoz, and T. Sánchez, "The potential of transcritical cycles based on CO_2 mixtures: An exergy-based analysis," *Renewable Energy*, vol. 199, pp. 1606–1628, 2022.

[42] E. Morosini, A. Ayub, G. di Marcoberardino, C. M. Invernizzi, P. Iora, and G. Manzolini, "Adoption of the $CO_2 + SO_2$ mixture as working fluid for transcritical cycles: A thermodynamic assessment with optimized equation of state," *Energy Conversion and Management*, vol. 255, p. 115263, 2022.

[43] S. I. Salah, F. Crespi, M. T. White, A. M. noz, A. Paggini, M. Ruggiero, D. Sánchez, and A. I. Sayma, "Axial turbine flow path design for concentrated solar power plants operating with CO_2 blends," *Applied Thermal Engineering*, 2023.

[44] G. D. Marcoberardino, E. Morosini, D. D. Bonac, P. Chiesabc, C. Invernizzia, P. Ioraa, and G. Manzolin, "Experimental characterisation of $CO_2 + C_6F_6$ mixture: thermal stability and vapour liquid equilibrium test for its application in transcritical power cycle," *Applied Thermal Engineering*, vol. 212, p. 118520, 2022.

[45] "NFPA 704: Standard System for the Identification of the Hazards of Materials for Emergency Response," 2022. Online, accessed February 6th 2022 .

[46] G. Di Marcoberardino, E. Morosini, D. Di Bona, P. Chiesa, C. Invernizzi, P. Iora, and G. Manzolini, "Experimental characterisation of CO_2+ c_6f_6 mixture: Thermal stability and vapour liquid equilibrium test for its application in transcritical power cycle," *Applied Thermal Engineering*, vol. 212, p. 118520, 2022.

[47] G. Di Marcoberardino, E. Morosini, and G. Manzolini, "Preliminary investigation of the influence of equations of state on the performance of $CO_2 + C_6F_6$ as innovative working fluid in transcritical cycles," *Energy*, vol. 238, p. 121815, 2022.

[48] D.-Y. Peng and D. B. Robinson, "A new two-constant equation of state," *Industrial & Engineering Chemistry Fundamentals*, vol. 15, no. 1, pp. 59–64, 1976.

[49] G. Soave, "Equilibrium constants from a modified redlich-kwong equation of state," *Chemical engineering science*, vol. 27, no. 6, pp. 1197–1203, 1972.

[50] J. Gross and G. Sadowski, "Perturbed-chain saft: An equation of state based on a perturbation theory for chain molecules," *Industrial & engineering chemistry research*, vol. 40, no. 4, pp. 1244–1260, 2001.

[51] T. Neumann, "Development of new helmholtz models for binary mixture relevant for ccs," *Ruhr-Universität Bochum*, 2017.

[52] "Simulis thermodynamics," Available online:http://www.prosim.net/en/software-simulis-thermodynamics-mixture-properties-and-fluid-phase-equilibria-calculations-3.php. [Accessed: 13-Nov-2019].

[53] G. Persico and M. Pini, "Chapter 8 - fluid dynamic design of organic rankine cycle turbines," in *Organic Rankine Cycle (ORC) Power Systems* (E. Macchi and M. Astolfi, eds.), pp. 253 – 297, Woodhead Publishing, 2017.

[54] S. Dixon and C. Hall, "Chapter 8 - radial flow gas turbines," in *Fluid Mechanics and Thermodynamics of Turbomachinery* (S. Dixon and C. Hall, eds.), pp. 265 – 299, Boston: Butterworth-Heinemann, sixth edition ed., 2010.

[55] "Softinway:turbomaschinen im griff," Available online:https://www.softinway.com/de/education/classroom-training/axial-turbine-reverse-engineering-and-re-design-4-day-course/.

[56] "https://www.cfdsupport.com/radial-turbine-cfd.html," Available online:https://www.cfdsupport.com/radial-turbine-cfd.html/.

[57] Y. Ahn, S. J. Bae, M. Kim, S. K. Cho, S. Baik, J. I. Lee, and J. E. Cha, "Review of supercritical CO_2 power cycle technology and current status of research and development," *Nuclear Engineering and Technology*, vol. 47, pp. 647 – 661, 2015.

[58] S. I. Salah, M. A. Khader, M. T. White, and A. I. Sayma, "Mean-line design of a supercritical CO_2 micro axial turbine," *Applied Sciences*, vol. 10, no. 15, p. 5069, 2020.

[59] O. P. Sharma and T. L. Butler, "Predictions of Endwall Losses and Secondary Flows in Axial Flow Turbine Cascades," *Journal of Turbomachinery*, vol. 109, pp. 229–236, 04 1987.

[60] H. R. M. Craig and H. J. A. Cox, "Performance estimation of axial flow turbines," *Proceedings of the Institution of Mechanical Engineers*, vol. 185, no. 1, pp. 407–424, 1970.

[61] O. E. Balje and R. L. Binsley, "Axial Turbine Performance Evaluation. Part A—Loss-Geometry Relationships," *Journal of Engineering for Power*, vol. 90, pp. 341–348, 10 1968.

[62] C. R. Soderberg *Gas Turbine Laboratory, Massachusetts Institute of Technology*, 1949.

[63] D. Ainley and G. Mathieson, *A Method of Performance Estimation for Axial-flow Turbines*. Aeronautical Research Council. Reports and memoranda, H.M. Stationery Office, 1951.

[64] J. Dunham and P. M. Came, "Improvements to the Ainley-Mathieson Method of Turbine Performance Prediction," *Journal of Engineering for Power*, vol. 92, pp. 252–256, 07 1970.

[65] S. C. Kacker and U. Okapuu, "A Mean Line Prediction Method for Axial Flow Turbine Efficiency," *Journal of Engineering for Power*, vol. 104, pp. 111–119, 01 1982.

[66] R. H. Aungier, *Turbine Aerodynamics: Axial-Flow and Radial-Flow Turbine Design and Analysis*. ASME Press, 01 2006.

[67] E. Macchi and M. Astolfi, "Chapter 9 - axial flow turbines for organic rankine cycle applications," in *Organic Rankine Cycle (ORC) Power Systems* (E. Macchi and M. Astolfi, eds.), pp. 299 – 319, Woodhead Publishing, 2017.

[68] J. Qi, T. Reddell, K. Qin, K. Hooman, and I. H. J. Jahn, "Supercritical CO_2 Radial Turbine Design Performance as a Function of Turbine Size Parameters," *Journal of Turbomachinery*, vol. 139, 03 2017.

[69] H. Moustapha, M. Zelesky, N. Balnes, and D. Japikse, "Chapter 3 - preliminary and through flow design," in *Axial and Radial Turbines*, pp. 65–95, Concepts NREC, 2003.

[70] N. Holaind, G. Bianchi, M. Miol, S. Sayad Saravi, S. Tassou, A. Leroux, and H. Jouhara, "Design of radial turbomachinery for supercritical CO_2 systems using theoretical and numerical CFD methodologies," vol. 123, pp. 313–320, 04 2017.

[71] D. Luo, Y. Liu, X. Sun, and D. Huang, "The design and analysis of supercritical carbon dioxide centrifugal turbine," *Applied Thermal Engineering*, vol. 127, pp. 527 – 535, 2017.

[72] A. Zhou, J. Song, X. Li, X. Ren, and C. Gu, "Aerodynamic design and numerical analysis of a radial inflow turbine for the supercritical carbon dioxide brayton cycle," *Applied Thermal Engineering*, vol. 132, pp. 245 – 255, 2018.

[73] G. Lv, J. Yang, W. Shao, and X. Wang, "Aerodynamic design optimization of radial-inflow turbine in supercritical CO_2 cycles using a one-dimensional model," *Energy Conversion and Management*, vol. 165, pp. 827 – 839, 2018.

[74] M. Saeed and M.-H. Kim, "Analysis of a recompression supercritical carbon dioxide power cycle with an integrated turbine design/optimization algorithm," *Energy*, vol. 165, pp. 93 – 111, 2018.

[75] S. H. Moustapha, S. C. Kacker, and B. Tremblay, "An Improved Incidence Losses Prediction Method for Turbine Airfoils," *Journal of Turbomachinery*, vol. 112, pp. 267–276, 04 1990.

[76] J. Lee, J. I. Lee, Y. Ahn, and H. Yoon, "Design methodology of supercritical CO_2 brayton cycle turbomachineries," in *Proceedings of the ASME Turbo Expo: Turbine Technical Conference and Exposition*, June 11–15, 2012, Copenhagen, Denmark.

[77] J. Schmitt, R. Willis, D. Amos, J. Kapat, and C. Custer, "Study of a supercritical CO_2 turbine with tit of 1350 k for brayton cycle with 100 mw class output: Aerodynamic analysis of stage 1 vane," *Proceedings of the ASME Turbo Expo*, vol. 3, 06 2014.

[78] L. Moroz, B. Frolov, M. Burlaka, and O. Guriev, "Turbomachinery flowpath design and performance analysis for supercritical CO_2," in *Proceedings of the ASME Turbo Expo: Turbine Technical Conference and Exposition*, June 16–20, 2014, Düsseldorf, German.

[79] H. Zhang, H. Zhao, Q. Deng, and Z. Feng, "Aerothermodynamic design and numerical investigation of supercritical carbon dioxide turbine," in *Proceedings of the ASME Turbo Expo: Turbine Technical Conference and Exposition*, June 15–19, 2015, Montreal, Quebec, Canada.

[80] D. Shi, L. Zhang, Y. Xie, and D. Zhang, "Aerodynamic design and off-design performance analysis of a multi-stage s-CO_2 axial turbine based on solar power generation system," *Applied Sciences*, vol. 9, p. 714, 02 2019.

245

[81] L. Da Lio, G. Manente, and A. Lazzaretto, "New efficiency charts for the optimum design of axial flow turbines for organic Rankine cycles," *Energy*, vol. 77, pp. 447–459, 2014.

[82] L. Talluri and G. Lombardi, "Simulation and design tool for ORC axial turbine stage," *Energy Procedia*, vol. 129, pp. 277–284, 2017.

[83] L. Da Lio, G. Manente, and A. Lazzaretto, "Predicting the optimum design of single stage axial expanders in ORC systems: Is there a single efficiency map for different working fluids?," *Applied Energy*, vol. 167, pp. 44–58, 2016.

[84] R. Agromayor and L. O. Nord, "Preliminary design and optimisation of axial turbines accounting for diffuser performance," *International Journal of Turbomachinery, Propulsion and Power*, vol. 4, no. 3, 2019.

[85] A. Meroni, *Design and Optimization of Turbomachinery for Thermodynamic Cycles Utilizing Low-Temperature Heat Sources*. PhD thesis, 2018.

[86] A. Meroni, A. La Seta, J. G. Andreasen, L. Pierobon, G. Persico, and F. Haglind, "Combined turbine and cycle optimization for organic Rankine cycle power systems—part A: turbine model," *Energies*, vol. 9, no. 5, 2016.

[87] A. K. Sleiti and W. A. Al-Ammari, "Off-design performance analysis of combined csp power and direct oxy-combustion supercritical carbon dioxide cycles," *Renewable Energy*, vol. 180, pp. 14–29, 2021.

[88] S. Hosseinimaab and A. Tousi, "A new approach to off-design performance analysis of gas turbine engines and its application," *Energy Conversion and Management*, vol. 243, p. 114411, 2021.

[89] L.-H. Zhi, P. Hu, L.-X. Chen, and G. Zhao, "Multiple parametric analysis, optimization and efficiency prediction of transcritical organic rankine cycle using trans-1, 3, 3, 3-tetrafluoropropene (R1234ze (E)) for low grade waste heat recovery," *Energy Conversion and Management*, vol. 180, pp. 44–59, 2019.

[90] H. Tobiasz, "Off-design performance of multistage turbines," *Journal of Engineering for Power*, vol. 93, p. 21, 1971.

[91] A. Baheta, M. Sidahmed, S. Suleiman, A. Fentaye, and G. Syed, "Development and validation of a twin shaft industrialgas turbine performance model," *ARPN Journal of Engineering and Applied Sciences*, vol. 22, no. 1819-6608, pp. 13365–13371, 2016.

[92] J. Kurzke, "Component map collection 2, compressor and turbine maps for gas turbine performance computer programs," *Joachim Kurzke, Dachau*, 2004.

[93] K. Touil and A. Ghenaiet, "Simulation and analysis of vane-blade interaction in a two-stage high-pressure axial turbine," *Energy*, vol. 172, pp. 1291–1311, 2019.

[94] R. Nicoara, V. Vilag, J. Vilag, and Z. Kolozvary, "Axial turbine performance estimation during dynamic operations," *International Journal of Aeronautical and Space Sciences*, vol. 22, no. 2, pp. 359–365, 2021.

[95] F. Payri, J. Serrano, P. Fajardo, M. Reyes-Belmonte, and R. Gozalbo-Belles, "A physically based methodology to extrapolate performance maps of radial turbines," *Energy Conversion and Management*, vol. 55, pp. 149–163, 2012.

[96] R. Martinez-Botas, "Opportunities and challenges. turbocharger trends and requirements forum," in *Annex in the proceedings of the 8th international conference on turbochargers and turbocharging, London*, pp. 15–18, 2006.

[97] D. Hu, S. Li, Y. Zheng, J. Wang, and Y. Dai, "Preliminary design and off-design performance analysis of an organic rankine cycle for geothermal sources," *Energy Conversion and Management*, vol. 96, pp. 175–187, 2015.

[98] M. White and A. I. Sayma, "The application of similitude theory for the performance prediction of radial turbines within small-scale low-temperature organic Rankine cycles," *Journal of Engineering for Gas Turbines and Power*, vol. 137, no. 12, 2015.

[99] L. Zhang, W. Zhuge, Y. Zhang, and T. Chen, "Similarity theory based radial turbine performance and loss mechanism comparison between R245fa and air for heavy-duty diesel engine organic Rankine cycles," *Entropy*, vol. 19, no. 1, p. 25, 2017.

[100] Y. Du, P. Han, X. Qiang, M. Hao, Y. Long, P. Zhao, and Y. Dai, "Off-design performance analysis of a combined cooling and power system driven by low-grade heat source," *Energy Conversion and Management*, vol. 159, pp. 327–341, 2018.

[101] R. Pili, N. Siamisiis, R. Agromayor, L. O. Nord, C. Wieland, and H. Spliethoff, "Efficiency correlations for off-design performance prediction of orc axial-flow turbines," in *Proceedings of the 5th International Seminar on ORC Power Systems, the National Technical University of Athens (NTUA)*, 2019.

[102] M. G. Kofskey and W. J. Nusbaum, "Design and cold-air investigation of a turbine for a small low-cost turbofan engine," tech. rep., 1972.

[103] J. J. Dyreby, S. A. Klein, G. F. Nellis, and D. T. Reindl, "Modeling off-design and part-load performance of supercritical carbon dioxide power cycles," in *Proceedings of the ASME Turbo Expo: Turbine Technical Conference and Exposition*, June 3–7, 2013, San Antonio, Texas, USA.

[104] N. Peng, E. Wang, and F. Meng, "Off-design performance comparison of single-stage axial turbines using CO_2 and zeotropic mixture for low-temperature heat source," *Energy Conversion and Management*, vol. 213, p. 112838, 2020.

[105] S. A. Wright, T. M. Conboy, and G. E. Rochau, "Break-even power transients for two simple recuperated s-CO_2 brayton cycle test configurations.," tech. rep., Sandia National Lab.(SNL-NM), Albuquerque, NM (United States), 2011.

[106] M. Walker, D. D. Fleming, and J. J. Pasch, "Gas foil bearing coating behavior in environments relevant to s-CO_2 power system turbomachinery.," tech. rep., Sandia National Lab.(SNL-NM), Albuquerque, NM (United States), 2018.

[107] J. Pasch and D. Stapp, "Testing of a new turbocompressor for supercritical carbon dioxide closed brayton cycles," in *Proceedings of the ASME Turbo Expo: Turbine Technical Conference and Exposition*, June 11–15, 2018, Oslo, Norway.

[108] L. M. Rapp, "Experimental testing of a 1mw sCO$_2$ turbocompressor.," tech. rep., Sandia National Lab.(SNL-NM), Albuquerque, NM (United States), 2019.

[109] E. M. Clementoni, T. L. Cox, and M. A. King, "Startup and operation of a supercritical carbon dioxide Brayton cycle," *Journal of Engineering for Gas Turbines and Power*, vol. 136, July 2014.

[110] E. M. Clementoni, T. L. Cox, and M. A. King, "Off-Nominal Component Performance in a Supercritical Carbon Dioxide Brayton Cycle," *Journal of Engineering for Gas Turbines and Power*, vol. 138, August 2015.

[111] "Echoge,echogen power systems,2020," Available online:https://www.echogen.com/ [Accessed: 05/06/2020].

[112] T. J. Held, "Initial test results of a megawatt-class supercritical CO$_2$ heat engine," in *The 4th international symposium–supercritical CO$_2$ power cycles*, pp. 9–10, 2014.

[113] C. S. Kalra, E. Sevincer, K. Brun, S. Antonio, D. C. Hofer, and J. J. Moore, "Development of high efficiency hot gas turbo-expander for optimized CSP supercritical CO$_2$ power block operation," in *The 4thInternational Symposium - Supercritical CO$_2$ Power Cycles*, September 9-10, 2014, Pittsburgh, Pennsylvania.

[114] J. Moore, K. Brun, N. Evans, and C. Kalra, "Development of 1 MWe supercritical CO$_2$ test loop," in *Proceedings of ASME Turbomachinery Technical Conference and Exposition*, June 15–19, 2015, Montreal, Quebec, Canada.

[115] J. Wilkes, T. Allison, J. Schmitt, J. Bennett, K. Wygant, R. Pelton, and W. Bosen, "Application of an integrally geared compander to an sCO$_2$ recompression brayton cycle," in *The fifth International Symposium—Supercritical CO$_2$ Power Cycles*, pp. 28–31, March 2016, Texas, USA.

[116] J. Marion, M. Kutin, A. McClung, J. Mortzheim, and R. Ames, "The step 10 MWe sCO$_2$ pilot plant demonstration," in *ASME Turbo Expo: Turbomachinery Technical Conference and Exposition*, American Society of Mechanical Engineers, June 17–21, 2019, Arizona, USA.

[117] R. J. Allam, M. R. Palmer, G. W. Brown Jr, J. Fetvedt, D. Freed, H. Nomoto, M. Itoh, N. Okita, and C. Jones Jr, "High efficiency and low cost of electricity generation from fossil fuels while eliminating atmospheric emissions, including carbon dioxide," *Energy Procedia*, vol. 37, pp. 1135–1149, 2013.

[118] R. Allam, S. Martin, B. Forrest, J. Fetvedt, X. Lu, D. Freed, G. W. Brown Jr, T. Sasaki, M. Itoh, and J. Manning, "Demonstration of the allam cycle: an update on the development status of a high efficiency supercritical carbon dioxide power process employing full carbon capture," *Energy Procedia*, vol. 114, pp. 5948–5966, 2017.

[119] H. Shin, J. Cho, Y.-J. Baik, J. Cho, C. Roh, H.-S. Ra, Y. Kang, and J. Huh, "Partial admission, axial impulse type turbine design and partial admission radial turbine test for sCO$_2$ cycle," in *Proceedings of ASME Turbo Expo: Turbomachinery Technical Conference and Exposition*, June 26–30, 2017, North Carolina, USA.

[120] A. Hacks, S. Schuster, H. J. Dohmen, F.-K. Benra, and D. Brillert, "Turbomachine design for supercritical carbon dioxide within the sCO$_2$-HeRo. EU project," in *Proceedings of ASME Turbomachinery Technical Conference and Exposition*, June 11–15, 2018, Oslo, Norway.

[121] S. Lee and H. Gurgenci, "A comparison of three methodological approaches for meanline design of supercritical CO$_2$ radial inflow turbines," *Energy conversion and management*, vol. 206, p. 112500, 2020.

[122] J. A. Keep and I. H. Jahn, "Numerical loss investigation of a small scale, low specific speed supercritical CO$_2$ radial inflow turbine," *Journal of Engineering for Gas Turbines and Power*, vol. 141, no. 9, 2019.

[123] M. Utamura, H. Hasuike, K. Ogawa, T. Yamamoto, T. Fukushima, T. Watanabe, and T. Himeno, "Demonstration of supercritical CO$_2$ closed regenerative Brayton cycle in a bench scale experiment," in *Proceedings of the ASME Turbo Expo: Turbine Technical Conference and Exposition*, June 11–15, 2012, Copenhagen, Denmark.

[124] T. Allison, J. Moore, R. Pelton, J. Wilkes, and B. Ertas, "7 - turbomachinery,"
in *Fundamentals and Applications of Supercritical Carbon Dioxide (sCO$_2$) Based
Power Cycles* (K. Brun, P. Friedman, and R. Dennis, eds.), pp. 147 – 215, Wood-
head Publishing, 2017.

[125] S. A. Wright, R. F. Radel, M. E. Vernon, P. S. Pickard, and G. E. Rochau, "Opera-
tion and analysis of a supercritical CO$_2$ Brayton cycle.," tech. rep., Sandia National
Laboratories (SNL), Albuquerque, NM, and Livermore, CA, 2010.

[126] "Step project home page,," Available online:
https://netl.doe.gov/coal/sCO$_2$/step10pilotplant. 2015, Accessed on: (26 November
2015).

[127] "Sunshot project home page," Available online:
https://www.energy.gov/eere/solar/project-profile-10-megawatt-supercritical-
carbon-dioxideturbine. Accessed on: (20 September 2021).

[128] "sCO$_2$ flex project home page," Available online: https://www.sCO$_2$-
flex.eu/about/structure/. Accessed on: (10 August 2021).

[129] "SOLARSCO2OL project home page," Available online:
https://www.solarsco2ol.eu/.

[130] A. J. Hacks, A. Vojacek, H. J. Dohmen, D. Brillert, A. Vojacek, *et al.*, "Experimental
investigation of the sCO$_2$-HeRo compressor," in *2nd European supercritical CO$_2$
Conference, Essen, Germany*, pp. 30–31, 2018.

[131] I. G. Wright, B. A. Pint, J. P. Shingledecker, and D. Thimsen, "Materials consid-
erations for supercritical CO$_2$ turbine cycles," in *Proceedings of ASME Turboma-
chinery Technical Conference and Exposition*, June 3–7, 2013, San Antonio, Texas,
USA.

[132] Y. Wang, G. Guenette, P. Hejzlar, and M. Driscoll, "Compressor design for the su-
percritical co2 brayton cycle," in *2nd International Energy Conversion Engineering
Conference*, 2004.

[133] R. Fuller, J. Preuss, and J. Noall, "Turbomachinery for Supercritical CO$_2$ Power Cycles," in *Proceedings of ASME Turbomachinery Technical Conference and Exposition*, June 11–15, 2012, Copenhagen, Denmark.

[134] Y.-S. Kang, J.-S. Huh, J. Cho, H. Shin, and Y.-J. Baik, "Design and Performance Assessments of a Partial Admission Axial Turbine Using Supercritical Carbon Dioxide," in *Fluids Engineering Division Summer Meeting*, July 2016.

[135] T. R.Bidkar, G.Musgrove,M. Day,C.Kulhanek, "Conceptual Designs of 50 MWe and 450 MWe Supercritical CO$_2$ Turbomachinery Trains for Power Generation from Coal. Part 2: Compressors," in *5th Int. Symp. - Supercrit. CO$_2$ Power Cycles*, pp. 1–18, March 28-31, 2016, San Antonio, Texas.

[136] S. F. Smith, "A simple correlation of turbine efficiency," *The Journal of the Royal Aeronautical Society*, vol. 69, no. 655, p. 467–470, 1965.

[137] E. Casati, S. Vitale, M. Pini, G. Persico, and P. Colonna, "Centrifugal Turbines for Mini-Organic Rankine Cycle Power Systems," *Journal of Engineering for Gas Turbines and Power*, vol. 136, 07 2014. 122607.

[138] D. Groschup, *Strömungstechnische Untersuchung einer Axialturbinenstufe im Vergleich zum Verhalten der erben Gitter ihrer Beschaufelung*. PhD thesis, 1977.

[139] J. Hirsch, C.and Denton, "Through flow calculations in axial turbomachines," AGARD Advisory Report N.175; Technical Report; AGARD, Propulsion and Energetics Panel, Working Group 12, Neuilly Sur Seine, France, 1981.

[140] P. Kötzing and B. Evers, "Test case e/tu-4, 4-stage low speed turbine," AGARD Report No.275 AR-275; Technical Report; AGARD, Neuilly Sur Seine, France, 1990.

[141] A. S. Abdeldayem, M. T. White, A. Paggini, M. Ruggiero, and A. I. Sayma, "Integrated aerodynamic and structural blade shape optimization of axial turbines operating with supercritical carbon dioxide blended with dopants," *Journal of Engineering for Gas Turbines and Power*, vol. 144, no. 10, p. 101016, 2022.

[142] A. S. Abdeldayem, S. I. Salah, O. Aqel, M. T. White, and A. I. Sayma, "Design of a 130 MW axial turbine operating with a supercritical carbon dioxide mixture for the scarabeus project," in *15*th *European Turbo-machinery conference*, 24-28th April 2023, Budapest, Hungry.

[143] M. White and A. Sayma, "A preliminary comparison of different turbine architectures for a 100 kW supercritical CO_2 Rankine cycle turbine," in *The 6*th *International Supercritical CO_2 Power Cycles Symposium*, 27-29 March 2018, Pennsylvania, USA.

[144] C. Spadacini, E. Pesatori, L. Centemeri, N. Lazzarin, R. Macchi, and M. Sanvito, "Optimized cycle and turbomachinery configuration for an intercooled, recompression sCO2 cycle," in *The 6*th *International Supercritical CO_2 Power Cycles Symposium*, 2018,Pennsylvania, USA.

[145] M. Kibsey and S. Sjolander, "Influence of Mach number on profile loss of axial-flow gas turbine blades," in *ASME Turbo Expo: Turbomachinery Technical Conference and Exposition*, American Society of Mechanical Engineers Digital Collection, June 13–17, 2016, Seoul, South Korea.

[146] K. W. Van Treuren, T. Simon, M. von Koller, A. R. Byerley, J. W. Baughn, and R. Rivir, "Measurements in a turbine cascade flow under ultra low Reynolds number conditions," *J. Turbomach.*, vol. 124, no. 1, pp. 100–106, 2002.

[147] J. Choi, S. Teng, J.-C. Han, and F. Ladeinde, "Effect of free-stream turbulence on turbine blade heat transfer and pressure coefficients in low Reynolds number flows," *International Journal of Heat and Mass Transfer*, vol. 47, no. 14, pp. 3441–3452, 2004.

[148] F. Satta, D. Simoni, M. Ubaldi, P. Zunino, and F. Bertini, "Profile and secondary flow losses in a high-lift LPT blade cascade at different Reynolds numbers under steady and unsteady inflow conditions," *Journal of Thermal Science*, vol. 21, p. 483–491, 2012.

[149] R. Brachmanski and R. Niehuis, "Mach number distribution and profile losses for low pressure turbine profiles with high diffusion factors," *Journal of Turbomachinery*, vol. 139, 2017.

[150] C. Prakash, D. Cherry, H. Shin, J. Machnaim, L. Dailey, R. Beacock, D. Halstead, A. Wadia, S. Guillot, and W. Ng, "Effect of loading level and distribution on LPT losses," in *ASME Turbo Expo: Power for Land, Sea, and Air*, June 9–13, 2008, Berlin, Germany.

[151] A. L. Braslow, "A review of factors affecting boundary-layer transition," *Langley Research Center, University of Virginia,, Washington, DC*, 1965.

[152] A. S. Lebedev and K. S. V., "Trends in increasing gas-turbine units efficiency," *Thermal Engineeringal Society*, vol. 55, no. 6, p. 461–468, 2008.

[153] G. Lozza, "A comparison between the Craig-Cox and the Kacker-Okapuu methods of turbine performance prediction," *Meccanica*, vol. 17, no. 4, pp. 211–221, 1982.

[154] Z. Zou, S. Wang, H. Liu, and W. Zhang, "Axial turbine aerodynamics for aero-engines," *Springer, Singapore. https://doi. org/10*, vol. 1007, pp. 978–981, 2018.

[155] J. D. Coull and H. P. Hodson, "Blade loading and its application in the mean-line design of low pressure turbines," *Journal of Turbomachinery*, vol. 135, 2012.

[156] A. Giuffre and M. Pini, "Design guidelines for axial turbines operating with non-ideal compressible flows," *J. Eng. Gas Turbines Power*, vol. 143, 2021.

[157] J. Moore and J. S. Tilton, "Tip leakage flow in a linear turbine cascade," *Journal of Turbomachinery*, 1988.

[158] A. Perdichizzi and V. Dossena, "Incidence angle and pitch–chord effects on secondary flows downstream of a turbine cascade," *Journal of Turbomachinery*, vol. 115, no. 3, pp. 383–391, 1993.

[159] V. Dossena, G. D'Ippolito, and E. Pesatori, "Stagger angle and pitch-chord ratio effects on secondary flows downstream of a turbine cascade at several off-design conditions," *Journal of Turbomachinery*, pp. 1429–1437, 2004.

[160] D. Bonalumi, S. Lasala, and E. Macchi, "CO_2-$TiCl_4$ working fluid for high-temperature heat source power cycles and solar application," *Renewable Energy*, vol. 147, pp. 2842–2854, 2020.

[161] "Andrea Paggini," personal communication, November 1, 2022.

[162] S. Dixon and C. Hall, "Chapter 2 - dimensional analysis: Similitude 2," in *Fluid Mechanics and Thermodynamics of Turbomachinery* (S. Dixon and C. Hall, eds.), pp. 97 – 141, Boston: Butterworth-Heinemann, sixth edition ed., 2010.

[163] M. V. Petrovic and W. Riess, "Off-design flow analysis and performance prediction of axial turbines," in *Proceedings of ASME 1997 International Gas Turbine and Aeroengine Congress and Exhibition*, June 2–5, 1997, Orlando, Florida, USA.

A Loss modeling correlations

This appendix details the loss models that are widely used for the design of turbomachinery operating with fluids such as air or steam. Some of these models are adopted into the mean-line design tool to predict the performance of sCO$_2$ axial turbine. In this section, Soderberg [62], Ainley and Mathieson [63], Dunham and Came [64], Kacker and Okapuu [65] and Aungier [66] correlations will be presented along with a brief discussion about the differences between the stated models.

A.1   Profile losses

A.1.1   Soderberg loss model

Soderberg's [62] loss model accounts for the effect of profile and secondary flow losses where tip clearance and trailing edge losses are ignored. In this model, the profile losses are calculated as a function of the blade deflection. It is considered to be an oversimplified model where the effect of Mach number and fluid non-dimensional parameters are neglected. Though, it is considered to be satisfactory for preliminary design phase as it allows the loss within the stator and rotor to be estimated based on the amount of expansion that occurs within each passage. The loss coefficients are represented as:

$$\zeta^* = 0.04 + 0.06\left(\frac{\varepsilon}{100}\right)^2 \tag{A.1}$$

$$\zeta_N = \left(\frac{10^5}{Re}\right)^{1/4}\left[(1+\zeta^*)\left(0.993 + 0.075\frac{l}{H}\right) - 1\right] \tag{A.2}$$

$$\zeta_R = \left(\frac{10^5}{Re}\right)^{1/4}\left[(1+\zeta^*)\left(0.975 + 0.075\frac{l}{H}\right) - 1\right] \tag{A.3}$$

$$\varepsilon_N = \alpha_1 + \alpha_2 \ \& \ \varepsilon_R = \beta_2 + \beta_3 \tag{A.4}$$

Where ζ^* is the nominal loss coefficient, H is the bade height, l is the blade chord length, H/l is the aspect ratio, α is the nozzle absolute angles, β is the rotor relative angles and Re is Reynolds number, 1, 2 and 2, 3 subscripts correspond to the inlet and exit conditions for

the stator and rotor respectively.

A.1.2   Ainley and Mathieson loss model

Following Soderberg's model, Ainley and Mathieson [63] firstly estimated the profile losses at zero incidence. Afterwards the stalling incidence, the incidence at which the profile loss is twice the loss achieved at zero incidence, is obtained and hence, the incidence and profile losses at non-zero incidence are determined. This has been done assuming that the profile losses ratio at non-zero incidence with respect to the zero incidence is function of the defined stalling incidence. Stalling incidence is assumed to be function of inlet blade, exit flow angle and pitch to chord ratio as shown in Figures A.1a and A.1b. Nonetheless, the defined formula is restricted for the maximum blade thickness to chord ratio (t/c) greater than 0.15 and less than 0.25 ($0.15 < t/c < 0.25$) for impulse turbine types. Profile losses are graphed for special cases where $\alpha_1{'} = 0$ and $\alpha_1{'} = \alpha_2$ [63]. Other than these cases, the following equation should be used:

$$Y_{p[AM]} = \left\{ Y_{p\ (\alpha_1{'}=0)} + \left(\frac{\alpha_1{'}}{\alpha_2} \right)^2 \left[Y_{p\ (\alpha_1{'}=\alpha_2)} - Y_{p\ (\alpha_1{'}=0)} \right] \right\} \left(\frac{t/c}{0.2} \right)^{\alpha_1{'}/\alpha_2} \qquad (A.5)$$

Where $\alpha_1{'}$ and α_2 : Blade and flow angles at the inlet and exit condition, i is the incidence angle, t/c is the maximum blade thickness to chord ratio. The same correlation applies for the stator profile losses at zero incidence angle where $\alpha_1{'}$ and α_2 will be replaced with $\beta_2{'}$ and β_3 respectively.

A.1.3   Dunham and Came Loss Model

Dunham and Came [64] reviewed the performance correlations by Ainley and Mathieson, for all losses including the profile, secondary and tip clearance losses, using more recent data. The effect of inlet angle, gas inlet and outlet angles, and blade pitch/chord ratio, blade thickness/chord and trailing edge thickness were included in the Ainley and Mathieson profile loss correlation. However, additional losses incurred when the blade row shocks have not been considered. Thus, the Dunham and Came model considered this effect by
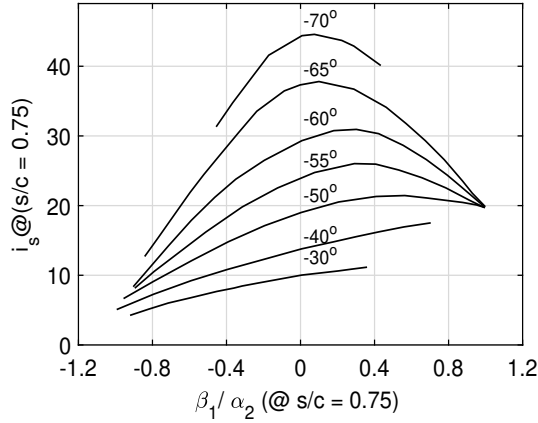
(a) Positive stalling incidence of turbine blades [63].
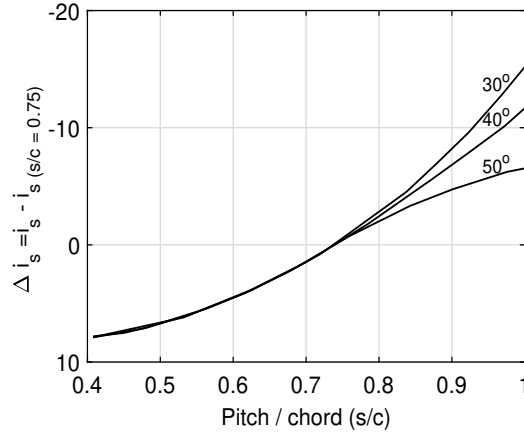
(b) Incidence correction [63].

introducing an arbitrary correction factor incorporating a numerical constant chosen to fit the overall efficiency data as presented in Equations A.6 [64]

$$Y_p = Y_p[\text{AM}] \times [1 + 60(\text{M}_n - 1)^2] \tag{A.6}$$

where $Y_p[\text{AM}]$ is the profile loss introduced by Ainley and Mathieson loss model and M_n is Mach number at the exit of the blade.

A.1.4   Kacker and Okapuu loss model

Further model modifications have been applied to the AMDC model [65]. In the Kacker and Okapuu model, $\left|\frac{\alpha_1'}{\alpha_2}\right|$ term is added to ADMC model to allow for the negative inlet angle as presented in Equation A.7.

$$Y_{p,AMDC} = \left\{ Y_{p\ (\alpha_1'=0)} + \left|\frac{\alpha_1'}{\alpha_2}\right| \left(\frac{\alpha_1'}{\alpha_2}\right) \left[Y_{p\ (\alpha_1'=\alpha_2)} - Y_{p\ (\alpha_1'=0)} \right] \right\} \left(\frac{t/c}{0.2}\right)^{\alpha_1'\ /\ \alpha_2} \tag{A.7}$$

Subsequent to the ADMC loss models, it has been revealed that profile loss is dependent on Mach number even in the sub-sonic flow regime. Profile losses can be affected by fluid compressibility in two different means, occurring shocks at the leading edges and the flow acceleration within the blade channel. Shock waves can happen at the blade leading edge in a low average inlet Mach number owing to the flow acceleration adjacent to high curved leading edge. Thus, inlet Mach number should be considered during the design

stage and it should be kept approximately less than 0.6 [65]. Shock loss were expressed as follows:

$$Y_{Shock} = 0.75 \left(f_{hub} \times Ma_{in,rel} - 0.4^{1.75} \right) \left(\frac{r_{hub}}{r_{tip}} \right) \left(\frac{P_{0rel,in} - P_{in}}{P_{0rel,out} - P_{out}} \right) \tag{A.8}$$

where P_{0rel} is the total relative pressure, P is the static pressure, Ma is the Mach number, r_{hub} and r_{tip} are the hub and tip radius respectively, in, out and rel subscripts stands for the inlet, outlet conditions and the relative property respectively.

$$\left(\frac{\Delta p}{q_2} \right)_{HUB} = 0.75 \left(M_{2hub} - 0.4 \right)^{1.75} \tag{A.9}$$

Since this loss is a local loss, it is an overestimation to consider this amount of loss for the whole blade and thus a mean-line loss of the blade inlet shocks were introduced as:

$$\left(\frac{\Delta p}{q_3} \right)_{SHOCK} = \left(\frac{R_h}{R_t} \right) \left(\frac{\Delta p}{q_2} \right)_{HUB} \tag{A.10}$$

$$\left(\frac{\Delta P}{q_2} \right)_{SHOCK} = Y_{SHOCK} = \left(\frac{\Delta p}{q_1} \right) \left(\frac{p_2}{p_3} \right) \frac{1 - \left(1 + \frac{k-1}{1} M_2^2 \right)^{\frac{k}{k-1}}}{1 - \left(1 + \frac{k-1}{1} M_3^2 \right)^{\frac{k}{k-1}}} \tag{A.11}$$

where q is the dynamic head and p is the static pressure, k is the ratio of specific heats, M_2 and M_3 are the relative Mach numbers at the inlet and exit of the blades.

$$K_P = 1 - K_2(1 - K_1) \tag{A.12}$$

$$K_1 = 1 - 1.25[M_3 - 0.2] \tag{A.13}$$

$$K_2 = [M_1/M_2]^2 \tag{A.14}$$

In the Kacker and Okapuu loss model, the loss coefficients are separated from each other where the trailing edge loss coefficient is separated from the rest of losses [65]. In the AMDC model, the profile losses are multiplied trailing edge loss collectively Y_{TET} at any thickness to pitch ratio (t/s) other than 0.02. From AMDC model Y_{TET} value is interpreted from graphs to be 0.914 at zero trailing edge thickness. However, the aerodynamic developments during the last three decades suggests that factor should be 2/3 instead. Even-

tually, the profile loss coefficient Y_P is expressed as follows for the subsonic regime of operation [65]:

$$Y_p = 0.914 \left(\frac{2}{3} Y_{p,ADMC} K_P + Y_{SHOCK} \right) \tag{A.15}$$

The Ainley and Mathieson loss model was introduced at reference Reynolds of 2×10^5 based on the true chord and gas exit conditions. Hence, a correction was presented as:

$$f_{(Re)} = \begin{cases} \left(\frac{Rec}{2 \times 10^5} \right)^{-0.2}, \, for \quad Rec \le 2 \times 10^5 \\ 1.0 \, , \, for \, 2 \times 10^5 < Rec < 10^6 \\ \left(\frac{Rec}{10^6} \right)^{-0.2}, \, for \, Rec > 10^6 \end{cases} \tag{A.16}$$

where Rec is Reynolds number based on true chord and exit gas conditions Since, there is little evidence in the literature that the other losses are affected by Reynolds number. The above correction is applied for the profile losses only [65] and Hence,

$$Y_p = f_{(Re)}[Y_p] \tag{A.17}$$

A.1.5   Craig and Cox loss model

Craig and Cox [60] interpreted profile losses for in-compressible flow conditions which included the variation blade angles, passage geometry and pitch to backbone length ratio only. Craig and Cox introduced profile losses function of the basic profile loss $X_{(pb)}$. Followed by applying corrections for Reynolds number effect (N_{pr}), incidence effect (N_{pi}) and trailing edge thickness losses effect (N_{pt}).

$$X_p = x_{pb} \, N_{pr} N_{pt} + (\Delta x_p)_t + (\Delta x_p)_{s/e} + (\Delta x_p)_m \tag{A.18}$$

The rest of profile loss increments $X p_{(s/e)}$, $X p_{(m)}$ and $X p_{(s/e)}$ are expressed as a functions of $F_L(s/b)$ and the blade passage contraction ratio (CR), Mach number and blade back radius ratio and loss ratios. They are presented in graphs function of Reynolds number, trailing edge thickness to pitch ratio and incidence ratio respectively (Figures A.2b - A.2f).
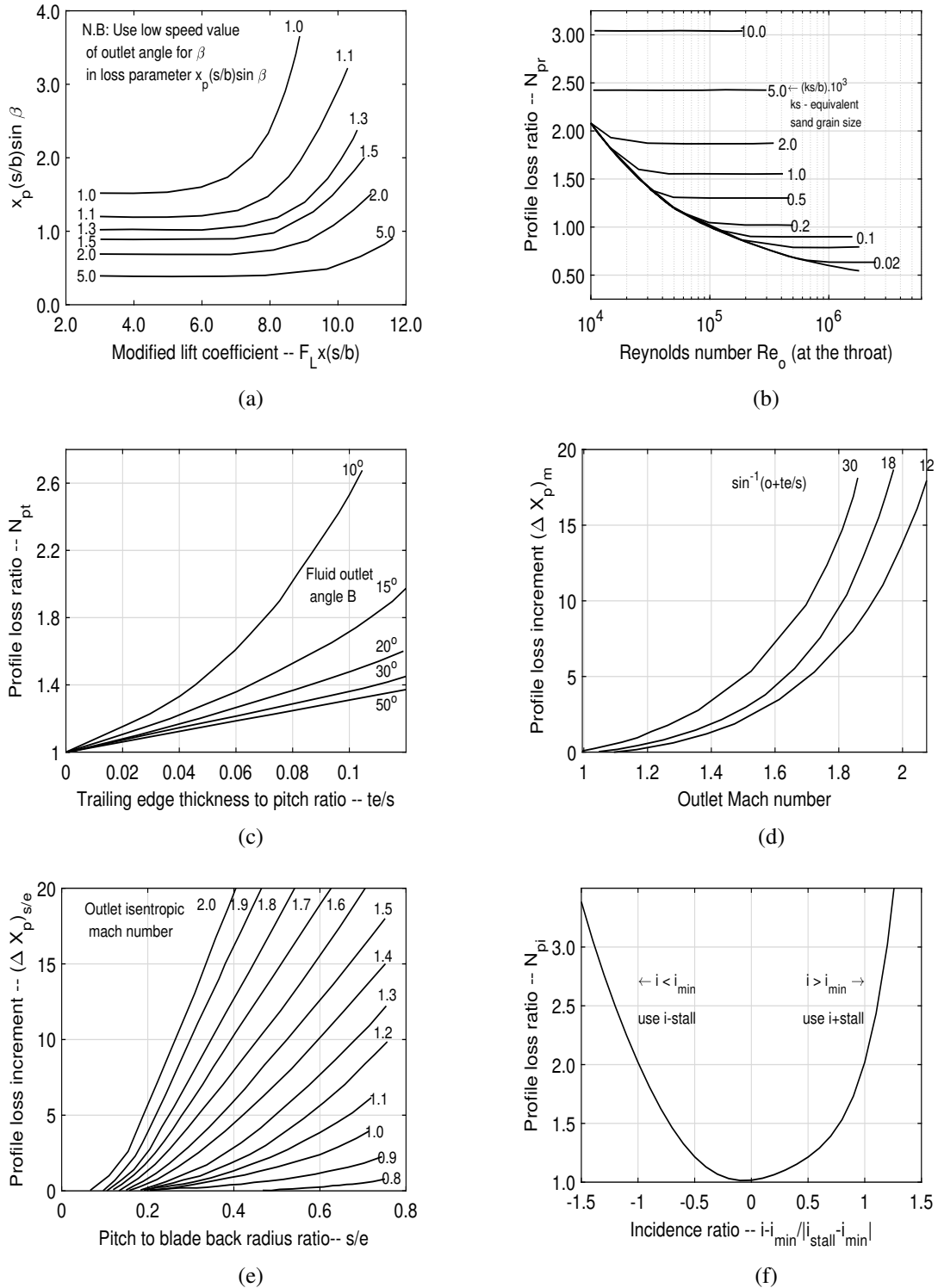
Figure A.2: (a) Basic profile loss [60](b) profile loss ratio against Reynolds number effect,(c) trailing edge thickness losses,(d) Mach number loss for convergent blading, (e) blade back radius losses (f) incidence losses

A.1.6 Aungier loss model

Ultimately, Aungier introduced a performance model that is based on the previously presented Ainley and Mathieson's model considering the refinements introduced by Kacker and Okapuu. The profile loss is expressed as:

$$Y_p = K_{mod}K_{inc}K_MK_pK_{RE}\left\{\left[Y_{p1}+\xi^2\left(Y_{p2}-Y_{p1}\right)\right]\left(5t_{max}/c\right)^{\xi}-\Delta Y_{TE}\right\} \tag{A.19}$$

where K_{mod} is an experience factor suggested by Kacker and Okapuu, K_{inc} is the correction for off-design incidence effects, K_M is the correction for Mach number effects, K_p is thecorrection for compressibility effect, K_{RE} is the correction for Reynolds number effects, Y_{p1} is the profile loss coefficients for stator blades ($\alpha_1' = 0$).

Within the profile loss model, Aungier presented an analytical model that extrapolates the graphical parameters presented by AM in Figure A.3
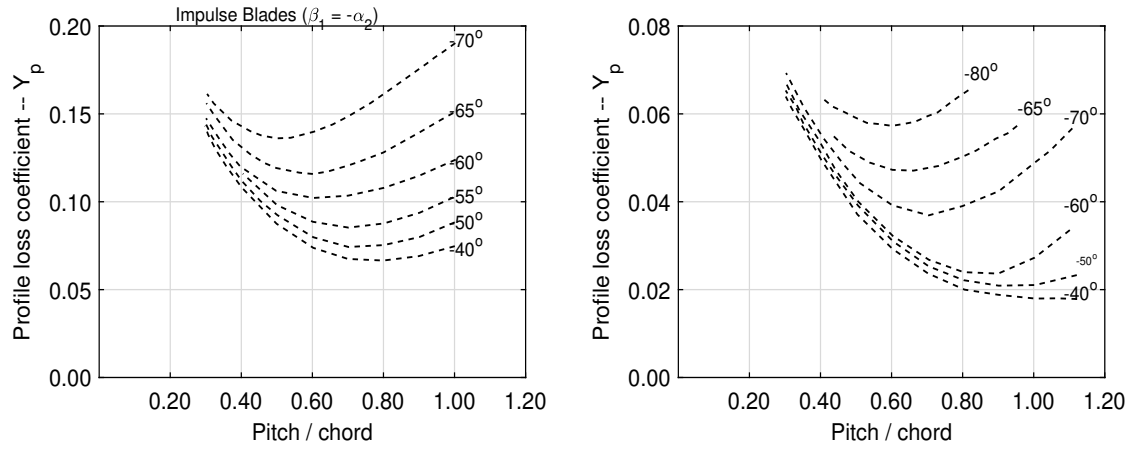

Figure A.3: (a) Profile loss coefficient (Impulse blades), (b) Profile loss coefficient (Nozzle blades) [63]

A.2 Secondary flow losses

A.2.1 Soderberg loss model

To predict the secondary flow losses, Soderberg presented a mathematical correlation where losses are interpreted as function of the aspect ratio neglecting the effect of inlet

boundary layer and blade geometry (Equations A.1 to A.4).

A.2.2   Ainley and Mathieson loss model

In Ainley and Mathieson model, the secondary and clearance loss have been treated simultaneously because of their similar forms. The secondary flow losses were introduced as a function of the pitch to chord ratio (s/c), lift coefficient based on mean velocity vector (C_L) and flow angles. The presented formula is restricted for use at an incidence ratio $-1.5 \leq i/i_s \leq 1.0$. At $i/i_s > 1.0$ & $i/i_s < -1.5$, both losses, secondary and tip clearance, are assumed to be constant and equal to the value at $i/i_s = 1.0$ & $i/i_s = -1.5$ respectively. The presented model assumed uniform turbine inlet conditions. This model is only applicable for blades with $t/s = 0.02$ and hence, a correction factor should be applied when the blade ratio deviates from the mentioned value. The secondary flow loss is represented as:

$$Y_s = [\lambda + B(k/h)] \left[\frac{C_L}{s/c} \right]^2 \left[\frac{\cos^2 \alpha_2}{\cos^3 \alpha_m} \right] \tag{A.20}$$

where

$$\alpha_m = \tan^{-1}[(\tan \alpha_2 - \tan \alpha_1/2)] \tag{A.21}$$

$$C_L = 2 \ (s/c) (\tan \alpha_1 + \tan \alpha_2) \cos \alpha_m \tag{A.22}$$

Where Y_s is the secondary loss coefficient, Y_k is the tip clearance loss coefficient, k is the radial tip clearance, h is the average blade height, λ is a factor function of the blade geometry.

A.2.3   Dunham and Came loss model

Secondary flow losses occur as a result of the interaction between the flow through the blade passage and end wall boundary layer. Additionally, the boundary layer thickness effect on the secondary loss is evident; thicker boundary layer results in higher secondary flow losses. Nevertheless, these effects have not been considered in the previous studies and hence, they provided un-realistic estimation for the real losses. Thus, Dunham and Came introduced a modification for the Ainley and Mathieson secondary loss model where

the effect of blade loading on secondary flow losses has been taken into consideration. Furthermore, they calculated the development of the boundary layer to achieve a more accurate model. Nonetheless, a single numerical constant is assumed in place of boundary layer thickness and blade shape function to avoid model complication [64]. Therefore, the secondary flow losses are expressed as:

$$Y_s = 0.0334 \left(\frac{c}{h}\right) \left(\frac{\cos \alpha_2}{\cos \alpha_1'}\right) \left[\frac{C_L}{s/c}\right]^2 \left[\frac{\cos^2 \alpha_2}{\cos^3 \alpha_m}\right] \tag{A.23}$$

$$\alpha_m = \tan^{-1}[(\tan \alpha_2 - \tan \alpha_1/2)] \tag{A.24}$$

$$C_L = 2 \ (s/c)(\tan \alpha_1 + \tan \alpha_2)\cos \alpha_m \tag{A.25}$$

Additionally, Reynolds number correction have been applied directly to the profile and secondary losses correlation as shown in Equation A.26

$$(Y_p + Y_s)_{corrected} = (Y_p + Y_s)\left(\frac{Re}{2 \times 10^5}\right)^{-0.2} \tag{A.26}$$

A.2.4   Kacker and Okapuu loss model

A similar secondary loss correlation to the ADMC model was introduced with the exception of its dependence on the blade aspect ratio. This modification has been performed owing to the more rapid increase in losses with respect to the decreased aspect ratio observed in AMDC model. Accordingly, the presented model shall result in less rapid increase in the losses with the decrease in the aspect ratio [65].

$$Y_{s,ADMC} = 0.0334 f_{(AR)} \left(\frac{C_L}{s/c}\right)^2 \left(\frac{\cos \alpha_2}{\cos \alpha_1'}\right) \frac{\cos^2 \alpha_2}{\cos^3 \alpha_m} \tag{A.27}$$

$$\frac{C_L}{s/c} = 2(\tan \alpha_1 + \tan \alpha_2) \cos \alpha_m \tag{A.28}$$

$$\alpha_m = \tan^{-1}\left[\frac{1}{2}(\tan \alpha_1 - \tan \alpha_2)\right] \tag{A.29}$$

$$
f_{(AR)} =
\begin{cases}
\left(\dfrac{1-0.25\sqrt{2-h/c}}{h/c} \right) & h/c \le 2 \\[2ex]
\left(\dfrac{1}{h/c} \right) & h/c > 2
\end{cases}
\tag{A.30}
$$

$$
K_3 = \left[\frac{1}{h/b_x} \right]^2
\tag{A.31}
$$

where $f_{(AR)}$ is aspect ratio function, h is the blade height, c is the chord length, b_x is the axial chord length.

To account for Mach number effect, a correction factor is defined to the secondary loss function of the profile loss and aspect ratio as shown in Equations A.32 to A.33.

$$
K_s = 1 - K_3 \left(1 - K_P \right)
\tag{A.32}
$$

$$
Y_s = 1.2\, Y_{s,AMDC} K_3
\tag{A.33}
$$

Where K_3 is a Mach number correction factor that's graphed against the b_x/h, b_x: the axial chord, h: the blade height. Regarding the leading-edge shock effects at high incidence Mach number, it has not been reconsidered again for the secondary flow losses, it was assumed that its effects is included in the previously calculated Y_{shock} [65].

A.2.5   Craig and Cox loss model

Craig and Cox [60] presented secondary flow losses correlation for shrouded blade rows that can be also applied for un-shrouded blades. The correlation has been interpreted by assuming that secondary flow losses are inversely proportional to the aspect ratio. Additionally, a similar Reynolds number effect to that of the profile losses have been applied to the secondary flow loss as shown in A.34. The derived relation is introduced as a function of the secondary loss ratio $(N_s)_{h/b}$ and factor $(x_s)_b$ which are graphed against the inverse aspect ratio (b/h), ratio of inlet and outlet velocity square respectively (Figures A.4a and A.4b) [60].

$$
X_s = (N_s)_r (N_s)_{h/b} (x_s)_b
\tag{A.34}
$$
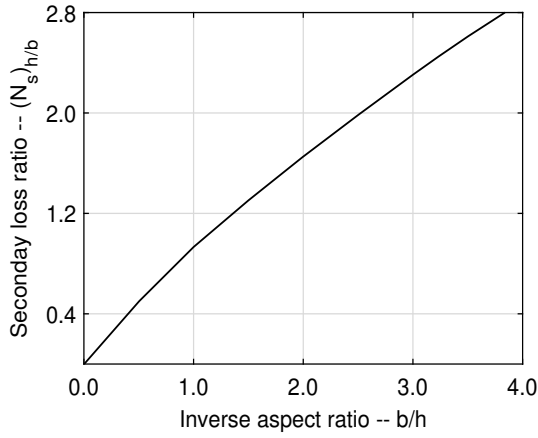
(a) Secondary loss-aspect ratio factor
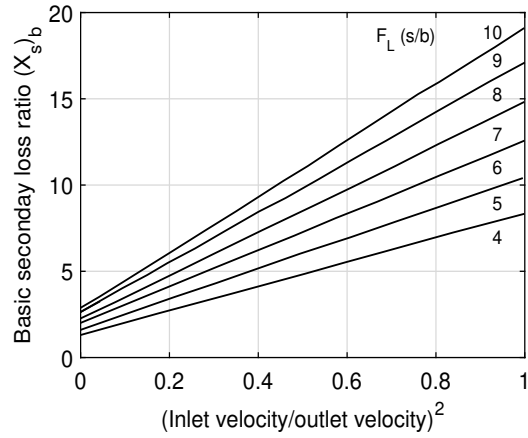
(b) Secondary loss-basic loss factor

A.2.6 Aungier Model

Aungier presented a secondary loss correlation that is quite similar to the correlation introduced by the ADMC model and refined by Kacker and Okapuu (Equations A.35 to A.38)

$$Y_s = 0.0334 f_{AR} \left(\frac{C_L}{s/c} \right)^2 \left(\frac{\cos \alpha_2}{\cos \alpha_1{}'} \right) \frac{\cos^2 \alpha_2}{\cos^3 \alpha_m} \tag{A.35}$$

$$\frac{C_L}{s/c} = 2(\tan \alpha_1 + \tan \alpha_2) \cos \alpha_m \tag{A.36}$$

$$\alpha_m = \tan^{-1} \left[\frac{1}{2} (\tan \alpha_1 - \tan \alpha_2) \right] \tag{A.37}$$

$$f_{(AR)} = \begin{cases} c/h & h/c \geq 2 \\ 0.5 \, (2c/h)^{0.7} & h/c > 2 \end{cases} \tag{A.38}$$

A.3 The trailing edge losses

The Soderberg's model ignored the effect of trailing edge losses. On the contrary, the Ainley and Mathieson model accounted for the trailing edge thickness effect on the profile loss by applying a correction factor for the correlation. Similarly in Craig and Cox correlations, profile losses are expressed function of the trailing edge loss. Kacker and Okapuu

introduced an equation for the trailing loss as a function of the energy coefficient $\Delta\Phi^2{}_{TET}$.
Two losses curves were presented for the axial entry nozzle and the impulse blades [65].
For blade types other than these, the following equation can be applied:

$$\Delta\Phi^2{}_{TET} = \Delta\Phi^2{}_{TET\,(\alpha_1'=0)} + \left|\frac{\beta_1}{\alpha_2}\right|\left(\frac{\alpha_1{}'}{\alpha_2}\right)\left[\Delta\Phi^2{}_{TET\,(\alpha_1'=\alpha_2)} - \Delta\Phi^2{}_{TET\,(\alpha_1'=0)}\right] \tag{A.39}$$

$$Y_{TE} = \frac{1}{1-\Delta\Phi^2{}_{TET}} - 1 \tag{A.40}$$

where $\Delta\Phi$ is the trailing edge K.E. loss coefficient.

Later, the above model has been modified by Aungier where the correlation is presented
in Equation A.41.

$$\Delta P_t = \frac{1}{2}\rho W_2{}^2 \left[s\,sin\beta_g/s\,sin\beta_g - t_2\right) - 1\right]^2 \tag{A.41}$$

$$Y_{TE} = 2\Delta P_t/\left(\rho W_2{}^2\right) = [t_2/s\,sin\beta_g - t_2]^2 \tag{A.42}$$

Where W is the relative velocity, t_2 is the trailing edge blade thickness, P_t is the the total
pressure. β_g is the gauging angle, ρ is the gas density.

A.4 Tip clearance loss

Ainley and Mathieson's model introduced the secondary and tip clearance losses together
in a single correlation. The Dunham and Came model proved that Ainley loading pa-
rameter is satisfactory in representing the blade loading effect on the tip clearance loses.
However, it has been recommended to replace the linear dependence of tip clearance loss
on the clearance nature by the power law for plain tip clearance; they proved to be better
for the turbine results [64].

$$Y_{t_{cl}} = B\left(\frac{c}{h}\right)\left[\frac{t_{cl}}{c}\right]^{0.78}\left[\frac{C_L}{s/c}\right]^2\left[\frac{\cos^2\alpha_2}{\cos^3\alpha_m}\right] \tag{A.43}$$

where $B = 0.47$ for plain tip clearance and 0.37 for shrouded blades.

In the case of shrouded turbine blades, the KO model implements the above correlation

proposed by ADMC (Equation A.43). However, Kacker and Okapuu claimed that ADMC model over-predicts the loss for un-shrouded blades. Hence, they presented the tip clearance losses separately from the secondary loss for un-shrouded blades as:

$$\Delta \eta_{t_{cl}} = \Delta \eta_0 \left(0.93 \times \frac{t_{cl}}{h \cos \alpha_2} \times \frac{r_{tip}}{r_{mean}} \right) \tag{A.44}$$

where h is the blade height, t_{cl} is the clearance gap, r_{tip} is the tip radius and r_{mean} is the mean radius. Ultimately, the Craig and Cox model presented a clearance losses correlation for un-shrouded blades function of the blade height (Equation A.45).

$$\Delta \eta_k = F_k \frac{A_k}{A_t} \eta_0 \tag{A.45}$$

where η_0 is the efficiency at zero clearance, A_k is the total effective area of clearance, A_t is the total blade throat area and F_k is the efficiency debit factor.